



UNIVERSITÀ DELLA CALABRIA


UNIVERSITA' DELLA CALABRIA

Dipartimento di Ingegneria Meccanica, Energetica e Gestionale (DIMEG)

Scuola di Dottorato Pitagora

In Scienze Ingegneristiche

Con il contributo di FSE – Fondo Sociale Europeo

CICLO XXVII

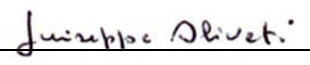
**FEASIBILITY OF A FREQUENCY-MODULATED, WIRELESS, MEMS
ACCELERATION EVALUATOR (ALE) FOR THE MEASUREMENT OF LOW-
FREQUENCY AND LOW-AMPLITUDE VIBRATIONS**

Settore Scientifico Disciplinare ING/IND 11


Direttore: Ch.mo Prof. Leonardo Pagnotta

Firma 

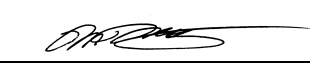
Supervisori: Ch.mo Prof. Giuseppe Oliveti

Firma 

Ch.mo Prof. Giancarlo Fortino

Firma 

Ch.mo Prof. Maria Q. Feng

Firma 

Dottorando: Ing. Alessandro Sabato

Firma 



UNIVERSITÀ DELLA CALABRIA


Università della Calabria

Dipartimento di Ingegneria Meccanica, Energetica e Gestionale (DIMEG)

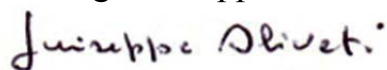
Doctoral School Pitagora
in
Engineering Sciences

DISSERTATION FOR THE DEGREE OF DOCTOR OF PHILOSOPHY

FEASIBILITY OF A FREQUENCY-MODULATED, WIRELESS, MEMS ACCELERATION EVALUATOR (ALE) FOR THE MEASUREMENT OF LOW- FREQUENCY AND LOW-AMPLITUDE VIBRATIONS

SUPERVISORS:

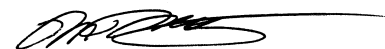
Prof. Ing. Giuseppe Oliveti



Prof. Ing. Giancarlo Fortino



Prof. Maria Q. Feng, Ph. D



CANDIDATE:

Ing. Alessandro Sabato



La presente tesi è cofinanziata con il sostegno della Commissione Europea, Fondo Sociale Europeo e della Regione Calabria. L'autore è il solo responsabile di questa tesi. La Commissione Europea e la Regione Calabria declinano ogni responsabilità sull'uso che potrà essere fatto delle informazioni in essa contenute.

This dissertation is co-funded with support from the European Commission - European Social Fund and Regione Calabria. The author is the only responsible for this dissertation. The European Commission and Regione Calabria disclaim any liability of use, which may be made of the information therein contained.

This dissertation is made of 235 pages, numbered from 1 to 215.

*“Press on!
Nothing in the world
can take place of persistence.
Talent will not. Nothing is more common
than unsuccessful man with talent.
Genius will not. Unrewarded
genius is almost a proverb.
Education will not. The world
is full of educated derelicts.
Persistence and determination
alone are omnipotent.”*

Calvin Coolidge

*I dedicate this work to my dad,
Prof. Ing. Adolfo Sabato,
my guide and source of inspiration.*

ABSTRACT

The necessity of measuring vibrations on structures and part of machineries is extremely important. Maintain under control aging structures, infrastructures and machinery – such as bridges, buildings, dams, pipelines, aircraft, ships, and railway tracks – plays a key role in the prediction of situations, which could jeopardize, or even destroy, the structure itself.

Recent advances in the Micro Electro-Mechanical System (MEMS) technology have made wireless MEMS accelerometers an attractive tool for Structural Health Monitoring (SHM) of civil engineering structures. MEMS technology refers to a family of devices which characteristic dimensions range from 10^{-3} to 10^{-6} m, that combine together electrical and mechanical components, and that are fabricated using integrated circuit batch-processing technologies. The SHM applications require the MEMS-based accelerometers to be accurate for measuring a wide range of structural vibrations: from ambient vibration (in the order of 10^{-2} $\text{m}\cdot\text{s}^{-2}$) to severe earthquakes (in the order of 10^1 $\text{m}\cdot\text{s}^{-2}$). In addition, natural frequencies in large civil engineering structures - including bridges and buildings - are generally in the order of 10^{-1} to 10^1 Hz. To date, sensors' low sensitivity and accuracy - especially at very low-frequencies - have imposed serious limitations for their application in monitoring large-sized structures. Conventionally, the MEMS sensor's analog signals are converted to digital signals before radio-frequency (RF) wireless transmission. The conversion can cause a low sensitivity to the important low-frequency and low-amplitude signals.

To overcome this difficulty, a prototype of a MEMS accelerometer system (Acceleration Evaluator - ALE) is presented. It converts the sensor output voltage to a frequency-modulated (FM) signal before RF transmission. This is achieved by using a Voltage to Frequency conversion (V/F) instead of the conventional Analog to Digital Conversion (ADC). The MEMS accelerometer system

presented in this study consists of a transmitter and receiver circuit boards. The former is equipped with a high sensitivity, low noise, MEMS-based accelerometer, a V/F converter and a wireless RF transmitter, whereas the latter contains a RF receiver and a F/V converter for demodulating the signal.

The efficacy of the designed prototype in measuring low-frequency and low-amplitude dynamic responses is validated to demonstrate wheatear or not it is useful to achieve resolution necessary for SHM purposes. It is done through extensive laboratory tests and experiments on real-world engineering structures. The firsts consist of calibration tests, studies about the effect of battery residual charge, maximum transmission distance evaluations, and dynamic comparisons with wired Integral Electronics Piezoelectric (IEPE) accelerometers. The latters consist of measurements on several typologies of structures: a flow-loop pipeline (industrial applications), a stone pinnacle (seismic applications), and a pedestrian bridge (civil infrastructures monitoring). In this study, the achieved results are discussed and indications for further prototype's developments given.

TABLE OF CONTENTS

ABSTRACT	I
TABLE OF CONTENTS	III
LIST OF TABLES	VI
LIST OF FIGURES	VIII
INTRODUCTION	1
CHAPTER I - THE MECHANIC OF VIBRATION	
1 – Introduction	5
2 – General concepts	6
3 – Classification of vibration	9
4 – Principal type of vibratory systems	12
4.1 - Undamped free vibration systems	13
4.2 - Damped free vibration systems	15
4.2.1 - Considerations on damped free vibration systems	19
4.3 - Undamped forced vibration systems	22
4.4 - Damped forced vibration systems	24
5 – Vibration transmissibility	30
CHAPTER II - INSTRUMENTATION FOR THE MEASUREMENT OF VIBRATIONS	
1 – Introduction	33
2 – Seismic instruments	35
2.1 - Instruments for displacement detection	35

2.2 - Instruments for acceleration detection	40
3 – Characteristics of vibration measuring instruments	44
3.1 - Sensitivity	44
3.2 - Transverse sensitivity	45
3.3 - Resolution	45
3.4 - Zero acceleration output	46
3.5 - Amplitude linearity	46
3.6 - Frequency range	47
4 – Typologies of accelerometers	48
4.1 - Piezoresistive accelerometers	49
4.2 - Capacitive accelerometers	50
4.3 - Linear Variable Differential Transformer (LVDT) accelerometers	52
4.4 - Fiber optic accelerometers	53
4.5 - Piezoelectric and Integral Electronics Piezoelectric (IEPE) accelerometers	54
4.6 - Micro Electro-Mechanical Systems (MEMS) accelerometers	62
5 – Problems connected to the usage of wire-based accelerometers	66
CHAPTER III - DESIGN OF A NEW SENSOR BOARD EMBEDDING A MEMS-BASED ACCELEROMETER	
1 – Introduction	68
2 – Summary review of MEMS-based accelerometer systems	70
2.1 - Academia-built platforms for WSN	70
2.2 - Commercial platforms for WSN	75
2.3 - MEMS-based accelerometer systems used for SHM	78
3 – Reasons for the realization of a new MEMS accelerometer system prototype	88
4 – Design of the Acceleration Evaluator (ALE)	91

4.1 - ALE transmitter board architecture	92
4.1.1 - Transmitter board sensing unit	95
4.1.2 - Transmitter board signal conditioning	98
4.1.3 - Transmitter board wireless RF antenna	101
4.2 - ALE receiver board architecture	102
4.2.1 - Receiver board wireless RF antenna	104
4.2.2 - Receiver board signal conditioning	105
4.2.3 - Receiver board Data Acquisition	105
5 – Cost analysis	107
CHAPTER IV - EVALUATION TESTS FOR THE ACCELERATION EVALUATOR (ALE) SYSTEM	
1 – Introduction	108
2 – Laboratory tests for the characterization of ALE’s performances	110
2.1 - Static calibration test	110
2.2 - Effects of battery residual charge	114
2.3 - Maximum transmission distance	116
2.4 - Comparative dynamic tests	125
2.4.1 - Sinusoidal wave input	125
2.4.2 - Periodic wave input	135
3 – Engineering structure experiments for the characterization of ALE’s performances	141
3.1 - Comparative tests on a flow-loop pipeline	142
3.2 - Comparative test on a stone pinnacle	148
3.3 - Vibration analyses of a pedestrian bridge	153
SUMMARY AND DISCUSSION	159
APPENDIX	166
REFERENCE	199
AKNOWLEDGEMENTS	213

LIST OF TABLES

Table 3.1 – Summary of the proposed MEMS-based accelerometer sensor boards	86
Table 3.2 – Summary of the investigate MEMS-based accelerometers	95
Table 3.3 – SiFlex 1600 SN. A specifications	96
Table 3.4 – ALE components cost	107
Table 4.1 – Relative error of wirelessly transmitted signal (Static calibration tests)	119
Table 4.2 – Relative error of wirelessly transmitted signal (Dynamic calibration tests - Indoor)	121
Table 4.3 – Relative error of wirelessly transmitted signal (Dynamic calibration tests – Outdoor)	121
Table 4.4 – ALE relative error and signals’ equivalent acceleration (Sinusoidal wave input)	131
Table 4.5 – ALE relative error and signals’ equivalent acceleration (Periodic wave input)	139
Table 4.6 – Summary results for the flow-loop pipeline test	147
Table 4.7 – Earthquake input features	150
Table 4.8 – Summary results of the pinnacle comparative test	151
Table 4.9 – Summary results of the pedestrian bridge test	158
Table A.1 – Calibration test data	167
Table A.2 – Effect of battery residual charge test data	168
Table A.3 – Calibration chart versus distance test data (5, 10 m)	169
Table A.4 – Calibration chart versus distance test data (15, 20 m)	170
Table A.5 – Calibration chart versus distance test data (25, 30 m)	171

Table A.6 – Mean values and standard deviations for the 5 Hz sinusoidal wave excitation	172
Table A.7 – Mean values and standard deviations for the 2 Hz sinusoidal wave excitation	173
Table A.8 – Mean values and standard deviations for the 1 Hz sinusoidal wave excitation	174
Table A.9 – Mean values and standard deviations for the 0.5 Hz sinusoidal wave excitation	176
Table A.10 – Mean values and standard deviations for the 0.2 Hz sinusoidal wave excitation	179
Table A.11 – Mean values and standard deviations for the 5 Hz periodic wave excitation	186
Table A.12 – Mean values and standard deviations for the 2 Hz periodic wave excitation	187
Table A.13 – Mean values and standard deviations for the 1 Hz periodic wave excitation	188
Table A.14 – Mean values and standard deviations for the 0.5 Hz periodic wave excitation	190

LIST OF FIGURES

Fig. 1.1 – Elements of a vibratory system	6
Fig. 1.2 – Time-history of an oscillatory motion made of a pure tone	8
Fig. 1.3 – Displacement, velocity and acceleration in the harmonic motion	8
Fig. 1.4 – Periodic vibration	9
Fig. 1.5 – Complex vibration	9
Fig. 1.6 – Deterministic vibration	10
Fig. 1.7 – Random vibration	10
Fig. 1.8 – Possible combinations of dynamic system's passive elements and applied forces	12
Fig. 1.9 – Time-histories of a dynamic system subjected to a damped free vibration	19
Fig. 1.10 – Time-histories of a dynamic system subjected to an undamped forced vibration	24
Fig. 1.11 – Magnification factor κ versus frequency ratio r for various values of damping factor ζ	27
Fig. 1.12 – Phase angle ψ versus frequency ratio r for various values of damping factor ζ	28
Fig. 1.13 – Amplitude X of the oscillation with different values of stiffness k	28
Fig. 1.14 – Amplitude X of the oscillation with different values of mass m	29
Fig. 1.15 – Transmissibility versus frequency ratio r for various values of damping factors ζ	31
Fig. 2.1 – Schematic sketch of a seismic instrument	35

Fig. 2.2 – Steady-state response of a vibrometer	38
Fig. 2.3 – Phase displacement of a vibrometer	38
Fig. 2.4 – Instrument amplitude response for different values of r and ζ	42
Fig. 2.5 – Amplitude distortion in accelerometers	43
Fig. 2.6 – Schematic diagram of a piezoresistive accelerometer	50
Fig. 2.7 – Schematic diagram of a capacitive accelerometer	51
Fig. 2.8 – Exploded view of a micro-machined capacitive accelerometer (source: Harris [5])	52
Fig. 2.9 – Schematic diagram of a LVDT accelerometer	53
Fig. 2.10 – Schematic diagram of a fiber optic accelerometer	54
Fig. 2.11 – Schematic diagram of a piezoelectric accelerometer	56
Fig. 2.12 – Shear-type piezoelectric accelerometer	57
Fig. 2.13 – Compression-type piezoelectric accelerometer	57
Fig. 2.14 – Components of an IEPE accelerometer	59
Fig. 2.15 – Electrical scheme of a piezoelectric accelerometer	60
Fig. 2.16 – MEMS-based accelerometer	63
Fig. 2.17 – MEMS-based accelerometer structure	63
Fig. 2.18 – Capacitors set in a MEMS-based accelerometer (LIS331DLH by STMicroelectronics)	64
Fig. 3.1 – Prototype of the wireless sensing unit proposed by Lynch (source: Lynch [63])	72
Fig. 3.2 – Crossbow Rene (a) and Rene2 (b) mote platforms	76
Fig. 3.3 – Crossbow Mica2 (a), Mica2DOT (b), and IRIS (c) mote platforms	76
Fig. 3.4 – Intel Imote2 platform (source: SIMLab – U. of Florida)	77
Fig. 3.5 – Crossbow MTS310 sensor board	79
Fig. 3.6 – Tadeo sensor board (source: Ruiz-Sandoval [94])	80

Fig. 3.7 – Sensor board prototype proposed by the UC Berkeley research group (source: Pakzad [99])	81
Fig. 3.8 – WiMMS unit modified by Wang (source Wang et al. [102])	82
Fig. 3.9 – Wireless Sensing Solution proposed by Whelan (source: Whelan and Janoyan [102])	83
Fig. 3.10 – ITS400 (a), SHM-H (b), and SHM-H (c) sensor boards (source: Jo et al. [108])	85
Fig. 3.11 – Traditional WSN sensor board block diagram	91
Fig. 3.12 – The ALE transmitter board block diagram	93
Fig. 3.13 – Prototype transmitter circuit tested on the solderless breadboard	93
Fig. 3.14 – Circuit diagram of the ALE transmitter board	94
Fig. 3.15 – PCB layout of the ALE transmitter board	94
Fig. 3.16 – Prototype of the ALE transmitter board	94
Fig. 3.17 – SF1600 dimensions and picture (source: www.colibrys.ch [127])	97
Fig. 3.18 – SF1600 block diagram	97
Fig. 3.19 – Electrical scheme of the TMR3-1222HI DC/DC converter	100
Fig. 3.20 – Wireless RF antenna top view (a) and bottom view (b)	101
Fig. 3.21 – The ALE receiver board block diagram	102
Fig. 3.22 – Prototype receiver circuit tested on the solderless breadboard	103
Fig. 3.23 – Circuit diagram of the ALE receiver board	103
Fig. 3.24 – PCB layout of the ALE receiver board	103
Fig. 3.25 – Prototype of the ALE receiver board	104
Fig. 3.26 – The ALE assembled prototype and battery package	106
Fig. 3.27 – The ALE transmitter functional diagram	106
Fig. 3.28 – The ALE receiver functional diagram	106

Fig. 4.1 – Determination of gravitational acceleration	
components acting on the SF1600 sensing element	111
Fig. 4.2 – Setup for the static calibration test	112
Fig. 4.3 – Results of static calibration test made on the ALE	113
Fig. 4.4 – Test setup for the evaluation of the battery residual	
charge effects	115
Fig. 4.5 – Effect of battery residual charge on sensor output	116
Fig. 4.6 – Calibration chart when receiver is 5 m away from transmitter	117
Fig. 4.7 – Calibration chart when receiver is 15 m away from transmitter	118
Fig. 4.8 – Calibration chart when receiver is 30 m away from transmitter	118
Fig. 4.9 – Setup for the maximum transmission distance dynamic	
test (Indoor)	120
Fig. 4.10 – Time histories of wirelessly transmitted signal (Indoor)	122
Fig. 4.11 – Time histories of wirelessly transmitted signal (Outdoor)	122
Fig. 4.12 – Detail of the time-history of wirelessly transmitted signal	
(30 m - Outdoor)	123
Fig. 4.13 – PSD of the signal received from the ALE	123
Fig. 4.14 – Setup for the shaking table test (sinusoidal waves input)	126
Fig. 4.15 – Comparison of measurements by the two sensors in	
time domain (5 Hz)	126
Fig. 4.16 – Comparison of measurements by the two sensors in	
frequency domain (5 Hz)	127
Fig. 4.17 – Comparison of measurements by the two sensors in	
time domain (2 Hz)	127
Fig. 4.18 – Comparison of measurements by the two sensors in	
frequency domain (2 Hz)	127
Fig. 4.19 – Comparison of measurements by the two sensors in	
time domain (1 Hz)	128
Fig. 4.20 – Comparison of measurements by the two sensors in	
frequency domain (1 Hz)	128

Fig. 4.21 – Comparison of measurements by the two sensors in time domain (0.5 Hz)	128
Fig. 4.22 – Comparison of measurements by the two sensors in frequency domain (0.5 Hz)	129
Fig. 4.23 – Comparison of measurements by the two sensors in time domain (0.2 Hz)	129
Fig. 4.24 – Comparison of measurements by the two sensors in frequency domain (0.2 Hz)	129
Fig. 4.25 – Comparison of measurements uncertainties (5 Hz)	132
Fig. 4.26 – Comparison of measurements uncertainties normalized to the reference sensor (5 Hz)	132
Fig. 4.27 – Comparison of measurements uncertainties (2 Hz)	133
Fig. 4.28 – Comparison of measurements uncertainties normalized to the reference sensor (2 Hz)	133
Fig. 4.29 – Comparison of measurements uncertainties normalized to the reference sensor (1 Hz)	134
Fig. 4.30 – Comparison of measurements uncertainties normalized to the reference sensor (0.5 Hz)	134
Fig. 4.31 – Comparison of measurements uncertainties normalized to the reference sensor (2 Hz)	134
Fig. 4.32 – Setup for the shaking table test (Periodic wave input)	135
Fig. 4.33 – Comparison of measurements by the two sensors in time domain (5 Hz)	136
Fig. 4.34 – Comparison of measurements by the two sensors in frequency domain (5 Hz)	136
Fig. 4.35 – Comparison of measurements by the two sensors in time domain (2 Hz)	136
Fig. 4.36 – Comparison of measurements by the two sensors in frequency domain (2 Hz)	137

Fig. 4.37 – Comparison of measurements by the two sensors in time domain (1 Hz)	137
Fig. 4.38 – Comparison of measurements by the two sensors in frequency domain (1 Hz)	137
Fig. 4.39 – Comparison of measurements by the two sensors in time domain (0.5 Hz)	138
Fig. 4.40 – Comparison of measurements by the two sensors in frequency domain (0.5 Hz)	138
Fig. 4.41 – Comparison of measurements uncertainties normalized to the reference sensor (5 Hz)	139
Fig. 4.42 – Comparison of measurements uncertainties normalized to the reference sensor (2 Hz)	139
Fig. 4.43 – Comparison of measure uncertainties normalized to the reference sensor (1 Hz)	140
Fig. 4.44 – Comparison of measure uncertainties normalized to the reference sensor (0.5 Hz)	140
Fig. 4.45 – Oil drilling pipeline layout	142
Fig. 4.46 – Setup for flow-loop pipeline test	143
Fig. 4.47 – Comparison of measurements by the two sensors in time domain ($8.00 \cdot 10^{-4} \text{ m}^3 \cdot \text{s}^{-1}$)	144
Fig. 4.48 – Comparison of measurements by the two sensors in frequency domain ($8.00 \cdot 10^{-4} \text{ m}^3 \cdot \text{s}^{-1}$)	144
Fig. 4.49 – Detail of the comparison of measurements by the two sensors in frequency domain ($8.00 \cdot 10^{-4} \text{ m}^3 \cdot \text{s}^{-1}$)	144
Fig. 4.50 – Comparison of measurements by the two sensors in time domain ($1.35 \cdot 10^{-3} \text{ m}^3 \cdot \text{s}^{-1}$)	145
Fig. 4.51 – Comparison of measurements by the two sensors in frequency domain ($1.35 \cdot 10^{-3} \text{ m}^3 \cdot \text{s}^{-1}$)	145
Fig. 4.52 – Detail of the comparison of measurements by the two sensors in frequency domain ($1.35 \cdot 10^{-3} \text{ m}^3 \cdot \text{s}^{-1}$)	145

Fig. 4.53 – Comparison of measurements by the two sensors in time domain ($2.00 \cdot 10^{-3} \text{ m}^3 \cdot \text{s}^{-1}$)	146
Fig. 4.54 – Comparison of measurements by the two sensors in frequency domain ($2.00 \cdot 10^{-3} \text{ m}^3 \cdot \text{s}^{-1}$)	146
Fig. 4.55 – Detail of the comparison of measurements by the two sensors in frequency domain ($2.00 \cdot 10^{-3} \text{ m}^3 \cdot \text{s}^{-1}$)	146
Fig. 4.56 – Pinnacle model from Washington National Cathedral	149
Fig. 4.57 – Pinnacle top view showing sensors location	149
Fig. 4.58 – Detail of the time-history comparison (low-amplitude)	151
Fig. 4.59 – Detail of the time-history comparison (high-amplitude)	151
Fig. 4.60 – Streicker bridge at Princeton University campus - Princeton, NJ	153
Fig. 4.61 – Test setup and the ALE deployment	153
Fig. 4.62 – Quasi-static test setup	154
Fig. 4.63 – Detail of the time-history recorded during the quasi-static test	155
Fig. 4.64 – Detail of the frequency domain analysis recorded during the quasi-static test	155
Fig. 4.65 – Detail of the time-history recorded during the 3 Hz-input solicitation test	156
Fig. 4.66 – Detail of the frequency domain analysis recorded during the 3 Hz-input solicitation test	156
Fig. 4.67 – Detail of the time-history recorded during the random run-input solicitation test	157
Fig. 4.68 – Detail of the frequency domain analysis recorded during the random run-input solicitation test	157
Fig. A.1 – Calibration chart when receiver is 10 m away from transmitter	193
Fig. A.2 – Calibration chart when receiver is 20 m away from transmitter	193
Fig. A.3 – Calibration chart when receiver is 25 m away from transmitter	193
Fig. A.4 – Comparison of measurements uncertainties (5 Hz)	194

Fig. A.5 – Comparison of measurements uncertainties (2 Hz)	194
Fig. A.6 – Comparison of measurements uncertainties (1 Hz)	194
Fig. A.7 – Comparison of measurements uncertainties (0.5 Hz)	195
Fig. A.8 – Corbin’s simulated earthquake acceleration time-history	195
Fig. A.9 – Corbin’s simulated earthquake frequency response	195
Fig. A.10 – Pinnacle displacement measured with the LVDT	196
Fig. A.11 – Acceleration time-history derived from the LVDT readings	196
Fig. A.12 – Acceleration frequency response derived from the LVDT readings	196
Fig. A.13 – Time-history recorded with the MEMS sensor	197
Fig. A.14 – Frequency response recorded with the MEMS sensor	197
Fig. A.15 – Time-history recorded with the reference sensor	197
Fig. A.16 – Frequency response recorded with the reference sensor	198
Fig. A.17 – Time-history recorded during the quasi-static test	198

INTRODUCTION

Vibration deals with the oscillatory motion of a dynamic system. Vibrational phenomena may arise in many operational processes: sometimes they are necessary for performing tasks, other times they may be trivial, but - in several circumstances - they are objectionable. In these cases, vibration has to be controlled since it is accompanied with undesirable conditions that may cause the malfunctioning, or the failure, of the system on which vibration is applied. In addition, oscillatory motions are characterized by the transmission of considerable quantities of energy to portions of the affected structure. In these situations, even if no critical conditions will occur, vibration is to be counted as one of the main causes for noise pollution.

The need for measuring vibrations on structures and part of machineries is extremely important. Maintain under control aging structures, infrastructures and machinery (e.g.: bridges, buildings, dams, pipelines, aircraft, ships, railway tracks, etc.) plays a key role in the prediction of situations, which could jeopardize, or even destroy, the structure itself.

The transducers used for measuring the vibration of a moving dynamic system are called accelerometers. On the market, there are several typologies of accelerometers (e.g.: piezoresistive, capacitive, Linear Variable Differential Transformer, fiber optic, piezoelectric, Integral Electronics PiezoElectric, Micro Electro-Mechanical Systems, etc.). Their number results from different applications and different operational principles with various requirements of range, natural frequency, damping, sensing element, and response. In general, these sensors use the movement of a sensing element (i.e.: inertial mass) to generate an electrical quantity (current or tension) proportional to detected oscillations.

Since the early 1990's on, there has been an increasing interest in the adoption of developing sensing technologies for instrumentation within a variety of structural systems. Recent advances in the Micro Electro-Mechanical System (MEMS) and Wireless Sensor Networks (WSNs) technologies have made wireless MEMS accelerometers an attractive tool for Structural Health Monitoring (SHM) of civil engineering structures. The SHM applications require the MEMS-based accelerometers to be accurate for measuring a wide range of structural vibration: from ambient vibration (in the order of $10^{-2} \text{ m}\cdot\text{s}^{-2}$) to severe earthquakes (in the order of $10 \text{ m}\cdot\text{s}^{-2}$). In addition, natural frequencies in large civil engineering structures - including bridges and buildings - are generally in the order of 10^{-1} to 10^1 Hz. Therefore, sensor systems able to accurately measure such low-frequency signals are required; otherwise, the recorded signal might be confused with a noise. To date, sensors' low sensitivity and accuracy - especially at very low-frequencies - have imposed serious limitations for their application in monitoring large-sized structures.

Acceleration Evaluator (ALE), the MEMS accelerometer system presented in this study, addresses two main problems of data acquisition in the field of vibration monitoring: the importance of going wireless and the signal quality when low-frequency and low-amplitude vibrations are considered. Wireless transmission, compared to its wired counterpart, is preferable for at least three reasons: absence of wires impedance, absence of triboelectric noise, and mounting facility. On the other hand, signal quality is important when accurate analyses have to be carried out. Conventionally, the MEMS sensor's analog signals are converted to digital signals before radio-frequency (RF) wireless transmission. The conversion can cause a low sensitivity to the important low-frequency and low-amplitude signals. Therefore, the designed MEMS accelerometer system converts the sensor output voltage to a frequency-modulated (FM) signal before radio-frequency transmission. This is achieved by using a Voltage to Frequency conversion (V/F) instead of the conventional Analog to Digital Conversion (ADC).

This study begins with an introductory part regarding the basic concepts associated to the mechanic of vibration. A description of the vibratory system elements (mass, spring, damper, external soliciting force) and an introduction of some basic physical quantities (frequency, period, amplitude, etc.), which control the oscillatory motions is given. Then a discussion of simple vibratory motions (forced, free, damped, undamped, and their combinations) and their equations are discussed in Chapter I.

The study continues with a report of the seismic instruments used for vibration measurement. A description of instruments for displacement detection (vibrometer) and instruments for acceleration detection (accelerometer) is examined along with a discussion about the equations defining their behavior and operational principles. Then, a summary of the vibration instrument characteristics is presented. It consists of an overview and explanation of the main technical features of a shock-and-vibration measuring instrument. These include: the instrument's sensitivity, transverse sensitivity, resolution, amplitude linearity, and frequency range. Chapter II finishes with a detailed description of the most common typologies of accelerometers. The main characteristics of piezoresistive, capacitive, Linear Variable Differential Transformer (LVDT), fiber optic, piezoelectric and Integral Electronics Piezoelectric (IEPE), and Micro Electro-Mechanical System (MEMS) accelerometers are specified.

In Chapter III a summary review regarding the state-of-the-art of the WSNs for SHM is first given. Academia-built and commercial platforms for WSN are described; their strengths and weaknesses for SHM aims are analyzed. Starting from these weaknesses, the newly designed Acceleration Evaluator (ALE) wireless system prototype, which consists of a transmitter and a receiver circuit boards, is presented. The transmitter board is equipped with a MEMS accelerometer, a V/F converter and a wireless RF transmitter, while the receiver board contains a RF receiver and a F/V converter for demodulating the signal. Therefore, the second part of the chapter focuses on the design choices, hardware characteristics, and operational properties of the prototype. It highlights how ALE

may overcome the difficulties met by previous systems as they are used for SHM purposes.

In Chapter IV, the real core of the study, ALE's efficacy in measuring low-frequency and low-amplitude dynamic responses is demonstrated through extensive laboratory tests and experiments on real-world engineering structures. Laboratory tests consist of calibration tests, studies about the effect of battery residual charge, maximum transmission distance evaluations, and dynamic comparisons with wired Integral Electronics Piezoelectric (IEPE) accelerometers. The first test is made for calibration purposes using an angle meter machine; the second allows evaluating ALE behavior under diminishing battery power. The third investigation consists of experiments for determining the performance of the wireless transmission distance in two different conditions (indoor and outdoor), whereas the fourth are made for exploring the prototype dynamic response using electromagnetic shakers and well-known soliciting signals. These tests, carried out in a controlled laboratory-environment, are necessary for characterizing the boards' technical features. Instead, the real-world experiments consist of measurements on several typologies of engineering structures: a flow-loop pipeline (industrial applications), a stone pinnacle (seismic applications), and a pedestrian bridge (civil infrastructures monitoring). In the first experiment the MEMS accelerometer system is used to measure oil flow-induced vibrations of a black-steel flow-loop pipeline. The second consists of a study on the earthquake-induced vibration on a special lab-scale model of one of the pinnacles of the Cathedral Church of St. Peter and St. Paul in Washington, DC. The third experiment describes the sensor's deployment on the Streicker Bridge in Princeton, NJ for ambient vibration detection and modal identification purposes. These experiments are executed to prove whether or not ALE is suitable and versatile for carrying out low-amplitude and low-frequency vibrational analyses.

To finish, a short overview of the designed prototype's further developments is discussed in the conclusive section of the study.

CHAPTER I

THE MECHANIC OF VIBRATION

1 – Introduction

Vibration deals with the oscillatory motion of a dynamic system. A dynamic system is any object which possesses mass and whose parts are capable of relative movements. The considered system could be in the form of a structure, a machinery, or its components.

Vibrational phenomena may arise in many operational processes: sometimes they are necessary for performing tasks, other times they may be trivial, but - in several circumstances - they are objectionable. In these cases, vibration has to be controlled since it is accompanied with undesirable conditions that may cause the malfunctioning, or the failure, of the system on which vibration is applied. Usually, two different failure mechanisms may occur: those connected to impulsive, high-intensity stresses (shock) [1], or those related to low-intensity events, which repeat several times (fatigue) [2].

In addition, oscillatory motions are characterized by the transmission of considerable quantities of energy to portions of the affected structure. In these situations, even if no critical conditions will occur, vibration is to be counted as one of the main causes for noise pollution [3], [4]. Therefore, the study of the oscillatory motion is crucial in those branches of engineering that aim to determine its effects on the performance and safety of the system being considered. The analyses of vibration can reduce risks arising from phenomena that may jeopardize civil and mechanical structures.

In this chapter a description of the elements of a vibratory system, an introduction of some terminology, and a discussion of simple harmonic motions are presented.

2 – General concepts

The term vibration is referred to an oscillatory motion of a body about its static equilibrium position [5]. Three elements are necessary for producing a vibration: a mass (for storing kinetic energy), a spring (for storing potential energy), and a damper (by means of which energy is gradually dissipated in the form of heat at each cycle of oscillation). These components are referred to as passive elements and they are assumed to be invariant in time [6]. The mass m is supposed to be a rigid body; it produces the vibration and it can gain or lose kinetic energy in accordance with its velocity change. The spring element k possesses elasticity and it is considered as having negligible mass. The force acting on the spring exists only if that element is deformed, extended or compressed. The damping element c has neither mass nor elasticity. Damping force only exists if there is a relative motion between the two ends of the damper. During this movement work or energy are converted into heat; therefore, the damper is not conservative [7]. Figure 1.1 shows those elements when an external force $F(t)$, capable of creating a displacement $x(t)$, is applied to the system.

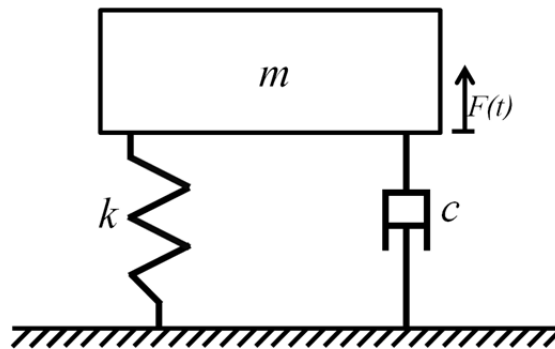


Fig. 1.1 – Elements of a vibratory system

The mass is constrained to a translational motion in the vertical direction so that its change of position is described fully by the value that the quantity $x(t)$ assumes in time. If the spring is compressed (or extended) and then released, the body will start moving around its static equilibrium position with regular time

periods. Motion is assumed to be periodic and, conceptually, the time-history of vibration is considered to be harmonic in form. The harmonic motion is simple to analyze; its law of motion, which is the mathematical function describing body's displacement pattern in time, is a constant amplitude sine curve.

$$x(t) = X \sin(2\pi ft + \varphi) = X \sin(\omega t + \varphi) \quad [1.1]$$

Vibration can be defined by means of physical quantities as the amplitude X , the phase φ , and the frequency f (or period T). The amplitude represents the maximum displacement of the oscillating body about its static equilibrium position and it is measured in meter (m); the phase is the initial angle of the sinusoidal function at its origin and it is measured in radian (rad); the period is the time necessary for the body to complete a whole cycle and it is measured in second (s); whereas, frequency represents the number of oscillations the body completes in a second and it is measured in Hertz (Hz). The following relation exists between frequency and period:

$$f = \frac{1}{T} \quad [1.2]$$

Another quantity used for describing the motion is the wavelength λ . It is the distance the wave travels in a time equal to the period T in its propagation direction. Wavelength can also be defined as the space over which the wave's shape repeats. For this reason, it is usually determined by considering the distance between consecutive corresponding points such as crests, troughs, and zero crossings. Wavelength is measured in meter (m) and can be evaluated using the equation:

$$\lambda = v_p T = \frac{v_p}{f} \quad [1.3]$$

where v_p is called phase speed and it is measured in $\text{m}\cdot\text{s}^{-1}$ [8]. Figure 1.2 plots the simplest oscillatory motion composed of a single frequency f (1 Hz pure tone). Deriving equation [1.1], the equations describing the velocity $\dot{x}(t)$ and the acceleration $\ddot{x}(t)$ of the body are obtained:

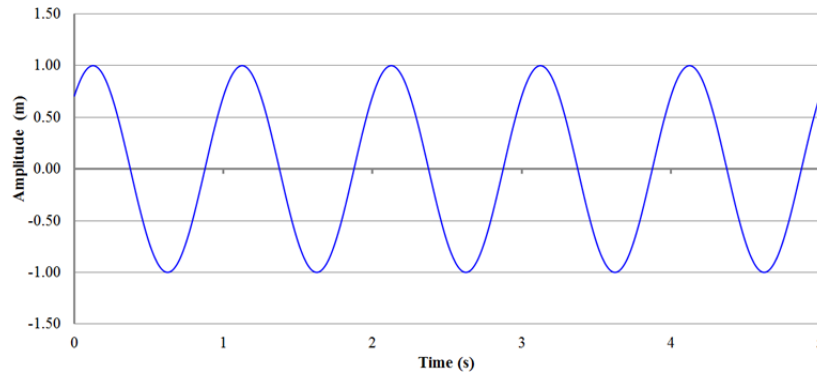


Fig. 1.2 – Time-history of an oscillatory motion made of a pure tone

$$\dot{x}(t) = \omega X \cos(\omega t + \varphi) \quad [1.4]$$

$$\ddot{x}(t) = -\omega^2 X \sin(\omega t + \varphi) = -\omega^2 x(t) \quad [1.5]$$

Figure 1.3 plots displacement, velocity, and acceleration for a harmonic motion made of a 0.2 Hz pure tone.

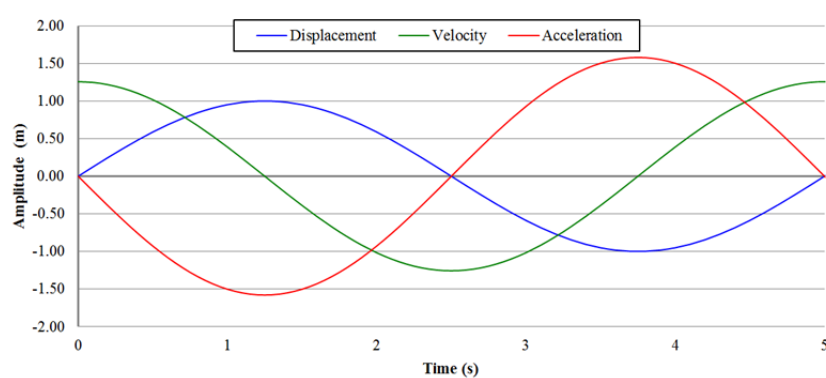


Fig. 1.3 – Displacement, velocity and acceleration in the harmonic motion

It is observed that velocity and acceleration are also harmonic functions of the same frequency. The only differences consist of an increase in amplitude by a factor of ω and a shift in phase angle by $\pi/2$ rad. The phase angle of the velocity is $\pi/2$ rad leading the displacement, while the acceleration is π rad leading the displacement.

3 – Classification of vibrations

Vibrations encountered in engineering practice seldom have the regular pattern shown in Figure 1.2. They may be a combination of several sinusoidal quantities, each having different frequencies and amplitudes. Nevertheless, to classify the vibration, some considerations about the frequency components of the motion can be done.

If each frequency component f_i is an integral multiple of the lowest frequency f_1 , the resultant vibration is no more sinusoidal. It repeats its waveform after a determined interval of time and it is called periodic. Otherwise, if there is not any integral relation among the frequency components, periodicity does not occur and the vibration is referred as complex [7]. Figures 1.4 and 1.5 plot an example of those vibrations.

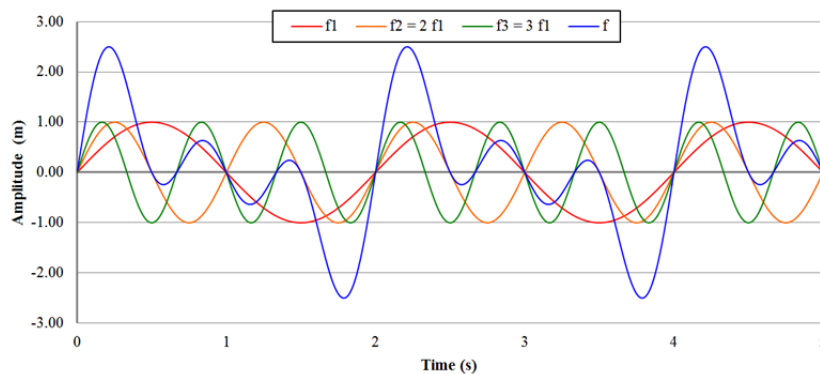


Fig. 1.4 – Periodic vibration

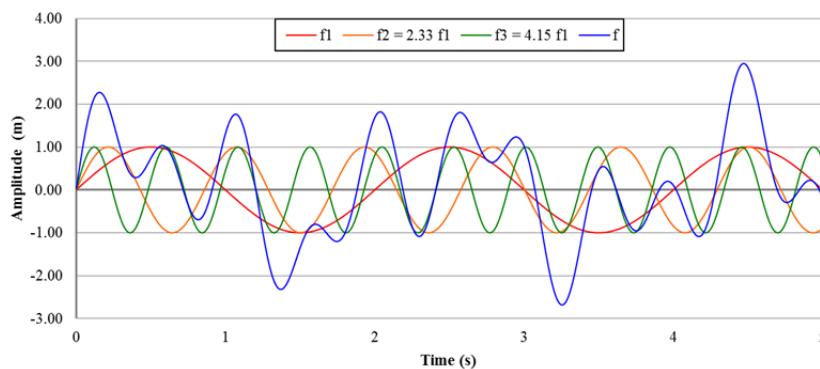


Fig. 1.5 – Complex vibration

In particular, the resultant vibration shown in Figure 1.4 is the sum of three pure tones (the fundamental frequency f_1 and the two harmonics $f_2 = 2f_1, f_3 = 3f_1$). The resultant time-history is not sinusoidal, but a recurrent shape it is found.

Another way to describe vibration considers the repeatability of the signal: thus, deterministic and random vibrations can be defined [7]. The former are characterized by a waveform that repeats itself at equal interval of time. As shown in Figure 1.6, it follows an established pattern so that the value of the vibration at any future time is completely predictable from the past history. In the second one, future values are unpredictable except on a probabilistic base. Therefore, random vibration can be solely defined in statistical terms wherein the probability of occurrence of designated magnitudes and frequencies can be indicated. Impulsive and irregular forces represent a possible cause for the generation of these vibrations. An example of random vibration is plotted in Figure 1.7.

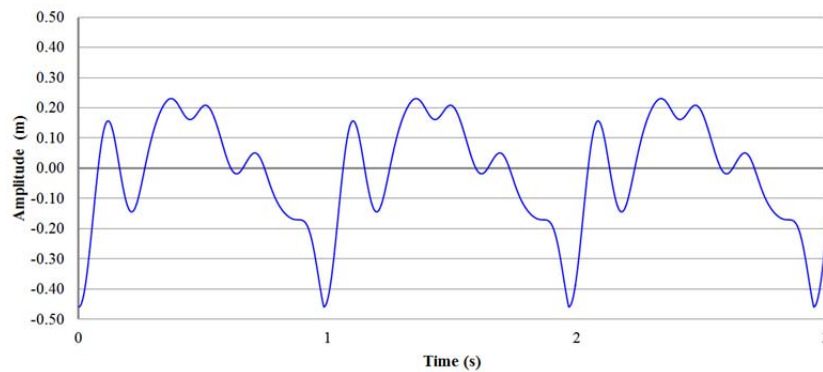


Fig. 1.6 – Deterministic vibration

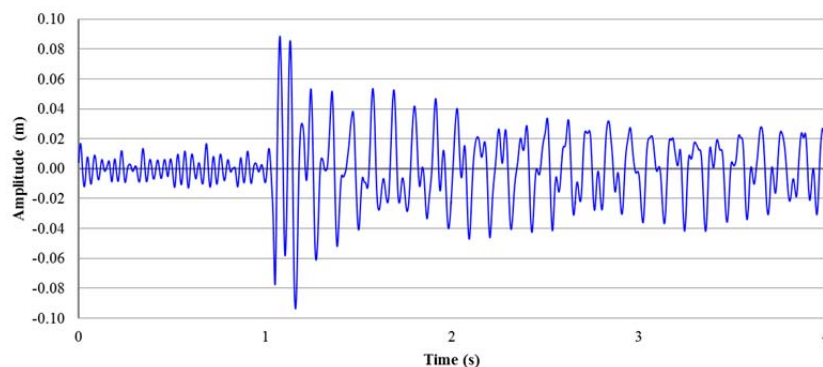


Fig. 1.7 – Random vibration

A third way used to classify vibrations considers the presence, or not, of external forces applied to the system. Thus, vibration can be defined as free or forced [7]. In the free vibration, there is not energy added to the system: the oscillation is the continue result of an initial disturbance. The system is set into motion by some event and thereafter no excitation is further applied. Free vibration represents the behavior of a system as it relaxes from an initial state of constraint to its equilibrium state. If the mass-spring-damper system shown in Figure 1.1 is considered, and if an initial displacement is given to the mass, it will be set into motion. If the system possesses damping, the motion will eventually get exhaust after a certain time. Thus, the mass will reach its equilibrium state, which corresponds to the static equilibrium position of the system. If the system does not posses damping, the motion will continue indefinitely about system's static equilibrium position. On the other hand, forced vibration continues even after system has reached its steady state because energy is continuously supplied. Forced vibration can be either deterministic or random, but in general they are defined as the vibrations that are caused and maintained by a periodic excitation. In both cases the frequency at which energy is supplied (i.e.: forcing frequency) appears in the vibration of the system.

4 – Principal types of vibratory systems

When different combinations of the passive elements and forces are applied to the system, four vibratory motions can be observed:

- 1) Undamped free vibration;
- 2) Damped free vibration;
- 3) Undamped forced vibration;
- 4) Damped forced vibration.

System configurations, for the four cases presented, are shown in Figure 1.8.

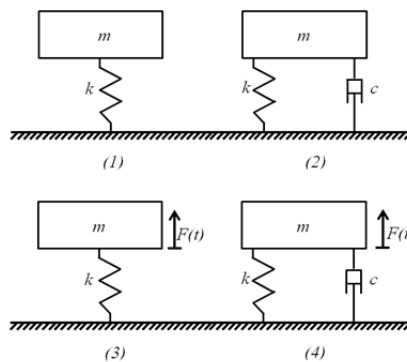


Fig. 1.8 – Possible combinations of dynamic system's passive elements and applied forces

The first two cases (1), (2) occur when there is not any external solicitation after the initial change of equilibrium status. The system will continue oscillating in time (undamped) or motion will die after a certain time (damped). Instead, the third and fourth cases (3), (4) appear as an excitation is continuously supplied to the system. The excitation may be a force applied to the mass, or the motion of the foundation that support the system itself. If the excitation is a force applied to the mass, the result is expressed in terms of amplitude of the resulting motion (motion response) or in terms of fraction of the applied force's amplitude transmitted to the foundation (force transmissibility). If the excitation is a motion of the foundation, the resulting response is expressed in terms of amplitude of the

mass's relative motion to the foundation (motion transmissibility). The response and transmissibility relations are function of the forcing frequency, and vary with different types and degree of damping [9]. All these systems are governed and can be described using second order differential equations [10].

4.1 - Undamped free vibration systems

Consider the system shown in Figure 1.8 (1), it consists of a mass m attached by means of a spring having stiffness constant equal to k to an immobile support. The mass is initially at rest at its static equilibrium position because it is acted upon two equal and opposite forces: the spring force and the gravitational force. The first force is equal to the product of the spring stiffness constant k (measured in $\text{kg}\cdot\text{s}^{-2}$) by the deflection x of the spring itself from the initial position x_0 . The second is equal to the product of the mass m by the gravitational acceleration g (in $\text{m}\cdot\text{s}^{-2}$). The equilibrium equation of the system is:

$$m \ddot{x} = k x \quad [1.6]$$

where the quantity \ddot{x} represents the second derivative with respect to time of the mass deflection.

Introducing the angular natural frequency ω_n (in $\text{rad}\cdot\text{s}^{-1}$), defined as the ratio between the spring stiffness constant and the mass:

$$\omega_n = \sqrt{\frac{k}{m}} \quad [1.7]$$

equation [1.6] can be rearranged as:

$$\ddot{x} = \frac{k}{m} x = \omega_n^2 x \quad [1.8]$$

it is important to notice that the angular natural frequency ω_n is inherent in the system's parameters. Indeed, it is determined by the mass and the spring stiffness values only; therefore, it is independent of initial conditions imposed on the system and uncorrelated to the amplitude of the oscillations.

Equation [1.8] is a second order differential equation. The solution can be expressed in the general form:

$$x(t) = A \sin(\omega t) + B \cos(\omega t) \quad [1.9]$$

Since mechanical systems do not usually observe linear laws, solution [1.9] contains several approximations. Nevertheless, if the amplitude of the oscillations is small, it is possible to apply a Taylor series [11] to the law of motion about its static equilibrium position, stop the series at the first order, and linearize the problem [5]. To evaluate the constants A and B , it is necessary to complete the Cauchy's problem by means of defining two suitable boundary conditions. Mass position and speed value at the time $t = 0$ are used.

$$\begin{cases} x_{t=0} = x_0 \\ \dot{x}_{t=0} = \dot{x}_0 \end{cases} \quad [1.10]$$

Once boundary conditions are fixed, equation [1.9] can be solved and results are shown in equations [1.11] and [1.12].

$$\begin{cases} A = \frac{\dot{x}_0}{\omega} \\ B = x_0 \end{cases} \quad [1.11]$$

$$x(t) = \frac{\dot{x}_0}{\omega} \sin(\omega t) + x_0 \cos(\omega t) \quad [1.12]$$

it can be observed that equation [1.12] is formally equivalent to equation [1.1].

To sum up, the mass is initially displaced by an amount x_0 from its static equilibrium position; thus, potential energy - corresponding to this displacement - is stored in the spring. When the mass passes through its equilibrium position, the potential energy of the spring is zero and it has been transformed into kinetic energy of the mass. As the mass moves above the equilibrium position, the spring is being compressed gaining potential energy from the kinetic energy of the mass. When all the kinetic energy has been transformed to become the potential energy, the mass is at its uppermost position. Through continuous exchanges of potential and kinetic energy between the spring and the mass, the system will oscillate

periodically at its natural frequency ω_n about the static equilibrium position. Since there is no damping element to dissipate energy, the system is conservative and the amplitude of the motion will not diminish from cycle to cycle as shown by the time history plotted in Figure 1.2.

4.2 - Damped free vibration systems

The systems shown in the paragraph 4.1 are completely ideal. In reality the damping exists and by means of that the oscillation amplitude decreases in time since the motion will die out. Furthermore, a damped system will oscillate more slowly than an undamped one. In other words, the amplitude of the oscillations decreases with each subsequent cycle of oscillation and the frequency of the oscillations is lower than the natural frequency ω_n of the system. An example of damped system is depicted in Figure 1.8 (2).

Usually, it is possible to identify among three types of damping: viscous, Coulomb, and hysteretic. Viscous damping is very common when a mass moves in a viscous fluid with low velocity. In this case, the resultant friction force F_f is proportional to the velocity and it has opposite direction to the motion. This model approximates the behavior of a mass moving on well-lubricated surfaces, into air, oil, and other fluids. If velocity to which mass is moving is higher, friction force becomes proportional to the square of velocity [12]. In Coulomb damping, the energy is absorbed via sliding friction. It is a common damping mechanism occurring in machineries. The friction, generated by the relative motion of two surfaces that press against each other, is a source of energy dissipation in which kinetic energy is converted into thermal energy. The friction force F_f is proportional to the product of the normal force N and the coefficient of friction μ , that can be experimental determined once geometrical characteristic and type of surface are known [13]. To finish, the third type of damping is due to material's internal frictions. Micro-displacements and deformations of a material can be seen as the sum of the internal deformations and displacements of the components. Usually, these displacements are connected to resistant forces that

allow absorbing energy in the form of heat. This kind of friction is nearly proportional to the displacement and it has not correlation to the frequency [14].

Consider the system depicted in Figure 1.8 (2) and assume – for the sake of simplicity – that the damper c is viscous only. The equilibrium equation of the system is:

$$m \ddot{x} + c \dot{x} + k x = 0 \quad [1.13]$$

where the terms represent the physical quantities already introduced. Equation [1.13] is a homogeneous linear equation with constant coefficients [10].

The general solution to this equation can be written as:

$$x = C e^{\alpha t} \quad [1.14]$$

where C is the constant coefficient defined by means of Cauchy's problem and α the root of the characteristic equation associated with [1.13].

The characteristic equation can be expressed using a quadratic expression as following:

$$\alpha^2 + 2 \zeta \omega_n \alpha + \omega_n^2 = 0 \quad [1.15]$$

in equation [1.15], ω_n represents the angular natural frequency of the system as already defined by equation [1.7]. For convenience reasons, the damping factor ζ is introduced. It is the ratio between the damping constant c and the critical damping coefficient c_c :

$$\zeta = \frac{c}{c_c} = \frac{c}{2\sqrt{k \cdot m}} = \frac{c}{2 m \cdot \omega_n} \quad [1.16]$$

System parameters are assumed to be positive; thus, ζ is a positive number as well. It can assume values smaller, bigger or equal to the unit, depending on the characteristics of the system.

To determine the displacement x of the system, it is necessary to solve equation [1.15], whose roots are equal to:

$$\begin{cases} \alpha_1 = \omega_n (-\zeta + \sqrt{\zeta^2 - 1}) \\ \alpha_2 = \omega_n (-\zeta - \sqrt{\zeta^2 - 1}) \end{cases} \quad [1.17]$$

considering the results introduced with [1.17], general solution [1.14] can be rewritten as:

$$x(t) = C_1 e^{\alpha_1 t} + C_2 e^{\alpha_2 t} \quad [1.18]$$

In function of the value $\sqrt{\zeta^2 - 1}$ assumes, three solutions are possible:

a) $\zeta > 1; c^2 > 4 k \cdot m:$

solutions α_1 and α_2 are both real, distinct, and negative. Regardless of the initial conditions applied, no oscillatory motion can be expected. The motion is called aperiodic and equation [1.18] becomes:

$$x(t) = C_1 e^{(-\zeta + \sqrt{\zeta^2 - 1}) \omega_n t} + C_2 e^{(-\zeta - \sqrt{\zeta^2 - 1}) \omega_n t} \quad [1.19]$$

this solution is referred as over-damped. It has to be pointed out that both terms of equation [1.19] are exponentially decreasing functions; therefore, whether mass is displaced from its static equilibrium position, it will return gradually to its original position according values assumed by the parameters of the equation. Constants C_1 and C_2 , can be either negative or positive and, as usual, their values can be determined once the boundary conditions are fixed. Depending on the values assumed by those two constants, different waveforms are possible.

b) $\zeta = 1; c^2 = 4 k \cdot m:$

solutions α_1 and α_2 are both real, identical, and equal to ω_n . The motion is called critical aperiodic, and equation [1.18] becomes:

$$x(t) = C_1 e^{-\omega_n t} + C_2 t e^{-\omega_n t} \quad [1.20]$$

it can be thought as sum of two different functions: a linear one equal to $[C_1 + C_2 t]$ and an exponentially decreasing function equal to $[e^{-\omega_n t}]$. The motion will diminish to zero in time.

c) $\zeta < 1; c^2 < 4 k \cdot m:$

in this case, the discriminant of equation [1.15] is negative; therefore, roots α_1 and α_2 are complex conjugates and they will be equal to:

$$\begin{cases} \alpha_1 = \omega_n (-\zeta + j\sqrt{\zeta^2 - 1}) \\ \alpha_2 = \omega_n (-\zeta - j\sqrt{\zeta^2 - 1}) \end{cases} \quad [1.21]$$

where j is the complex part equal to $\sqrt{-1}$ [15]. Defining the damped frequency of the system ω_d as following:

$$\omega_d = \omega_n \sqrt{1 - \zeta^2} \quad [1.22]$$

and using Euler's formula:

$$e^{\pm j\theta} = \cos \theta \pm j \sin \theta \quad [1.23]$$

equation [1.18], becomes:

$$x(t) = e^{-\zeta \omega_n t} (D_1 e^{j \omega_d t} + D_2 e^{-j \omega_d t}) \quad [1.24]$$

$$x(t) = e^{-\zeta \omega_n t} [(D_1 + D_2) \cos \omega_d t + j (D_1 - D_2) \sin \omega_d t] \quad [1.25]$$

where D_1 and D_2 are arbitrary constant. Since displacement $x(t)$ is a real physical quantity, D_1 and D_2 must be complex conjugates; that is the coefficient of the cosine and sine functions in this equation must be real.

The previous equation [1.25] can be rewritten as:

$$x(t) = e^{-\zeta \omega_n t} [C_1 \cos \omega_d t + C_2 \sin \omega_d t] \quad [1.26]$$

where C_1 and C_2 are always arbitrary constants to be specified by the boundary conditions. Furthermore, considering that:

$$\begin{cases} X = \sqrt{C_1^2 + C_2^2} \\ \varphi = \tan^{-1} \frac{C_2}{C_1} \end{cases} \quad [1.27]$$

the two harmonic functions of equation [1.26] can be combined to give:

$$x(t) = X e^{-\zeta \omega_n t} \sin(\omega_d t + \varphi) \quad [1.28]$$

The motion will be called under-damped and consists of a harmonic motion of frequency ω_d and amplitude X , which decreases exponentially in time $[e^{-\zeta \omega_n t}]$.

In the three cases enumerated, the type of motion depends on whether the damping factor ζ is greater than, equal to, or less than one. The system is referred to as over-damped if ζ is greater than one, critically damped if ζ is equal to one, and under-damped if ζ is less than the unit. It has to be pointed out that vibratory motion exists only if the system is under-damped and that the frequency of oscillation ω_d is lower than the natural frequency ω_n of the system itself. From equation [1.22] and [1.28] it is observed that the rate of exponential decay and the frequency of the oscillation are inherent in the system parameters; they are independent of the arbitrary constants of the equation and of the manner by which the system is set into motion.

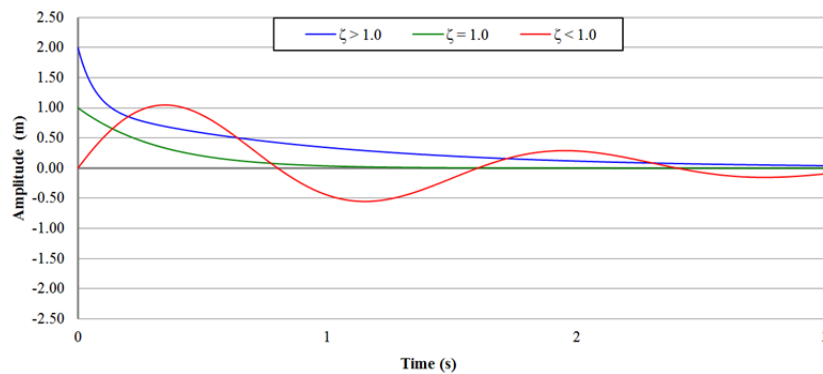


Fig. 1.9 – Time-histories of a dynamic system subjected to a damped free vibration

In addition, since oscillation will die out, the function $x(t)$ gives the transient motion of the system. As a limiting case, if the system does not possess damping, the amplitude X will not diminish with time and the frequency of the motion is equal to the natural frequency ω_n of the system as shown in paragraph 4.1. Figure 1.9 plots the motion time histories for the three above-described solutions.

4.2.1 - Considerations on damped free vibration systems

The two main effects the damping has on the system are to reduce the amplitude of the oscillations and decrease the time lag that intervenes between

two homologous points (maximum, minimum, zero-crossing, etc.) as shown by the following equation:

$$\omega t = \frac{\arcsin \sqrt{1-\zeta^2}}{\sqrt{1-\zeta^2}} \quad [1.29]$$

Indeed, when the damping factor ζ is equal to zero, the step $[\omega t]$ between a zero of the function and a point of peak is equal to $\pi/2$ and this value will decrease with the increase of ζ . This means that, an increase in the damping factor ζ will decrease the time necessary to obtain the next point of peak. Furthermore, damping increases the time in which body passes through its static equilibrium position (i.e.: it crosses the X -axis) as shown below:

$$\omega t = \frac{\pi}{\sqrt{1-\zeta^2}} \quad [1.30]$$

when the damping factor ζ is equal to zero, function will cross the X -axis every π and this value will rise with the growth of ζ .

In certain practical applications, characterized by under-damped vibrations, it may be interesting quantify the damping of the system. Analytically, it can be done using the logarithmic decrement of two successive peak-values in a record of free oscillations. Let x_i be the amplitude of the oscillation at the time t_i and x_{i+1} the amplitude of the following oscillation at the time t_{i+1} , so that their difference ($t_{i+1} - t_i$) is equal to the period T of the oscillation. According to equation [1.28] the amplitude of two successive oscillations is equal to:

$$\begin{cases} x_i(t) = X e^{-\zeta \omega_n t_i} \sin(\omega_d t_i + \varphi) \\ x_{i+1}(t) = X e^{-\zeta \omega_n t_{i+1}} \sin(\omega_d t_{i+1} + \varphi) \end{cases} \quad [1.31]$$

therefore, their ratio is:

$$\frac{x_i}{x_{i+1}} = e^{\zeta \omega_n (t_{i+1} - t_i)} = e^{\zeta \omega_n T} = e^{\zeta \omega_n \left(\frac{2\pi}{\omega_d}\right)} \quad [1.32]$$

Introducing equation [1.22], which correlates the damped frequency ω_d with the angular natural frequency ω_n , equation [1.32] becomes:

$$\frac{x_i}{x_{i+1}} = e^{\frac{2\pi\zeta}{\sqrt{1-\zeta^2}}} \quad [1.33]$$

where the logarithm of the ratio x_i/x_{i+1} is called logarithmic decrement δ . For small values of the damping factor ζ (less than 0.10) [5], logarithmic decrement can be approximated to:

$$\delta \cong 2\pi\zeta \quad [1.34]$$

Even if the use of two consecutive amplitudes is more convenient, the same evaluation can be done for any two points, one period apart, on the same time-history. The logarithmic decrement can be evaluated considering the amplitude of more cycles far away from each other. Referring as x_n the amplitude of the oscillation n cycles after the initial amplitude x_0 , the ratio between these two values can be indicated as following:

$$\frac{x_0}{x_n} = \frac{x_0}{x_1} \cdot \frac{x_1}{x_2} \cdot \dots \cdot \frac{x_{n-1}}{x_n} = \left(\frac{x_0}{x_{i+1}}\right)^n \quad [1.35]$$

therefore, the natural logarithm will be equal to:

$$\ln\left(\frac{x_0}{x_n}\right) = n \ln\left(\frac{x_0}{x_n}\right)^n = n\delta \quad [1.36]$$

that can be inverted to explicit the number of cycles n :

$$n = \frac{1}{\delta} \ln\left(\frac{x_0}{x_n}\right) \quad [1.37]$$

Equation [1.37] becomes extremely useful when the number of cycles necessary to obtain a specific amplitude reduction has to be determined. Once this value is known, it is possible to calculate the time interval Δt necessary to obtain that amplitude reduction as:

$$\Delta t = nT \quad [1.38]$$

Combining equations [1.22] and [1.37], equation [1.38] can be rewritten as:

$$\Delta t = \frac{1}{\zeta\omega} \ln\left(\frac{x_0}{x_n}\right) \quad [1.39]$$

this relation is extremely useful when experimental determinations on the system must be carried out; in particular, it can be used to evaluate the quantities ζ and c .

4.3 - Undamped forced vibration systems

Systems are often subjected to external forces coming out from various sources. Furthermore, it is of engineering interest to study the mechanical response of a system to forces having high intensity but that are applied for a short period of time. Figure 1.8 (3) shows a graphical representation of these systems. The mass m is subjected to the action of the force $F(t)$, which - if it is harmonic - has the following expression:

$$F(t) = F_0 \sin(\omega_f t + \chi) \quad [1.40]$$

where F_0 represents the amplitude of the applied force, ω_f is the forcing angular frequency, and χ the phase angle. However, this last parameter is here considered as negligible for the sake of simplicity.

The equilibrium equation can be written as following:

$$m \ddot{x} + k x = F_0 \sin(\omega_f t) \quad [1.41]$$

and its general solution $x(t)$ is the sum of two components: a complementary function $x_c(t)$ and a particular integral $x_p(t)$ [10]. The complementary function $x_c(t)$ satisfies the corresponding homogeneous equation [1.9]. It represents the free undamped vibration introduced in paragraph 4.1, whereas the particular integral $x_p(t)$ takes into account the forced vibration. The form of equations assumed as solution are here proposed again for reader's convenience:

$$\begin{cases} x_c(t) = A \sin(\omega t) + B \cos(\omega t) \\ x_p(t) = C \sin(\omega_f t) \end{cases} \quad [1.42]$$

where the constant term A and B can be calculated once boundary conditions are fixed. Instead, the constant C can be evaluated substituting equation [1.42b] in equation [1.41] and obtaining the following equation:

$$-m \omega_f^2 C \sin(\omega_f t) + k C \sin(\omega_f t) = F_0 \sin(\omega_f t) \quad [1.43]$$

which explicated gives:

$$C = \frac{F_0}{k - m \omega_f^2} \quad [1.44]$$

Including this result in equation [1.42b], the solution to the particular integral can be determined:

$$x_p(t) = \frac{F_0}{k - m \omega_f^2} \sin(\omega_f t) = \frac{F_0/k}{1 - \frac{\omega_f^2}{k/m}} \sin(\omega_f t) \quad [1.45]$$

Indicating as X_0 the ratio between the applied force F_0 and the spring stiffness constant k , remembering that the ration of the spring stiffness constant k and the mass m is defined as the angular natural frequency ω_n of the system, and indicating as r the ratio between the forcing angular frequency ω_f and that of the system ω_n , the previous equation can be rewritten as:

$$x_p(t) = \frac{X_0}{1 - r^2} \sin(\omega_f t) \quad [1.46]$$

According to equation [1.46], several scenarios may occur for different values of the frequency ratio r . As usual, significant cases are when it is greater than, less than, or equal to one. When r is less than the unit, the denominator of equation [1.46] is positive; the displacement and the excitation are in phase with one other. If the frequency ratio r is greater than one, the component of the motion representing the forced vibration is in opposition of phase with the force. To finish, when frequency ratio is unitary the motion is still harmonic, but its amplitude linearly soars in time and after a certain time the amplitude becomes infinite (resonance) [7]. In addition, equation [1.46] is no more valid in that form.

Figure 1.10 plots the time histories of a dynamic system subjected to an undamped forced vibration for different values of the frequency ratio r , whereas the set of equations [1.47] summarizes the motion equations.

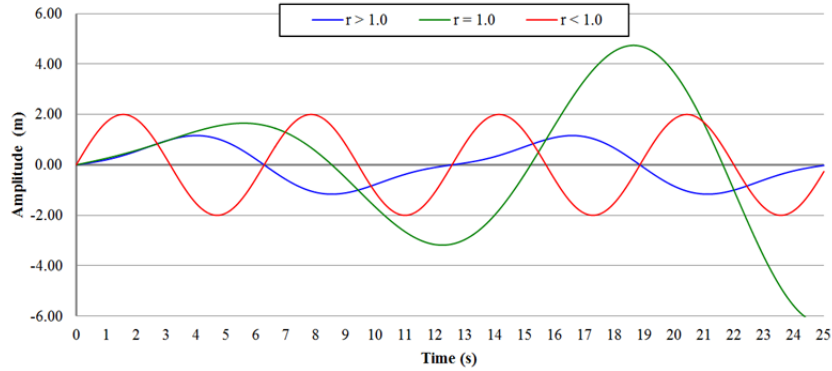


Fig. 1.10 – Time-histories of a dynamic system subjected to an undamped forced vibration

$$\begin{cases} x(t) = X \sin(\omega_n t) + \frac{X_0}{1-r^2} \sin(\omega_f t), & r < 1 \\ x(t) = X \sin(\omega_n t) - \frac{X_0}{r^2-1} \sin(\omega_f t), & r > 1 \\ x(t) = X \sin(\omega_n t) - \frac{X_0 \omega_f t}{2} \cos(\omega_f t), & r = 1 \end{cases} \quad [1.47]$$

Equations [1.47] incorporate the contribution of the free vibration $[X \sin(\omega_n t)]$ and that of the forced one. Therefore, they represent the complete equations of the motion. First two are made of the sum of two sinusoidal functions having different frequencies ω_n and ω_f . The third one is made of a sinusoidal wave having constant amplitude and a sinusoidal wave having increasing amplitude. The main contribution will be supplied by the first waveform in the first steps of the motion, while the importance of the second one will rise proportionally with time.

4.4 - Damped forced vibration systems

To conclude this overview on the principal vibratory motions, consider the system depicted in Figure 1.8 (4), where the mass-spring-damper system is subjected to the action of a harmonic force of the type expressed by equation [1.40]. The equilibrium equation of the system is:

$$m \ddot{x} + c \dot{x} + k x = F_0 \sin(\omega_f t) \quad [1.48]$$

and its general solution $x(t)$ is, again, the sum of two components: a complementary function $x_c(t)$ and a particular integral $x_p(t)$. The complementary

function $x_c(t)$ satisfies the corresponding homogeneous equation [1.28] and it represents the free vibration. However, in damped systems this term represents the transient state and it dies out rapidly after the initial stages. On the other hand, the particular integral $x_p(t)$ represents the steady-state motion developed because of the forcing input $F(t)$.

As already observed in paragraph 4.3, the following equation can be assumed as solution to the particular integral:

$$x_p(t) = D \sin(\omega_f t) + E \cos(\omega_f t) \quad [1.49]$$

where the constants D and E can be evaluated substituting equation [1.49] in equation [1.48]:

$$\begin{aligned} -m \omega_f^2 [D \sin(\omega_f t) + E \cos(\omega_f t)] + c \omega_f [D \cos(\omega_f t) - E \sin(\omega_f t)] + \\ k [D \sin(\omega_f t) + E \cos(\omega_f t)] = F_0 \sin(\omega_f t) \end{aligned} \quad [1.50]$$

that can be rewritten using the following system:

$$\begin{cases} (k - m \omega_f^2) C \sin(\omega_f t) - c \omega_f D \sin(\omega_f t) = F_0 \sin(\omega_f t) \\ c \omega_f C \cos(\omega_f t) - (k - m \omega_f^2) D \cos(\omega_f t) = 0 \end{cases} \quad [1.51]$$

Resolving equations [1.51], the value of the constant D and E can be calculated:

$$\begin{cases} D = \frac{(k - m \omega_f^2) F_0}{(k - m \omega_f^2)^2 - (c \omega_f)^2} \\ E = \frac{c \omega_f F_0}{(k - m \omega_f^2)^2 - (c \omega_f)^2} \end{cases} \quad [1.52]$$

Plugging in the equations [1.52] in the particular integral [1.49], the solution can be explicated as:

$$x_p(t) = \frac{F_0}{\sqrt{[(k - m \omega_f^2)^2 - (c \omega_f)^2]}} \sin(\omega_f t - \psi) \quad [1.53]$$

where the phase shift ψ of $x_p(t)$, with respect to the acting force $F_0 \sin(\omega_f t)$, can be evaluate using equation [1.27b] and it is equal to:

$$\psi = \tan^{-1} \frac{c \omega_f}{k - m \omega_f^2} \quad [1.54]$$

The motion described by equation [1.53] is harmonic and it has the same frequency ω_f as the exciting force $F(t)$. Thus, the equation of the motion $x(t)$, considering both the contributions of the free vibration and the forced vibration, is equal to:

$$x(t) = X e^{-\zeta \omega_n t} \sin(\omega_d t + \varphi) + \frac{F_0}{\sqrt{[(k - m \omega_f^2)^2 - (c \omega_f)^2]}} \sin(\omega_f t - \psi) \quad [1.55]$$

where the terms represent the physical quantities introduced in the previous paragraphs.

From equations [1.53] and [1.54] it is observed that the motion depends on the damping factor ζ and the frequency ratio r only. Therefore, these equations are often reduced to a non-dimensional form. Dividing the numerator of equation [1.53] by the stiffness of the spring k , defining as X_0 the ratio F_0/k , introducing the relation [1.7] for defining the angular natural frequency of the system ω_n , and introducing the following relation [1.56]:

$$2 \frac{\zeta \omega_f}{\omega_n} = \frac{c \omega_f}{k} \quad [1.56]$$

equations [1.54] and [1.55] can be rewritten in the following way:

$$\frac{X}{X_0} = \frac{1}{\sqrt{[1 - (\frac{\omega_f}{\omega_n})^2]^2 + (2 \frac{\zeta \omega_f}{\omega_n})^2}} = \frac{1}{\sqrt{[1 - r^2]^2 + (2 \zeta r)^2}} = \kappa \quad [1.57]$$

$$\psi = \tan^{-1} \frac{2 \frac{\zeta \omega_f}{\omega_n}}{1 - (\frac{\omega_f}{\omega_n})^2} = \tan^{-1} \frac{2 \zeta r}{1 - r^2} \quad [1.58]$$

where the ratio X/X_0 is called magnification factor κ and the other symbols assume the meaning previously explained.

The magnification factor κ can be considerably greater than, equal to, or less than the unit. Figure 1.11 plots a representation of equation [1.57] for different values of the damping factor ζ .

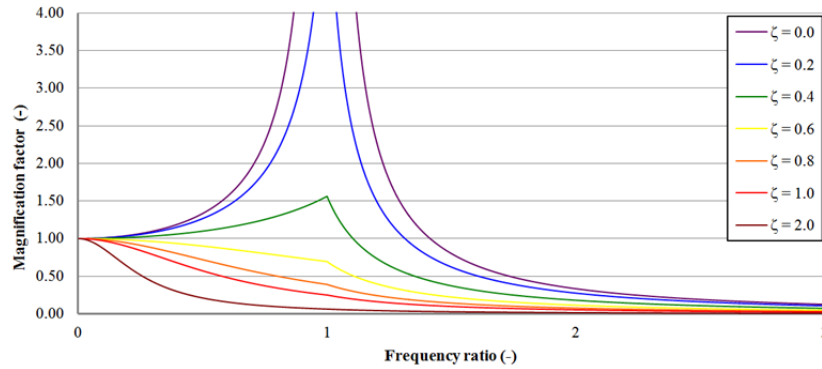


Fig. 1.11 – Magnification factor κ versus frequency ratio r for various values of damping factor ζ

The figure shows that a reduction in the value of the magnification factor κ , and of the amplitude, is only possible for high values of the frequency ratio r . That is when the forcing frequency ω_f is bigger than the natural frequency of the system ω_n . At resonance, when r is equal to one, magnification factor is limited only by the damping factor ζ . In other words, the amplitude of vibration is only limited by the presence of damping in the system. Without damping, the amplitude is theoretically infinite, and for low values of the damping factor ζ (up to 0.4) amplification is still present. A damping factor of nearly 0.6 is necessary to reduce the oscillations.

Furthermore, since the excitation is given as a periodic input $[F_0 \sin(\omega_f t)]$ and the steady state response is proportional to $[\sin(\omega_f t - \psi)]$, the excitation and the response do not attain their maximum values at the same time. Equation [1.58] supplies a measure of this difference and Figure 1.12 plots the trend of the phase angle ψ in function of the frequency ration r in systems having different damping factors ζ .

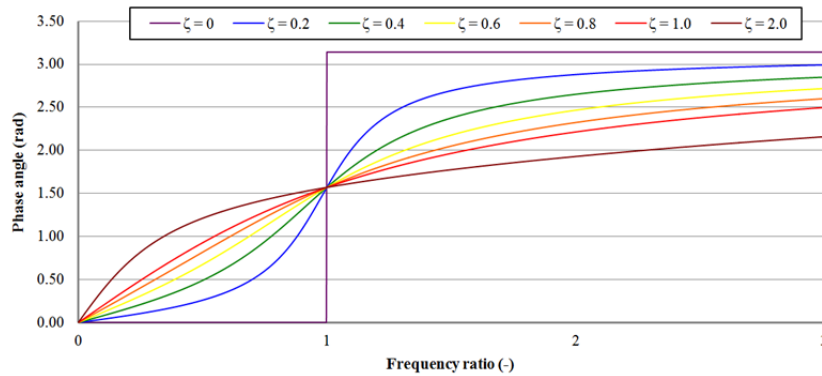


Fig. 1.12 – Phase angle ψ versus frequency ration r for various values of damping factor ζ

Variations in the phase angle are caused by the presence of damping in the system. Without damping, the phase angle is equal to zero for values of r smaller than one, and it is equal to π for r bigger than the unit. Instead, at resonance ($r = 1$), the phase angle is always equal to $\pi/2$ for every value of the damping factor ζ .

Another aspect, that it is worth pointing out, is the influence spring stiffness k and mass m have on the system. Changes in mass and stiffness determine changes in the frequency ratio ($r = \omega_f \sqrt{(m/k)}$) and in the damping factor ζ ($\zeta = c / (2 \sqrt{(m/k)})$). In addition, a change in k implies a change in the value of X as well. These changes can be highlighted plotting the trend of the amplitude X in function of the spring stiffness k for different values of damping c as shown in Figure 1.13. It is observed that amplitude reductions can be obtained for high values of the stiffness k .

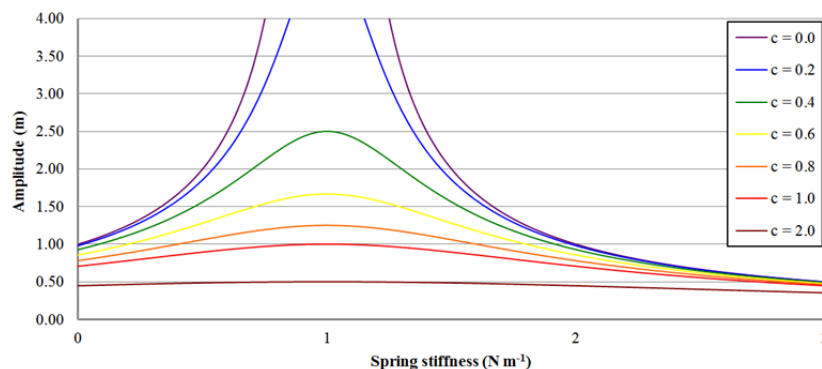


Fig. 1.13 – Amplitude X of the oscillation with different values of stiffness k

Analogous considerations can be carried out when the behavior of the amplitude X is studied for different values of the mass. A reduction in amplitude is only possible for high values of the mass of the system, while the amplitude is theoretically infinite for undamped systems.

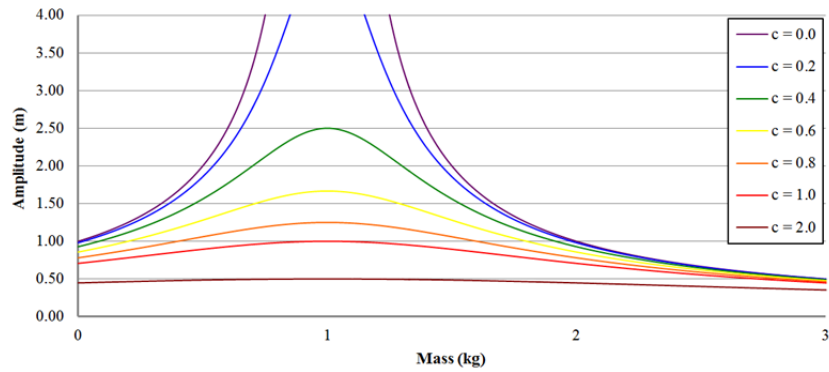


Fig. 1.14 – Amplitude X of the oscillation with different values of mass m

5 – Vibration transmissibility

The systems shown in the previous paragraphs may transmit a portion of the exciting force to the support they are placed on. This problem recurs in several technical operations and it can create many issues as, for instance, noise pollution phenomena [3], [4] and safety troubles. Machineries are often mounted on springs and dampers to minimize transmission of forces to the foundations. Since the machine is supported by these two elements, the transmitted force is the sum of the spring force and the damping force. If deflections of the foundation are negligible, the transmitted force F_T , is given by the following relation:

$$F_T = c \dot{x} + kx \quad [1.59]$$

As usual, the interest is in studying the force transmitted under steady state conditions; therefore, using results given by equation [1.53] and referring as X the term before the sine function, equation [1.59] becomes:

$$F_T = c \omega_f X \cos(\omega_f t - \psi) + k X \sin(\omega_f t - \psi) \quad [1.60]$$

this equation, using trigonometric relations [16], can be rewritten as:

$$F_T = \sqrt{(k X)^2 + (c \omega_f X)^2} \sin(\omega_f t - \psi + \gamma) \quad [1.61]$$

$$\begin{aligned} F_T &= \frac{X}{k} \sqrt{1 + (2 \zeta r)^2} \sin(\omega_f t - \psi + \gamma) = \\ &= F_{eq} \kappa \sqrt{1 + (2 \zeta r)^2} \sin(\omega_f t - \psi + \gamma) \end{aligned} \quad [1.62]$$

where

$$\gamma = \tan^{-1} \frac{c \omega_f}{k} = \tan^{-1} 2 \zeta r \quad [1.63]$$

and the other terms have the same meaning already specified.

The transmitted force is maximum when the sine function is equal to one. Therefore, using equation [1.53], equation [1.63] can be rewritten as:

$$F_T = X \sqrt{(k)^2 + (c \omega_f)^2} = \frac{F_0}{\sqrt{[(k - m \omega_f^2)^2 - (c \omega_f)^2]}} \sqrt{(k)^2 + (c \omega_f)^2} \quad [1.64]$$

Dividing and multiplying by k the numerator and the denominator of equation [1.64], it can be rearranged as:

$$F_T = F_0 \frac{\sqrt{1 + (2 \zeta r)^2}}{\sqrt{[(1 - r^2)^2 - (2 \zeta r)^2]}} \quad [1.65]$$

The ratio of the amplitude of the transmitted force F_T to that of the impressed force F_0 is called transmissibility TR :

$$TR = \frac{F_T}{F_0} = \frac{\sqrt{1 + (2 \zeta r)^2}}{\sqrt{[(1 - r^2)^2 - (2 \zeta r)^2]}} \quad [1.66]$$

Equation [1.66] defines the quality of the suspension. Indeed, if the spring-damper system is seen as suspension, the best value is that minimizes the ratio. Equation [1.66] is plotted in Figure 1.15 for various values of the damping factor ζ .

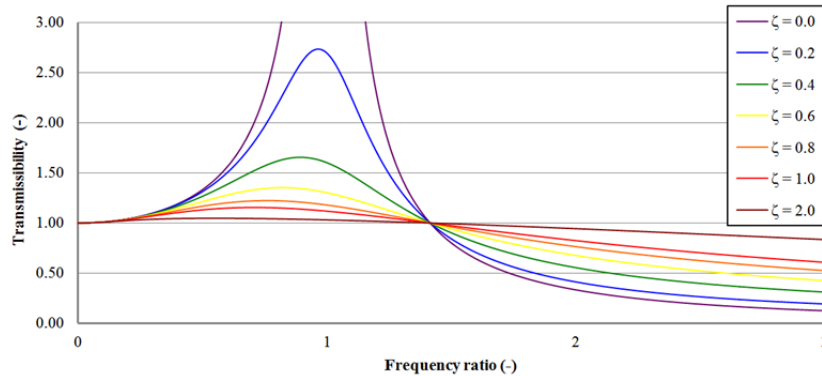


Fig. 1.15 – Transmissibility versus frequency ratio for various values of damping factor ζ

Since all the curves in Figure 1.15 cross at TR equal to one and frequency ratio r equal to $\sqrt{2}$, it is clear that the presence of damping will decrease the transmissibility when the machine is operated below this frequency ratio, whereas TR will increase when the machine is operated above it. Furthermore, the value of transmissibility is lower for high value of the frequency ratio r . To conclude, it possible to observe that for r equal to unit, the curves present a point of maximum

for little values of the damping, and that the maximum decreases when damping factor increases.

CHAPTER II

INSTRUMENTATION FOR THE MEASUREMENT OF VIBRATIONS

1 – Introduction

The necessity of measuring vibrations on structures and parts of machineries is extremely important. Maintaining under control aging structures, infrastructures and machinery – such as bridges, buildings, dams, pipelines, aircraft, ships, and railway tracks – plays a key role in the prediction of situations, which could jeopardize, or even destroy, the structure itself [17]. In this chapter, an overview of the theoretical principles, which explain how instrumentation works is given. Then the main typologies of shock-and-vibration measuring devices are described in detail.

Shock and vibration are measured with reference to a fixed point in a given space. For this purpose, two typologies of instruments can be distinguished: fixed reference and mass-spring devices. In the fixed reference instruments, a terminal of the device is attached to a point fixed in space, whereas the other terminal is connected to the point whose motion is to be measured. The motion of the moving part is measured, relatively to the fixed reference, by attaching a scale on the immobile reference and a pointer on the moving part. Despite the fact that these instruments are easy to build, they are not suitable for carrying out high-fidelity measurements. Indeed, because the pointer follows the motion of the vibrating system, these devices are subject to errors arising from the deformations produced by the inertia forces in the transmission linkage [18].

On the other hand, the mass-spring instruments have a single terminal only (i.e.: the base of the system). It has to be considered as part of the structure being

studied. Therefore, the amplitude of the vibration is inferred from the motion of the mass relative to the base. These systems are mainly known as seismic instruments and in this chapter considerable importance will be given to them.

2 – Seismic instruments

A mass-spring instrument consists of a mass m suspended from the transducer's case by means of a spring having stiffness constant k . The device includes a damper, with damping coefficient c , in the form of a viscous fluid or an electric current. Figure 2.1 plots a schematic sketch of a seismic instrument, as described above. In particular, the base and the case are subjected to a motion $x_1(t)$, the mass to a motion $x_2(t)$, as the relative displacement d between the two parts is equal to $x_2(t) - x_1(t)$.

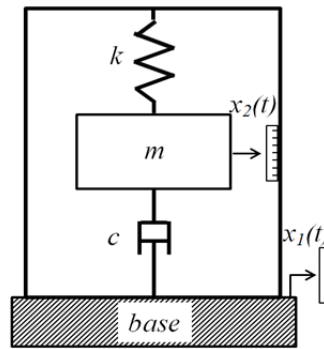


Fig. 2.1 – Schematic sketch of a seismic instrument

2.1 - Instruments for displacement detection

An instrument for measuring displacements is called a vibrometer. For evaluating the relative displacement $d(t)$, consider the following scenario. The excitation is applied to the base of the system; thus, the mass is subjected to an inertial force equal to $m \cdot \ddot{x}_2(t)$, where $\ddot{x}_2(t)$ is the second derivative with respect to the time of the mass motion $x_2(t)$. The excitation causes the base to move at a quantity equal to $x_1(t)$; therefore, the force acting on the spring is due to its deformation and it is equal to $k \cdot (x_2 - x_1)$. To conclude, the damping force is proportional to the relative velocity $(\dot{x}_2 - \dot{x}_1)$ and is equal to $c \cdot (\dot{x}_2 - \dot{x}_1)$. Therefore, the equation of equilibrium can be written as:

$$m \ddot{x}_2 + c (\dot{x}_2 - \dot{x}_1) + k (x_2 - x_1) = 0 \quad [2.1]$$

Assuming the following two hypotheses:

- a) If the motion of the base $x_1(t)$ is harmonic, and the structure is excited by a force having angular frequency ω_f , the equation of the motion of the base can be written as:

$$x_1(t) = X_1 \sin(\omega_f t) \quad [2.2]$$

where X_1 is the maximum amplitude of the soliciting waves.

- b) If the motion of the mass $x_2(t)$ is harmonic too, the mass will start oscillating with an angular frequency ω_n and the equation of the motion of the mass assumes the form:

$$x_2(t) = X_2 \sin(\omega_n t) \quad [2.3]$$

The relative displacement $d(t)$, is equal to:

$$d(t) = x_2(t) - x_1(t) = D \sin(\omega t - \psi) \quad [2.4]$$

therefore, equation [2.1] can be rewritten as:

$$m \ddot{x}_2 + c \dot{d} + k d = 0 \quad [2.5]$$

or, introducing equation [2.4], in the following form:

$$m(\ddot{d} + \ddot{x}_1) + c \dot{d} + k d = 0 \quad [2.6]$$

Deriving equation [2.2] twice, it is possible to obtain the value of the acceleration of the base \ddot{x}_1 :

$$\ddot{x}_1 = -X_1 \omega_f^2 \sin(\omega_f t) \quad [2.7]$$

then, plugging in equation [2.7] into equation [2.6], it becomes:

$$m \ddot{d} + c \dot{d} + k d = m X_1 \omega_f^2 \sin(\omega_f t) \quad [2.8]$$

when equation [2.8] is solved, the steady-state solution is obtained as:

$$d(t) = X_1 \frac{\frac{m \omega_f^2}{k}}{\sqrt{\left(1 - \frac{\omega_f^2}{\omega_n^2}\right)^2 + \left(2 \zeta \frac{\omega_f}{\omega_n}\right)^2}} \sin(\omega_f t - \psi) \quad [2.9]$$

Equation [2.9] represents the mathematical formulation on which the technique for constructing the vibrometer is based [9]. Introducing equations [1.7] and [1.16], it can be rewritten in a more compact way as shown in equation [2.10]:

$$d(t) = X_1 \frac{\frac{\omega_f^2}{\omega_n^2}}{\sqrt{\left(1 - \frac{\omega_f^2}{\omega_n^2}\right)^2 + \left(2\zeta \frac{\omega_f}{\omega_n}\right)^2}} \sin(\omega_f t - \psi) \quad [2.10]$$

where the symbols assume the meaning already explained in Chapter I.

Furthermore, remembering the definition of magnification factor κ (equation [1.57]), equation [2.10] can be expressed as:

$$d(t) = X_1 \frac{\omega_f^2}{\omega_n^2} \kappa \sin(\omega_f t - \psi) \quad [2.11]$$

in addition, introducing the frequency ratio $r = \omega_f / \omega_n$, equation [2.11] becomes:

$$d(t) = X_1 r^2 \kappa \sin(\omega_f t - \psi) \quad [2.12]$$

Similarly to what is stated with equation [1.58], the phase angle - which is a measure of the phase displacement between the two systems - can be expressed as:

$$\psi = \tan^{-1} \frac{2\zeta \frac{\omega_f}{\omega_n}}{1 - \left(\frac{\omega_f}{\omega_n}\right)^2} = \tan^{-1} \frac{2\zeta r}{1 - r^2} \quad [2.13]$$

and the maximum amplitude of the displacement D is:

$$D = X_1 r^2 \kappa \quad [2.14]$$

Figure 2.2 plots a representation of the amplitude ratio D/X_1 (steady-state response) for the system shown in Figure 2.1 in function of the frequency ratio r and the magnification factor κ . It is observed that a reduction in the value of amplitude D , is only possible for high values of the frequency ratio r , that is, when the forcing frequency ω_f is bigger than the natural frequency of the system ω_n .

At resonance, when r is equal to the unit, it is noted that the amplitude is limited by the damping factor ζ only. In other words, the amplitude of vibration is limited by the presence or non-presence of damping in the system. Without damping ($\zeta = 0.0$), the amplitude is theoretically infinite; but even for low values of the damping factor ($\zeta \leq 0.4$), amplification is still significant. A damping factor of nearly 0.7 is needed for reducing the amplitude of the oscillations.

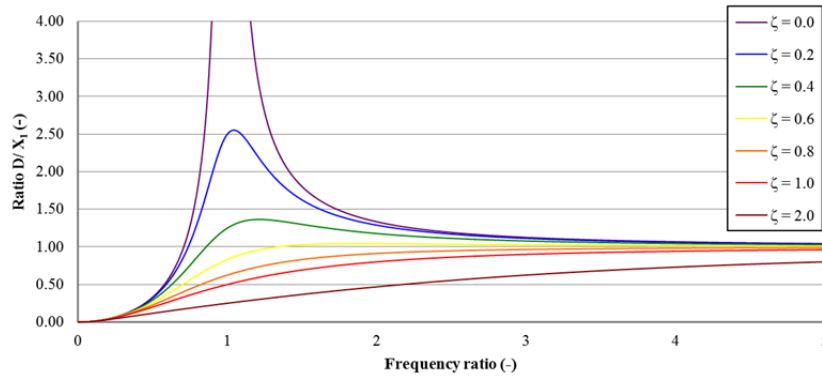


Fig. 2.2 – Steady-state response of a vibrometer

Since the excitation is given as a periodic input $[X_1 \sin (\omega_f t)]$ and, as shown in equation [2.11], the steady state response is proportional to $[\sin (\omega_f t - \psi)]$, the excitation and the response do not attain their maximum values at the same time. Equation [2.13] gives a measure of this difference, while Figure 2.3 shows graphically the trend of the phase angle ψ in function of the frequency ratio r for different values of the damping factor ζ .

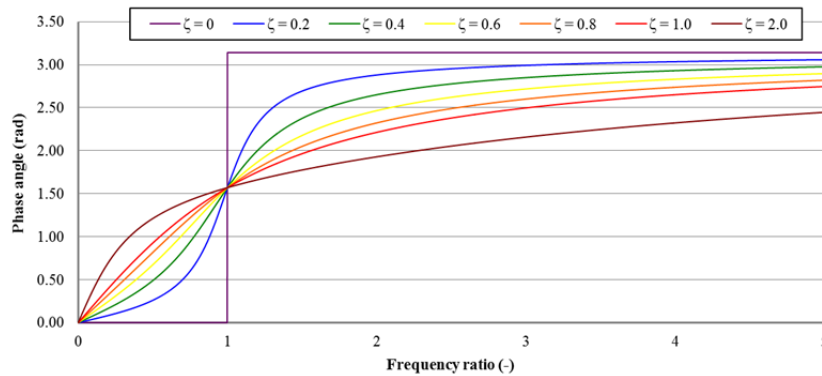


Fig. 2.3 – Phase displacement of a vibrometer

Also in this case, the phase angle between the base of the device and the spring-mass section depends on the damping in the system. Without damping, the phase angle ψ is equal to zero for values of r smaller than one, and equal to π for r bigger than the unit. On the other hand, at resonance ($r = 1$), it is always equal to $\pi/2$ for each value of the damping factor ζ .

As stated, equation [2.9] represents the mathematical formulation on which the technique for constructing shock-and-vibration measuring instrumentation is

based. Furthermore, if the product $r^2 \cdot \kappa$ is almost equal to one, which means that the ratio:

$$\frac{\frac{\omega_f^2}{\omega_n^2}}{\sqrt{\left(1 - \frac{\omega_f^2}{\omega_n^2}\right)^2 + \left(2\zeta \frac{\omega_f}{\omega_n}\right)^2}} \approx 1 \quad [2.15]$$

equation [2.12], representing the relative displacement $d(t)$, can be approximated to:

$$d(t) \approx X_1 \sin(\omega_f t - \psi) \quad [2.16]$$

A comparison between the equation describing the motion of the bases $x_I(t)$ [2.2] and that describing the relative displacement $d(t)$ [2.16], shows that the relative displacement represents the motion of the vibrating structure beside the phase displacement ψ . The time delay τ , with which the instrument records the relative displacement $d(t)$ compared to the displacement of the structure, can be evaluated as:

$$\tau = \frac{\psi}{\omega_f} \quad [2.17]$$

In event of harmonic motion, the delay does not imply any consequence in the analyses of the phenomenon. Therefore, equation [2.14] and the relative displacement $d(t)$ are valid representations of the motion of the structure. It is true, if the condition expressed in equation [2.15] is respected. This occurs for high values of the frequency ratio ω_f/ω_n , that is, when the natural angular frequency of the instrument ω_n is smaller than the angular natural frequency of the vibration ω_f which is to be measured [7]. The frequency ratio r is the only parameter that allows equation [2.15] to be easily satisfied. Indeed, as shown in Figure 2.2, values assumed by the damping coefficient ζ are not so significant. From equation [2.15], it can be observed that devices characterized by high values of the damping coefficient, obtain a value of the product $r^2 \cdot \kappa$ that approaches the unit, only for high values of r (e.g. for $\zeta = 0.8$ that condition is satisfied for values of the frequency ratio r equal or bigger than 3). Such a high value of the frequency ratio can be obtained for small values of the natural angular frequency ω_n , that

means with mass-spring systems having a large mass m or a small value of the spring's constant of stiffness k (equation [1.7]). Therefore, by acting in this way, the instrument may result as too big or heavy for many practical applications. For this reason, it is necessary to maintain these parameters within a specific range.

Because ω_n is a characteristic of the instrument, frequency range for which equation [2.15] is satisfied depends mainly on the frequency ω_f of the forcing vibration. This means that there are no reasons for which it is not possible to use the instrument when a vibration having high amplitude excites the structure. The possibility of using this instrument in any situation is, of course, theoretical only. The limit depends on the sensitivity of the device itself, on the vibration amplitude, and on the level of energy. For these reasons, the upper frequency limit, for which the instrument can be used, has to be always indicated [5].

As stated, a vibrometer works for high values of the frequency ratio r . Referring to the example shown above ($\zeta = 0.8$; $r \geq 3$) and considering Figure 2.3, it should be noted that the phase angle of the relative displacement $d(t)$ is nearly $\pi/2$ rad out of phase with the motion of the base $x_I(t)$. This means that the movement of the mass inside the instrument is opposite to that of the structure on which it is fixed [9].

2.2 - Instruments for acceleration detection

When the natural frequency of the instrument ω_n , is higher than the frequency of the excitation ω_f , the instrument is used to measure acceleration and is called an accelerometer [6]. Assuming that the excitation of the base $x_I(t)$ is harmonic, and the structure is excited by a force having angular frequency ω_f , the equation of the motion is the same as that expressed in equation [2.2]. Therefore, the acceleration of the base is the same as that expressed by equation [2.7], here reported simply for the reader's convenience as equation [2.18]:

$$\ddot{x}_1 = -X_1 \omega_f^2 \sin(\omega_f t) \quad [2.18]$$

furthermore, equation [2.10] can be rearranged in the following form:

$$d(t) \omega_n^2 = \frac{1}{\sqrt{\left(1 - \frac{\omega_f^2}{\omega_n^2}\right)^2 + \left(2 \zeta \frac{\omega_f}{\omega_n}\right)^2}} X_1 \omega_f^2 \sin(\omega_f t - \psi) \quad [2.19]$$

where all the symbols represent the physical quantities already defined.

If the ratio representing the amplification factor of the amplitude X_1 , is nearly equal to one

$$\frac{1}{\sqrt{\left(1 - \frac{\omega_f^2}{\omega_n^2}\right)^2 + \left(2 \zeta \frac{\omega_f}{\omega_n}\right)^2}} \approx 1 \quad [2.20]$$

equation [2.19] can be rewritten as:

$$-d(t) \omega_n^2 = -X_1 \omega_f^2 \sin(\omega_f t - \psi) \quad [2.21]$$

Comparing the last equation [2.21] with equation [2.18], which gives a measure of the acceleration of the base of the measuring devices, it is observed that the two relations are equivalent. Therefore, apart from the case in which the phase angle ψ assumes high values, the first member of equation [2.21] is a measure of the acceleration of the structure. Moreover, because the natural frequency of the device ω_n is a constant for the used instrument, the first member of equation [2.21] is proportional to the displacement $d(t)$ to which the measurement instrumentation is subjected. This means that the value of the acceleration can be directly evaluated from the displacement by means of opportune calibrations [6]. The delay with which the instrument records the accelerations is again equal to:

$$\tau = \frac{\psi}{\omega_f} \quad [2.22]$$

The frequency ratio values that allow for satisfaction of the condition expressed in equation [2.20] are limited, independently of the value assumed by the damping factor ζ . Usually, the vibration to be measured consists of a number of harmonic motions with several frequencies; therefore, it may occur that if the acceleration of one of these harmonics is amplified more than the others, the measured signal is no more than the original one.

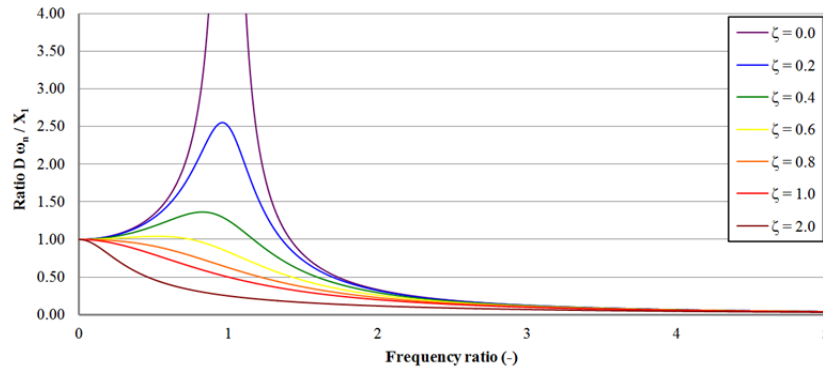


Fig. 2.4 – Instrument amplitude response for different values of r and ζ

This phenomenon is called amplitude distortion. Figure 2.5 shows the trend of equation [2.20] for low values (≤ 1) of the frequency ratio r . If the transducer is undamped, the response curve of Figure 2.5 is substantially flat when the frequency ratio r is approximately less than 0.2. Consequently, an undamped accelerometer can be used for measuring acceleration when the vibration frequency ω_f does not exceed, approximately, 20% of the natural frequency of the accelerometer ω_n [5].

It is observed that the measurable range of frequency increases as the damping of the accelerometer is increased. An accelerometer should be built with ζ between 0.60 and 0.70 to minimize the amplitude distortion [6]. In that range, a seismic instrument gives reasonably accurate results in the measurement of vibration at frequencies ω_f as much greater as approximately 60% of the natural frequency ω_n of the accelerometer. As indicated in Figure 2.4, the useful frequency range of an accelerometer increases as its natural frequency ω_n increases. However, the deflection of the spring in an accelerometer is inversely proportional to the square of the natural frequency ω_n . As a consequence, the signal from the transducing element may be very small; thereby, a large amplification is required to increase the signal to a level at which recording is feasible. For this reason, a compromise is made between high sensitivity and the highest attainable natural frequency, depending upon the desired application [5].

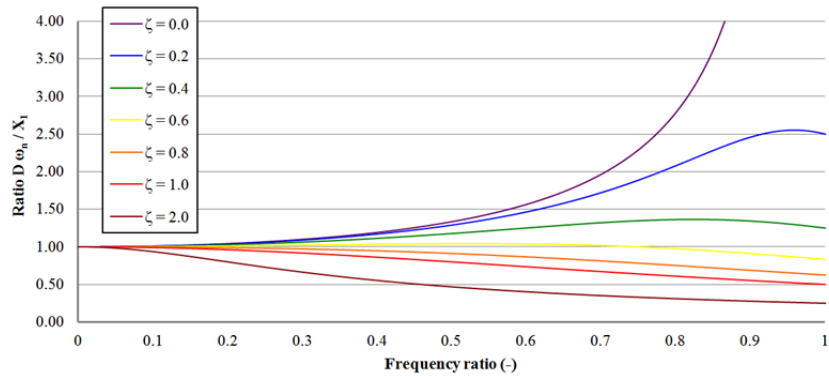


Fig. 2.5 – Amplitude distortion in accelerometers

To obtain an amplitude value close to the unit, the frequency ratio r must be small. This means that the angular frequency of the vibration that excites the system ω_f is low. As an alternative, the angular frequency characteristic of the spring-mass system ω_n has to be high. This can be achieved using a short spring (to have high values of the constant of stiffness k) and a small mass. By this means, an accelerometer can be fabricated quite small compared with a vibrometer [9].

The last issue regards the phase distortion that occurs if the relative phase of the recorded harmonics is different from that of the vibrations to be measured. For zero phase distortion, the phase shift ψ increases in a linear manner with the frequency of the harmonic motion. The phase shift at the resonance ($r = 1$) is always equal to $\pi/2$. For zero phase distortion, the phase shift for $0 < r < 1$ should be $(r = \pi/2)$. Again, it can be seen that an appropriate damping in the accelerometer is necessary to minimize the phase distortion.

3 – Characteristics of vibration measuring instruments

One of the thorniest issues in selecting an accelerometer for a particular application is to understand and interpret the accelerometer's specifications. In this paragraph, an overview and explanation of the main technical features of a shock-and-vibration measuring instrument will be given. These include: the instrument's sensitivity, transverse sensitivity, resolution, amplitude linearity, and its frequency range.

3.1 - Sensitivity

The sensitivity of an accelerometer is defined as the scale factor of the device. Basically, it is the ratio of its electrical output to its mechanical input (since accelerometers convert mechanical acceleration into a proportional electrical signal) [19].

Usually, the output is expressed in terms of voltage per unit of displacement, velocity, or acceleration ($\text{mV}\cdot\text{m}^{-1}\cdot\text{s}^2$ or $\text{pC}\cdot\text{m}^{-1}\cdot\text{s}^2$ for analog-output accelerometers, $\text{m}\cdot\text{s}^{-2}\cdot\text{LSB}^{-1}$ for digital-output accelerometers, where the acronym LSB stands for Less Significant Bit). This specification of sensitivity is enough for instruments that generate their own voltage (independently of an external voltage power source). On the other hand, the sensitivity of an instrument requiring an external voltage is specified in terms of output voltage per unit of displacement, velocity, or acceleration normalized to the unit of supplied voltage (e.g.: millivolts per supplied volt per g of acceleration) [20].

Sensitivity refers to a particular frequency, conventionally 100 Hz, whereas for other frequencies the sensitivity may change, but in a way that does not affect the reliability of the measurement. Furthermore, since accelerometers are influenced by temperature as well, the specified sensitivity is also valid only over a narrow temperature range, typically $25 \pm 5^\circ\text{C}$. Therefore, the sensitivity is always specified with a tolerance, usually $\pm 5\%$ or $\pm 10\%$, which supplies a deviation of the measure from the stated nominal value.

Because the sensitivity is used for programming a signal conditioner or a data acquisition system (DAQ), it is an extremely important technical feature of a shock-and-vibration measuring instrument. This value is used for processing and interpreting the signal coming from the transducer [21].

3.2 - Transverse sensitivity

The transverse sensitivity (also referred to as cross-axis sensitivity) is the scale factor of the accelerometer in the orthogonal direction to the main sensitive axis of the sensor. It is expressed as a percentage of the sensitivity. Ideally, it would be null yet, due to manufacturing tolerances, it can be as much as 5% [23].

3.3 - Resolution

The resolution of a transducer is the smallest detectable change in mechanical input for which a change in the electrical output is discernible. The resolution of an accelerometer depends on the transducing element, the mechanical design, and it is limited by the other auxiliary equipment used with the accelerometer (i.e.: Analog to Digital Converters) [24]. It can be evaluated, using the following equation, as:

$$R = N \sqrt{1.6 BW} \quad [2.23]$$

where N is the power spectral density noise (in $\mu\text{ms}^{-2}\cdot\text{Hz}^{-0.5}$) and BW the bandwidth of the sensor.

Equation [2.23] shows that the accelerometer bandwidth will determine the measurement resolution, while the noise level in the instrument or in the system limits it. This is because any signal change, smaller than those noise levels, will be obscured by the noise itself, making it impossible to discern between the real signal and the disturbance. According to equation [2.23], the resolution can be improved in two ways: by decreasing the bandwidth of the instrument applying a low-pass filter on the output of the accelerometer's sensing axis, or by filtering the output signal to lower the noise floor.

3.4 - Zero acceleration output

It specifies the electrical output level indicated by an accelerometer when there is no acceleration (zero input). This parameter is commonly referred to as zero acceleration output (ZAO), zero-offset, or zero output bias [5].

With an accelerometer whose output is electrically AC-coupled (Alternating Current-coupled), the zero acceleration reference is at ground potential or, alternatively, at some reference level called zero output bias.

With an accelerometer that is capable of detecting static acceleration (DC-coupled or Direct Current-coupled), the ZAO reference should ideally be at zero output units or at a specified DC level. Nevertheless, it is technically impractical due to the component's tolerance; therefore, sensor manufacturers specify this parameter within a range [24].

3.5 - Amplitude linearity

When one of the parameters of the measuring instrument remains constant within specified limits, the transducer is said to be linear within those limits. Therefore, amplitude linearity is a measure of how linear the output of an accelerometer is over a specified amplitude range. Sometimes, this is referred to as amplitude non-linearity, because it specifies the deviation from the perfect linearity [19].

Any transducer is linear over a certain range of amplitude values only. The lower limit of that range is determined by the electrical noise of the device, while the upper limit may be imposed by the electrical characteristics, the size, and the fragility of the instrument [24].

The amplitude linearity is an important parameter to be evaluated in the selection of a suitable accelerometer. A wrong estimation of this feature may cause signal distortions, particularly in high amplitude accelerations and in systems where multiple vibration frequencies occur. It results in intermodulation

distortion (IMD), a phenomenon that creates frequencies in the instrumentation that are not mechanically present at the accelerometer [25].

3.6 - Frequency range

It is the frequency range over which the output of the accelerometer is within a specified deviation, typically $\pm 5\%$ [6]. It is limited by electrical and mechanical characteristics of the transducer or by the auxiliary equipment associated with the device. Basically, it is possible to interpret the frequency range as transducer sensitivity over its entire bandwidth. Therefore, an upper and a lower limit can be indicated.

The lower limit depends on the electrical characteristics of the transducer and the associated electronic equipment. For instance, a DC-coupled accelerometer (such as the piezoresistive and the variable capacitive accelerometers), which utilizes an external power source, is capable of sensing static acceleration and does not have low-frequency limit. On the contrary, self-generating transducer types, such as the piezoelectric accelerometers, are not operative at zero frequency. Thus, its low-frequency response is solely determined by the connecting charge amplifier [19].

On the other hand, the upper limit depends on mechanical characteristics of the devices such as its natural frequency and damping [5]. It is observed that the natural frequency of the spring-mass system ω_n is higher compared with the natural frequency of vibration being measured ω_f ; thus, the accelerometer has an upper usable frequency limit because it responds to vibration whose frequency is less than the natural frequency of the transducer [24]. An attempt to use the accelerometer beyond the frequency limit may result in a distortion of the signal.

4 – Typologies of accelerometers

There are several typologies of accelerometers on the market. The number of accelerometers results from different applications with various requirements of range, natural frequency, damping, sensing elements, and response. In general, one of the basic differences consists of the coupling output type. Alternating Current (AC - coupled) and Direct Current (DC - coupled) accelerometers can be distinguished.

In an AC - response accelerometer, as the name implies, the output is AC - coupled. This device cannot be used to measure static accelerations such as gravity and constant-centrifugal. AC - coupled accelerometers can be used to measure dynamic events only. On the other hand, a DC - response accelerometer is DC - coupled and can be used to measure static as well as dynamic accelerations.

Nevertheless, the most common categorization in which accelerometers are distinguished is based on the sensing principle. Based on this classification, the following categories are usually indicated:

- 1) Piezoresistive;
- 2) Capacitive;
- 3) Linear Variable Differential Transformer (LVDT);
- 4) Fiber optic;
- 5) Piezoelectric and Integral Electronics Piezoelectric (IEPE);
- 6) Micro Electro-Mechanical System (MEMS).

In the following sections, the main characteristics of the above-listed accelerometers are briefly described.

4.1 - Piezoresistive accelerometers

Piezoresistivity is widely used as a sensing principle for sensors. Piezoresistive materials are capable of following deformations of the surface on which they are fixed and produce an equivalent electrical output. The piezoresistance effect is defined as the change in resistivity of a semiconductor or other materials as a function of the applied stress [26]. The stress may be a tension, a hydrostatic pressure, a shear, or a torque. Many metals produce this effect, but the change in the resistivity is not very elevated; thus, a semiconductor material, usually silicon, germanium, indium, or gallium, is added as a strain-sensing element because of its higher sensitivity [27], [28]. The sensing material changes its resistivity in proportion to an applied stress or strain, which modifies the dimension of the sensing element and, consequently, its electrical nature. A variable resistor represents the equivalent electric circuit of a piezoresistive transducing element.

Piezoresistive elements are almost always arranged in pairs; thus, a given acceleration places one element in traction and the other one in compression. This causes the resistance of one element to increase and the resistance of the other to decrease [29]. In normal practice, two different configurations can be used: full-bridge configuration and half-bridge configuration. In the first arrangement, two pairs of elements are used (and the four elements are connected electrically in a Wheatstone-bridge circuit [30]); instead, in the second only one pair is used. The use of transducing elements by pairs increases the sensitivity and it also cancels the zero-output errors, which occur in each resistive element due to temperature changes [31]. Figure 2.6 shows a schematic diagram of a piezoresistive accelerometer.

To provide environmental shock resistance, over travel stops are added, whereas to extend the usable frequency range and enhance shock survivability, the damping coefficient of the devices is increased by surrounding the mechanism with silicon oil, gas, or fluid.

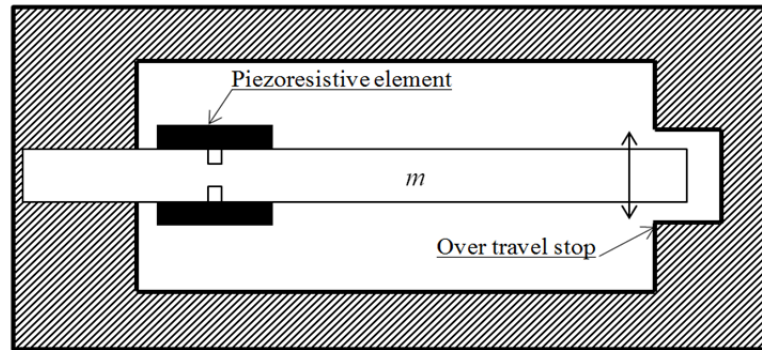


Fig. 2.6 – Schematic diagram of a piezoresistive accelerometer

The advantages of this design are high sensitivity, the broad frequency response (up to 5 kHz), and over-range protection for surviving ordinary shipping and handling. Furthermore, because the piezoresistive sensor output is differential and purely resistive, signal to noise performances are generally good. In addition, since the piezoresistive accelerometers require an external power supply to operate, they are capable of responding down to DC (0 Hz). On the other hand, construction complexity and a limited operative temperature range are among the main disadvantages of this design. Indeed, since the temperature influences the viscosity of the damping fluid, the damping coefficient changes significantly with this parameter [32].

Damping characteristics are an important factor in choosing an accelerometer. Indeed, in applications where the mechanical input may contain very high frequency inputs (or excite high frequency responses), a damped accelerometer can prevent resonance phenomena and preserve or improve the dynamic range.

4.2 - Capacitive accelerometers

Capacitive accelerometers are displacement-sensitive devices. Their output is proportional to the change in the capacitance between two plates (fixed capacitors) caused by the change of the relative position as a result of the motion of a center plate [33]. A schematic diagram of a capacitive accelerometer and its operational principle is shown in Figure 2.7.

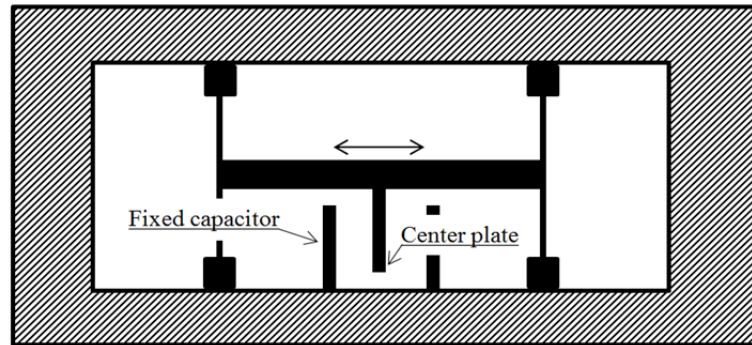


Fig. 2.7 – Schematic diagram of a capacitive accelerometer

Among the main advantages of the capacitive accelerometers there are the simplicity in installation, the negligible effect on the operation of the vibrating system (since they are proximity-type sensors, which add no mass or restraints), high sensitivity, a wide displacement range (due to their low background noise), and a wide frequency range (limited only by the electrical circuit used) [34].

In recent years, advancements in technology have allowed for the production of silicon micro-machined capacitive accelerometers suitable for measuring low-level accelerations (2 g to 100 g) and capable of withstanding to high-level shocks (5000 g to 20000 g) as well. Acceleration sensing is accomplished by using a half-bridge variable-capacitance micro sensor. The capacitance of one circuit element increases with the applied acceleration, while that of the other one decreases. With the use of signal conditioning, the accelerometer provides a linearized high-level output [35].

One of the most common configurations for this typology of sensors is shown in Figure 2.8. It is fabricated bonding together an array of three micro-machined single-crystal silicon wafers using an anodic bonding process [36]. The top and bottom wafers contain the fixed capacitor plates, which are electrically isolated from the middle wafer. The middle wafer contains the inertial mass, the suspension, and the supporting ring frame. The stiffness k of the flexure system is controlled by varying shape, cross-sectional dimensions, and number of suspension beams; the damping ζ is controlled by varying the dimensions of the

orifices on the parallel plates whereas, over range protection is extended by adding over travel stops [5].

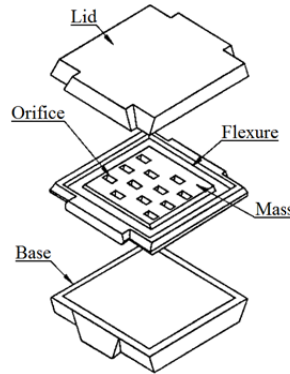


Fig. 2.8 – Exploded view of a micro-machined capacitive accelerometer (source: Harris [5])

The full-scale displacement of the seismic mass in the micro sensor element is extremely restrained; therefore, to detect minor capacitance changes, high-precision supporting electronic circuits are required.

4.3 - Linear Variable Differential Transformer (LVDT) accelerometers

In Linear Variable Differential Transformer (LVDT) accelerometers, a mass (the ferromagnetic core of the sensor) moves inside another channel wrapped within coils used for detecting the position of the mass itself [37]. The device consists of a primary solenoidal coil and two secondary solenoidal coils symmetrically spaced on a cylindrical form, as shown in Figure 2.9.

Therefore, LVDT accelerometers are electromechanical devices that produce an electrical output proportional to the displacement of the movable core. The transducer output depends on the mutual inductance between the primary and secondary coils. When the primary solenoidal coil is energized by an external power source, voltages are induced in the two secondary solenoidal coils. These two are connected in order to generate two opposite-polarity voltages. The net output of the transducer is given by the difference between these voltages, which is zero when the core is at the center or null position. On the other hand, when the core is moved from the null position, the induced voltage in the coil toward which

the core is moved increases, while the induced voltage in the opposite coil decreases. This action produces a differential voltage output that varies linearly with changes in core position [37].

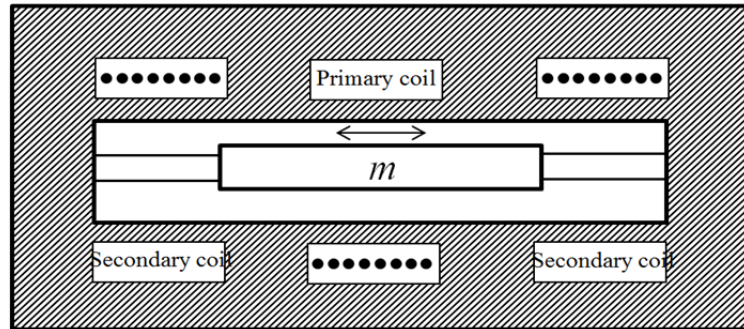


Fig. 2.9 – Schematic diagram of a LVDT accelerometer

LVDT accelerometers are used for low-frequency measurements. The sensitivity varies with the carrier frequency of the current in the primary coil, which should be at least 10 times the highest frequency of the motion to be measured. Modern LVDTs have a carrier frequency at 10 kHz; then the usable bandwidth is from 0 to 1 kHz [5].

4.4 - Fiber optic accelerometers

A fiber-optic reflective displacement sensor measures the amount of light normal to, and vibrating along, the optical axis of the device. The measurement is based on comparing the transmitted light intensity against that of the reflected light. The comparison provides information on the displacement between the probe (the fiber-optic transmitting/receiving element) and the target (reflecting surface), which act as the mass of the device [38].

The sensor is composed of two bundles of single optical fibers. One of these bundles transmits the light to the reflecting surface, whereas the other one traps the reflected light and transmits it to a detector. The intensity of the detected light depends on how far the reflecting surface is from the fiber optic

transmitting/receiving element. Light is transmitted from the bundle of fibers in a solid cone as shown in Figure 2.10.

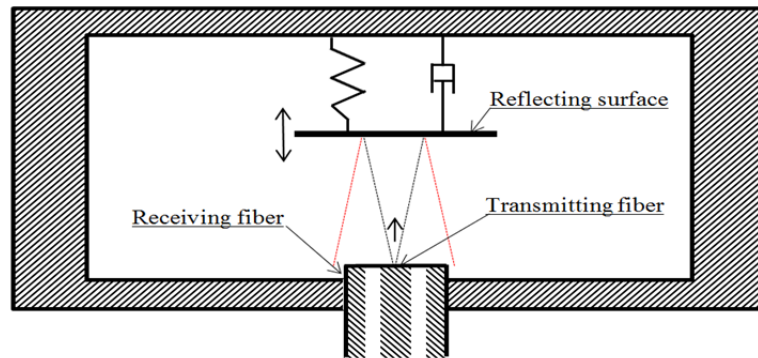


Fig. 2.10 – Schematic diagram of a fiber optic accelerometer

Since the angle of reflection is equal to the angle of incidence, the size of the spot that strikes the fiber-optic transmitting/receiving element after reflection is twice that of the spot that hits the reflecting surface initially. When the distance from the reflecting surface increases, the spot size increases as well. Therefore, the intensity of the reflected light is inversely proportional to the spot's size. Sensitivity of these devices can be varied using various optical configurations [39].

These sensors are extremely accurate; they are so sensitive, that even a rotation of the reflecting surface may be detected (e.g. for rotations of $\pm 3^\circ$ or less, the error is less than $\pm 3\%$ and this value increases for bigger rotations). Therefore, they have to be carefully deployed to prevent errors in measurement [40].

4.5 - Piezoelectric and Integral Electronics Piezoelectric (IEPE) accelerometers

Piezoelectric accelerometers are the most commonly used sensors typology for vibration detection. A piezoelectric accelerometer is a seismic transducer utilizing a piezoelectric element in such a way that relatively large electric charges, proportional to the applied acceleration, are produced when the sensor is excited with the oscillations [24].

These devices use the capacity of certain solid materials to generate an electric charge on their surface in response to an applied mechanical or physical stress. Piezoelectricity differs from the piezoresistance effect because piezoresistive materials experience a change in their electrical resistance rather than a change in their electrical charge or voltage [20].

Normally used piezoelectric materials are: natural single crystals (quartz and tourmaline), synthetic crystalline materials (ammonium di-hydrogen phosphate), polarized ceramic materials (PZT), and engineering plastics (PVDF).

The first ones are the most widely used since they offer a long life span in terms of sensitivity and their characteristics are very stable with temperature (up to nearly 800 °C). The disadvantage is that they are generally less sensitive than some piezoelectric ceramics [5]. The second type has a higher piezoelectric constant (sensitivity), a wider bandwidth than the natural crystals, and it is less expensive to produce. Nevertheless, it can resist temperature of up to nearly 300 °C only and the sensitivity changes in time as a result of ageing [26]. On the other hand, polarized ceramic materials can be used to measure smaller stresses extended over a longer time due to their higher dielectric constant and high sensitivity [24]. The fourth type: polarized polyvinylidene fluoride (PVDF), is made of an inexpensive, highly resistant to shock, thin film. When a PVDF material is used in compression mode, it allows very high frequency measurements, but it is generally less stable with temperature (up to nearly 150 °C) than ceramics or single-crystal materials [24].

A seismic piezoelectric transducer can be represented by the elements plotted in Figure 2.11 where a mass is supported on a linear spring, fastened to the frame of the instrument. The piezoelectric crystal, which produces the charge, acts as the spring.

The inertial force of the mass causes a mechanical strain in the piezoelectric element, which produces an electric charge proportional to the stress. If the dielectric constant of the piezoelectric material does not change with electric charge, the generated voltage is proportional to the acceleration. Metallic

electrodes are applied to the piezoelectric element, and electrical leads are connected to the electrodes for measurement of the electrical output of the piezoelectric element.

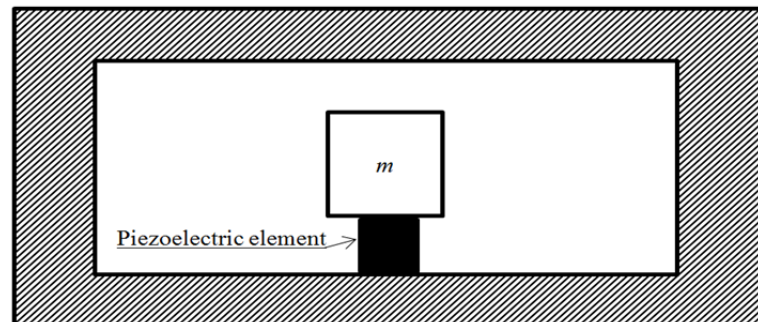


Fig. 2.11 – Schematic diagram of a piezoelectric accelerometer

From an operational point of view, piezoelectric accelerometers can be of two types: shear and compression [41]. In shear-type accelerometers, as the name implies, the stress is applied to the internal piezoelectric crystal in a shear manner. In this type of sensor design, the crystals-sensing elements are sandwiched between a center post and the mass (or masses). The piezoelectric crystals are held in place by a preload ring as shown in Figure 2.12. In particular, in one of the most common designs (called delta-shear type), three piezoelectric elements and three masses are deployed in a triangular shape close to each other. A ring maintains this disposition and ensures a preload action. The output signal is then obtained connecting the wires to the base of that ring.

On the other hand, compression-type is a more simplistic design. In it, the crystal-sensing element sits between an isolating base and the inertial mass. A preload stud (not visible in Figure 2.13) is deployed through the center of the mass and the crystal to hold it in place. Early piezoelectric accelerometers were of compression-type design, mainly due to the relatively easy manufacturing process, and subsequent sensor assembly.

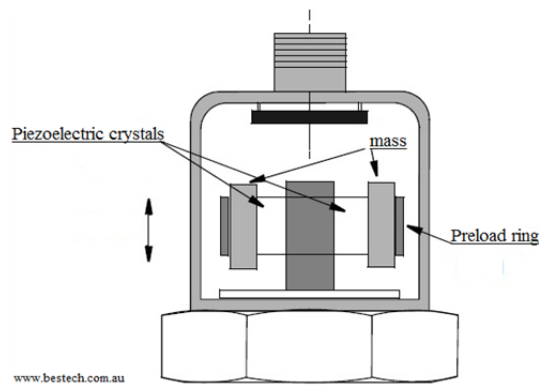


Fig. 2.12 – Shear-type piezoelectric accelerometer

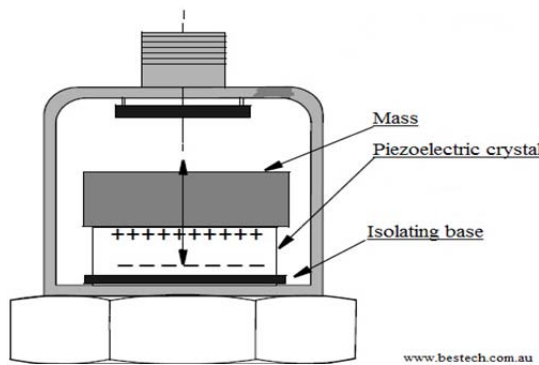


Fig. 2.13 – Compression-type piezoelectric accelerometer

The compression design offers a higher stiffness than the shear one; this results in an accelerometer having a higher natural frequency, and a slightly higher frequency response (10 - 20%) [24]. Nevertheless, compression mode may generate errors in the output signal. In compression-type accelerometers even vibrations produced by solicitations different from those being analyzed (e.g.: changes in temperature, base bending, etc.) may excite the piezoelectric sensing element. This depends on the mounting of the stud-base system, which acts as a spring connected in parallel with the sensing element and capable of exciting it. Therefore, the produced output can be very significant in structures having a large amount of flexure or when the accelerometer is placed in a hot or cold environment. Instead, in shear mode designs, crystals and masses are essentially isolated mechanically from base bending and thermal stresses. Thus, they are much less sensitive to these errors, and provide readings that are more reflective

of the actual vibration to be measured [41]. For these reasons, although shear design is more complex than compression one, most modern accelerometers adopt this construction.

Piezoelectric accelerometers can provide a voltage output instead of the electrical charge. These types of devices are accomplished by incorporating a charge amplifier inside the case of the accelerometer. Nowadays, piezoelectric accelerometers are available with simple electronic circuits internal to their cases to provide signal amplification and a low-impedance output. Indeed, piezoelectric accelerometers with integral electronics (IEPE) are relatively immune to cable-induced noise and spurious response, they can be used with lower-cost cable, and they have a lower signal-conditioning cost [42]. Internal electronics provide an overall reduction in the noise levels because this minimizes the cable capacitance between the sensor itself and the signal-conditioning components [43].

Voltage mode devices feature three-wires (Signal, Ground, Power) or two-wires (Power/Signal, Ground) design. In particular, the latter is a class of piezoelectric accelerometer that incorporates an electronic amplifier and uses a single two-pole coaxial connector for both power input and signal output. Power is supplied to the accelerometer through the inner conductor of the coaxial cable from an external constant current, whereas the output signal from the device is also transmitted on the inner conductor, and it consists of an AC voltage. The shield of the cable serves as the ground return for the supply current and also protects the inner conductor from electromagnetic interference. Nevertheless, these advantages do not come without compromises. The impedance-matching circuitry is built into the transducer; thus, gain cannot be adjusted to utilize the wide dynamic range of the basic transducer. Furthermore, operational ambient temperature is limited to that which the circuit can withstand, and this value is considerably lower than that of the piezoelectric sensor itself. Figure 2.14 shows the scheme of an IEPE accelerometer with its main features.

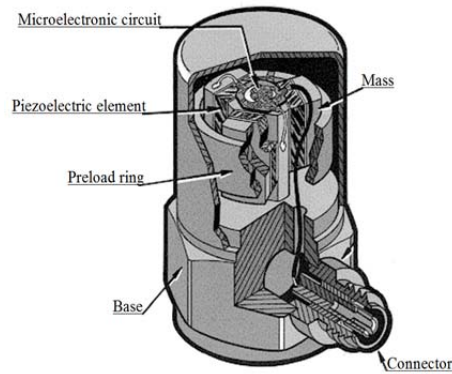


Fig. 2.14 – Components of an IEPE accelerometer

In the ideal seismic system shown in Figure 2.1, the mass and the case have infinite stiffness, the spring has zero mass, and viscous damping exists only between the mass and the frame. In real-world piezoelectric accelerometers, these assumptions cannot be fulfilled. In some accelerometers, the mass and the spring are inherently a single structure. Furthermore, in those practical designs where the case is used to hold the mass and the piezoelectric element, a case distortion may produce mechanical forces upon the seismic element as well. All these factors may change the accelerometer performances from those calculated using the equations based on the ideal system. In particular, the resonance frequency may be substantially lower than that indicated by theory [42].

The resonance frequency ω_r of these devices is usually in the order of 10^1 kHz, but mounting type can have a significant effect on this value. If the accelerometer is properly mounted on the system being tested, the upper frequency limit is taken to be $\omega_r/3$ with a deviation of 12% (1 dB) from the mean value of the response and $\omega_r/5$ for a deviation of 6% (0.5 dB).

On the other hand, the lower frequency limit depends primarily on the characteristics of the preamplifier that follows the accelerometer. Indeed, from an electrical point of view, the piezoelectric element looks like a source capacitor with a finite internal resistance, (typically in the order of $10^9 \Omega$). It forms the time constant of the RC circuit, which defines the high-pass characteristics of the device [44]. For this reason, a piezoelectric accelerometer cannot be used to

measure static events because the DC-coupling component of the signal is lost. In general, it is possible to affirm that piezoelectric materials are useful for measuring stresses, which vary rapidly with time, whereas for static or quasi-static stresses, the dielectric constant of the material causes the produced charge to leak off [43].

It is observed that, to operate, seismic devices use a variation of electrical quantities produced on a sensitive element by an external stress (i.e.: acceleration). The accelerometer converts the electrical charges generated on the crystal in an electric potential difference. This is achieved by placing the sensing element into a suitable electrical circuit.

If piezoelectric accelerometers are considered, that circuit is deployed outside the accelerometer within a pre-amplifier connected in series with the device's output. This setup is called high-impedance. The pre-amplifier, to detect the electric potential difference before the crystal discharges, has to have an input impedance of the same order of magnitude as the crystal's output impedance (nearly $10^9 \Omega$) [19]. If electrical charges leave the electrodes too fast, accelerometer sensitivity is reduced and significant errors in the measurement are committed. Figure 2.15 plots a simplified electrical scheme of the circuit, where Q is the electrical charge produced by the piezoelectric element, C_Q and R_Q are the capacitance and the resistance of the piezoelectric element, C_W and R_W those of the connection wire, and C_A and R_A the capacitance and the resistance of the amplifier.

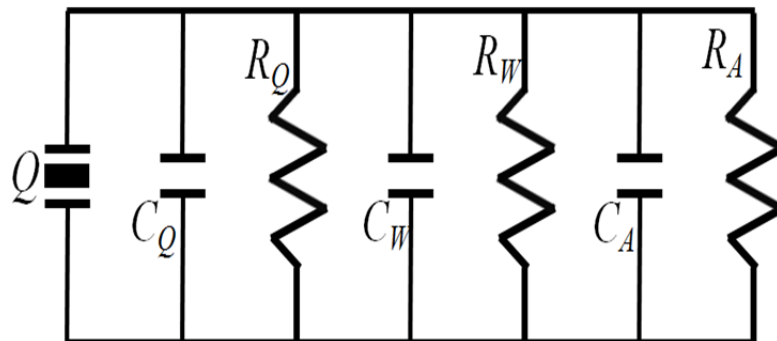


Fig. 2.15 – Electrical scheme of a piezoelectric accelerometer

Referring to the equivalent capacitance C and resistance R as:

$$C = C_Q + C_W + C_A \quad [2.24]$$

$$\frac{1}{R} = \frac{1}{R_Q} + \frac{1}{R_W} + \frac{1}{R_A} \quad [2.25]$$

it is possible to describe the equivalent RC circuit and evaluating the output tension $V(t)$ of the accelerometer as:

$$V(t) = V_0 e^{-\frac{t}{RC}} \quad [2.26]$$

where V_0 is the tension at the time $t = 0$.

If the product RC is not higher than the period of the signal being measured, the condenser will discharge before the measure is achieved. Because both the wire and its connectors have a finite capacitance C , small and depending on the length of the cable itself [45], it is necessary that the input impedance of the amplifier be as high as possible. This is a further explanation because piezoelectric accelerometers barely measure low-frequency signals (of the order of 10^{-1} Hz) and cannot measure static accelerations.

The connection wires between the accelerometer and the charge amplifier are an extremely important element of the measurement chain. They have to be of low-noise and high-insulation type; furthermore, their length cannot exceed a few meters. Therefore, as has been noted, the main limitation to the use of piezoelectric accelerometers is that the pre-amplifier should be mounted close to the transducer, because the connection wire cannot exceed a certain length so as not to reduce the input impedance too much. Also, in particular types of measurements, cables cannot be well fixed and their movements may influence the result of the measurement as shall be shown in the next paragraph.

IEPE accelerometers partially overcome these problems. Since they have an integrated circuit within the transducer itself, they do not require any external pre-amplifier but an AC-coupled power supply only. This type of measurement setup is referred to as low-impedance. The IEPE accelerometer is connected to the power source using a coaxial cable, which may be up to tens of meter long, and is used for acquiring data also.

Nevertheless, this type of accelerometer is not the final solution to the problem of signal quality. Indeed, in many practical applications, especially civil and mechanical engineering ones, acceleration is characterized by very low-amplitude, which means a very low electrical signal (usually in the order of millivolts). Because of cable lengths, this signal may be disturbed and corrupted, invalidating the measurement. Impedance decreases with length; therefore, because signal attenuation, an amplifier is always necessary after a certain distance, even in low-impedance measurement chains.

4.6 - Micro Electro-Mechanical Systems (MEMS) accelerometers

Micro Electro-Mechanical Systems (MEMS) technology refers to a family of devices having characteristic dimensions in the range 10^{-3} - 10^{-6} meters, that combine electrical and mechanical components, and which are manufactured using integrated circuit batch-processing technologies [26].

Current manufacturing techniques for MEMS include: surface silicon micromachining, bulk silicon micromachining, lithography, electro-deposition, plastic molding (LIGA), and electro-discharge machining (EDM) [46]. This technology has experienced an increasing growth during the last decade: sensors for pressure, temperature, mass flow, velocity, acceleration, sound, and chemical composition have been manufactured [36]. In MEMS-based accelerometers, the entire working mechanism (mass, spring, and support) is etched from a single crystal of silicon, a process known as micromachining [47]. An example of a MEMS-based accelerometer is shown in Figure 2.16. It is observed that electronic components are assembled together over a silicon wafer and they are extremely small in size.

MEMS-based accelerometers are capacitive-type devices; therefore, they are made of moveable inertial masses with plates that are attached through a mechanical suspension system to a reference frame, as shown in Figure 2.17. The moveable plates and the fixed outer plates represent the capacitors of the system [34].

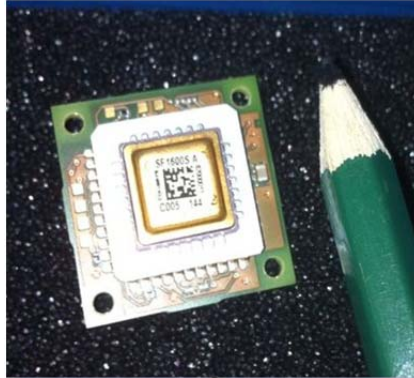


Fig. 2.16 – MEMS-based accelerometer

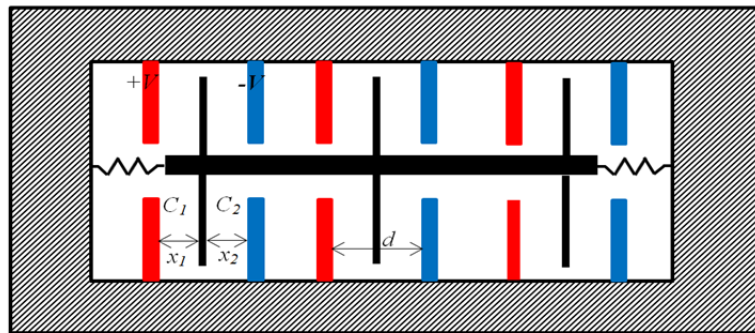


Fig. 2.17 – MEMS-based accelerometer structure

The deflection x of the inertial masses is measured using the capacitance difference ΔC between the moveable plate (in black in Figure 2.17) and the stationary outer plates (highlighted in red and blue in the same picture). In general, the capacitance C_0 can be evaluated as:

$$C_0 = \varepsilon_0 \frac{S}{d} = \varepsilon_A \frac{1}{d} \quad [2.27]$$

where ε_0 is the permittivity of the material separating the two plates of the capacitor, S is the surface of the electrodes, and d their mutual distance. With reference to Figure 2.17, the capacitance between the two condensers C_1 and C_2 is equal to:

$$\begin{cases} C_1 = \varepsilon_A \frac{1}{x_1} = \varepsilon_A \frac{1}{d+x} = C_0 - \Delta C \\ C_2 = \varepsilon_A \frac{1}{x_2} = \varepsilon_A \frac{1}{d-x} = C_0 + \Delta C \end{cases} \quad [2.28]$$

where x represents the displacement of the inertial mass. When the acceleration is null, the capacitance C_1 and C_2 are equal because x_1 is equal to x_2 and x is null. If this parameter is different from zero, the net capacitance is equal to:

$$C_2 - C_1 = 2 \Delta C = 2 \varepsilon_A \frac{x}{d^2 - x^2} \quad [2.29]$$

which corresponds to the algebraic non-linear equation [2.30]:

$$\Delta C x^2 + \varepsilon_A x + \Delta C d^2 = 0 \quad [2.30]$$

the first term at the first member of equation [2.30] is negligible; therefore, the solution of that equation can be evaluated as:

$$x \approx \frac{d^2}{\varepsilon_A} \Delta C = d \frac{\Delta C}{C_0} \quad [2.31]$$

Equation [2.31] proves that the displacement x of the mass can be evaluated once the variation in capacitance is measured. To conclude, it has to be noted that each sensor has several capacitors set as shown in Figure 2.18.

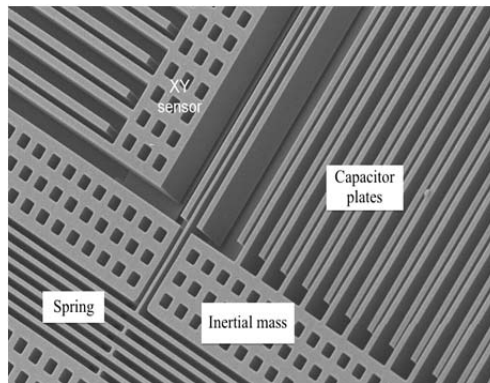


Fig. 2.18 – Capacitors set in a MEMS-based accelerometer (LIS331DLH by STMicroelectronics)

Among the main advantages of a MEMS-based accelerometer there are: the integrated multiple functions, the reduced manufacturing cost and time, the portability, the ruggedness, the low-power consumption, the easy and massive deployment, the very small size of the device, and the very high resonance frequency. This type of accelerometer is used to measure a wide range of accelerations (from a few to over thousands of g) on a wide frequency domain (from DC to several kHz).

A more recent MEMS-based accelerometer design offers squeezed-film gas damping as an alternative to the silicone oil damping to improve the damping behaviors of the moving plate inside the two capacitors. Nevertheless, this class of low-price capacitive accelerometer typically suffers from poor signal to noise ratio and limited dynamic range [48].

5 – Problems connected to the usage of wire-based accelerometers

The previous paragraphs address two important problems regarding the usage of wire-based accelerometers. Wires impedance and how this parameter affects the quality of the transmitted signal increasing the produced noise.

The first issue is connected to a technological limitation due to the cable length. Connection wires between the accelerometer and the acquisition section are extremely delicate elements of the measurement chain: well-isolated and low-noise cables are required and preferred. In addition, their length cannot exceed a few meters of extension, because of signal impedance. Impedance decreases with length [45]; therefore, an amplifier is always necessary after a certain distance because of signal attenuation.

The second reason is connected with noise introduced in the signal due to wire (triboelectric noise), which can create problems when signals having low amplitude – such as those characterizing the vibration of large civil structures – are analyzed. Triboelectric noise is produced because of mechanical movements of the wire itself and it is characterized by the generation of local currents which can interfere with the transmitted signal [49]. Thus, a charge may be generated when a cable is flexed, bent, struck, squeezed, or distorted. This friction takes place between the dielectric and the outer shield of the cable or between the dielectric and the center conductor. Fixing the cable on a stable support can significantly reduce the problems, but such an operation is not always feasible or easy to achieve.

Another mechanism by which noise may be induced in the cable results from the change in capacitance of the cable when it is flexed. If the transducer produces a charge across the cable, the change in capacitance results in a voltage change across the output of the cable, appearing as noise at the input of a voltage amplifier. Suppose that the dielectric surfaces within the cable are coated so that an electrical leakage path is provided along the dielectric surface. Then - if because of deformation - the cable shield is separated from the outer surface of the

dielectric, the charges flow along the surface to the nearest point of contact of the dielectric and shield; without this leakage path, the charges would flow to the terminating impedance, where they would give rise to a noise signal. Such coatings are provided in low-noise cables.

CHAPTER III

DESIGN OF A NEW SENSOR BOARD EMBEDDING A MEMS-BASED ACCELEROMETER

1 – Introduction

The fast growth of wireless-based technologies, such as Electro Mechanical Impedance (EMI) and Micro Electro-Mechanical Systems (MEMS), is changing the way civil structures and mechanical systems are monitored, controlled, and maintained. While EMI techniques result in high frequency signals [50 – 55], MEMS-based techniques prove to be an attractive tool in the sampling of low frequency signals for Structural Health Monitoring (SHM) purposes [56 – 58].

From the early 1990's onwards, there has been an increasing interest in the adoption of developing sensing technologies for instrumentation within a variety of structural systems. Wireless sensor networks (WSNs) are emerging as a sensing paradigm and they are considered to be suitable substitutes for traditional wired-based monitoring systems. Nevertheless, to date, low sensitivity and accuracy - especially at very low frequencies and low-amplitude - have imposed serious limitations for their application in monitoring the mechanical behavior of civil structures and machinery parts. The SHM applications require the MEMS-based accelerometers to be accurate for measuring a wide range of structural vibration: from ambient vibration (in the order of $10^{-2} \text{ m}\cdot\text{s}^{-2}$) to severe earthquakes (in the order of $10^1 \text{ m}\cdot\text{s}^{-2}$). In addition, natural frequencies in large civil engineering structures - including bridges and buildings - are generally in the order of 10^{-1} to 10^1 Hz [59]. Therefore, sensor systems able to measure such low-frequency signals accurately are required; otherwise, the recorded signal might be confused with a noise.

In this chapter, a summary review regarding the state-of-the-art of the WSNs for SHM is first given. Then, a prototype wireless system, which embeds a MEMS-based accelerometer, is presented. Design choices, hardware characteristics, and operational properties of the prototype are detailed and described to highlight how the proposed system may overcome the difficulties met by previous systems as they were used for SHM purposes.

2 – Summary review of MEMS-based accelerometer systems

In 1986, researchers from the Center for Engineering Design at the University of Utah, in a proposal submitted to the Defense Advanced Research Projects Agency (DARPA), introduced for the first time the term MEMS. In the mid-1990s, the potential military applications of this technology became clear and another proposal, called the Smartdust project, was submitted to the same agency by researchers at the University of California, Berkeley [60]. Smartdust refers to a system of several small MEMS-based sensors, robots, and other transducers, which can detect physical quantities such as light, temperature, vibration, magnetism, or chemicals. Usually, these devices are operated wirelessly on a computer network and are distributed over an area to perform tasks (e.g.: sensing through radio-frequency identification). Since the expiration of the military patent, this technology has been applied in several engineering fields. Numerous academia-built and commercial prototypes have been designed and built. In the following paragraphs, a short overview of the most significant of these is given.

2.1 - Academia-built platforms for WSN

One of the first efforts in designing a low-cost, wireless sensing unit for application to civil engineering structures was made by Straser and Kiremidjian in 1998, when they built a wireless, modular, monitoring, smart sensor (WiMMS) [61]. The design included the integration of an eight-channel 16-bit Analog to Digital Converter (ADC), which allows the accommodation of sensors for recording the physical data, a microcontroller core for on-board computational tasks, and a 900 MHz ISM (Industrial Scientific and Medical) wireless radio modem for the communication. The microcontroller, a Motorola 68HC11, features an 8-bit counter, a 16-bit timer, one asynchronous RS-232 serial port, and 64 kB for data and programs storage. Furthermore, additional 32 kB of Random Access Memory (RAM) and 16 kB of Read Only Memory (ROM) are included in the design to store embedded firmware for local data processing. Most of the time,

the sensing unit is maintained in a sleep mode to save battery life. Therefore, it is also equipped with an acceleration-based trigger circuit to awake the system in case of significant seismic motions. Even though WiMMS was characterized by low computational power and low accuracy, it paved the way for the development of several other wireless sensing units.

Several researchers started proposing their own systems for sensing diverse physical parameters. Bennett, in 1999, designed a wireless sensing unit mounting two thermometers and two thin-film strain gages embedded in flexible asphalt highway surfaces [62]. The design includes a four-channel 8-bit ADC, a Hitachi H8/329 8-bit microcontroller, and a narrow-band 418 MHz wireless radio capable of communicating in a 300-meters range. To provide ample memory for the storage of embedded software that operates the sensor, 32 kB of external ROM is included in the computational core design. For power, four AA alkaline batteries offering a total voltage of 6 V are included.

In 2001, Lynch [63 - 64] designed a wireless sensing unit embedding a Texas Instrument one-channel 16-bit ADC, an 8-bit Atmel AVR8515 microcontroller core, and a 900 MHz ISM band wireless radio modem. The system incorporates 8 kB of programmable flash memory, 512 bytes of Static Random Access Memory (SRAM), and 512 bytes of Electronically Erasable Programmable Read Only Memory (EEPROM) to perform local processing and data storage tasks. The system was one of the first to be equipped with a two-axis MEMS-based accelerometer: an ADXL2010 by Analog Device [65]. Figure 3.1 shows the wireless sensing unit built by Lynch where there are clearly identifiable an RS-232 Serial Port, the ADC, the microcontroller, the two-axis accelerometer, and the radio modem with the antenna.

In the same year, Wang and Liao [67] presented a wireless signal retrieval system. This system is extremely important because it is the first to use a frequency modulation (FM) technology before transmitting. In particular, the wireless transmitter subsystem is composed of the following units: the sensor signal processor, the Voltage to Frequency (V/F) converter, and the transmitter.

On the other hand, the wireless receiver subsystem is mainly composed of the opposite units: the receiver, the signal processor, the Frequency to Voltage (F/V) converter, and the low pass filter. In Wang and Liao's study, an example of transmission of a sinusoidal wave is presented. And it shows that the system is far below the threshold of accuracy to be usable for SHM purposes. Indeed, the received signal yielded the same frequency content, but the amplitude is increased. Additionally, when the power spectral density of a random with noise is studied, the reception of the signal below 5 Hz suffers a sharp decrease.

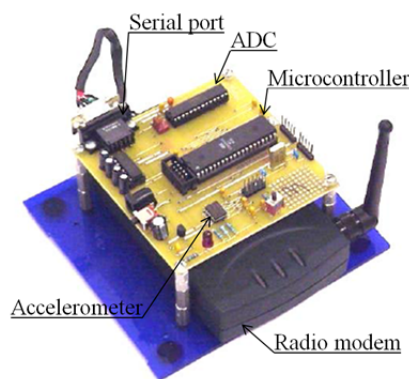


Fig. 3.1 – Prototype of the wireless sensing unit proposed by Lynch (source: Lynch [63])

Mitchell, in 2002, [68] proposed a SHM architecture using wireless sensors. Based upon three generations of hardware and software designs, the designed wireless monitoring system emphasizes the partitioning of the monitoring system functionality between wireless sensors and wireless data servers (called wireless cluster nodes). In this system, a Cygnal 8051F006 microcontroller is used for data collection whereas an Ericsson Bluetooth wireless transceiver, operating on the 2.4 GHz radio band, is integrated for communication. Data from sensors are sent to the cluster node using a short-range radio. Each cluster node is equipped with both a short-range radio (for communication with the wireless sensors in its cluster) as well as a long-range radio (for communication with other remote cluster nodes). The central cluster server is designed both to store and process the data collected from the cluster's wireless sensors. The cluster node is designed using a single board computer (SBC) running the Microsoft Windows operative

system. A key element of the proposed SHM system is its interface to the Internet, which allows professionals to access the structural response data remotely.

In 2003, Kottapalli [69] presented a wireless sensor network architecture that was intended to overcome the major challenges associated with time synchronization and limited power availability in wireless SHM systems powered by batteries. The system is made of several sensing units, whose goal is to simply collect measurement data and wirelessly transmit to the designed base station. The microcontroller embedded on the system is an 8-bit Atmel AVR. For data collection, an 8-bit ADC is also included in the unit design whereas communication is achieved through a 915 MHz radio transceiver. The study demonstrated that due to the low-power consumption of the embedded devices, the system can work for 18 months using six AA alkaline batteries.

After that, studies have started mainly to focus on enriching the computational power of the sensing units, omitting the part regarding the sensitivity and the accuracy of the embedded instrumentation and sensors. In 2004, Lynch [70 - 71] proposed a dual-processor computational core design. Based on his earlier wireless sensing unit design [63 - 64], a low-power 8-bit Atmel AVR AT90S8515 microcontroller is utilized for overall unit operation and real-time data acquisition. When data are ready for local processing, the unit turns on the second microcontroller, a 32-bit Motorola MPC555 PowerPC. Here, intensive data processing algorithms stored in the ROM (e.g.: damage detection routines) are executed. For data collection, a 16-bit, single-channel ADC ADS7821 by Texas Instruments is used, whereas for wireless communication a 2.4 GHz radio modem is employed. To supply power to the wireless sensor, a Li/FeS₂ 7.5 V battery pack is chosen. This study demonstrated that the selected power unit allowed the system to work for nearly one year.

In the same year, Ou [72] – based on previous experiences with commercial wireless sensor platforms - presented his wireless sensor prototype for structural monitoring. The core of the system is the low-power Atmel AVR ATmega8L microcontroller. This 8-bit microcontroller has 8 kB of flash memory for storing

embedded programs and 1 kB of SRAM for storing measurement data. In total, eight sensing channels are provided for the interface of sensors. Six of the channels supported the conversion from analog sensor outputs into digital formats with resolutions of 8 and 10 bits, whereas the last two channels are for measuring the output of digital sensors such as the Analog Devices ADXL202E MEMS-based accelerometers. Wireless communication between sensors is provided by a 433 MHz Chipcon CC1000 wireless transceiver.

Nowadays, another problem addressed in WSN is that connected to power consumption. In recent years, a new wireless communication standard, IEEE802.15.4 [73], has been developed explicitly for wireless sensor networks. This wireless standard is intended for use in energy-constrained WSNs because of its extreme power efficiency. Sazonov [74] was one of the first to propose the design of a low-power wireless system based on this communication protocol. The proposed unit employed the IEEE802.15.4 – compliant, 2.4 GHz wireless transceiver. To reduce power consumption a 16-bit microcontroller is selected as computational core, while the MSP430 provided the unit with a six-channel 12-bit ADC and a two-channel 12-bit DAC. With 2 MB of non-volatile EEPROM, the MSP430 is capable of storing sophisticated data interrogation algorithms. Studies by Lynch [56], [75] and Spencer [76], among the others, supply a complete list of academia-built WSN systems for SHM purposes.

To conclude, it can be observed that the presented systems are all characterized by the presence of more or less powerful computational devices (microcontrollers) installed on-board. Indeed, one of the main ideas at the base of SHM technologies is that data stream has to be as simple as possible, and only the essential information must be sent to the collecting Data Acquisition (DAQ) System. Furthermore, analog signals sampled with sensors are converted into digital signals through a suitable ADC. For power-consumption reasons, the resolution of the used ADCs varies in the range 8 – 16 bit. It may be a limitation for the accuracy of the measurement when low-amplitude and low frequency signals are analyzed.

2.2 - Commercial platforms for WSN

A number of commercial wireless sensor platforms have emerged in recent years that are well suited for use in SHM applications. Many academic and industrial research teams have begun to explore these generic wireless sensors for use within SHM systems. The first prototype ever commercialized was the mote wireless sensor platform initially developed at the University of California, Berkeley and subsequently sold by Crossbow [77 - 78]. Mote is an open source wireless sensor platform with both its hardware and software (TinyOS) design available to the public.

The Berkeley platform has been under development since the late 1990's. In 1999, the WeC mote, commercialized by Crossbow as Rene, was released [79]. It is a small low-power electronic device integrated with wireless communication capabilities and sensors having dimension comparable with an American quarter (\$0.25 coin). The design included the integration of an eight-channel, 10-bit ADC, and an 8-bit Atmel AT90LS8535 AVR microcontroller. Since only 8 kB of ROM and 512 Bytes of RAM were included in the microcontroller, an additional 32 kB of external RAM was included within the platform. Wireless communication was ensured using a 916 MHz, amplitude modulated (AM), single channel transceiver. Two years later, the WeC platform was substituted by the Rene2 mote platform. It had an identical design to the WeC except for the microcontroller, which was replaced with a more powerful Atmel ATmega163L having larger internal memory banks [80]. Figure 3.2 shows the Rene and Rene2 mote platforms. The successors to these two were the Mica [81] and the Mica2 [82] mote platforms. They have continued the modular design but upgrade the system to a more powerful microcontroller: the Atmel ATmega 103 at 4 MHz and ATmega 128l at 7.37 MHz respectively. Again, the internal eight-channel, 10-bit ADC of the microcontroller is utilized as the primary sensing interface for the Mica Mote with sample rates up to 1 kHz. On the other hand, for communication purposes the Mica motes use the same single-channel amplitude modulation wireless transceiver embedded in the previous models. The Mica2 mote platform was

released to overcome radio interference and data loss, which characterized the Mica platform. A frequency modulation (FM) wireless transceiver operating on the 900 MHz radio band was installed showing excellent noise immunity.

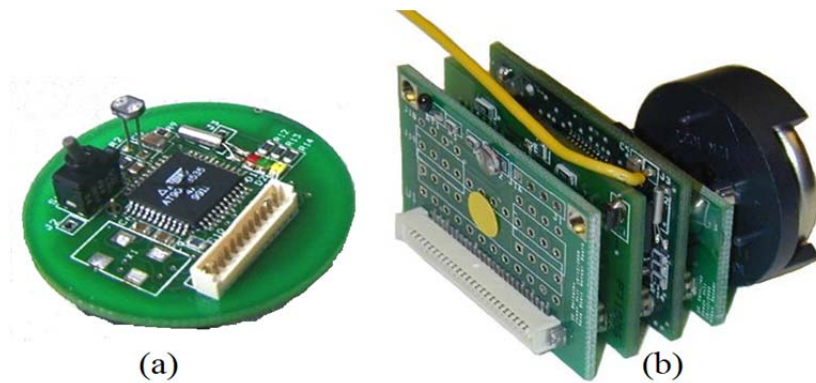


Fig. 3.2 – Crossbow Rene (a) and Rene2 (b) mote platforms

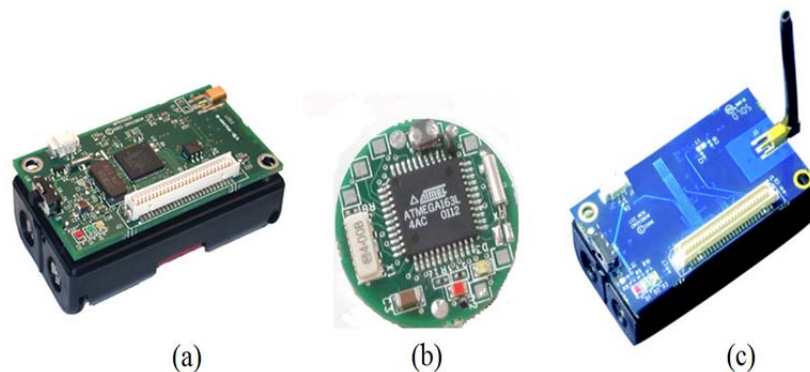


Fig. 3.3 – Crossbow Mica2 (a), Mica2DOT (b), and IRIS (c) mote platforms

In 2004, the Mica2 was upgraded with a 2.4 GHz IEEE802.15.4-compliant wireless transceiver and renamed as MicaZ [75] and then with another module used for enabling low-power, wireless sensor networks platform called IRIS [79]. One of the main features of the Mica2 and its derivate (Mica2DOT, MicaZ) is that they are designed without a battery voltage up conversion (step-up or boost converter). For this reason, they operate on unregulated battery voltage [80]. Therefore, as the battery depletes, the voltage drops affecting components such as the radio and the sensors as demonstrated in other studies [83]. The above-described platforms are shown in Figure 3.3.

The collaborations between the University of California, Berkeley and the Intel Research Berkeley Laboratory resulted in another generation of Mote platform called Imote. The core of the Imote is the 32-bit ARM7TDMI microcontroller operating at 12 MHz. This processor selection provides four times greater computational power than the previously mentioned Mica family. On the wireless communication end, a 2.4 GHz Bluetooth radio is integrated with the microcontroller on a single circuit chip. Selection of Bluetooth for wireless communication is motivated by its high data rate and high reliability [84]. The hardware design of the Imote is different from those of the Mica, Mica2, and MicaZ motes. The Imote was designed with only a computational core board and a wireless transceiver, but it employs a highly modular construction, which allows sensing interfaces - fabricated as separate boards - to be snapped onto the circuit board. Figure 3.4 shows a model of the Imote2 platform owned by the Smart Infrastructure Management Laboratory SIMLab at the University of Florida, FL.

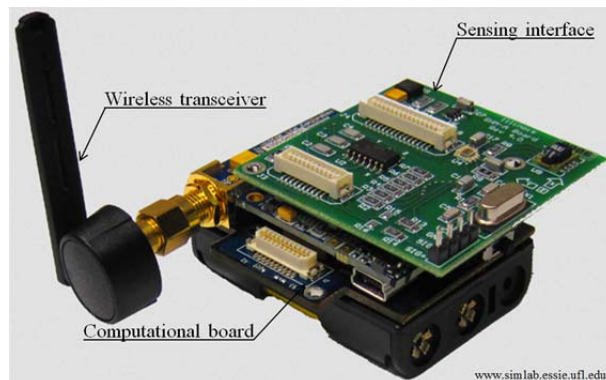


Fig. 3.4 – Intel Imote2 platform (source: SIMLab – University of Florida)

Aside from the open-source platforms presented in the first part of this paragraph, other commercially available wireless sensor platforms were designed for SHM. For instance, researchers at the Rockwell Science Center designed AWAIRS: a wireless sensing unit for military applications, which could potentially include structural monitoring. Its defining feature is the ability to self-organize when deployed in the field [85]. The prototype mounted a 32-bit Intel StrongARM 1110 microcontroller as computational core. The platform has been

designed to embed a variety of sensors such as geophones, acoustic sensors, magnetometers, and accelerometers using a 20-bit ADC. To render the network self-organizing, a 900 MHz wireless cordless telephone radio with encrypted spectrum is installed. Many other platforms, such as Shimmer [86], Telos-B [87], and Sun SPOT [88], are now available on the market and they can all be adopted for SHM purposes.

2.3 - MEMS-based accelerometer systems used for SHM

The platforms introduced in the previous paragraphs are the communication modules only. They do not have any sensing capability if not implemented with a sensor board well suited for vibration detection. Therefore, an overview of the most important systems embedding MEMS-based accelerometers is reported to conclude this section.

In 2003, Kurata [89] presented a study in which the Mica mote was used as a risk-monitoring tool. In this analysis, a two-story metallic structure was deployed on a shaking table and subjected to the Kobe earthquake's ground motion. A Mica mote and a reference accelerometer were deployed at the top of the structure and a comparative measure between the data sampled with the two systems was carried out in the time domain. The Mica mote was equipped with the commercially available MTS310 sensor board manufactured by Crossbow Technology, Inc. This sensor board, shown in Figure 3.5, has acceleration, magnetic, light, temperature, and acoustic sensors, as well as a sounder. In particular, the accelerometer embedded in the system is an ADXL202E manufactured by Analog Device. It is a low-cost, low-power, two-axis MEMS-based accelerometer with a measurement range of $\pm 19.61 \text{ m}\cdot\text{s}^{-2}$, a sensitivity of $0.02 \text{ V}\cdot\text{m}^{-1}\cdot\text{s}^2$, a bandwidth in the range DC - 50Hz, and a noise-density of $1960 \text{ }\mu\text{m}\cdot\text{s}^{-2}\cdot\text{Hz}^{-0.5}$ [90]. Its resolution, evaluated using equation [2.23], is equal to $1.75\cdot 10^{-2} \text{ m}\cdot\text{s}^{-2}$.

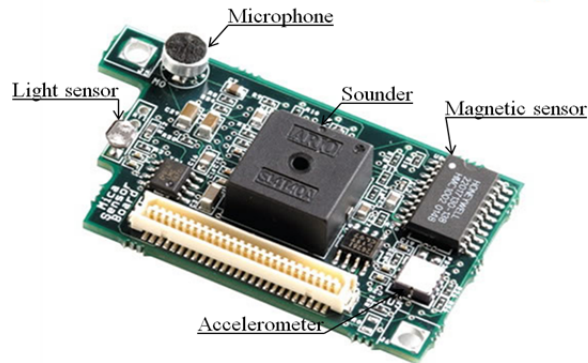


Fig. 3.5 – Crossbow MTS310 sensor board

The study has demonstrated that the Mica mote and the associated sensor board are able to detect high amplitude excitations (damages of the structure). Nevertheless, due to its low resolution, low amplitude signals are confused with noise and lost. In addition, the study has highlighted data losses during the transmission of the signal to the receiver. From this experience, it is clear that the second generation of motes proposed is not well suited for SHM purposes.

Additional studies regarding the performance of the ADXL202E accelerometer embedded on the MTS310 sensor board were carried out by Ruiz-Sandoval [91]. In this study, the Mica mote was deployed on a shaking table along with a reference sensor and excited with two random accelerations. The sensor used as reference is a model 393B04 by PCB Piezotronics Inc. It is a high-sensitivity, IEPE, seismic, shear-type accelerometer with a sensitivity of $0.10 \text{ V}\cdot\text{m}^{-1}\cdot\text{s}^2$, a bandwidth in the range $0.06 - 450 \text{ Hz}$, and a noise-density of $0.39 \mu\text{m}\cdot\text{s}^{-2}\cdot\text{Hz}^{-0.5}$ [92]. Its resolution, evaluated using equation [2.23], is equal to $2.22\cdot 10^{-5} \text{ m}\cdot\text{s}^{-2}$. The study has showed that, when the sensors are subjected to relatively high amplitude random acceleration ($4.10\cdot 10^{-1} \text{ m}\cdot\text{s}^{-2}$), the response in time domain of the ADXL202E accelerometer with respect to the 393B04 is reasonably good. On the other hand, in the frequency domain the responses between the two accelerometers are in good agreement above 2 Hz only. When low-amplitude random acceleration ($4.80\cdot 10^{-2} \text{ m}\cdot\text{s}^{-2}$) is supplied, it is observed that the response in the time domain of the ADXL202E accelerometer compared with the reference

accelerometer is quite poor. Besides, in the frequency domain, the responses between the two accelerometers did not correlate at all. To address these limitations, a new sensor board (Tadeo, shown in Figure 3.6) was proposed to replace the MTS310. The new sensor board was designed using the high sensitivity accelerometer SD1221 manufactured by Silicon Designs, Inc. It is a low noise, MEMS-based accelerometer with a measurement range of $\pm 19.61 \text{ m}\cdot\text{s}^{-2}$, a sensitivity of $0.10 \text{ V}\cdot\text{m}^{-1}\cdot\text{s}^2$, a bandwidth in the range DC – 400 Hz, and a noise-density of $49.03 \text{ }\mu\text{m}\cdot\text{s}^{-2}\cdot\text{Hz}^{-0.5}$ [93]. Its resolution – evaluated using equation [2.23] – is equal to $1.24\cdot 10^{-3} \text{ m}\cdot\text{s}^{-2}$. When the two systems were subjected to a random acceleration ($2.55\cdot 10^{-2} \text{ m}\cdot\text{s}^{-2}$), the response in time and frequency domains between the two accelerometers was reasonably good, even below 2 Hz. The study concluded stating that small differences still present below 2 Hz were due to the limitations of the 10-bit ADC of the Mica.

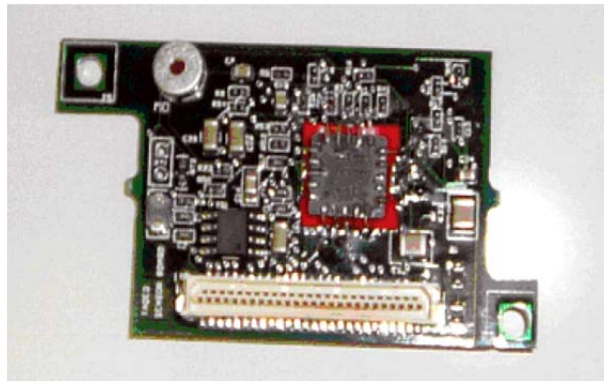


Fig. 3.6 – Tadeo sensor board (source: Ruiz-Sandoval [94])

In 2004, Glaser evaluated the hardware reliability of the Crossbow Rene2 mote with field experiments in the Tokachi Port, Japan. Rene2 mote is equipped with a MTS310 sensor board embedding an ADXL202E accelerometer. The study consisted of measuring the ground acceleration caused by large controlled underground explosions that caused the ground to liquefy and compare data obtained from the ADXL202E with those recorded with reference sensors [95], [96]. Results show that due to the high intensity of the ground motion, the time histories recorded using the Rene mote are comparable with those recorded from

the reference sensors. Little differences are observed when results in the frequency domain are considered. On the other hand, the study reports several problems with the reliability of the single-channel wireless radio. During testing, it experienced significant communication interferences and lock-up phenomena, resulting in the loss of transmitted data. The reliability of the transmission is further reduced in the presence of other electronic equipment including cameras, cell phones, and radios as well.

Between 2005 and 2007, researchers at the University of California, Berkeley implemented a new accelerometer sensor board integrated within a Mica2 mote. With the standard Mote sensor boards (e.g.: MTS310) poorly suited for structural monitoring ([89], [91], [95]), the newly proposed sensor board was strictly intended for SHM purposes. It was conceived for detecting range of vibrations of a civil infrastructure from low-amplitude ambient to earthquake strong motions [97], [98]. The range $\pm 19.61 \text{ m}\cdot\text{s}^{-2}$, characteristic of the original sensor board, is divided between two types of accelerometers to provide both the required range for an earthquake's strong motion (in the order of $10^1 \text{ m}\cdot\text{s}^{-2}$) and accuracy for ambient vibrations (in the order of $10^{-2} \text{ m}\cdot\text{s}^{-2}$). The first sensing capability is ensured using the default accelerometer of the MTS310 sensor board: the ADXL202E accelerometer. On the other hand, low-amplitude ambient vibrations due to wind loading and traffic are resolved by a Silicon Designs SD1221 accelerometer. A picture of this prototype is shown in Figure 3.7.

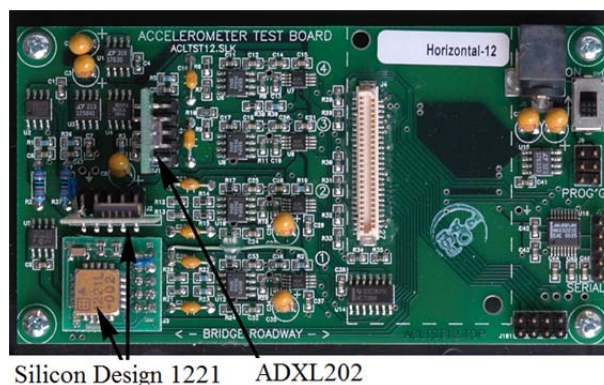


Fig. 3.7 – Sensor board prototype proposed by the UC Berkeley research group (source: Pakzad [99])

To increase its resolution, the dynamic range of the SD1221 accelerometer is artificially reduced from $\pm 19.61 \text{ m}\cdot\text{s}^{-2}$ to $\pm 0.98 \text{ m}\cdot\text{s}^{-2}$, whereas the bandwidth is cut from 400 Hz to 25 Hz using a low-pass filter. Therefore, with the modification made, the new resolution of the SD1221 accelerometer becomes equal to $3.10\cdot 10^{-4} \text{ m}\cdot\text{s}^{-2}$. In this study, to overcome limitations due to the presence of a 10-bit resolution ADC, the filtered analog signal is fed to a 16-bit ADC for each of the four channels. The system was successfully validated through its deployment over a pedestrian bridge over passing I-80 at Berkeley, CA [97], and over the Golden Gate Bridge at San Francisco, CA [98], [100]. In the Golden Gate Bridge deployment, 64 nodes were distributed over the main span and the tower, collecting ambient vibrations synchronously at 1 kHz rate, with less than $10\cdot 10^{-6} \text{ s}$ jitter, and with the highest accuracy ever measured by previous systems (nearly $3.00\cdot 10^{-4} \text{ m}\cdot\text{s}^{-2}$). The collected data allowed dynamic and modal analyses, which agreed with theoretical models and previous studies of the bridge.

In 2008, Cho proposed an application of smart wireless sensors for the monitoring of civil structures [101]. In particular, he tried to extract modal information (i.e.: modal frequency and modal shape) using the WiMMS unit modified by Wang in 2005 [102], as shown in Figure 3.8.



Fig. 3.8 – WiMMS unit modified by Wang (source: Wang et al. [102])

The unit mounts an accelerometer PCB3801 by PCB Piezotronics Inc. It is a single axis, low-cost capacitive accelerometer with a sensitivity of $0.10 \text{ V}\cdot\text{m}^{-1}\cdot\text{s}^2$, a bandwidth in the range DC - 80 Hz, and a resolution equal to $1.18\cdot 10^{-3} \text{ m}\cdot\text{s}^{-2}$

[103]. In the first stages of the test, the PCB3801 accelerometers were connected directly to the sensing interface of each wireless sensing unit without signal conditioning. During the validation tests carried out, the system showed a good agreement with data recorded using a reference sensor (393393B04 by PCB Piezotronics Inc.), but a more detailed analysis of the frequency domain responses showed that the proposed sensor board did not match very well the response of the reference accelerometer for frequencies below 3 Hz. The low sensitivity of the sensor embedded on the WiMMS sensor board is a clear deficit for the proposed system. Therefore, the use of a signal conditioning section is necessary. Before feeding the 16-bit ADC of the wireless sensing unit, the signal is filtered. The filtering circuit includes one high-pass filter and one low-pass filter. The high-pass filter is an RC filter with a cut-off frequency of 0.02 Hz, and the low-pass filter is a 4th order Bessel filter with a cut-off frequency of 25 Hz. Validation tests have demonstrated that the sensor data with signal conditioning are smoother than the data without signal conditioning. In his study, Cho was more focused on the embedded decentralized algorithm than on the hardware structure of the sensor board, leaving to previous studies the task of validating the built system.

Whelan, in 2009, presented a wireless sensing solution (WSS) designed for concurrent measurement of both static and dynamic structural response through strain transducers, accelerometers, and temperature sensors [104] (Figure 3.9).



Fig. 3.9 – Wireless Sensing Solution proposed by Whelan (source: Whelan and Janoyan [102])

The network protocol supports real-time, high-rate data acquisition from large

wireless sensor arrays with essentially no data loss. It enables high-rate acquisition of up to 40 channels across 20 wireless units on a single peer-to-peer network. The developed wireless sensor node incorporates a Tmote Sky wireless sensor network platform integrating an ultra-low power microcontroller and chip transceiver on a single printed circuit board with a USB interface to the host computer for microcontroller programming and communication [105]. Communication among nodes of the network is ensured by a 2.4 GHz transceiver. The WSS hardware features a low-power signal conditioning board that improves the quality of the analog sensor signals relative to the ADC range and sampling parameters prior to digital conversion. The conditioning interfaces are designed to be optimized for measurement of vibrations resulting from both ambient and forced excitation as well as acquisition of strain transducer outputs during typical load ratings. The sensing system is instrumented with a LIS2L02AL MEMS-based accelerometer manufactured by STMicroelectronics and positioned in an external sensor housing for direct placement on the structure. The accelerometer is a two-axis, ultra-compact linear accelerometer with a measurement range of $\pm 19.61 \text{ m}\cdot\text{s}^{-2}$, a sensitivity of $0.07 \text{ V}\cdot\text{m}^{-1}\cdot\text{s}^2$, a bandwidth in the range DC - 100Hz, and a noise-density of $295 \text{ }\mu\text{m}\cdot\text{s}^{-2}\cdot\text{Hz}^{-0.5}$ [106]. Its resolution, evaluated using equation [2.23], is equal to $3.72\cdot 10^{-3} \text{ m}\cdot\text{s}^{-2}$. The study does not show any comparison with reference sensors, but shows the capacity of the system to detect acceleration having amplitude of $2.94\cdot 10^{-2} \text{ m}\cdot\text{s}^{-2}$ and frequency around 10 Hz, values not significant for SHM purposes.

To conclude this short overview, the prototypes of two high-sensitivity sensor boards (SHM-A and SHM-H) are presented and shown in Figure 3.10. They were built in 2010 by Professor Spencer's research group for the Imote2 platform [107], [108]. In Professor Spencer's study, the performance of the designed sensor boards is compared with those of the commercially available ITS400 sensor board and validated through extensive static and dynamic testing. Because the Imote2 has no sensing capabilities, a separate sensor board is required for collecting data. The ITS400 basic sensor board developed by Intel [109] employs a three-axis

digital accelerometer LIS3L02DQ manufactured by STMicroelectronics [110], a temperature/humidity sensor, a light sensor, and a four-channel 12-bit ADC.

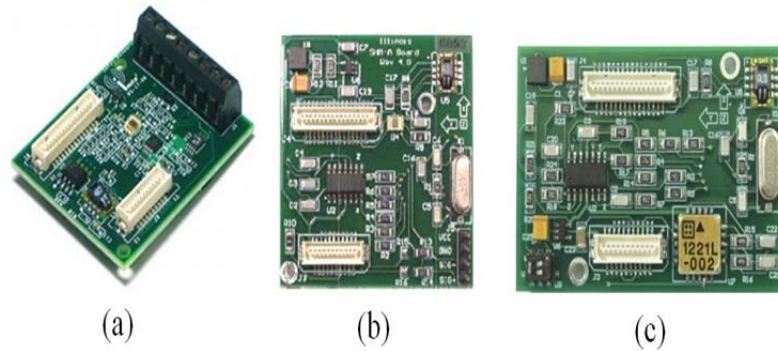


Fig. 3.10 – ITS400 (a), SHM-H (b), and SHM-H (c) sensor boards (source: Jo et al. [108])

During the study, it is noted that the resolution of the accelerometer with the built-in ADC was only $9.81 \cdot 10^{-3} \text{ m} \cdot \text{s}^{-2}$, definitely coarse for SHM of low amplitude vibration. For this reason, a new accelerometer sensor board (SHM-A) has been built to overcome the limitations highlighted in the previous version [111]. The SHM-A sensor board has a digital accelerometer LIS344ALH manufactured by STMicroelectronics. It is a three-axis, ultra-compact linear accelerometer with a measurement range of $\pm 19.61 \text{ m} \cdot \text{s}^{-2}$, a sensitivity of $0.07 \text{ V} \cdot \text{m}^{-1} \cdot \text{s}^2$, a bandwidth in the range DC - 1.8kHz (reduced to 20 Hz with a low-pass filter), and a noise-density of $490.30 \text{ } \mu\text{m} \cdot \text{s}^{-2} \cdot \text{Hz}^{-0.5}$ [112]. Its resolution, evaluated using equation [2.23], is equal to $2.77 \cdot 10^{-3} \text{ m} \cdot \text{s}^{-2}$. Nevertheless, the key component of the SHM-A sensor board is its programmable four-channel 16-bit ADC and signal conditional [113]. In addition, a new high-sensitivity sensor board (SHM-H) has been developed for measuring low-level ambient vibrations of structures. The SHM-H board is the extension version of the SHM-A board (general purpose acceleration board) and it has embedded a low-noise and high-sensitivity accelerometer. The Silicon Designs SD1221 [93] is used for the purpose. To improve the resolution of the accelerometer up to $4.22 \cdot 10^{-4} \text{ m} \cdot \text{s}^{-2}$, the accelerometer's sensing range is reduced by nearly one order of magnitude. Intensive tests have proved that the designed board could be effectively used for

measuring the low-level ambient vibration of the structure [108], [114].

The following table summarizes the most important features of the proposed systems.

Table 3.1 – Summary of the proposed MEMS-based accelerometer sensor boards

Study	Sensor	Sensitivity	BW	Noise	Resol.	Platform	ADC	BW 2	Resol. 2
(-)	(-)	($V \cdot m^{-1} \cdot s^{-2}$)	(Hz)	($\mu m s^{-2} Hz^{-0.5}$)	($10^{-3} m \cdot s^{-2}$)	(-)	(bit)	(Hz)	($10^{-3} m \cdot s^{-2}$)
Kurata	ADXL202E	0.02	DC - 50	1961	17.50	Mica	10	-	-
Tadeo	SD1221L	0.20	DC - 400	49.03	1.24	Mica	10	-	-
UCB	SD1221L	0.20	DC - 400	49.03	1.24	Mica2	16	DC - 25	0.31
Wang	PCB3801	0.10	DC - 80	104.69	1.18	WiMMS	16	0.02 - 25	0.66
Whelan	LIS2L02AL	0.07	DC - 100	294.18	3.72	WSS	16	-	-
Jo et al.	LIS3L02DQ	0.10	DC - 56	105.65	9.81	Imote2	12	-	-
Jo et al.	LIS344ALH	0.07	DC-1800	490.30	26.30	SHM - A	16	DC - 20	2.77
Jo et al.	SD1221L	0.20	DC - 400	49.03	1.24	SHM - H	16	DC - 45	0.41

From data summarized in Table 3.1, it is observed that the first released platforms are characterized both by low resolution of the accelerometer and low resolution of the ADC. Consider, for instance, the prototype proposed by Kurata [89]. The resolution of the accelerometer is equal to $17.50 \cdot 10^{-3} m \cdot s^{-2}$. The system uses a voltage of 3V for working; therefore, when a 10-bit ADC is used, the maximum resolution reached is equal to $143.64 \cdot 10^{-3} m \cdot s^{-2}$. It is, basically, one order of magnitude bigger than the resolution of the accelerometer. The precision of the sensing element is made even worse because of the precision of the ADC. This point is more evident when the prototype designed by Ruiz-Sandoval [91] (Tadeo) is analyzed. The accelerometer would allow measuring acceleration having amplitude as low as $1.24 \cdot 10^{-3} m \cdot s^{-2}$, but this precision is nullified by the low accuracy of the ADC ($23.94 \cdot 10^{-3} m \cdot s^{-2}$ at 5V). On the other hand, it is of interest to analyze the case in which the UCB's platform [97], [98], [99], [100] is considered. The default resolution of the accelerometer is equal to $1.24 \cdot 10^{-3} m \cdot s^{-2}$, but when it is matched with a 16-bit ADC - capable of measuring signal as low as $0.38 \cdot 10^{-3} m \cdot s^{-2}$ - the sensor becomes the limiting factor of the system. For this reason, it is necessary to reduce the bandwidth and the sensing range of the

accelerometer to improve its resolution artificially to a value ($0.31 \cdot 10^{-3} \text{ m}\cdot\text{s}^{-2}$) comparable with the resolution of the ADC. In all prototypes further developed [102], [107], [108], where the sensor board embeds a high-resolution 16-bit ADC, the dynamic range of the accelerometer has been artificially reduced to prevent nullifying the decision to use such an accurate ADC.

3 – Reasons for the realization of a new MEMS accelerometer system prototype

The MEMS accelerometer system presented in this study addresses two main problems of data acquisition in the field of vibration monitoring:

- Importance of going wireless;
- Signal quality when low-frequency and low-amplitude vibrations are considered.

Firstly, it is important to focus on the role a wireless transmission can play when a physical response is sampled compared to its wired counterpart. This for at least three reasons: a) wires impedance and quality of the signal, b) noise produced and c) mounting facility. The first point is connected to technological limitations due to cable length. Connection wires between the accelerometer and the acquisition section are extremely delicate elements of the measurement chain: well-isolated and low-noise cables are required and preferred. In addition, their length cannot exceed a few meters of extension because of signal impedance [45]. Impedance decreases with length; therefore, after a certain distance, an amplifier is always necessary because of signal attenuation. The second reason is connected with the noise introduced in the signal due to wire (triboelectric noise), which can create problems when signals having low amplitude, such as those characterizing the vibration of large civil structures, are analyzed. Triboelectric noise is produced because of mechanical movements of the wire itself and this causes the generation of local currents, which can interfere with the transmitted signals. Fixing the cable on a stable support can significantly reduce this, but this operation is not always feasible or easy to achieve. The last consideration introduces the third problem, which is connected to wire deployment as well. In many operational conditions, it is extremely difficult to manage several cables. Consider, for instance, measurements on a bridge: wires have to be deployed and run on the whole length of the span, from measurement points to the acquisition system, and this operation

is often challenging because of the geometry of the structure or because they can interfere with the structure's functionality. Furthermore, *in-situ* wires can easily be damaged during the different phases of work and for these reasons particular care must be taken during their positioning (e.g.: protection shells, wire passages, etc.). Installation time and efforts are significantly reduced when a wireless system is used compared to its wired counterpart. It is easy to understand why signals retrieval using wireless transmissions have their advantages, especially where wiring connections are difficult or impossible. In addition to these labor-intensive installations, it is worth noting that the cost of a wired system is extremely high. For example, in conventional structural health monitoring methods, wired systems are a great obstruction because prices may range from \$3,000 [95] up to \$5,000 [115] per channel, and costs grow much faster than a linear rate with the complexity of the system [116]. In addition, maintenance costs have to be considered.

Wireless technology is not entirely new and many applications using wireless sensors and networks have already been successfully tested. For instance, habitat monitoring [117 - 119], detection of environmental parameters (e.g.: temperature, humidity [120], and solar irradiation [121]), healthcare [122], and supply chain management [123] are among the first and well-known applications of this technology. Due to the speed at which investigated quantities change in time, the above-mentioned examples are easy to achieve. They require a very low duty-cycle, a low data rate, and small data size.

This consideration marks a turning point for engineering applications and for vibration measurement in particular. It requires a high sampling rate, a large data volume and, especially, a high fidelity sensing. Furthermore, it may happen that unsymmetrical loading inputs cause different outputs in symmetrical structures [95]. This is a clear example, which proves that a dense array of sensors is desirable to efficiently investigate local and global damage in large structures or systems [124].

It is observed that the focus of the currently developed researches in the field of sensors for SHM, have moved from the design of an accurate and reliable sensor board to the construction of scalable WSNs [100], to the analysis of the performances of the network itself [125], and on creating embedded computational algorithms for reducing transmitted data volume [63], [102], [126]. Basically, research has forgotten about sampled signal quality and improvements for making it equivalent to the signal sampled with wired accelerometers.

In this study, a MEMS accelerometer system, named Acceleration Evaluator (ALE), is designed and developed. It will be shown that, because of its performances and electronic characteristics, this device can be a perfect substitute for traditional wired sensors in carrying out analyses of low amplitude and low frequency vibration.

4 – Design of the Acceleration Evaluator (ALE)

From the block diagram in Figure 3.11, it can be observed that traditional WSNs sensor boards are made of three different parts: a sensing (or more than one) element, a computational core unit (microcontroller, ADC, flash memory, etc.), and a wireless radio modem for the communication. The most important part of the sensor board is the computational core. This part contains algorithms, programs, and codes, which enable the system pre-processing data and transmission of only a small part of them to the receiving board. In addition, the computational core contains the ADC, which determines the measured data resolution. A high sensitivity (16-bit or higher) ADC is preferable for obtaining high-resolution measurements; nevertheless, for energetic and power consumption reasons this operation is not always feasible.

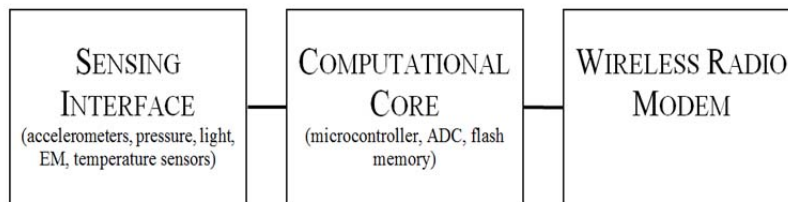


Fig. 3.11 – Traditional WSN sensor board block diagram

The proposed Acceleration Evaluator (ALE) consists of a transmitter board and a receiver board. The transmitter board is equipped with a MEMS accelerometer, a Voltage to Frequency (V/F) converter and a wireless radio-frequency (RF) transmitter, whereas the receiver board contains an RF receiver and a Frequency to Voltage (F/V) converter for demodulating the signal. It should be observed that the Acceleration Evaluator system embeds only one sensor. Several traditional WSN sensor boards install more than one sensing unit for more than one physical quantity (e. g.: acceleration, light intensity, humidity, temperature, EM fields, etc.) [89], [91], and [98]. Since all these physical parameters are characterized by different optimal sampling times, mounting more than one typology of sensor

may affect the quality of the measurement [77]. Furthermore, another difference between ALE and other systems is that no computational operations are carried out on-board. In the proposed system, raw data are downloaded to an external laptop or computer to be post-processed. Even though one of the basic ideas of SHM is to transmit essential information only, the ALE moves in the opposite direction. Many other engineering sectors need several data elements to determine the occurrence of possible critical scenarios; therefore, limiting the quantity of data transmitted may reduce their utility. Transmitting a large amount of data is definitely more power-expensive, but may result in more accurate analyses since these tasks may be carried out using more powerful microprocessors.

Moreover, another difference between the proposed system and the others is introduced in the typology of signal conversion used. Conventionally, the MEMS sensor's analog signals are converted to digital signals before RF transmission. The conversion can cause a loss in the resolution, especially to the important low frequency and low-amplitude signals. To overcome this difficulty, ALE converts the sensor output voltage to a frequency-modulated (FM) signal before RF transmission. This is achieved by operating a V/F conversion instead of the conventional ADC conversion. In the following paragraphs, a detailed description of the transmitter and receiver boards' components is given.

4.1 - ALE transmitter board architecture

The transmitter board is made of the three sections shown in Figure 3.12. The first is the sensing unit, which embeds a high sensitivity, low-noise, MEMS-based accelerometer. Only one typology of sensor is installed on-board. This because the sensor board's goal is to measure vibrations with accuracy comparable to that of the IEPE, high sensitivity, wired accelerometers. The second section, the signal conditioning, is equipped with a V/F converter, a signal amplifier, a trimmer for adjusting the offset of the accelerometer coupled to gravity, and a tension stabilizer to guarantee a constant supplied tension. To conclude, the third section

consists of a wireless RF transmitter with antenna for communicating the sampled data.

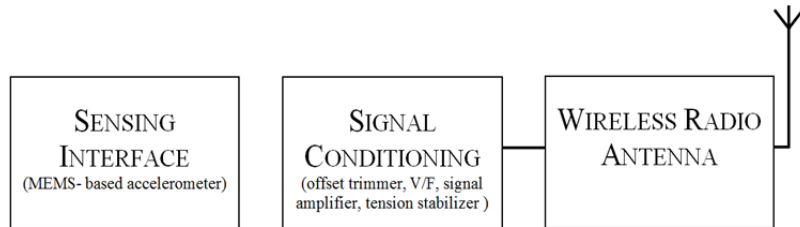


Fig. 3.12 – The ALE transmitter board block diagram

It can be observed that the designed system is extremely simple and easy to use. The accelerometer is deployed on the structure for which vibrations are to be recorded and it produces an electrical output proportional to the sensed acceleration. The sensor output voltage (in the form of a tension value) moves to the next section where it is converted to a frequency signal proportional to the output voltage by means of the V/F converter. It then continues toward the last section, the RF radio antenna, to be transmitted wirelessly to the receiver.

Several tests were carried out and different dispositions of circuit design were experimentally tried to find the right equipment, which maximized the efficiency of the selected accelerometer. For the sake of brevity, one of the latest designs studied on the solderless breadboard is shown in Figure 3.13.

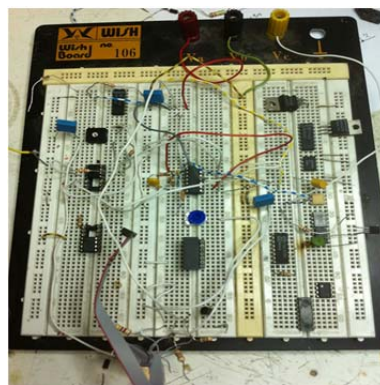


Fig. 3.13 – Prototype transmitter circuit tested on the solderless breadboard

Once the optimum circuit has been designed (Figure 3.14), it was reproduced on a copper Printed Circuit Board (PCB) and assembled. The following Figures

(3.14 through to 3.16) show the designed electric diagram of the sensor board, the PCB layout, and the finite prototype with all the components plugged in.

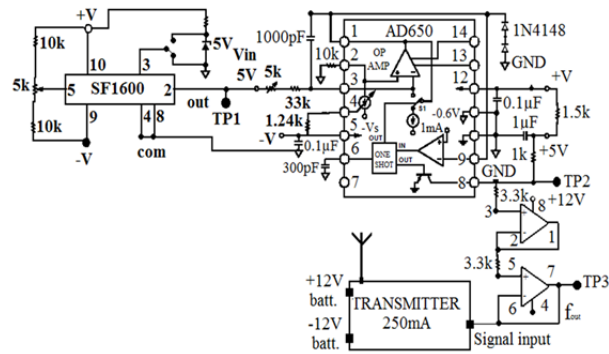


Fig. 3.14 – Circuit diagram of the ALE transmitter board

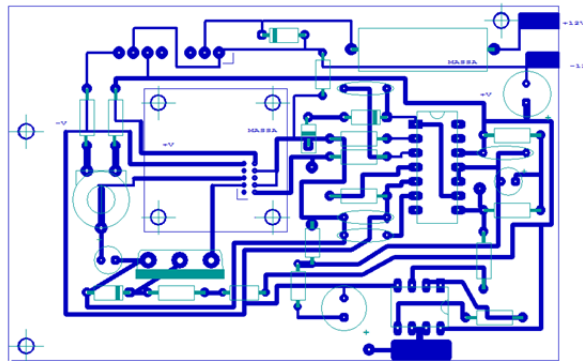


Fig. 3.15 – PCB layout of the ALE transmitter board

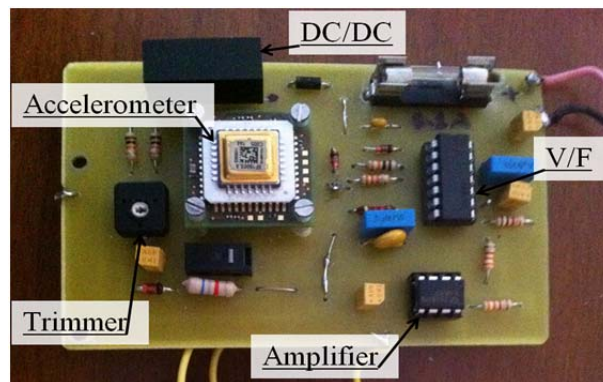


Fig. 3.16 – Prototype of the ALE transmitter board

It should be noted that the system shown in Figure 3.16 is the first prototype ever built - dimensions are provisional and no miniaturization has been carried out

yet. It is made for testing purposes only. At this stage, it would be easier to produce modifications to the sensor board if microelectronic components were not used. Adjustments can be effected changing components on-board, with no need to build a new small-sized board every time. Miniaturization using microelectronic components and space optimization will be carried out once the very final version of the prototype is designed. MEMS accelerometer system dimension will be reduced from that of the current one to a few square centimeters.

4.1.1 - Transmitter board sensing unit

The first challenge met is the choice of an appropriate accelerometer. Several types exist on the market, but very few of them are capable of sensing low amplitude and low frequency vibrations with an accuracy suitable for SHM purposes. Table 3.2 shows a list of accelerometers investigated as a possible sensing unit for the designed sensor board.

Table 3.2 – Summary of the investigate MEMS-based accelerometers

Type	Producer	Axes	Range	Sensitivity	BW	Noise	Resolution
(-)	(-)	(-)	($\text{m}\cdot\text{s}^{-2}$)	($\text{V}\cdot\text{m}^{-1}\cdot\text{s}^{-2}$)	(Hz)	($\mu\text{m}\cdot\text{s}^{-2}\cdot\text{Hz}^{-0.5}$)	($10^{-3}\text{ m}\cdot\text{s}^{-2}$)
MMA7361LC	Freescale	X, Y, Z	± 58.84	0.08	400	3431.10	86.83
MMA6361L	Freescale	X, Y	± 58.84	0.08	400	3431.10	86.83
MMA2260	Freescale	X	± 14.71	0.12	50	3431.10	30.70
ADXL103	Analog Device	X	± 16.67	0.10	500	1078.66	30.51
ADXL 202	Analog Device	X, Y	± 16.67	0.10	500	1078.66	30.51
VS9002	Colibrys	X	± 19.61	0.10	800	245.15	8.77
SCA610	Murata	X or Y	± 9.81	0.20	80	294.18	3.33
SCA620	Murata	X or Y	± 16.67	0.12	80	196.12	2.22
1221L	Silicon Design	X	± 19.61	0.20	400	49.03	1.24
SF2600	Colibrys	X	± 49.03	0.08	1000	8.82	0.35
SF1600	Colibrys	X	± 29.42	0.12	1500	2.94	0.14

A SiFlex 1600SN.A (SF1600) accelerometer, manufactured by the Swiss Colibrys Ltd., has been selected as sensor for the transmitter board. It is a single-axis MEMS-based accelerometer, with low noise-density ($2.94\ \mu\text{m}\cdot\text{s}^{-2}\cdot\text{Hz}^{-0.5}$), a

wide linear output range ($\pm 29.42 \text{ m}\cdot\text{s}^{-2}$) and frequency response (DC - 1500 Hz), and a sensitivity of $0.12 \text{ V}\cdot\text{m}^{-1}\cdot\text{s}^2$. Therefore, its full band resolution - evaluated using equation [2.23] – is equal to $0.14\cdot 10^{-3} \text{ m}\cdot\text{s}^{-2}$, one order of magnitude smaller than the default resolution of the most sensitive accelerometer shown in Table 3.1 ($1.24\cdot 10^{-3} \text{ m}\cdot\text{s}^{-2}$). This characteristic made the accelerometer suitable for inertial, tilt, and vibration, as well as seismic analyses. The SF1600 operates with a power supply voltage that can range from $\pm 6 \text{ V}$ to $\pm 15 \text{ V}$ with a typical current consumption of 11 mA at $\pm 6 \text{ V}$. Table 3.3 summarizes the main features of the accelerometer determined at $+ 20 \text{ }^\circ\text{C}$ and 15 V DC power supply [127].

Table 3.3 – SiFlex 1600SN. A specifications

Quantity	Unit	Typical Value
Linear output range	$\text{m}\cdot\text{s}^{-2}$	± 29.42
DC bias	$\text{m}\cdot\text{s}^{-2}$	± 1.96
Sensitivity	$\text{V}\cdot\text{m}^{-1}\cdot\text{s}^2$	0.12 ± 0.01
Dynamic range (0.1/100 Hz)	dB	117.00
Output noise (10/1000 Hz)	$\mu \text{ m}\cdot\text{s}^{-2}\cdot\text{Hz}^{-0.5}$	2.94
Frequency response	Hz	DC - 1500

The accelerometer consists of the multi-chip module (MCM) of the MEMS capacitive element assembled in a custom ceramic package (golden part of Figure 3.17 (c)). The MCM is attached through an interconnect board (with the part of Figure 3.17 (c)) to a customized Application Specific Integrated Circuit (ASIC) [128] and to a printed circuit board. The ASIC enables analog closed-loop force-feedback operations of the accelerometer, whereas the PCB consists of power conditioning electronics employing linear regulators, output amplifiers, 10 connection pins and mounting holes, and other support electronics. The precise sensor dimensions are given in Figure 3.17 (a) and (b), whereas Figure 3.18 depicts a block diagram of the SF1600 accelerometer.

The core of the accelerometer is the capacitive bulk micro-machined silicon sensor made of three silicon wafers. The center wafer supports the proof mass through a spring. This inertial mass is also the center electrode of the capacitive

sensor. Upper and lower wafers constitute the external fixed electrodes of the sensor. The three wafers are bounded together with Silicon Fusion Bonding (SFB) techniques. This bonding process insures a perfect balance between the three wafers of the system, but also allows the building of a hermetic sealed cavity for the mass - spring system. The bonding process is carried out at high temperature and at low pressure to ensure an optimal gas damping and bandwidth control [48].

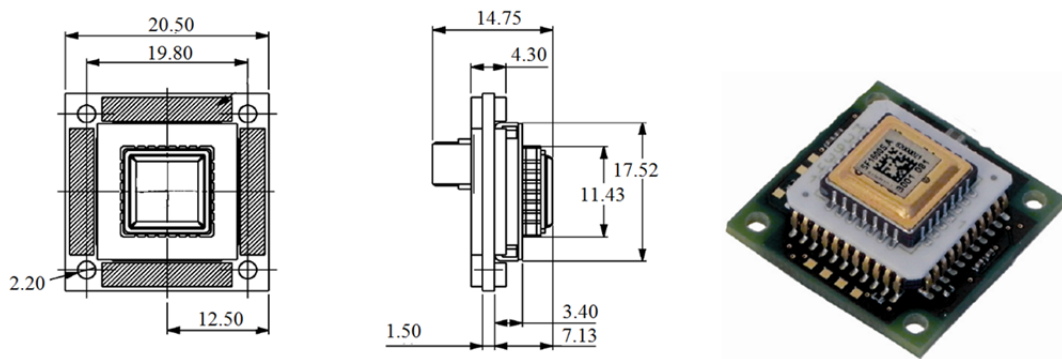


Fig. 3.17 – SF1600 dimensions and picture (source www.colibrys.ch [127])

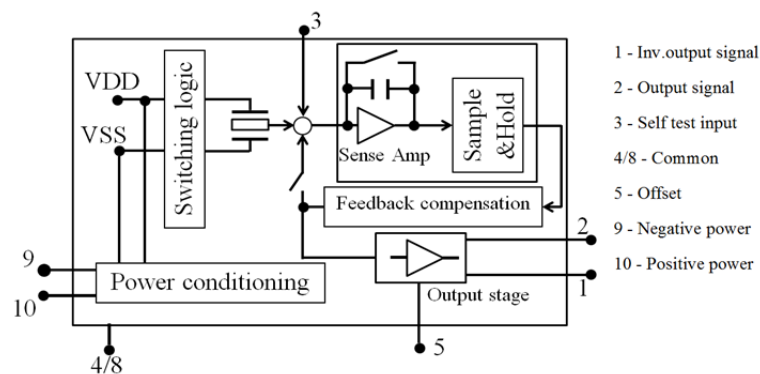


Fig. 3.18 – SF1600 block diagram

Applied acceleration or tilt to the sensitive axis changes the inertia, causing the mass to move between the upper and lower electrodes, which results in a change to the values of the capacitors. This differential variation of the sensing capacitors is measured by the ASIC. As changes in capacitance are sensed, a restoring electrostatic force is applied to maintain the mass in a central (neutral) position. The output signal of the sensor is derived directly from the correction signal used to keep the center-mass in the neutral position. This correction signal is linearly

proportional to the acceleration applied to the sensor. This type of closed-loop design generally provides better output linearity than open-loop designs [129 - 130].

To finish, the chosen version of the accelerometer (SN. A) is not supplied with an internal oscillator. This is because, in the event that a synchronization of signals coming from different devices is required, this will be externally installed on demand. This is a precaution that considers the possibility of installing, in the near future, several accelerometers with different axial orientations on the same sensor board.

4.1.2 - Transmitter board signal conditioning

The signal conditioning section allows processing of the signal sensed by the accelerometer before transmitting it via RF wireless. This section is equipped with a trimmer for adjusting the offset of the accelerometer coupled to gravity, a V/F converter, a signal amplifier, and a tension stabilizer to guarantee a constant power supply to the transmitter board.

One of the main characteristics of MEMS-based accelerometers is that they can be used for measuring static accelerations and tilt angles. Practically, the output tension supplied by the sensor at rest (i.e.: offset), will assume different values depending on the device's inclination. For this reason, a unit for removing DC coupled to gravity is designed and embedded on-board. The section is made of two 10 k Ω resistors and a 5 k Ω multi-turn trimmer potentiometer deployed in series and connected to pin number five of the SF1600. The section is a very important feature of ALE when dynamic measures are carried out. It permits correction of the sensor's output tension value to remove the DC signals associated with the sensor orientation directly on the board with no need to correct data later. By means of this feature, it is possible to deploy the sensor horizontally, vertically or equivalently in any other position and correct the tension value in order to be sure that the given one corresponds to a null acceleration, by simply turning a screw.

It should be pointed out that ALE does not embed any ADC. Considering the accelerometer resolution ($0.14 \cdot 10^{-3} \text{ m} \cdot \text{s}^{-2}$), if a traditionally used 16-bit ADC were installed, the resolution of the system would be lowered to $1.50 \cdot 10^{-3} \text{ m} \cdot \text{s}^{-2}$, one order of magnitude higher than the sensor's resolution. Installing that ADC would nullify the decision to use such a sensitive accelerometer. The SF1600 should be matched with a 24-bit ADC to achieve the designed performance and maintain the resolution of the conversion equal to $5.84 \cdot 10^{-6} \text{ m} \cdot \text{s}^{-2}$. It is clear that such an ADC is extremely power-demanding and not well suited for low-power applications. To overcome this difficulty, ALE converts the sensor output voltage to a FM signal using a V/F converter instead of the conventional ADCs. The AD650 manufactured by Analog Devices, Inc. is selected to convert the sensor output to a sequence of pulses. The AD650 V/F/V (voltage-to-frequency or frequency-to-voltage converter) is a monolithic converter that can operate up to 1 MHz [131]. V/F converters are electronic circuits that supply as an output signal a square wave whose frequency is proportional to the input voltage value. It is important to point out that neither analyses nor computations are made on the amplitude of the input signal. In the proposed MEMS accelerometer system, the AD650 has been installed to receive the analogic signal coming from the SF1600 and convert it into FM pulses in the range 0 – 100 kHz. The 0 V sensor output is converted to 50 kHz. This technique is quite slow, but operating with high-sampling rate devices (order of MHz) and a narrow sensor bandwidth (0 to 1.5 kHz), it is possible to overcome this limitation [132]. Furthermore, because the converter does not consider the amplitude of the signal (which degrades with transmission distance) but its frequency only, the decision to use this device allows for a signal more immune to noise [133], [134]. To conclude, since the output of the accelerometer is an extremely low frequency DC, converting this signal in an AM one, is difficult and it may cause signal distortions. To obtain more accurate data, it is preferable to convert the signal into a frequency value before transmitting it.

The output of the AD650 is connected to a voltage buffer amplifier circuit. Typically, a voltage buffer amplifier is used to transfer a current from a first

circuit, having a high output impedance level, to a second circuit with a low input impedance level. The interposed buffer amplifier prevents the second circuit from loading the first unacceptably and interfering with its desired operation [132], [135]. In the ALE prototype, the voltage buffer circuit connects the V/F to the wireless RF transmitter. If the buffer were not installed, the transmitter would demand the V/F converter for the necessary current, altering and damaging the signal sampled by the SF1600. The model TL082, a high speed, Junction Gate Field-Effect transistor (JFET) input, dual operational amplifier, manufactured by STMicroelectronics is selected for the transmitter board [136].

To finish, to provide a stable ± 12 V power supply to compensate for the gradual decrease in the battery power output over time, a DC-to-DC converter (DC/DC) is used. A DC/DC converter is an electronic circuit, which converts a source of direct current from one voltage level to another. Since the battery voltage declines as its stored energy is drained, DC/DC converters offer a method to increase voltage from a partially lowered battery voltage thereby saving space instead of using multiple batteries to accomplish the same thing.

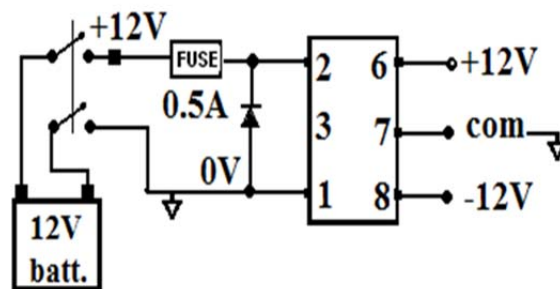


Fig. 3.19 – Electrical scheme of the TMR3-1222HI DC/DC converter

For the MEMS accelerometer sensor board presented in this study, the TMR3-1222HI model, manufactured by Traco Power, is installed on board and shown in Figure 3.19. It is a 3W DC/DC converter module, which converts an input voltage in the range 9 - 18 V to a constant voltage of ± 12 V, with an output maximum current of ± 125 mA, and an efficiency of nearly 80% [137]. It can be observed

that power consumption is elevated (if compared to other parts of the sensor board), but the importance of a stable input tension is easily understandable, and this will be analyzed in detail in the following chapter and validated through laboratory tests and experiments.

4.1.3 - Transmitter board wireless RF antenna

Once signal is sampled and converted to frequency pulses proportional to the input voltage values, it is ready to be transmitted to a receiver board. The ALE's last section consists of a low-cost, four-channel, 2.4 GHz ISM, audio-video, omnidirectional antenna having a bandwidth of 7 MHz. Its theoretical transmission range is approximately 150 m in free field conditions. The reasons for this RF system depend on the bandwidth of the V/F output signal (100 kHz). A bandwidth of 7MHz can easily cover that range without signal distortions; an operation that an audio antenna cannot do (audio bandwidth is nearly 20 kHz). Since the signal is FM transmitted and the frequency of the acceleration for SHM purpose is small, it would be possible to use a commercially available audio antenna, which automatically transforms the signal in a frequency pulse. Nevertheless, the lower limit of these systems is around 20 Hz, higher than the frequency of considered vibrations. Transmitting a signal with an audio FM antenna would produce a distorted and lower-limited signal as well.

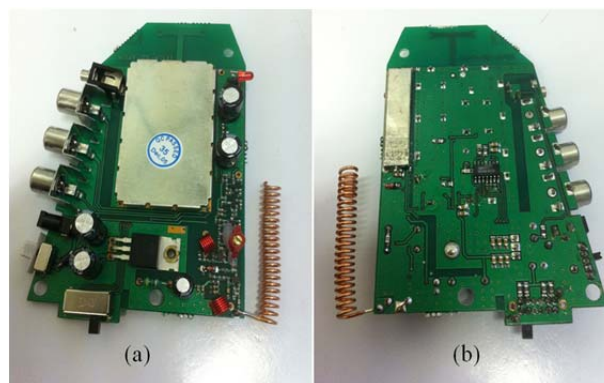


Fig. 3.20 – Wireless RF antenna top view (a) and bottom view (b)

The RF transmitter works with a power supply of ± 12 V; therefore, this

characteristic determines the operation voltage of the whole transmitter board and the need to use a DC/DC converter from $\pm 9 - 18 \text{ V}$ to $\pm 12 \text{ V}$. Nevertheless, in real-world engineering practices, the dimensions of this type of batteries could be a serious issue for the MEMS accelerometer system deployment [98], [114]. As shown in the following chapter, the authors consider this wireless RF antenna as temporary. Indeed, once a different transmitter-receiver apparatus is selected, it will be possible to use a different and smaller cell to power the device. For instance, the use may be considered of a 9 V battery (which traditionally has dimension of 6.5 x 17.5 x 48.5 mm) or a set of AA alkaline batteries, both smaller than the currently used cell (54.5 x 97.0 x 48.0 mm).

4.2 - ALE receiver board architecture

The receiver board is made of three sections as well. These are shown in Figure 3.21. The first is the receiving unit, which consists of a wireless RF antenna tuned on the same frequency of the transmitter. The second, the signal conditioning section, is equipped with a F/V converter, a signal amplifier, and a tension stabilizer. Finally, the third section consists of an external Data Acquisition (DAQ) board.

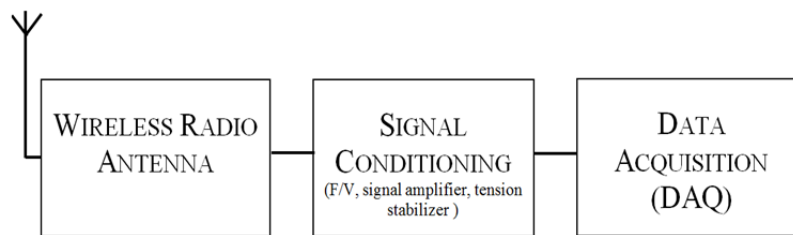


Fig. 3.21 – The ALE receiver board block diagram

Again, it can be observed that the designed system is extremely simple and easy to use. The signal sent from the transmitter board is received by means of the wireless RF antenna and passed through the F/V converter. Here it is demodulated from a frequency value into a voltage value equal to that recorded as sensor output. It is then amplified and transmitted to the DAQ board to be downloaded

onto a laptop or a computer. Analogously to what was done for the transmitter board, to find the right equipment and maximize the efficiency of the selected wireless RF transmitter, different dispositions of circuit design were experimentally tried on the solderless breadboard as shown in Figure 3.22.

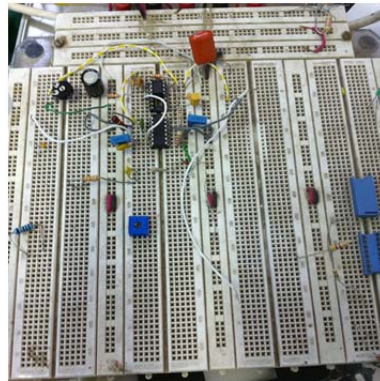


Fig. 3.22 – Prototype receiver circuit tested on the solderless breadboard

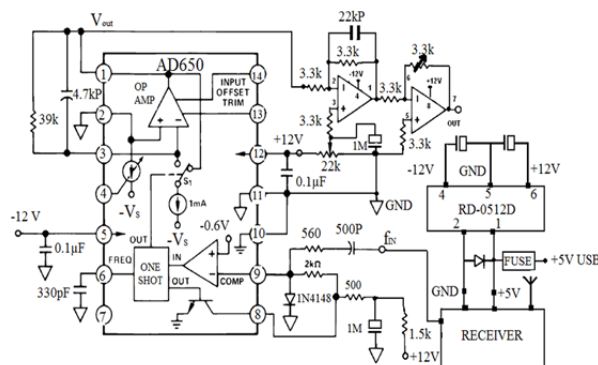


Fig. 3.23 – Circuit diagram of the ALE receiver board

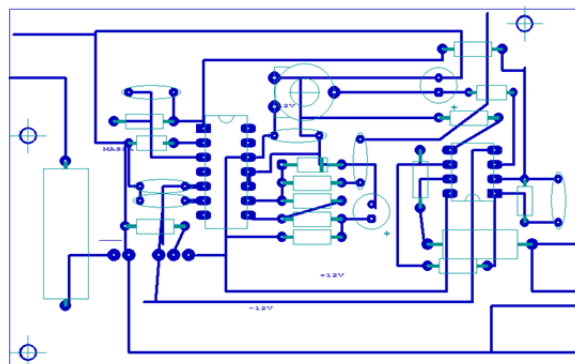


Fig. 3.24 – PCB layout of the ALE receiver board

Once the optimum circuit was designed (Figure 3.23), it was reproduced on a copper PCB and assembled. Figures 3.23 through to 3.25 show the designed electric diagram of the ALE receiver board, the PCB layout, and the finite prototype with all the components plugged in.

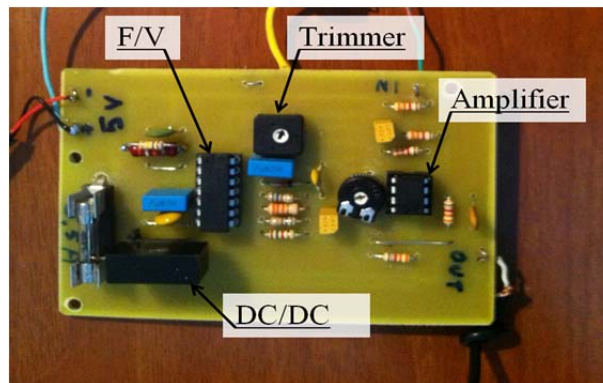


Fig. 3.25 – Prototype of the ALE receiver board

In particular, Figure 3.25 shows a detail of the PCB transmitter board with all components installed. The main task of the receiver board is to collect the wirelessly-transmitted data and demodulate the signal. A detailed description of equipment installed on the ALE receiver board is given in the following sections of this paragraph.

4.2.1 - Receiver board wireless RF antenna

Analogously to the transmitter board, the receiver board is equipped with a low-cost, four-channel, 2.4 GHz ISM, audio-video, omnidirectional antenna having a bandwidth of 7 MHz, and tuned to the same frequency as the transmitter board. The radio signal is not encrypted. In addition, a low-threshold discriminator is embedded in the board. The wireless RF transmitter works with a power supply of ± 12 V; therefore, another DC/DC converter is installed on-board. The model selected is an RD-0512D manufactured by Recom Power. The installed DC/DC has been selected because it can convert an input voltage of ± 5 V to ± 12 V with a power consumption of 2 W and an efficiency of nearly 80% [138]. This equipment, allows powering of the receiver board using the Universal

Serial Bus (USB) port of any laptop or computer, which is convenient for in-field measurements. The USB port supplies a voltage of ± 5 V, which by means of the DC/DC converter, is transformed in ± 12 V suitable for the antenna to work.

4.2.2 - Receiver board signal conditioning

This section is composed of two components: a F/V converter and a signal amplifier. In the receiver board, the pulses received by the antenna are processed through the F/V converter to be reconverted to the original sensor signal analog voltage. The obtained signal is then passed through an amplification section and normalized in the range 0 – 10 V. The amplifier, made of two resistors and a multi-turn trimmer potentiometer, can be manually set for adjusting the gain. This section also embeds a DC/DC converter

4.2.3 - Receiver board Data Acquisition

The last section of the ALE receiver board consists of a Data Acquisition (DAQ). It can be observed that no computational operations are carried out on-board; therefore, data have to be downloaded onto a laptop or a computer to be post-analyzed (time and frequency domains analyses, filtering, averaging, etc.). These operations are achieved using customized software for remote control and data download. For this study, an external DAQ is used. It is an NI-USB 6009 with eight analog input channels, able to sample up to 48 kilo Samples per second (kS/s) [139]. The output signal from the amplifier is sent to it directly via electrical wires and then downloaded using the USB port of a laptop.

Figure 3.26 shows the assembled transmitter prototype put into a protective plastic box having dimensions of 120.0 x 80.0 x 50.0 mm and the 12 V rechargeable battery used for powering ALE, while Figure 3.27 summarize the ALE whole functionality, from vibration sensing to data download, through a block diagram.

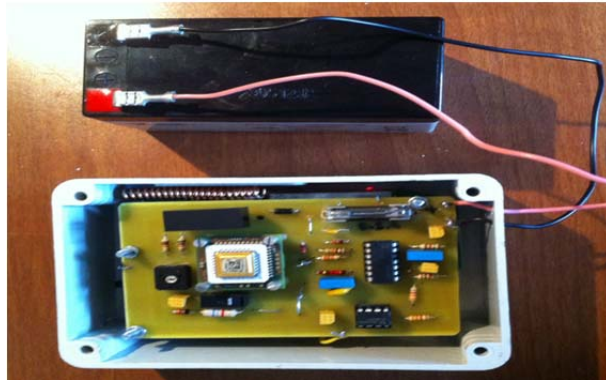


Fig. 3.26 – The ALE assembled prototype and battery package

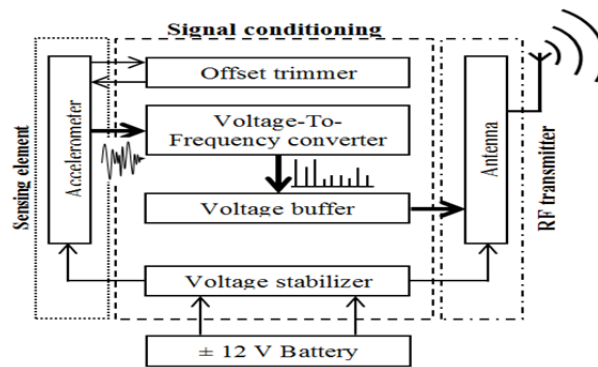


Fig. 3.27 – The ALE transmitter functional diagram

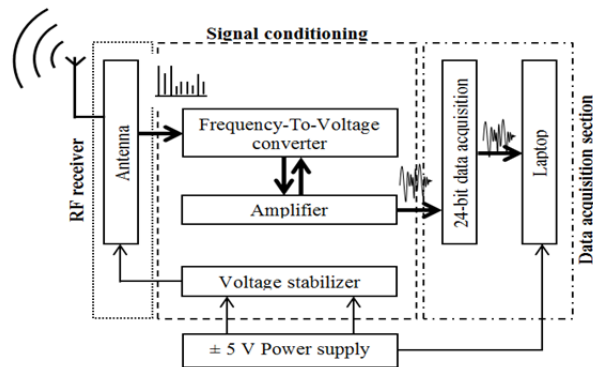


Fig. 3.28 – The ALE receiver functional diagram

5 – Cost analysis

To conclude the designed prototype description, a short overview of the production costs is carried out to prove that the ALE is definitely cheaper than previously proposed SHM systems, and its cost is comparable to that of an equivalent-accuracy wired, seismic, IEPE accelerometers, traditionally used in measurement activities. Table 3.4 summarizes the ALE components cost.

Table 3.4 – The ALE components cost

Component	Price
(-)	(USD)
Electric	175.00
Sensor	670.00
Antenna	25.00
DAQ (16-Ch.)	600.00
TOTAL	907.50

The final cost of the assembled system is nearly \$ 900. It is important to point out that since the ALE is in a prototypical stage, this price has to be considered temporary and if an industrial production would be developed, it will become lower. Nevertheless, the ALE price-per-channel is definitely lower than those indicated for previously developed SHM systems, which range between \$ 3,000 and \$ 5,000 [115, 116].

In addition, the ALE price is competitive even if it is compared with that of a traditional, wired, IEPE, accelerometer having resolution equivalent to that of the MEMS-based one. Usually, this typology of accelerometers cost nearly \$ 800, while the cost-per-meter of the wire is nearly \$30. Furthermore, if a low-cost signal conditioning section and the DAQ system are considered, the final price of the measurement chain rises up to nearly \$ 1,200. It proves that the designed MEMS-accelerometer system is even cheaper than a commercially available sensor for SHM.

CHAPTER IV

EVALUATION TESTS FOR THE ACCELERATION EVALUATOR (ALE) SYSTEM

1 – Introduction

It can be observed that sensor boards' low sensitivity and accuracy have imposed serious limitations for their application in monitoring large-sized structures. For this reason, when a dynamic system has had to be monitored to date, traditional wired accelerometer systems were mainly used despite their high installation and management costs. The MEMS accelerometer system introduced in the previous chapter has been specifically designed to overcome the accuracy limitations, which characterize other MEMS-based sensor boards, when low amplitude and low frequency vibration are investigated. The main idea at the base of the ALE design is to realize a system that can replace the traditionally used wired accelerometers when vibration analyses have to be carried out. The ALE would be an instrument that ensures the same reliability and accuracy guaranteed by wired, IEPE accelerometers, when measures of low amplitude and frequency vibration are effectuated, but at the same time a device that can be free from limitations and restrictions due to cables and wired connections.

The design choices made for the ALE need, in order to be validated, to demonstrate whether or not they are useful in achieving the resolution necessary for SHM purposes. The ALE's efficacy in measuring low frequency and low amplitude dynamic responses is demonstrated through extensive laboratory tests and experiments on real-world engineering structures. The first allows characterization of the system's performances in a controlled environment, to

effectively validate the design choices. The latter are useful in demonstrating the system's behavior when traditional vibration measurements are carried out.

2 – Laboratory tests for the characterization of ALE's performances

To evaluate the capabilities of the prototype wireless MEMS accelerometer system, several laboratory tests were carried out. These include:

- 1) Static calibration test;
- 2) Effects of battery residual charge;
- 3) Maximum transmission distance;
- 4) Comparative dynamic tests.

The first test is carried out for calibration purposes using an angle meter machine; the second allows evaluation of the ALE behavior under diminishing battery power. The third test consists of experiments to determine the performance of the wireless transmission distance in two different conditions (indoor and outdoor), whereas the fourth was carried out to explore the prototype dynamic response using electromagnetic shakers. It should be pointed out that in the latter set of investigations, the wirelessly acquired ALE signals are compared with those given by a traditional wired sensor used as reference.

2.1 - Static calibration test

Despite the fact that companies supply customers with calibration charts, the SF1600 needs to be individually calibrated because of the elements placed on the transmitter board (i.e.: V/F converter, signal amplifier, offset trimmer, etc.), which can affect the accelerometer's normal behavior.

As is known, MEMS-based accelerometers can be used for tilt angles evaluation and are capable also of detecting static accelerations. Therefore, deploying the SF1600 accelerometer with different inclinations, it is possible to subject its inertial mass (i.e.: accelerometer's center wafer) to diverse values of static acceleration. Once that angle is noted, and so also are the two orthogonal components of the gravitational acceleration vector g , it is possible to correlate

these values with the correspondent tensions provided by the sensor itself. The transmitter board is naturally subjected to the gravitational acceleration g . The sensing axis of the SF1600 is deployed vertical ($\alpha = 0$ rad) to the silicon wafer; therefore, when the sensor board is placed in vertical, the ALE is subjected to a static acceleration equal to the gravitational acceleration g ($9.806 \text{ m}\cdot\text{s}^{-2}$). Once the sensor board is turned by an angle equal to α , the gravitational acceleration vector will be composed of two orthogonal components: g_{\perp} perpendicular to the SF1600 sensing axes and $g_{//}$ parallel to it, as explained in Figure 4.1. Since the accelerometer can only detect accelerations perpendicular to its sensing axes, the value of static acceleration sensed by the SF1600 will decrease from the maximum value $9.806 \text{ m}\cdot\text{s}^{-2}$ to zero when the accelerometer is deployed in horizontal ($\alpha = \pi/2$ rad). Therefore, the static acceleration to which the SF1600 is subjected is equal to:

$$g_{\perp} = \cos \alpha \quad [4.1]$$

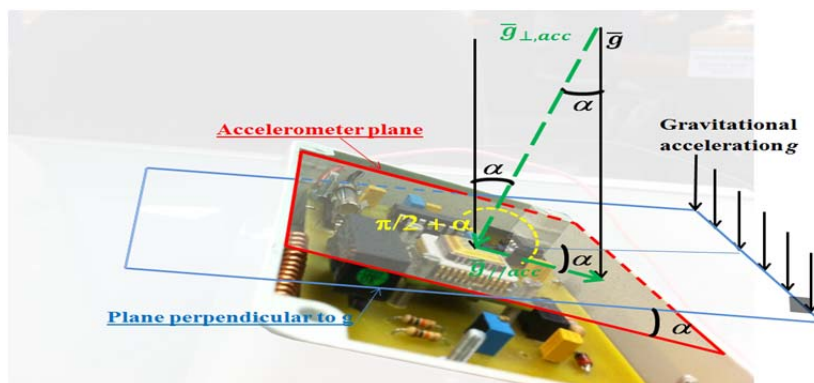


Fig. 4.1 – Determination of gravitational acceleration components acting on the SF1600 sensing element

The aim of this test is to subject the sensor to different values of static acceleration and record the output tension value coming from the sensor. This operation enables plotting of a calibration curve, which correlates these output values with the corresponding acceleration value in physical and engineering units ($\text{m}\cdot\text{s}^{-2}$ or g). To do this, the SF1600 was fixed on an angle meter machine, and rotated to 0 through 2π rad at intervals of $\pi/36 \pm \pi/18 \cdot 10^3$ rad ($5^\circ \pm 0.01^\circ$). The

receiver board, connected to a laptop for DAQ, was placed one meter away to measure the wirelessly transmitted sensor output signal. Figure 4.2 shows a detail of the setup used for the static calibration tests. In particular, it is possible to observe that, for a more accurate and easy deployment, the SF1600 was removed from the transmitter board and connected to it by means of a 10-pin insulation displacement connector (IDC), whereas the receiver board and the DAQ apparatus are not visible in the image.

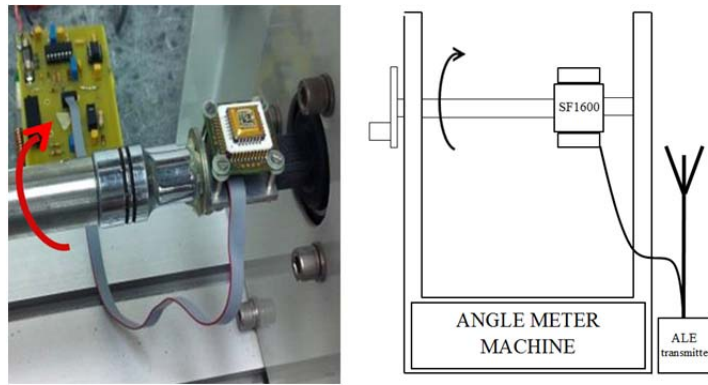


Fig. 4.2 – Setup for the static calibration test

For each inclination, a 10-minute measurement was made and the wirelessly transmitted accelerometer output signals (in Volt) were acquired with a 3 kHz sampling rate using the external DAQ device connected to the receiver board. This large amount of data was analyzed using statistical descriptors; in particular, the mean and the standard deviation σ values of each set of sampled data were evaluated. Analyses of the standard deviation may be used for estimating the signal quality. Low values of σ mean that the signal is stable and there are no, or very few, fluctuations around a mean and expected value, whereas for higher values the signal is not stable at all and that several interferences occur. The complete set of measured values, their mean and standard deviation are given in Table A.1, attached in the Appendix at the end of this dissertation. Here it is observed that, in all tests carried out, the standard deviation was always smaller than $8.71 \cdot 10^{-3}$ mV, demonstrating the stability of the wirelessly transmitted sensor output data over the 10-minute measurement period.

In Figure 4.3, for each inclination, the component of the gravitational acceleration g_{\perp} - orthogonal to the accelerometer's sensing axes - is plotted against the mean value of the measured accelerometer output voltage.

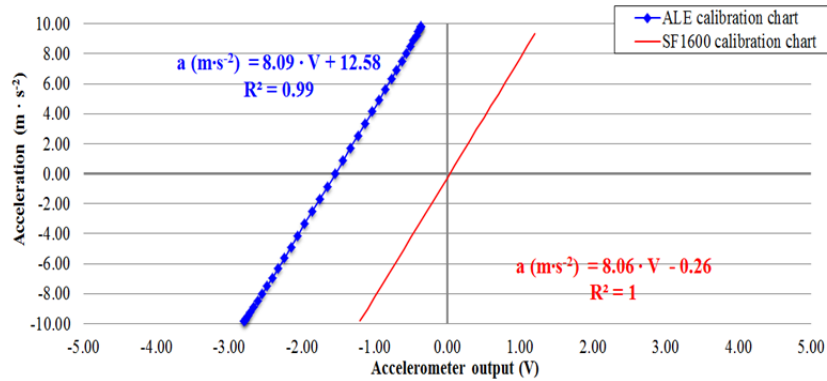


Fig. 4.3 – Results of static calibration test made on the ALE

Experimental results permit evaluation of the ALE system's calibration equation, which is equal to:

$$a (m \cdot s^{-2}) = 8.0857 \cdot V_{out} + 12.5827 \quad [4.2]$$

where the value V_{out} is the output tension recorded using the DAQ at the exit section of the receiver board. The calibration test data shown in Figure 4.3 confirm the linear relation between the acceleration and the sensor output voltage with a high correlation of $R^2 = 0.99$. The ALE calibration equation (dotted blue line) is similar to that provided by the manufacturing company (continuous red line). The experimental data equation slope (accelerometer scale factor, K_1 [127]) is $8.09 \text{ m}\cdot\text{s}^{-2}\cdot\text{V}^{-1}$, a value close to the sensor-maker supplied $8.06 \text{ m}\cdot\text{s}^{-2}\cdot\text{V}^{-1}$. Therefore, no modifications occur due to the electronic elements placed on the transmitter board. The only difference consists of the equation's constant term ($12.58 \text{ m}\cdot\text{s}^{-2}$). Nevertheless, adjusting the offset trimmer on the transmitter board this value can be easily modified - by simply turning the multi-turn potentiometer screw - without affecting the slope of the line. This means that the calibration chart can be moved left and right to modify the offset value without changing the equation's slope, but only its Y-intercept. In particular, in the example plotted in Figure 4.3, a random offset value of $12.58 \text{ m}\cdot\text{s}^{-2}$ is used.

2.2 - *Effects of battery residual charge*

This test was necessary because the MEMS accelerometer system works using a ± 12 V battery, which powers both the SF1600 and the wireless RF transmitter. Previous studies [83], [95] suggest that an unstable battery power supply voltage would affect the performance of a wireless sensor system. In particular, we observed that offset values (i.e.: accelerometer output value as it is in rest) are influenced by battery residual charge and that these values decrease in time with power level. Furthermore, when battery charge decreases, the number of data-packets sent to the receiver decreases as well, and it becomes smaller than the originally fixed sampling rate.

To overcome this problem, as described in the previous chapter, the TMR3-1222HI DC/DC converter has been incorporated in the transmitter board. It ensures a stable ± 12 V power supply even when the battery power starts to run out. To investigate the effectiveness of the DC/DC converter, tests were carried out to measure the SF1600 accelerometer outputs under power supply voltages less than ± 12 V. In the test designed for determining the effect of battery residual charge on the SF1600 offset, the ALE transmitter board was powered using a programmable DC power supply PWS4602 [140] as shown in Figure 4.4 (a). The transmitter board is placed horizontally at rest (i.e., 0° inclination) and the supplied voltage was dropped from 12.5 V to 6.5 V at the 0.1 V interval to simulate the progressive battery exhaustion. The receiver board, connected to a laptop for data acquisition, was deployed one meter away from the transmitter board in the setup shown in Figure 4.4 (b). For each battery tension value, a 10-minute measurement was carried out with a sampling rate of 3 kHz. As usual, data were analyzed using statistical descriptors such as the mean value and the standard deviation to double-check the stability of the recorded data. Since the ALE is at rest, it is subjected to the gravitational acceleration only; therefore, it should supply as output reading a constant value of $9.806 \text{ m}\cdot\text{s}^{-2}$, or, as an alternative, an output tension value, evaluated inverting equation [4.2], equal to -0.3434 V. Figure 4.5 plots the means of the measured sensor outputs (in Volt),

recorded from the receiver board, corresponding to the different power supply voltage. In the range 12.5 – 7V, the output values are constant and remain stable.

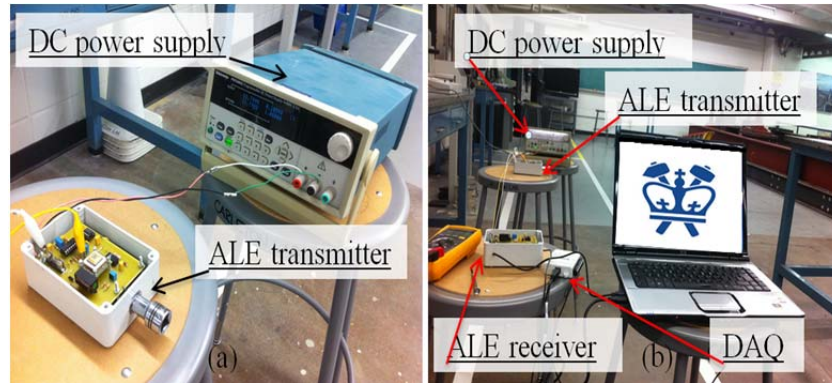


Fig. 4.4 – Test setup for the evaluation of the battery residual charge effects

Decreasing battery voltage does not influence the sensor output as in the previous sensor board. This means that the DC/DC converter neutralizes the effect of battery residual charge. This feature is quite expensive in terms of board energy-consumption (125 mA), but it allows more stable data and then more accurate measures. When the battery power is below 7 V, however, the sensor output data become unstable and no longer reliable. Despite this, tension values below 7 V are theoretical only and can be reached because of the programmable DC power supply. Realistically speaking, a 12 V cell will quickly run almost completely out of power and will stop working when its residual charge drops to nearly 8 V (a tension for which tests show that output response is still stationary). In addition, it is interesting to notice that the SF1600 output stays constant and then suddenly drops. This means that the system is able to operate up to a specific voltage and then it suddenly turns off. Unlike what occurs in the Mica2 family nodes - designed without a battery voltage up converter - there are no transition phases [77], [83]. Furthermore, since no microprocessor is embedded, the signal conditioning section cannot be influenced by battery depletion and no data loss occurs. Once the transmitter is not powerful enough to transmitting data, the communication is stopped instead of being only partially achieved. To be rigorous, analyzing the measurements in Figure 4.5, the maximum difference in

the output values in the range 12.5 - 7V is equal to $0.197 \cdot 10^{-3}$ V (Output value_{max} = -0.343399 V, at 10.4 V and Output value_{min} = -0.343596 V, at 11.2 V). Plugging these values into equation [4.2] the corresponding values of acceleration are calculated. These are equal to $9.806 \text{ m}\cdot\text{s}^{-2}$ for the maximum value and equal to $9.805 \text{ m}\cdot\text{s}^{-2}$, which is a fluctuation in the order of $10^{-3} \text{ m}\cdot\text{s}^{-2}$, a value comparable to SF1600 resolution.

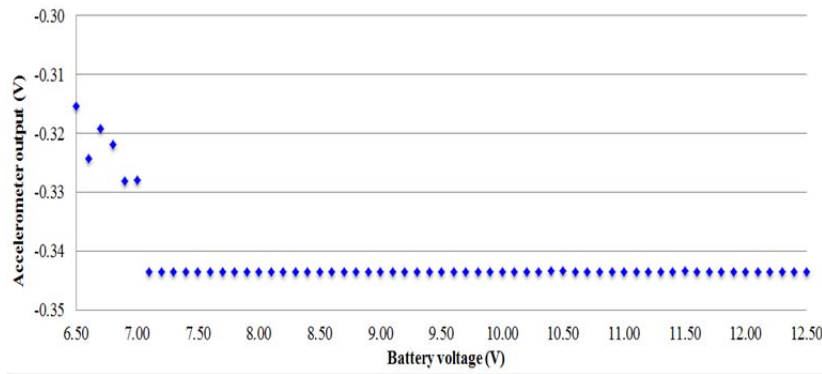


Fig. 4.5 – Effect of battery residual charge on sensor output

A list of the complete results for this test is reported in Table A.2 attached in the Appendix. Analyzing these data, it is observed that when the maximum output value and its standard deviation are considered (- 0.343399 V and $0.15 \cdot 10^{-3}$ V), the interval in which results may be is [- 0.343249; - 0.343549] V, while when the minimum output is considered the results may be in the range [- 0.343356; - 0.343640] V. Since, there is an intersection between the two intervals, the measure is consistent and the errors are contained in the physiologic variation range of the instrument. This result further validates ALE quality. Indeed, it implies that the fluctuation in acceleration values is due to physiological measurement errors and not to problems connected to the assembled sensor board.

2.3 - Maximum transmission distance

One of the main strengths of the MEMS accelerometer system is that signal can be transmitted wirelessly. This peculiarity frees it from limitation due to cable connections. As described in Chapter 3, the ALE transmitter board is connected to

a low-cost, 2.4 GHz ISM, wireless RF transmission system, which sends the sampled data to the correspondent receiver board, connected to an external DAQ. It should be pointed out that the antenna's nominal transmission range in free-field conditions is equal to 150 meters, and its bandwidth equal to 7 MHz, whereas the bandwidth of the transmitted pulses changes in the range 0 – 100 kHz.

In order to evaluate the wireless signal transmission capability of the prototype sensor system, the calibration tests (as shown in Figure 4.2) were repeated by placing the receiver board at increasing distances from the transmitter board placed in the angle meter machine. Distance was increased to 5 through to 30 meters. This time, at each of the inclinations ($0 \leq \alpha \leq \pi$ rad), and for each of the distances (5, 10, 15, 20, 25, and 30 m) the sensor output signal was recorded at the exit of the transmitter board and at the entrance of the receiver board placed away. Again, data were acquired for 10 minutes at 3 kHz through the external DAQ device. Figures 4.6 to 4.8 plot the SF1600 output signals sampled at the output section of the transmitter board (continuous red line) versus those sampled at the receiver board (blue dots) placed 5, 15, and 30 m away from the transmitter board (figures related to the distances of 10, 20, and 25 m are not shown here for the sake of brevity; they are reported in Figures A.1 through to A.3 in the Appendix).

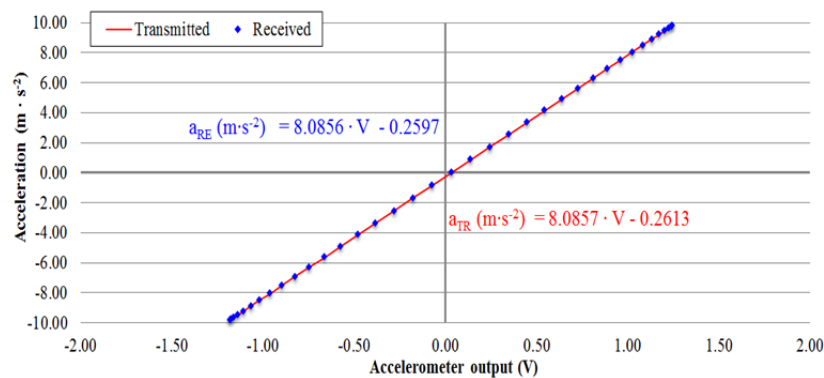


Fig. 4.6 – Calibration chart when receiver is 5 m away from transmitter

It can be observed that the equations interpolating the data measured when the receiver board is deployed up to 25 meters away from the transmitter board are

similar to the equation interpolating the data measured at the output section of the transmitter board. Therefore, there is an excellent agreement between the data directly measured at the accelerometer output and those obtained at the receiver board. In addition, data confirm the linear relation between the acceleration and the sensor output voltage with a correlation coefficient R^2 nearly equal to one.

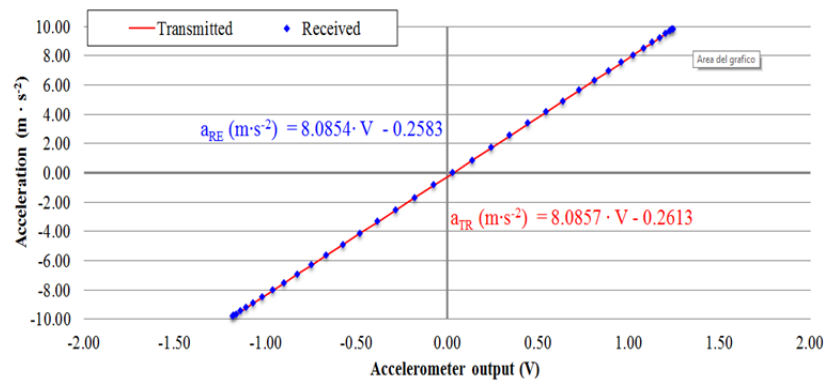


Fig. 4.7 – Calibration chart when receiver is 15 m away from transmitter

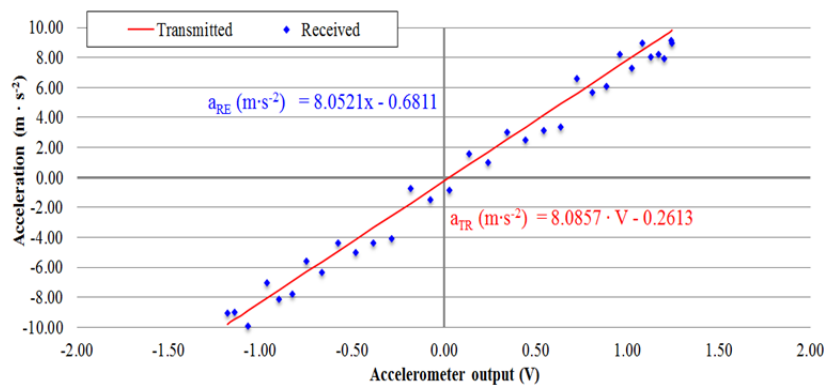


Fig. 4.8 – Calibration chart when receiver is 30 m away from transmitter

On the other hand, when the two boards are distanced 30 meters apart, the wirelessly transmitted signals become less accurate. Analyzing the measurements in Figure 4.8, it can be observed that the signal degraded extremely and the relation between the two output values is no longer perfectly linear ($R^2 = 0.97$). Data appear to be randomly arranged around the line representing the signals sampled at the output section of the transmitter board. This behavior could be due to several interferences occurring and to decreases in signal strength. Basically,

the receiving wireless RF antenna cannot recognize the signal sent by the transmitter board and thus it collects signals coming from different sources as well.

To evaluate the quality of the transmitted signal, a relative error ε_r (%) was computed using the following equation:

$$\varepsilon_r (\%) = \frac{1}{N} \sum_i^N \left(\left| \frac{a_{TR}(\alpha) - a_{RE}(\alpha)}{a_{TR}(\alpha)} \right| \right)_i \cdot 100 \quad [4.3]$$

where $a_{TR}(\alpha)$ is the acceleration value measured at the output section of the transmitter board for the generic inclination α , $a_{RE}(\alpha)$ is the acceleration value recorded at the receiver board, and N is the total number of data points measured (equal to nearly 2 millions in the reported examples). Table 4.1 tabulates the relative error with the distance evaluated over the $0 - \pi$ static calibration procedure interval.

Table 4.1 – Relative error of wirelessly transmitted signal (Static calibration tests)

Distance	ε_r
(m)	(%)
5	0.12
10	0.15
15	0.15
20	0.16
25	0.17
30	20.29

It is observed that the quality of the wirelessly transmitted signal decreases as the distance between the transmitter and receiver increases. The signal remains stable for distances between the two boards of less than 25 m, whereas the signal is distorted when the distance is 30 m, as confirmed by the relative error soaring from 0.12% to 20.29%. A possible explanation for this behavior is that over a short-medium range the signal is powerful enough to cover possible interferences; while over certain distances the transmitter sends a weak signal and the receiver board may also listen in to other RF sources. The theoretical transmission range of

the antenna is nearly 150 m in free-field conditions, but the tests show that the effective distance drops by nearly 80%.

This problem is even more evident when a dynamic test is carried out. The MEMS accelerometer was excited with a 100Hz sinusoidal wave with constant amplitude of $1.00 \text{ m}\cdot\text{s}^{-2}$, while the receiver board was placed at different distances away from the transmitter board to measure the wirelessly transmitted sensor output signal. The test was carried out in two different conditions:

- Indoor;
- Outdoor.

In the first case, the ALE was deployed in a controlled environment in the basement of a laboratory with no, or a few, wireless and RF sources different from the MEMS based system (as shown in Figure 4.9). On the other hand, in the latter case the MEMS accelerometer system was placed in a noisy urban University campus in the center of Manhattan, NY, an environment characterized by a widespread use of RF systems, radio-communications, Wi-Fi networks, mobiles, etc.

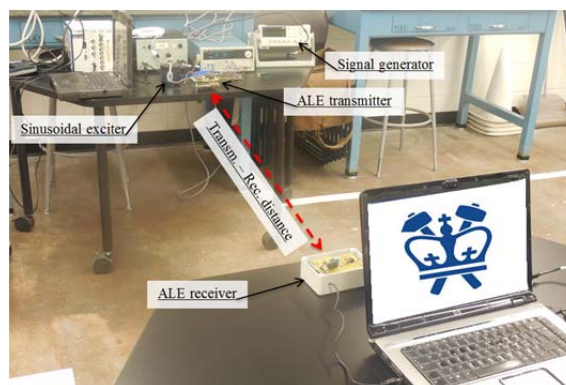


Fig. 4.9 – Setup for the maximum transmission distance dynamic test (Indoor)

For each of the distances, a 10-minute measurement was made. The wirelessly transmitted sensor output signals were acquired with a 3 kHz sampling rate using the external DAQ device connected to the receiver board and compared with the

signal measured at the exit of the transmitter board. To evaluate the quality of the transmitted sinusoidal signal, a relative error ε_r (%) was computed using the following equation:

$$\varepsilon_r (\%) = \frac{1}{N} \sum_i^N \left(\left| \frac{a_{TR}(t) - a_{RE}(t)}{a_{TR}(t)} \right| \right)_i \cdot 100 \quad [4.4]$$

where $a_{TR}(t)$ is the acceleration value measured at the output section of the transmitter board for at time t , $a_{RE}(t)$ is value recorded at the receiver board, and N is the total number of data points measured during the 10-minute period. Tables 4.2 and 4.3 tabulate the relative error with the distance evaluated over the 10-minute measurement period, whereas Figures 4.10 and 4.11 plot a segment of the time histories of the wirelessly transmitted sensor output signals measured at the receiver placed at the different distances, indoor and outdoor.

Table 4.2 – Relative error of wirelessly transmitted signal (Dynamic calibration tests - Indoor)

Distance	ε_r
(m)	(%)
5	0.41
15	0.42
30	7.26

Table 4.3 – Relative error of wirelessly transmitted signal (Dynamic calibration tests – Outdoor)

Distance	ε_r
(m)	(%)
5	1.08
15	9.17
30	18.67

Analyses on sinusoidal wave time histories confirm that in indoor conditions, the signal remains stable for distances between the two boards of less than 30 m. Observing the waveforms plotted in Figure 4.10, the signal recorded at distances of 5 and 15 m (green and blue dotted lines) match that recorded at the output section of the ALE transmitter board (continuous red line). Instead, when the distance overcomes 30 m, the signal is distorted as confirmed by the relative error

soaring from 0.42% to 7.26%. The performance further deteriorates in the outdoor environment, as shown in Table 4.3 and Figure 4.11.

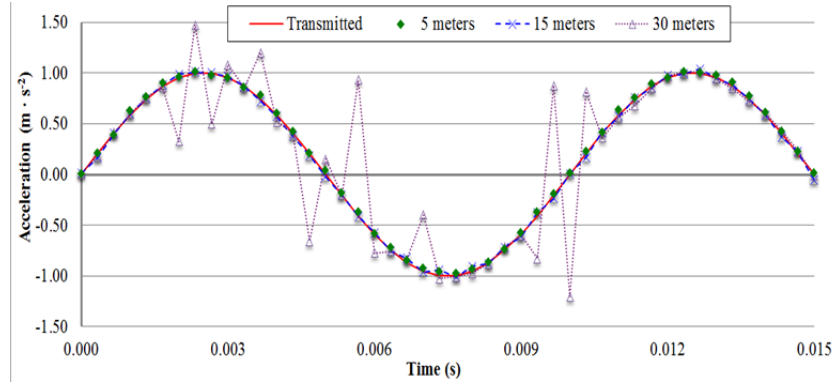


Fig. 4.10 – Time-histories of wirelessly transmitted signal (Indoor)

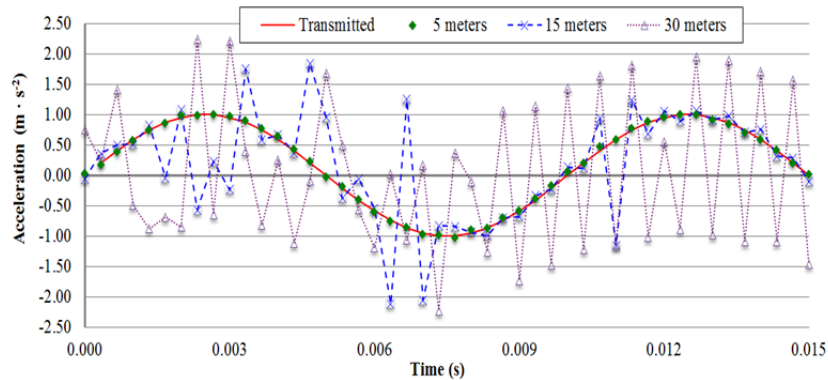


Fig. 4.11 – Time-histories of wirelessly transmitted signal (Outdoor)

Relative errors soar from 1.08% at the 5-meter distance to 9.17% and 18.67%, respectively, at the 15-meter and 30-meter distances from the receiver board. When the outdoor test is carried out, it can be observed that the maximum distance, for which signal is still consistent with the transmitted one, is halved. For mutual distances between transmitter and receiver of 15 m, the quality of the signal is comparable with the quality of the signal recorded when the mutual distance is 30 m and the test is carried out indoors. Increases in the relative error depend on interferences, which destroy the original waveform as shown in Figure 4.12, where a detail of the time-history recorded when the receiver is outdoors and 30 m away from the transmitter is plotted. The wireless RF antenna captures signals different from those sent by the transmitter, then the F/V converter

demodulates them into voltage values before downloading to the DAQ. When the signal is recomposed, the DAQ considers the external values as a portion of the original signal; therefore the waveform is corrupted as plotted in the following figure, where several small saw-teeth around the 30 Hz waveform and other main peaks can be observed.

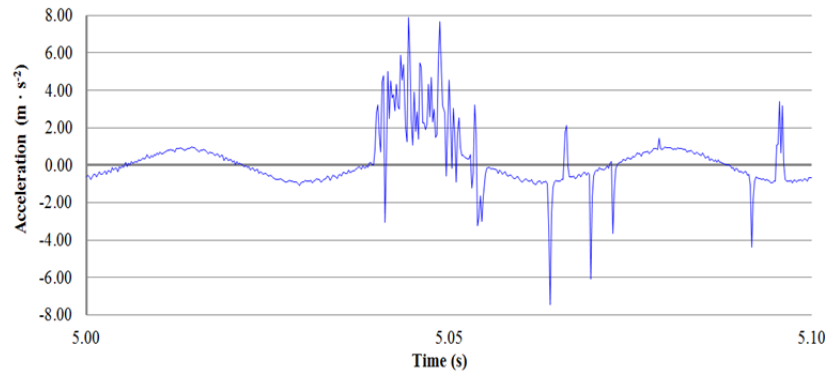


Fig. 4.12 – Detail of the time-history of wirelessly transmitted signal (30 m - Outdoor)

This interpretation is confirmed when an analysis in the frequency is carried out. Since the SF1600 is excited with a 30 Hz sinusoidal wave with constant amplitude of $1.00 \text{ m}\cdot\text{s}^{-2}$, when a Power Spectral Density (PSD) of the signal is plotted, it is reasonable to expect a single-mode frequency response peaked around the excited frequency. Figure 4.13 plots the PSD of the signal received from the ALE.

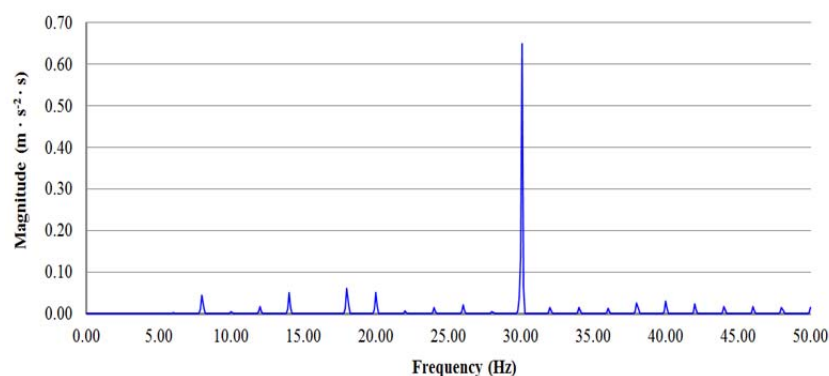


Fig. 4.13 – PSD of the signal received from the ALE

It is observed that the dominant frequency is 30 Hz, but several, less-intense frequencies are highlighted (e.g.: 8, 14, 18 Hz, etc.). They have smaller intensity

than the dominant frequency ($0.05 \text{ m}\cdot\text{s}^{-2}\cdot\text{s}$ compared to $0.64 \text{ m}\cdot\text{s}^{-2}\cdot\text{s}$) because their temporal persistence is smaller, but they still affect the accuracy of the signal. None of these components are present in the transmitted signal and they appear in the received one because of interfering signals that are transformed into voltage value by means of the F/V converter. Since transmitted signal is not encoded, the receiver detects RF signals coming from the ALE transmitter board as well as signals coming from other sources. The result is a recorded signal no longer consistent with that originally sampled. It would be reasonable to think that the quality of the signal may be improved through post processing analyses (e.g.: filtering, averaging, etc.). On the other hand, when the received signal is processed using a low-pass filter having bandwidth equal to SF1600's bandwidth (i.e.: 1500 Hz), no differences are observed between the unfiltered signal and the filtered one. To obtain a smoother waveform, it is necessary to apply a narrower filter (i.e.: 300 Hz), but by doing so the original signal shape is distorted. This test proves the necessity of installing an anti-aliasing filter in the receiver board. Indeed, at the present, when signals having frequency higher than the Nyquist frequency are collected with the receiver, they are not excluded, but recorded. This results in several frequencies flipped around the cutting frequency of the instrument that are not, however, originally present in the signal.

These tests have demonstrated that, to date, ALE maximum transmission distance depends on the surrounding environment. Interference with the surrounding RF noise leads to significant concerns about the quality of signals. The massive presence of several Wi-Fi networks and RFs is a clear problem for the selected antenna. The receiver cannot recognize the signal sent by the sensor board and thus it collects signals coming from different sources. In addition, the low-threshold discriminator embedded in the receiver board appears to be more a flaw than a merit. At the present, experiments demonstrate that the MEMS accelerometer system cannot be used for carrying out measurements on areas of wide extension. It is reasonable to think that a more effective wireless RF transmitter-receiver apparatus may solve problems related to signal deterioration

over distance. Further developments of this study will involve the selection of a wireless RF antenna more suitable for SHM purpose over a wider area.

2.4 - Comparative dynamic tests

To achieve a complete characterization of the MEMS accelerometer system, comparisons with wired accelerometers - traditionally used in vibration monitoring - were carried out. By means of these tests, it is possible to verify whether or not the ALE is sensitive enough to measure low amplitude and low frequency vibrations. To do so, shaking table tests were carried out using a wired IEPE accelerometer (model 393B04 by PCB Piezotronics Inc. [92]) as a reference sensor. The sensors were excited by:

- 1) sinusoidal wave input (pure tone);
- 2) periodic wave input;

and the wirelessly transmitted sensor output signals were compared, in time and frequency domains, with those recorded by the reference sensor.

2.4.1 - Sinusoidal wave input

This test consisted of deploying the ALE transmitter board, together with a traditional wired IEPE reference accelerometer, over a shaking table and positioning the receiver board five meters away from the transmitter. To allow for easier deployment on the shaking table support, the SF1600 was removed from the transmitter board and connected to it by means of a 10-pin IDC.

According to recommendations provided by [141], both sensors were attached to the moving support using mounting threaded pin screw to guarantee a better connection with the object being tested as shown in the experiment setup shown in Figure 4.14. The table was excited with 5, 2, 1, 0.5, and 0.2 Hz sinusoidal waves. For each frequency, a 5-minutes measurement was made and the wirelessly transmitted sensor output signals were acquired with a 100 Hz

sampling rate using the external DAQ device connected to the receiver board and the reference sensor. In other words, data from both of the sensors were acquired by the same DAQ system. The goal of this test is to study the behavior of the board in a very simple context: analyzing the sampled data when the sensor detects acceleration, which remains constant and stable in time. In particular, the test aims to demonstrate that the ALE behaves as a wired accelerometer even at very low frequencies (far below 1 Hz) as well.

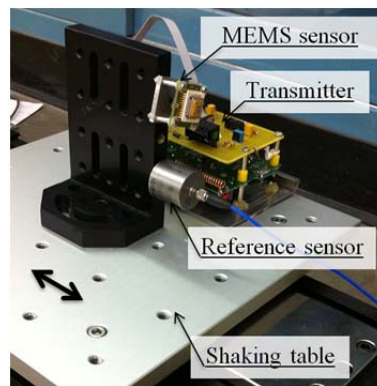


Fig. 4.14 – Setup for the shaking table test (sinusoidal waves input)

In addition, the test seeks to prove that features adopted in its design allow to overcome problems highlighted in previous studies. Figures 4.15 to 4.24 plot the recorded time-histories and (PSDs).

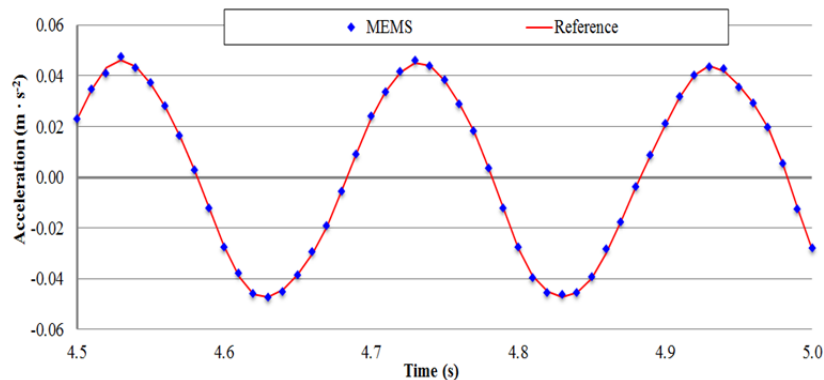


Fig. 4.15 – Comparison of measurements by the two sensors in time domain (5 Hz)

A good agreement is observed between the data measured by the reference sensor and those by the MEMS sensor and obtained at the receiver board. The ALE shows a capacity to measure low amplitude vibration (in the order of $10^{-2} \text{ m} \cdot \text{s}^{-2}$)

with accuracy comparable with that of accelerometers nowadays used in vibration measurements and SHM. Furthermore, it is possible to observe a good match, even when frequency domain responses are analyzed. The MEMS accelerometer system permits identification of the fundamental frequency of the vibration.

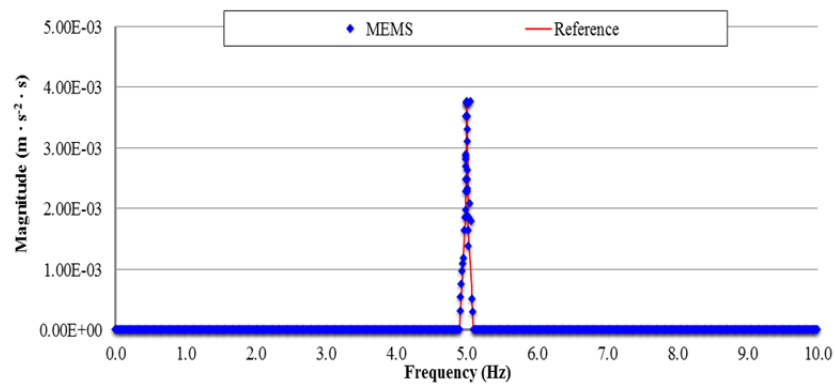


Fig. 4.16 – Comparison of measurements by the two sensors in frequency domain (5 Hz)

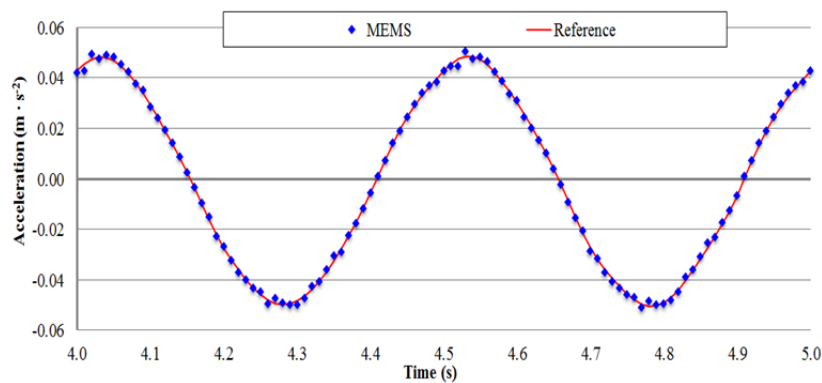


Fig. 4.17 – Comparison of measurements by the two sensors in time domain (2 Hz)

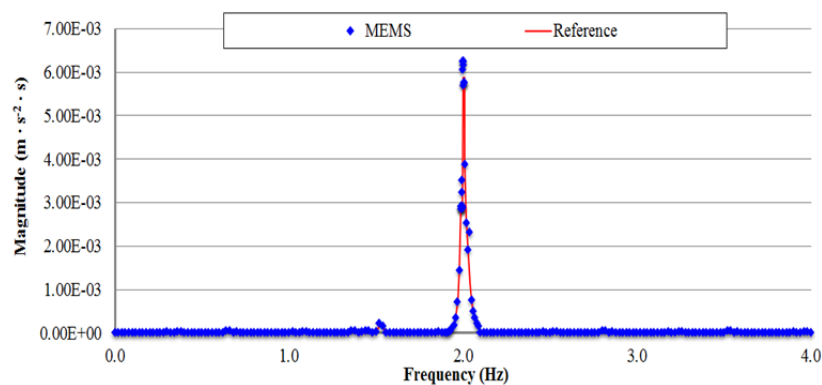


Fig. 4.18 – Comparison of measurements by the two sensors in frequency domain (2 Hz)

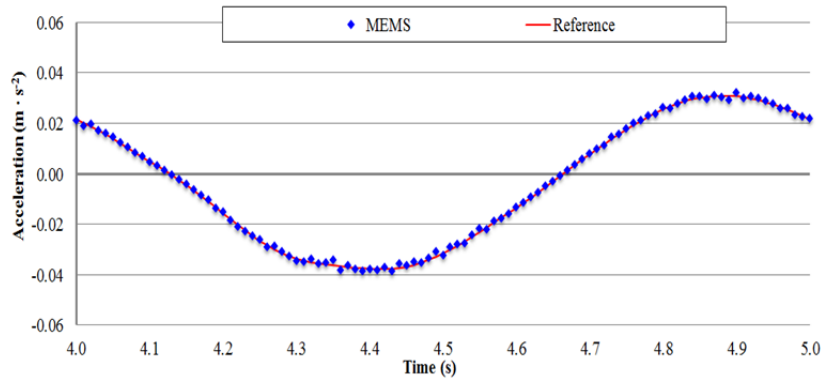


Fig. 4.19 – Comparison of measurements by the two sensors in time domain (1 Hz)

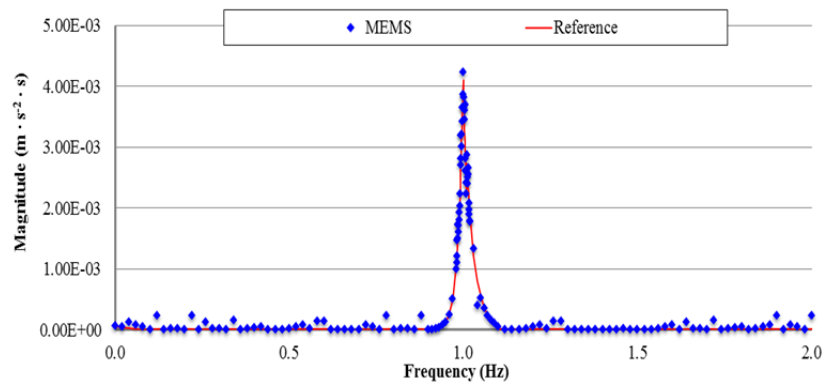


Fig. 4.20 – Comparison of measurements by the two sensors in frequency domain (1 Hz)

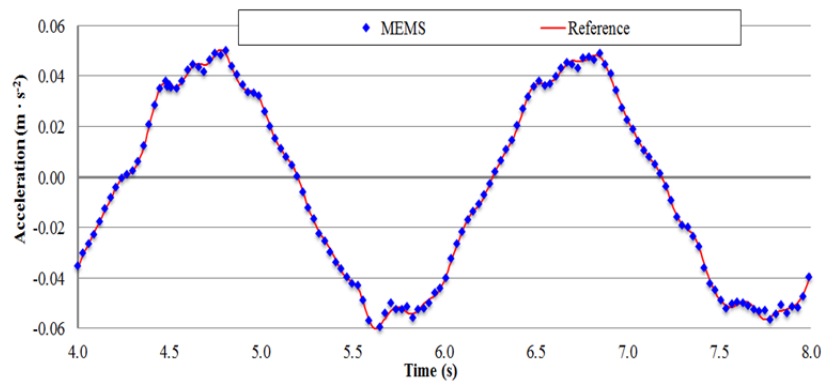


Fig. 4.21 – Comparison of measurements by the two sensors in time domain (0.5 Hz)

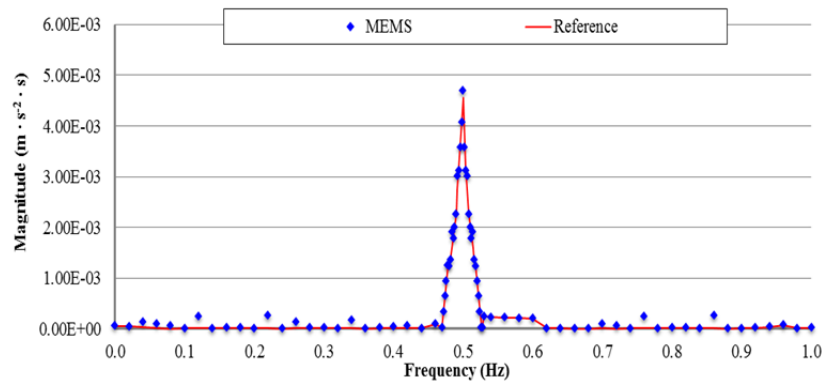


Fig. 4.22 – Comparison of measurements by the two sensors in frequency domain (0.5 Hz)

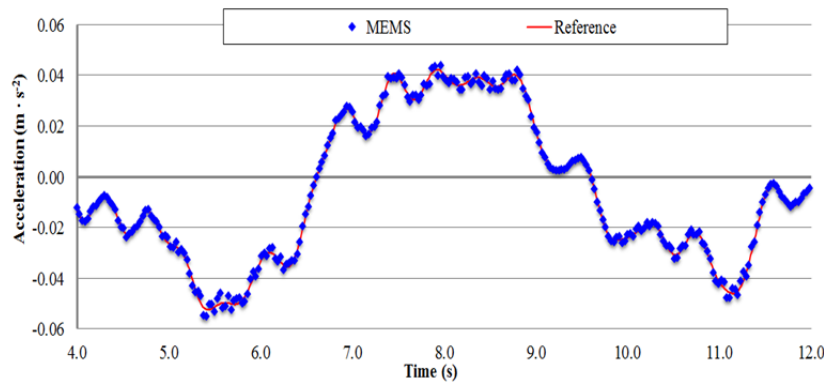


Fig. 4.23 – Comparison of measurements by the two sensors in time domain (0.2 Hz)

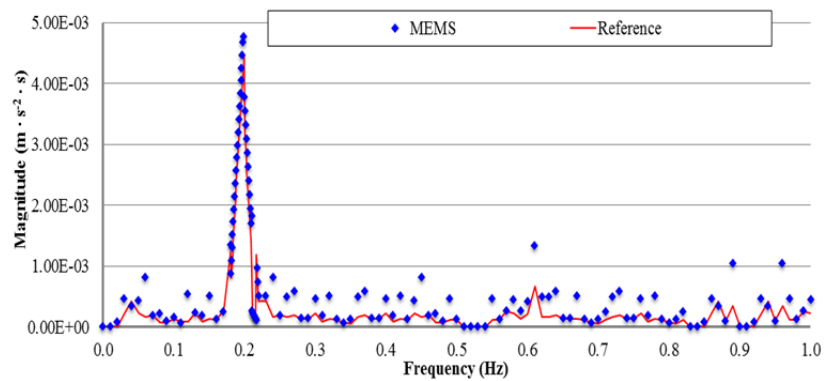


Fig. 4.24 – Comparison of measurements by the two sensors in frequency domain (0.2 Hz)

The only remark that can be made is that at very low frequencies (below 1 Hz), the ALE tends to overestimate the magnitude of the dominant frequency component. To evaluate the correlation between the signals sampled with the two

sensors analytically, an estimation of the relative error ε_r was computed using the following equation:

$$\varepsilon_r (\%) = \frac{1}{N} \sum_i^N \left(\left| \frac{a_{ref}(t) - a_{MEMS}(t)}{a_{ref}(t)} \right| \right)_i \cdot 100 \quad [4.5]$$

where $a_{ref}(t)$ is the acceleration value measured with the reference sensor at time t , $a_{MEMS}(t)$ is the value recorded with the wireless MEMS accelerometer, and N is the total number of data points measured.

In addition, an evaluation of the equivalent acceleration a_{eq} was computed [142]. The equivalent acceleration is considered to be the average acceleration to which the system is subjected during a period of time T . It is the acceleration value, maintained constant over time, that exhibits the same energy of the real fluctuating signal [143], and it is defined using the equation:

$$a_{eq} = \sqrt{\frac{1}{T} \int_0^T a^2(t) \cdot dt} \quad [4.6]$$

where T is the length of the sampled signal, $a(t)$ is the acceleration at the generic time t , and dt is the sampling rate. For each of the frequencies tested, the relative error and the equivalent accelerations - computed using the acceleration values recorded with the two sensors - are listed in Table 4.4.

It can be observed that the measurement error increases as the vibration frequency decreases. This decrease is not linear. Nevertheless, the relative error is less than 1%, and, thus, the MEMS accelerometer system achieved performance comparable to that of the reference sensor, demonstrating its capability in measuring low-frequency vibration, with frequency as low as 0.2 Hz with a suitable accuracy for normal engineering practices.

It is of interest to notice that the equivalent accelerations supplied with the reference sensor are slightly higher than those supplied with the MEMS one. However, this difference is always smaller than 0.40% (0.20Hz case). On the contrary, signal magnitudes evaluated from data recorded with the MEMS accelerometer system result slightly higher than those computed from data

sampled with the reference sensor. As observed from data listed in Table 4.4, this difference is still negligible.

Table 4.4 – ALE relative error and signals' equivalent acceleration (Sinusoidal wave input)

Frequency	ϵ_r	$a_{eq, ref}$	$a_{eq, MEMS}$	PSD _{ref}	PSD _{MEMS}
(Hz)	(%)	($10^{-2} \text{ m}\cdot\text{s}^{-2}$)	($10^{-2} \text{ m}\cdot\text{s}^{-2}$)	($10^{-3} \text{ m}\cdot\text{s}^{-2}\cdot\text{s}$)	($10^{-3} \text{ m}\cdot\text{s}^{-2}\cdot\text{s}$)
5.00	0.29	3.293	3.289	3.760	3.760
2.00	0.53	3.436	3.438	5.872	6.260
1.00	0.53	2.472	2.466	4.107	4.230
0.50	0.84	3.671	3.663	4.563	4.700
0.20	0.99	3.245	3.232	4.444	4.768

To validate the accuracy of the measures carried out, a statistical analysis of the data sampled with the reference and the MEMS accelerometer is done. This consists of an evaluation of the expected values \bar{x} (average) and of the variance $\pm \sigma$ (standard deviation) of a set of data. As is well known, when a measurement is carried out, mistakes in the evaluation of the measured parameter are made. Therefore, to be accurate, the results should be expressed as the interval $[\bar{x} - \sigma; \bar{x} + \sigma]$.

In the examples reported below, a statistical evaluation of the acceleration's expected values measured with the two devices is carried out, along with an evaluation of the accuracy of that measurement. Since the shaking table supplies the two sensors with the same input in time, each oscillation can be considered as a population of data. Therefore, when a signal having frequency f_s , period T , and time length L is considered, if it is divided in many sub-signals each having length T a total number of L/T similar signals is generated. These signals represent the population on which the statistical analysis is carried out. With reference to the 5Hz sinusoidal waveform, recorded with a sampling rate of 100 Hz, a portion of the signal having length 0.2 seconds contains 20 data. If 30 sets of 5 Hz sinusoidal waveforms are considered, for each of the 20 points composing the signal it will be possible to evaluate their mean value and their standard deviation. If these results are plotted in a chart (as shown in Figure 4.25), it is observed that the

continuous red line (expected value, calculated as the average of the homologous point recorded with the reference sensor) is between two dotted red lines ($[\bar{x} - \sigma_{Ref}; \bar{x} + \sigma_{Ref}]$), which represent the fluctuations the expected value may have. To be more specific, the values in that range have all the same likelihood of being considered expected values. A similar operation can be carried out with data recorded with the MEMS accelerometer, the expected values of which are between two dotted blue lines representing the uncertainty of the measurement. This procedure allows for a graphical evaluation of the quality of the measurements.

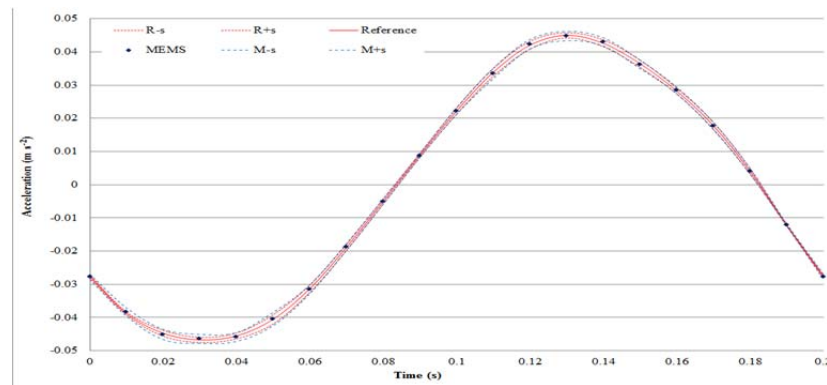


Fig. 4.25 – Comparison of measurement uncertainties (5 Hz)

Results obtained for the two accelerometers are reported in Table A.6 in the Appendix and normalized to the values recorded with the reference sensor for easier understanding (Figure 4.26).

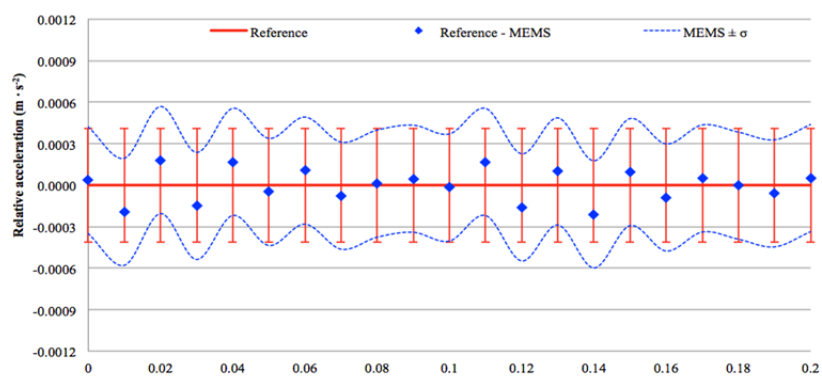


Fig. 4.26 – Comparison of measurement uncertainties normalized to the reference sensor (5 Hz)

Figure 4.26 plots the interval in which values recorded with the reference sensor are supposed to be (continuous line and vertical error interval valuated as average standard deviation), the values given by the difference of records from the MEMS and reference accelerometers (blue dots), and the interval in which values recorded with the MEMS sensor are supposed to be (dotted blue lines $MEMS \pm \sigma$). If any intersection between the two intervals (Reference $\pm \sigma$) and (MEMS $\pm \sigma$) exists, it means that data recorded with the two systems are equivalent despite the errors committed in the measurement. Analyzing results plotted in Figures 4. 25 and 4.26 a substantial correspondence is observed between data recorded with the two devices.

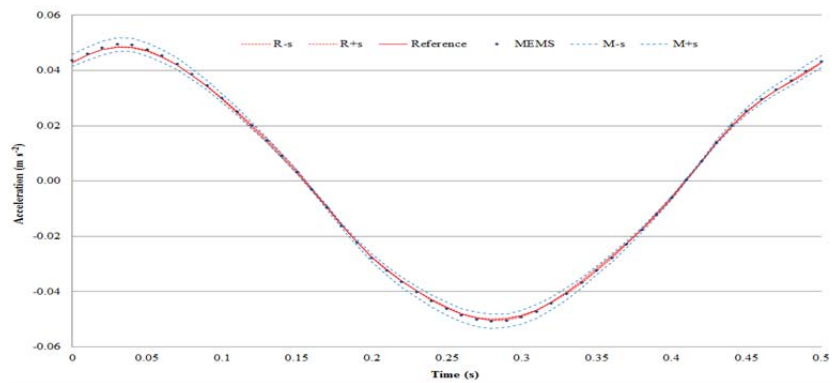


Fig. 4.27 – Comparison of measurement uncertainties (2 Hz)

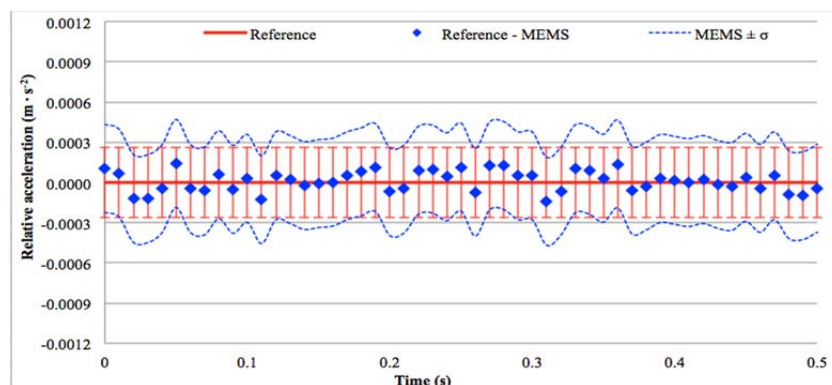


Fig. 4.28 – Comparison of measurement uncertainties normalized to the reference sensor (2 Hz)

The values measured with the MEMS-based accelerometer are constantly within the reference sensor's interval of tolerance, showing that the measurements

carried out with the ALE can be considered as equivalent to those carried out with a traditional wired accelerometer. The same considerations can be made when data related to the 2 Hz sinusoidal wave are analyzed as shown in Figures 4.27 and 4.28 and for the other frequencies sinusoidal waves plotted in Figure 4.29 through 4.31.

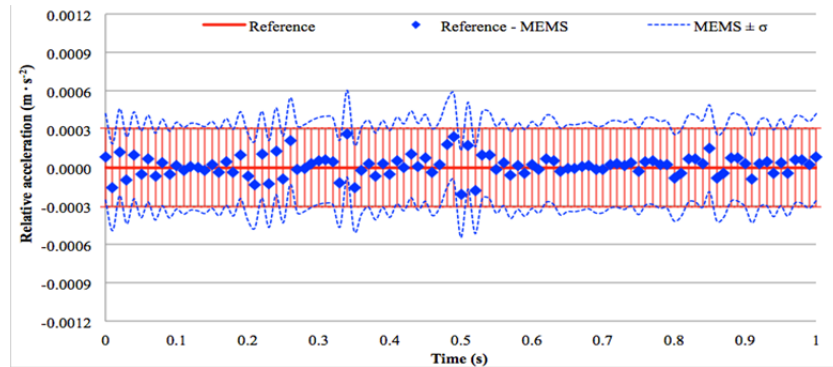


Fig. 4.29 – Comparison of measurement uncertainties normalized to the reference sensor (1 Hz)

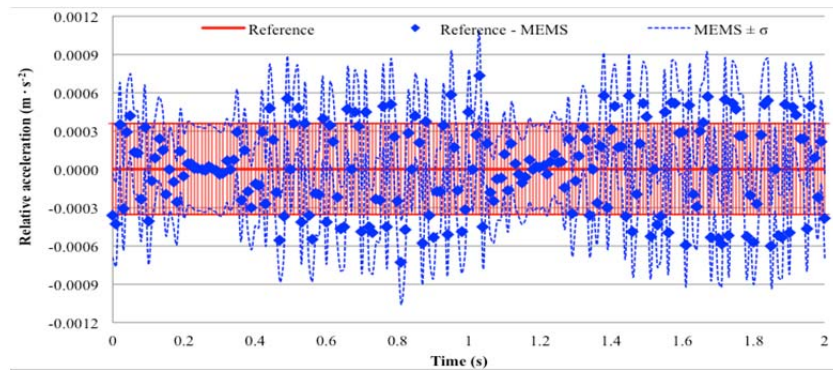


Fig. 4.30 – Comparison of measurement uncertainties normalized to the reference sensor (0.5 Hz)

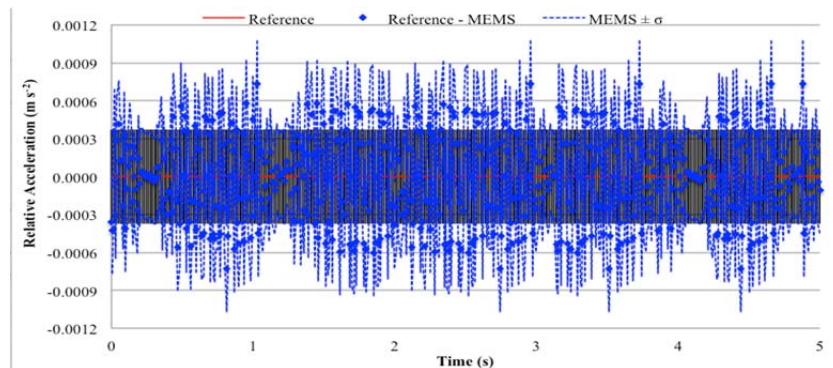


Fig. 4.31 – Comparison of measurement uncertainties normalized to the reference sensor (0.2 Hz)

Analyzing the results, a substantial correspondence is observed between data recorded with the two devices (see Appendix A.6 through A.10). The values measured with the MEMS accelerometer are constantly within the reference sensor interval of tolerance for frequencies up to 1 Hz, whereas for lower frequencies several data point are external to that interval. It shows that measurement error increases as the frequency of the vibration decreases. Nevertheless, when the MEMS sensor interval of tolerance is considered, the intersection of the two ranges is always verified.

2.4.2 - Periodic wave input

The second test consisted of positioning the MEMS accelerometer system, together with the same IEPE accelerometer of the previous test, over a vertical electromagnetic shaker and deploying the receiver board five meters away from the transmitter board. The system was then solicited with periodic vibrations of 5, 2, 1, and 0.5 Hz. For each frequency, a 5-minutes measurement was made and the transmitted sensor output signals were acquired with a 100 Hz sampling rate using the external DAQ device connected to the receiver board (deployed 5 m away from the transmitter board) and the reference sensor. The setup of the experiment is shown in Figure 4.32.

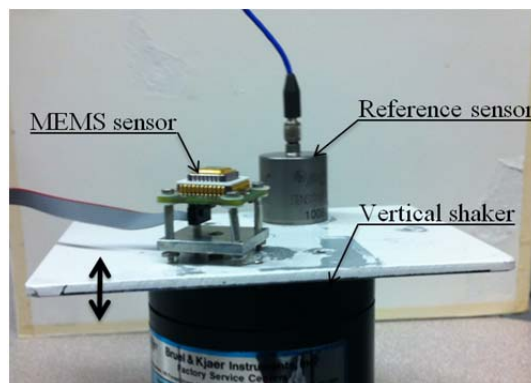


Fig. 4.32 – Setup for the shaking table test (Periodic wave input)

The goal of this test is to evaluate the MEMS accelerometer system when more complex waves excite the structure on which the sensor is mounted. Figures 4.33

to 4.40 plot a detail of the recorded time-histories and the corresponding frequency domain analyses calculated using a PSD analysis. Again, a good agreement between the data measured with the two sensors is observed. Even for vibration having frequency lower than 1 Hz (the value suggested by Directive as lower limit for detecting acceleration instead of displacement [143]).

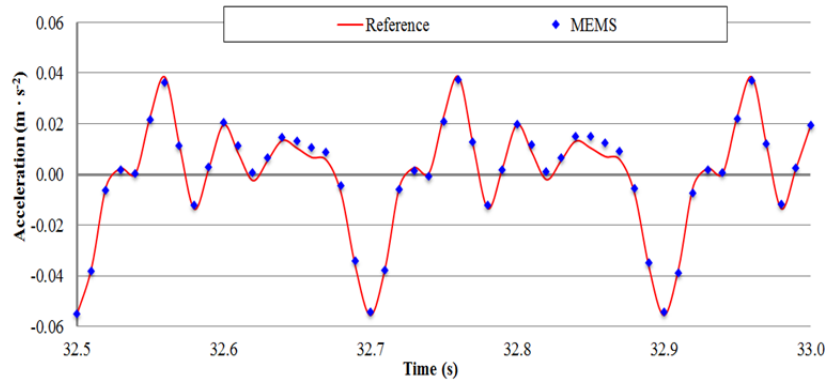


Fig. 4.33 – Comparison of measurements by the two sensors in time domain (5 Hz)

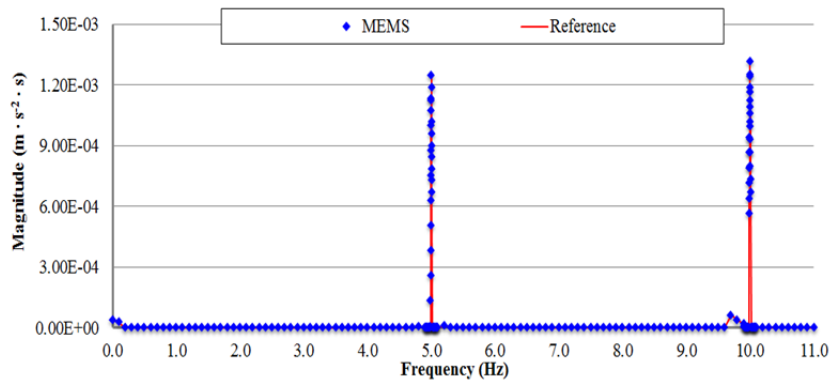


Fig. 4.34 – Comparison of measurements by the two sensors in frequency domain (5 Hz)

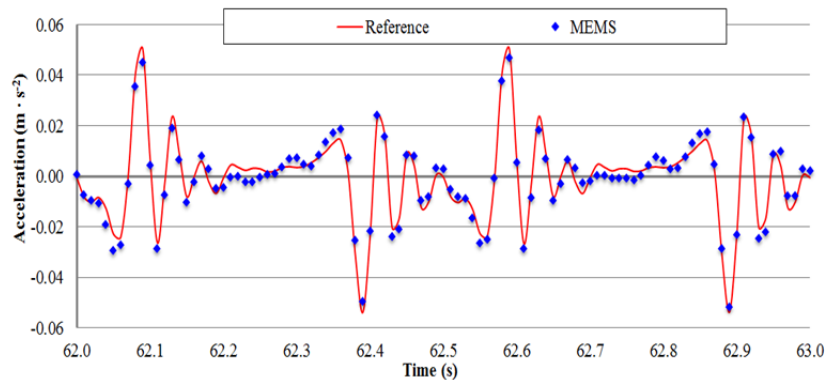


Fig. 4.35 – Comparison of measurements by the two sensors in time domain (2 Hz)

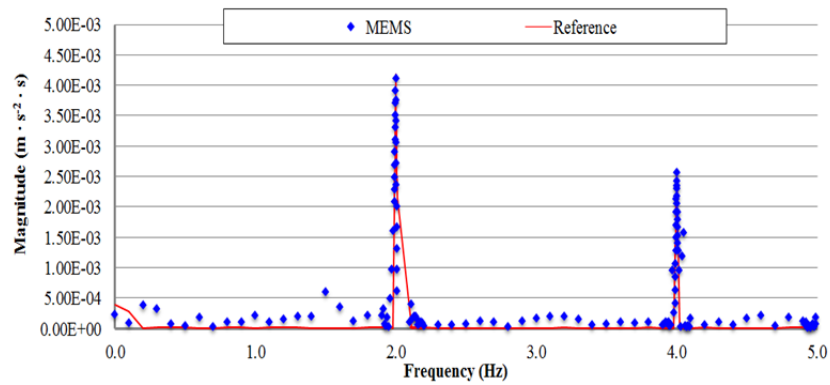


Fig. 4.36 – Comparison of measurements by the two sensors in frequency domain (2 Hz)

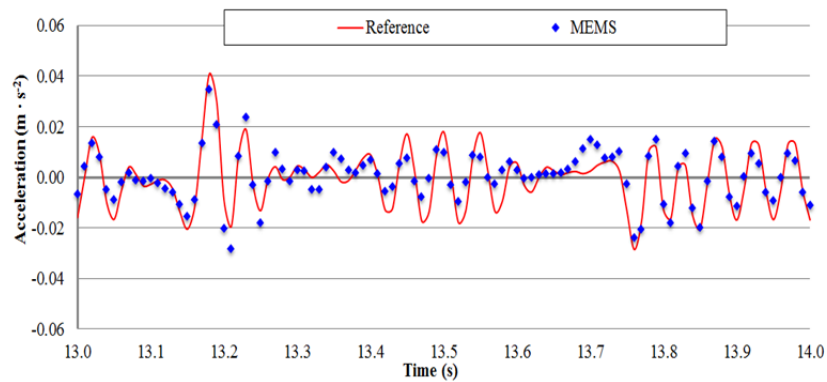


Fig. 4.37 – Comparison of measurements by the two sensors in time domain (1 Hz)

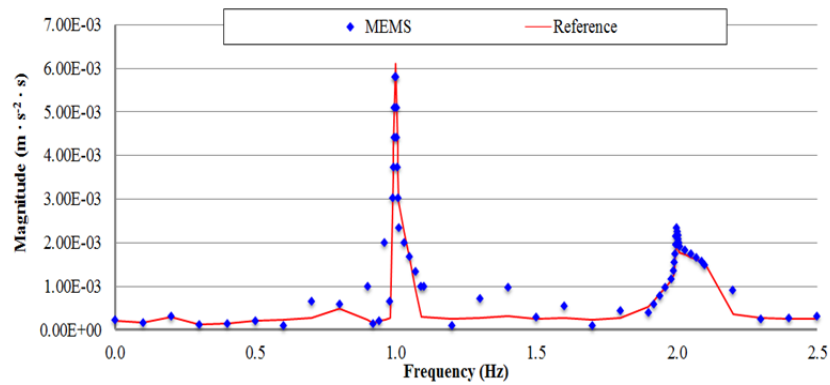


Fig. 4.38 – Comparison of measurements by the two sensors in frequency domain (1 Hz)

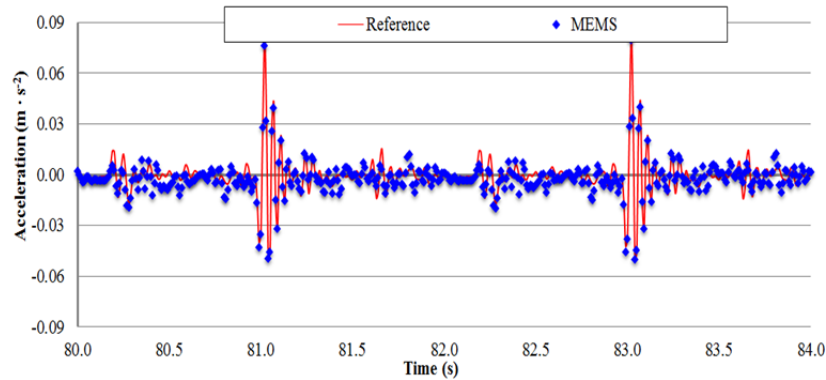


Fig. 4.39 – Comparison of measurements by the two sensors in time domain (0.5 Hz)

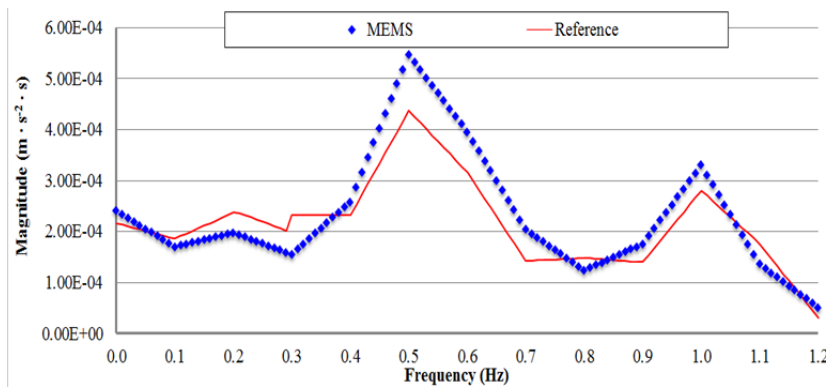


Fig. 4.40 – Comparison of measurements by the two sensors in frequency domain (0.5 Hz)

Overall the measurements by the two sensors agree well with each other. Furthermore, from the PSD analyses, it can be observed that the MEMS accelerometer system can identify the first frequency of the vibration and its high frequency harmonics as well. The relative error ε_r of the MEMS accelerometer in comparison with the reference sensor is calculated using Equation [4.5], while the evaluation of the equivalent acceleration a_{eq} is done using Equation [4.6]. The results are shown in Table 4.5. It is observed that similar to the sinusoidal excitations, the measurement error increases as the frequency of the periodic vibration decreases. To be accurate, the only difference that can be observed between the two signals is that data coming from the MEMS accelerometer underestimate the peak value of accelerations having amplitude far below $0.01 \text{ m}\cdot\text{s}^{-2}$.

Table 4.5 – ALE relative error and signals' equivalent acceleration (Periodic wave input)

Frequency	ϵ_r	$a_{eq,ref}$	$a_{eq,MEMS}$	PSD_{ref}	PSD_{MEMS}
(Hz)	(%)	($10^{-2} \text{ m}\cdot\text{s}^{-2}$)	($10^{-2} \text{ m}\cdot\text{s}^{-2}$)	($10^{-3} \text{ m}\cdot\text{s}^{-2}\cdot\text{s}$)	($10^{-3} \text{ m}\cdot\text{s}^{-2}\cdot\text{s}$)
5.00	0.32	2.117	2.125	1.317	1.319
2.00	0.53	1.685	1.671	4.109	4.188
1.00	1.56	1.154	1.005	6.100	5.795
0.50	1.99	1.130	1.154	0.437	0.547

Nevertheless, this contribution is clearly negligible in the study of the vibratory phenomenon as confirmed with data presented in this study. Further demonstration of data quality is given when a statistical analysis of errors and uncertainties is carried out, as shown in the previous paragraph 2.4.1. The following Figures 4.41 through to 4.44 plot the data trend normalized to the values recorded with the reference sensor, while calculated mean values and standard deviations are reported in Tables A.11 through to A.14 in the Appendix, along with the comparison of the recorded signals (Figures A.4 through to A.7).

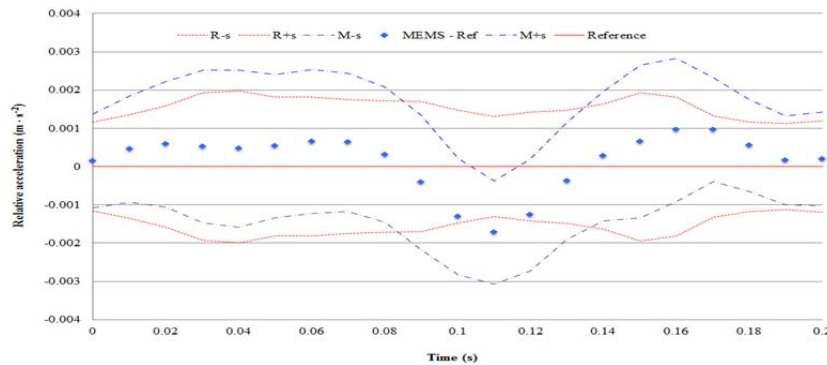


Fig. 4.41 – Comparison of measurement uncertainties normalized to the reference sensor (5 Hz)

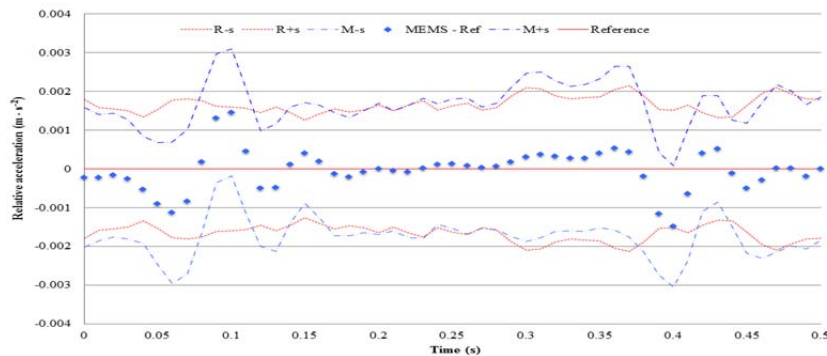


Fig. 4.42 – Comparison of measurement uncertainties normalized to the reference sensor (2 Hz)

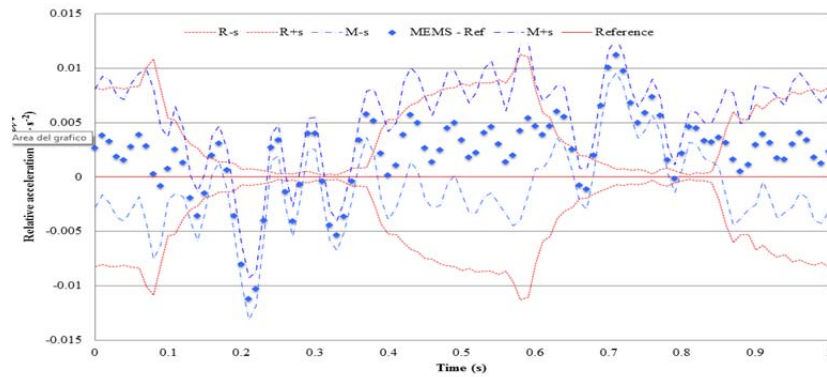


Fig. 4.43 – Comparison of measurement uncertainties normalized to the reference sensor (1 Hz)

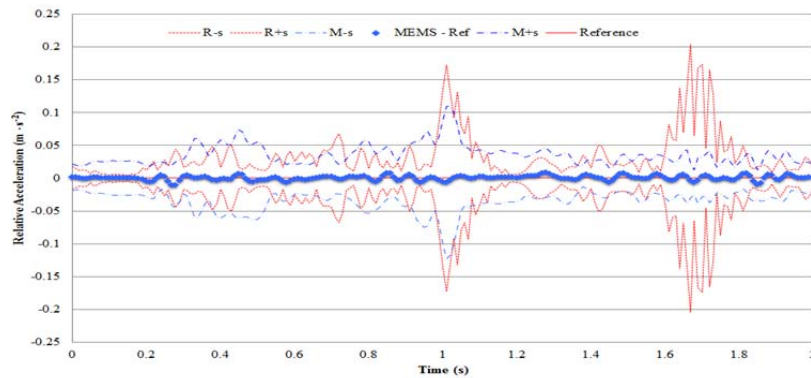


Fig. 4.44 – Comparison of measurement uncertainties normalized to the reference sensor (0.5 Hz)

A substantial correspondence can be observed; in particular, when the 5 and 2 Hz periodic signals are considered, all values measured using the MEMS accelerometer are within the uncertainty interval of the reference sensor. The accuracy decreases when frequency decreases as observed when the 1Hz periodic signal case is studied. Here several data elements are external to the uncertainty interval, but an overall agreement still exists.

3 – Engineering structure experiments for the characterization of ALE's performances

Finally, the wireless MEMS accelerometer system was used to carry out measurement on civil structures to demonstrate ALE efficacy in monitoring vibration of real engineering structures. In particular, vibrational analyses on three different structures have been executed:

- 1) Flow-loop pipeline;
- 2) Pinnacle;
- 3) Pedestrian bridge.

In the first experiment, the MEMS accelerometer system was used to measure the oil flow-induced vibration of a black-steel flow-loop pipeline. This activity was executed as part of an ongoing project at Columbia University in the City of New York – New York City, NY and the aim of the study was to investigate experimentally the correlation between the dynamic behavior of the oil well production tubing and changes in its external pressure. The second consists of a study of the earthquake-induced vibration on a special lab-scale model of one of the stone pinnacles of the Cathedral Church of St. Peter and St. Paul in Washington, DC. To conclude, the third experiment was carried out deploying the sensor on the Streicker Bridge, a pedestrian bridge which spans the Southern edge of Princeton University campus – Princeton, NJ. These tests aimed to demonstrate that the prototype is extremely versatile. It can be used for detecting vibration arising from moving part in industrial fields, for carrying out seismic analyses, eventually being used as alert devices, and for executing typical SHM analyses such as ambient vibration detection and modal identification on large civil structures.

3.1 - Comparative tests on a flow-loop pipeline

This project, founded by a private client at Columbia University, NY, aims to investigate experimentally the dynamic behavior of a scaled loop model of an oil drilling extraction pipe under external changes in pressure. As shown in Figure 4.45, the model is composed of a 3 m black steel pipe (rated to 862 kPa) with a $5.3 \cdot 10^{-2}$ m inside diameter. The pipe was filled with heavy hydraulic oil compliant with DIN 51524-2: 2006-09 [144] and it was moved through the loop using a reciprocating pneumatic diaphragm pump.



Fig. 4.45 – Oil drilling pipeline layout

The studied environment was vastly instrumented using wired, single axes, oil proof, W352C67, accelerometers manufactured by PCB Piezotronics Inc [145]. The sensitivity is $0.01 \text{ V} \cdot \text{m}^{-1} \cdot \text{s}^2$, the bandwidth in the range 0.5 - 6000 Hz, and a noise-density equal to $144.14 \mu \text{ m} \cdot \text{s}^{-2} \cdot \text{Hz}^{-0.5}$ [90]. Its resolution - evaluated using equation [2.23] - is $1.41 \cdot 10^{-2} \text{ m} \cdot \text{s}^{-2}$. The MEMS accelerometer was placed close to one of these sensors, used as a reference sensor for a back-to-back comparison. Figure 4.46 shows the deployment of the two sensors on the flow-loop. It is important to note that the MEMS sensor was secured to the tube using a magnet. This method minimizes attenuation and the effects of resonant interference, while

the wired sensor - because of its small dimension - was attached using epoxy, according to the recommendation provided by the ISO Directive [141].

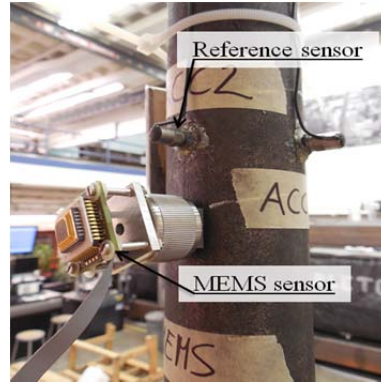


Fig. 4.46 – Setup for flow-loop pipeline test

The tests were run with different flow rates: $8.00 \cdot 10^{-4}$, $1.35 \cdot 10^{-3}$, and $2.00 \cdot 10^{-3}$ $\text{m}^3 \cdot \text{s}^{-1}$ and for each of them a 10-minute measurement was made. The wirelessly transmitted sensor output signals were acquired with a 1 kHz sampling rate using the external DAQ device connected to the receiver board and the reference sensor. The receiver board (not visible in Figure 4.46) was deployed 5 m away from the transmitter board. Instrumenting an oil drilling pipeline is extremely challenging because of wires which can be damaged due to the extraction operations. Having the chance to operate with a wireless sensor may be helpful. Indeed, the only problem would be the deployment of the sensor on the extraction pipe, while the receiver board and the DAQ system may be placed in a safe place away from the danger area. Data was sampled in compliance with ISO 4866:2010 [146] and ISO 21289:2008 [147]. The resultant data were analyzed and processed pursuant to ISO 18431-1:2005 [148] and ISO 1683:2008 [149]. The equivalent acceleration a_{eq} - as defined in the previous paragraph with equation [4.6] - and the acceleration continuous equivalent level L_{eq} of the signals sampled with the two sensors were calculated. In particular it is defined as:

$$L_{eq} = 10 \log \left[\frac{1}{T} \int_0^T \left(\frac{a(t)}{a_0} \right)^2 dt \right] \quad [4.7]$$

where the terms have the meaning already explained and the reference value a_0 is equal to $10^{-6} \text{ m}\cdot\text{s}^{-2}$ [149]. Figures 4.47 to 4.55 plot a segment of the time history measured by the two sensors under each of the three flow rates, its correspondent frequency response by PSD, and a zoomed frequency response around the first mode frequency.

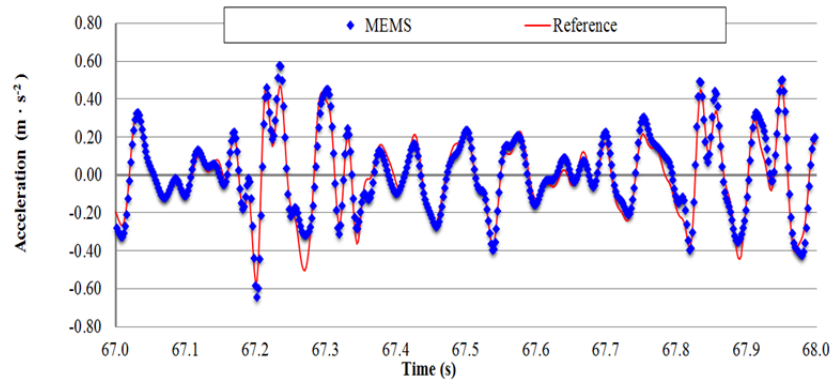


Fig. 4.47 – Comparison of measurements by the two sensors in time domain ($8.00\cdot 10^{-4} \text{ m}^3\cdot\text{s}^{-1}$)

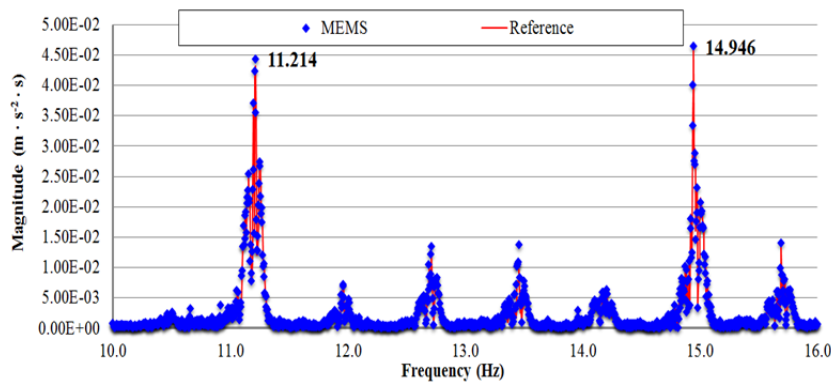


Fig. 4.48 – Comparison of measurements by the two sensors in frequency domain ($8.00\cdot 10^{-4} \text{ m}^3\cdot\text{s}^{-1}$)

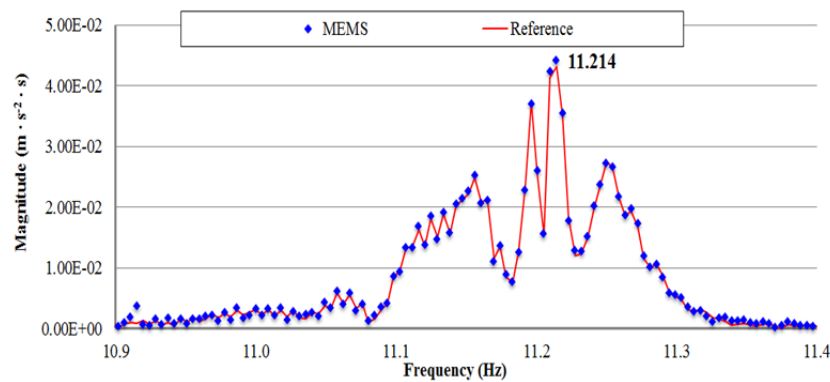


Fig. 4.49 – Detail of the comparison of measurements by the two sensors in frequency domain ($8.00\cdot 10^{-4} \text{ m}^3\cdot\text{s}^{-1}$)

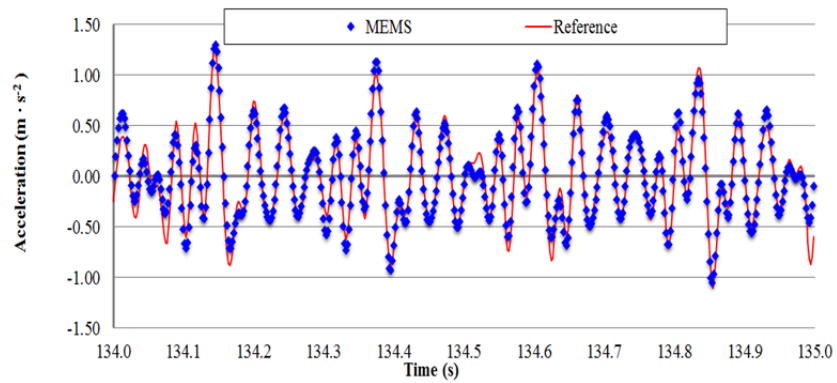


Fig. 4.50 – Comparison of measurements by the two sensors in time domain ($1.35 \cdot 10^{-3} \text{ m}^3 \cdot \text{s}^{-1}$)

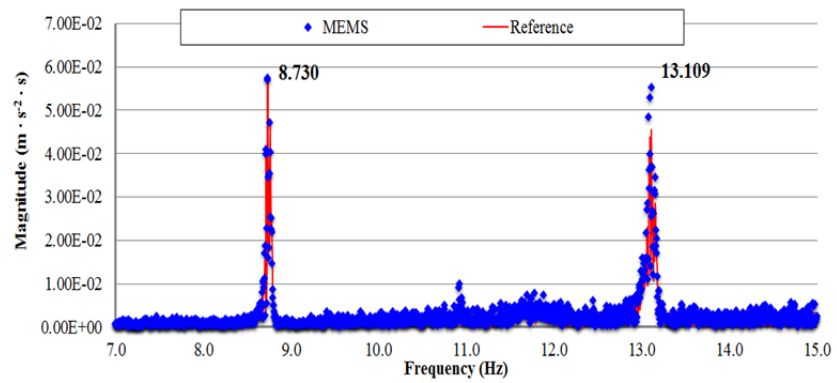


Fig. 4.51 – Comparison of measurements by the two sensors in frequency domain ($1.35 \cdot 10^{-3} \text{ m}^3 \cdot \text{s}^{-1}$)

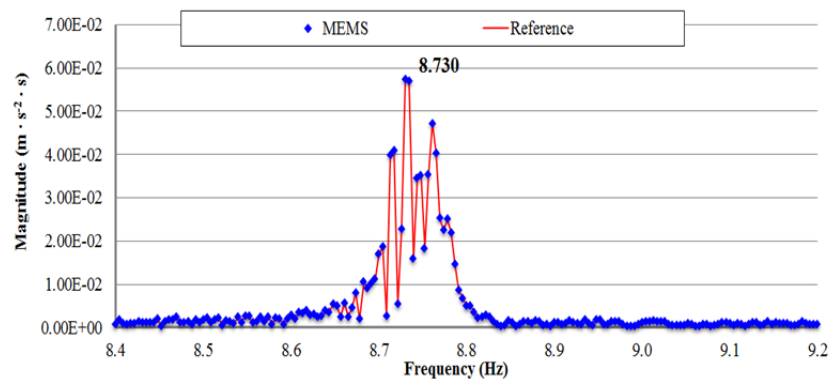


Fig. 4.52 – Detail of the comparison of measurements by the two sensors in frequency domain ($1.35 \cdot 10^{-3} \text{ m}^3 \cdot \text{s}^{-1}$)

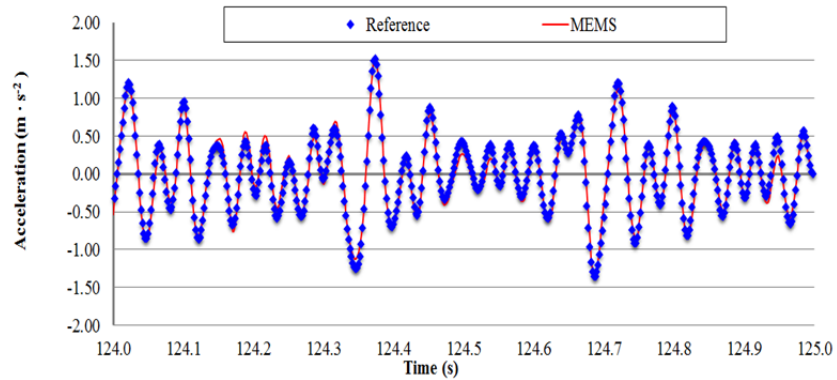


Fig. 4.53 – Comparison of measurements by the two sensors in time domain ($2.00 \cdot 10^{-3} \text{ m}^3 \cdot \text{s}^{-1}$)

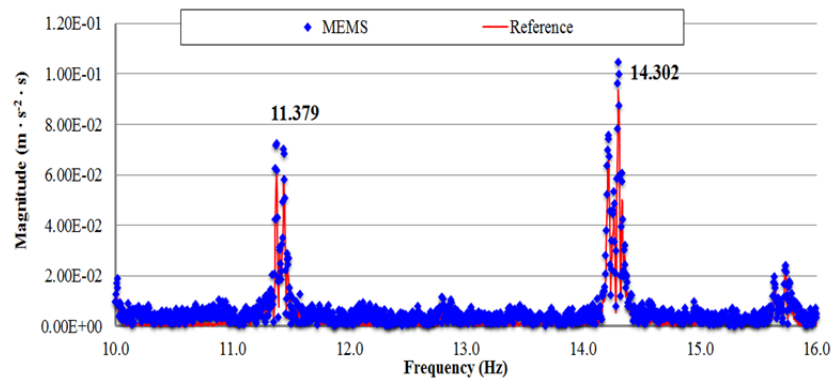


Fig. 4.54 – Comparison of measurements by the two sensors in frequency domain ($2.00 \cdot 10^{-3} \text{ m}^3 \cdot \text{s}^{-1}$)

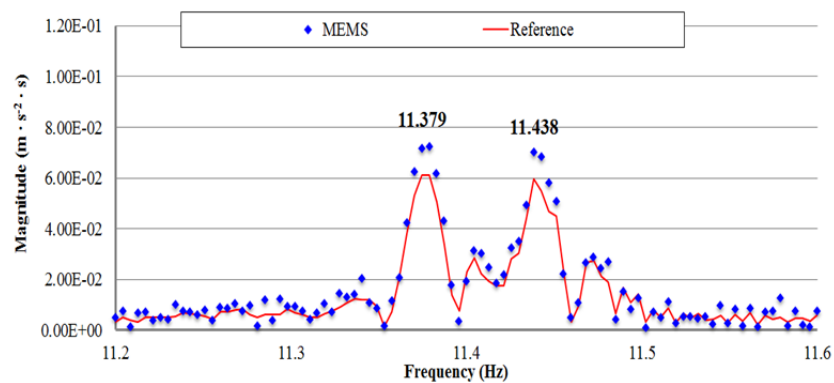


Fig. 4.55 – Detail of the comparison of measurements by the two sensors in frequency domain ($2.00 \cdot 10^{-3} \text{ m}^3 \cdot \text{s}^{-1}$)

For all of the three flow rates there is good agreement, in both time and frequency domains, between the measurements by the MEMS accelerometer system and the reference sensor. Again, the relative error ε_r of the MEMS

accelerometer in comparison with the reference sensor is calculated using equation [4.5] and the results are shown in Table 4.6. The small errors are comparable with those computed in the shaking table tests. Consistent with the observations made in the shaking table tests, the measurement error increases as the first mode frequency decreases from 11.379 Hz (under the $2.00 \cdot 10^{-3} \text{ m}^3 \cdot \text{s}^{-1}$ flow rate) to 8.730 Hz (under the $1.35 \cdot 10^{-3} \text{ m}^3 \cdot \text{s}^{-1}$ flow rate).

Table 4.6 – Summary results for the flow-loop pipeline test

Flow rate	ϵ_r	$a_{\text{eq,ref}}$	$a_{\text{eq,MEMS}}$	$L_{\text{eq,ref}}$	$L_{\text{eq,MEMS}}$	Peak_{ref}	$\text{Peak}_{\text{MEMS}}$	f_{ref}	f_{MEMS}	PSD_{ref}	PSD_{MEMS}
($\text{m}^3 \cdot \text{s}^{-1}$)	(%)	($\text{m} \cdot \text{s}^{-2}$)	($\text{m} \cdot \text{s}^{-2}$)	(dB)	(dB)	($\text{m} \cdot \text{s}^{-2}$)	($\text{m} \cdot \text{s}^{-2}$)	(Hz)	(Hz)	($\text{m} \cdot \text{s}^{-2} \cdot \text{s}$)	($\text{m} \cdot \text{s}^{-2} \cdot \text{s}$)
$8.00 \cdot 10^{-4}$	0.26	0.037	0.039	105.724	105.961	0.485	0.573	11.214	11.214	$4.321 \cdot 10^{-2}$	$4.424 \cdot 10^{-2}$
$1.35 \cdot 10^{-3}$	0.38	0.155	0.170	111.916	112.312	1.284	1.293	8.730	8.730	$5.745 \cdot 10^{-2}$	$5.745 \cdot 10^{-2}$
$2.00 \cdot 10^{-3}$	0.21	0.272	0.290	114.359	114.621	1.516	1.559	11.379	11.379	$6.129 \cdot 10^{-2}$	$7.223 \cdot 10^{-2}$

To be rigorous, the only difference can be observed when very high-amplitude peaks are analyzed. In those cases, signals sampled using the reference sensor have, usually, smaller amplitude if compared to the same value measured by the MEMS sensor. The reason for this behavior could be due to differences in sensitivity. Indeed, MEMS accelerometer sensitivity is one order of magnitude higher than the sensitivity of the wired accelerometers used for instrumenting the pipeline ($0.12 \text{ V} \cdot \text{m}^{-1} \cdot \text{s}^2$ compared to $0.01 \text{ V} \cdot \text{m}^{-1} \cdot \text{s}^2$). Nevertheless, when an evaluation of the continuous vibration equivalent level L_{eq} and of the equivalent acceleration a_{eq} is carried out, an excellent agreement is observed. Thus, it is possible to conclude by stating that no relevant differences exist when measures are carried out with one or the other of the systems. The same conclusion can be made when a critical analysis of the frequency response is performed. The data supplied by the wireless sensor board match very well with those given by the traditional wired accelerometer used as a reference sensor. The equivalency can be observed regarding the value of the solicited frequencies and their magnitude as well. Furthermore, the frequency response plots show the capability of the wireless MEMS accelerometer in measuring the closely coupled modes of vibration. It is observed that the MEMS accelerometer system can detect changes

in the pipeline's dynamic behavior under changing operational conditions (i.e.: flow rate). Therefore, it is possible to conclude by stating that the prototype has the right characteristics for being used as a detection device during industrial activities. Since the signal is wireless transmitted, it would be possible to achieve a remote control system to constantly check the operational conditions of the structure being tested.

3.2 - Comparative tests on a stone pinnacle

The second test consists of another comparison with two sensors, a wired IEPE accelerometer and a laser displacement sensor, made during a seismic test carried out in Carleton Laboratory at Columbia University, NY. The test aimed to simulate an earthquake to see if a 2500 Kg, 3 m high pinnacle model from the Cathedral Church of St. Peter and St. Paul (Washington National Cathedral) could withstand the vibrations similar to the 5.8-magnitude tremor that struck the District of Columbia area in August 2011 [150]. The church, a neo-gothic style building whose construction was begun in 1907 and finished in 1990, sustained damage to its structure during the earthquake: several pinnacles twisted out of alignment or collapsed entirely; many of the pinnacles' finial stones broke off; carvings were damaged; and falling masonry punched holes through the metal-clad roof. A newly designed pinnacle, reinforced with a steel rod, was tested to check if the applied structural modification could resist seismic motions. Figure 4.56 shows the model of the pinnacle tested on the Carleton Laboratory's shaking table. The pinnacle was instrumented with several sensors, as can be observed from Figure 4.57. It is observed that both sensors are connected to an L-shaped piece of metal attached to the top of the pinnacle using a thick layer of double-sided tape compliant with recommendations provided by the ISO Directive [141]. The MEMS sensor is connected to the metal support by means of a metal stud, whereas the reference sensor is mounted using a magnet.



Fig. 4.56 – Pinnacle model from Washington National Cathedral

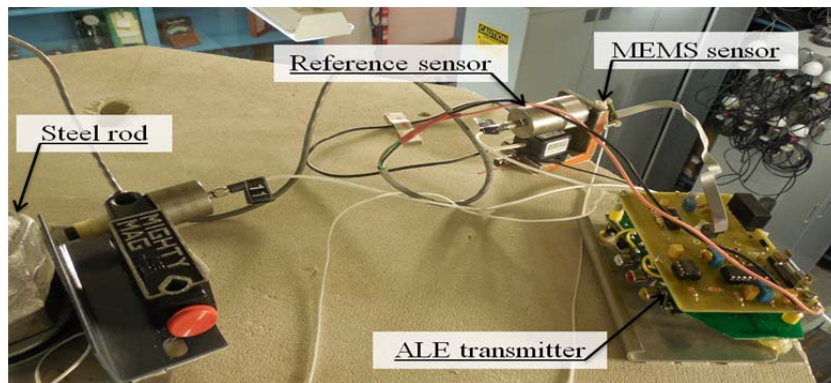


Fig. 4.57 – Pinnacle top view showing sensors location

The system was subjected to uniaxial acceleration time history input created from readings taken from the Corbin, VA seismograph station. In particular, the example shown in this study refers to a simulated earthquake having peak ground acceleration (PGA) equal to $1.562 \text{ m}\cdot\text{s}^{-2}$ (50% of Corbin's record), whose main features are listed in Table 4.7. Earthquake time-history and frequency response (recorded by the accelerometer embedded in the shaking table) are plotted in Figure A.8 and A.9 in the Appendix.

Table 4.7 – Earthquake input features

Duration	PGA	I_A	f_1	f_2	f_3
(s)	($m \cdot s^{-2}$)	($m \cdot s^{-1}$)	(Hz)	(Hz)	(Hz)
23.000	1.562	0.206	0.759	1.027	1.612

The quantity I_A that appears in the table is the Arias Intensity, a measure of the strength of a ground motion, which can be evaluated as:

$$I_A = \frac{\pi}{2 \cdot g} \int_0^T a^2(t) dt \quad [4.8]$$

During the test, the wirelessly transmitted sensor output signals were acquired with a 100 Hz sampling rate using the external DAQ device connected to the receiver board and the reference sensor. The wired accelerometer, used as reference, was again the model 393B04, manufactured by PCB Piezotronics Inc. [92]. In addition, a displacement reading of the pinnacle's top portion was taken using a high accuracy laser variable displacement transducer (LVDT) manufactured by Keyence and deployed at 0.3 m away from the pinnacle and visible in the top left corner of Figure 4.56. The recorded displacement time-history (shown in the Appendix as Figure A.10) was derived twice to obtain an acceleration time-history whose characteristics are listed in Table 4.8 and plotted in Figures A.11 and A.12. Figures A.13 through to A.16, (in the Appendix) plot the whole time and frequency domains responses recorded with the two sensors, while the following Figures 4.58 and 4.59 show a zoomed time-history before the beginning of the earthquake (low-amplitude) and at its end (high-amplitude). In particular, Figure 4.58 refers to vibrations produced by the shaking table supporting machineries (e.g.: pump, oil circuit, etc.). These can be considered as ambient vibrations characterized by low-amplitude (10^{-2} - 10^{-1} $m \cdot s^{-2}$) and can be used for evaluating the natural frequency of the pinnacle (f_4). On the other hand, Figure 4.59 refers to the earthquake and to high-amplitude vibrations (10^0 $m \cdot s^{-2}$). In particular, correspondence in the frequency domain can be observed in the earthquake characteristic frequencies (f_1, f_2, f_3), as well as in the natural frequency of the pinnacle (f_4).

Table 4.8 – Summary results for the pinnacle comparative test

Sensor	PGA	I_A	f_1	PSD ₁	f_2	PSD ₂	f_3	PSD ₃	f_4	PSD ₃
(-)	($m \cdot s^{-2}$)	($m \cdot s^{-1}$)	(Hz)	($m \cdot s^{-2} \cdot s$)	(Hz)	($m \cdot s^{-2} \cdot s$)	(Hz)	($m \cdot s^{-2} \cdot s$)	(Hz)	($m \cdot s^{-2} \cdot s$)
LVDT	4.960	4.287	0.745	$4.15 \cdot 10^{-1}$	1.031	$3.55 \cdot 10^{-2}$	1.602	$9.65 \cdot 10^{-2}$	17.930	$1.015 \cdot 10^{-2}$
Reference	4.517	4.990	0.746	$5.87 \cdot 10^{-1}$	1.031	$0.67 \cdot 10^{-1}$	1.603	$1.06 \cdot 10^{-1}$	17.932	$1.126 \cdot 10^{-2}$
MEMS	4.518	4.886	0.746	$5.63 \cdot 10^{-1}$	1.031	$0.70 \cdot 10^{-1}$	1.603	$1.04 \cdot 10^{-1}$	17.932	$1.130 \cdot 10^{-2}$

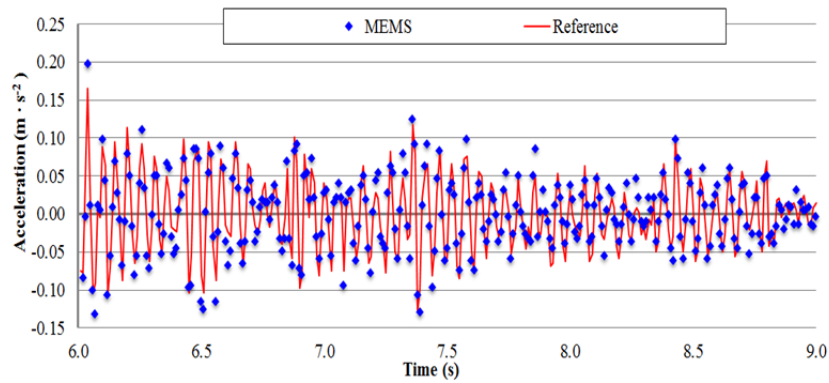


Fig. 4.58 – Detail of the time-history comparison (low-amplitude)

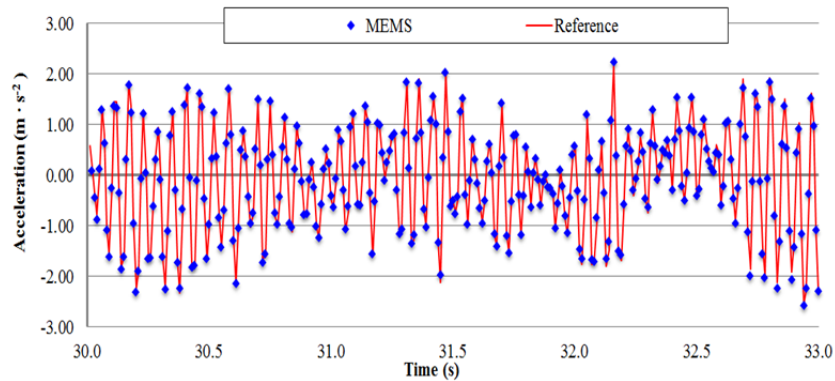


Fig. 4.59 – Detail of the time-history comparison (high-amplitude)

When data obtained from the MEMS accelerometer system are compared with those obtained from the laser displacement sensor, it can be observed that results only partially match. Despite an overall good agreement, the PGA evaluated from MEMS readings is smaller than that evaluated from the LVDT. On the contrary, the Arias Intensity I_A results higher. The relative errors committed are equal to -9.78% and 12.26% respectively. Analogously, when frequency responses are considered, a slight difference can be observed. In particular, the first three

frequencies match with good accuracy, while their magnitude does not. Magnitudes evaluated from data recorded with the ALE are higher than those evaluated deriving the displacement signal twice (on average 27.59%). These differences may be due to the fact that the acceleration time-history from the LVDT sensor has been analytically derived from the displacement records. The acceleration time history is not experimentally evaluated; therefore, errors may arise during the derivative process.

Indeed, when data evaluated using the MEMS accelerometer system are compared with data recorded with an IEPE accelerometer (Reference), an excellent match is observed. The PGA and the Arias Intensity I_A values are basically the same (relative errors equal to 0.02% and -2.08% respectively). This means that the prototype can detect the peak acceleration acting on the system and the incident energy as well, with accuracy comparable to that of a high sensitivity, wired, seismic accelerometer. When analyses in frequency domain are carried out, the same conclusions can be made. The signal detected using the ALE has the exact same frequencies as those detected using the reference sensor. Even the calculated magnitude values are close to each other (average relative error equal to 0.49%). Once more, it is observed that the MEMS accelerometer system can detect vibration with frequency around 1Hz with the same accuracy as a traditional accelerometer. It is a further demonstration of the qualities of the built prototype.

To conclude, this test shows that the ALE can be used for seismic monitoring of civil structures as well. This may lead to the development of a network made of several sensors for controlling the real time dynamic response of art works and monuments. It is clear how a wireless, non-invasive, monitoring system is preferable to a wired one. This system, if further developed, may allow for controlled maintenance of the state of aging structures (e.g.: churches, monuments, sculptures, etc.) without interfering with their functionalities and architectural characteristics.

3.3 - Vibration analyses of a pedestrian bridge

In the last test presented, the ALE was used to carry out a vibrational analysis on a pedestrian bridge. Test aims were to control whether or not the MEMS accelerometer system can be used for achieving traditional SHM analyses for ambient vibration detection and modal identification. The structure tested was the Streicker Bridge, a 104 m deck-stiffened arch bridge, located on the Princeton University campus in Princeton, NJ. It has a main span and four approach legs. The legs are horizontally curved and supported by steel columns. The shape of the main span follows this curvature, resulting in a varying cross-section, while the leg cross-section is nearly constant. The arch and columns are weathering steel while the decks are reinforced post-tensioned concrete [151]. A picture of the bridge is shown in Figure 4.60.



Fig. 4.60 – Streicker bridge at Princeton University campus – Princeton, NJ



Fig. 4.61 – Test setup and the ALE deployment

The ALE transmitter was deployed in the middle of the southeast leg, while the receiver along with the DAQ board were placed under the deck at road level. Figure 4.61 shows the mutual position of the transmitter and receiver board and a detail of the ALE deployment on the bridge deck. Three different tests were carried out: the first consisted of a quasi-static test using a truck as moving static load as shown in Figure 4.62.



Fig. 4.62 – Quasi-static test setup

The truck, with a total load of nearly 40 kN, was positioned sequentially at different locations along the southeast approach leg and measurements were taken continuously during the vehicle's moving phases and the stops. The second test consisted of a group of eight people jumping, in correspondence of one quarter of the bridge's southeast approach ramp total length, at approximately 3 Hz for 30 s and then stopping, whereas the last test consisted in a group of eight people running at different random frequencies on the same approach leg. This study is based on the principle that the natural frequencies of a bridge can be determined with classic tests such as a shaker test or an impact test that introduce free vibrations in the structure. Nevertheless, by exciting the structure with ambient vibrations, the frequencies found would be approximately equal to the natural frequencies of the bridge with the advantage of the simplicity of the tests. During the test, the wirelessly transmitted sensor output signals were acquired with a 30 Hz sampling rate using the external DAQ device connected to the receiver board.

The following Figures 4.63 and 4.64 plot a detail of the time and frequency domains analyses of the solicitations evaluated during the quasi-static test (the complete time history record is plotted in the Appendix in Figure A.17). It is observed that the PGA has extremely low-amplitude and, in general, it is smaller than $0.02 \text{ m}\cdot\text{s}^{-2}$ (Root Mean Square, RMS equal to $1.21\cdot 10^{-2} \text{ m}\cdot\text{s}^{-2}$). Despite the fact that these amplitudes are low, the MEMS accelerometer system can clearly identify them. Furthermore, the frequency domain analysis clearly highlights the value of 3.079 and 3.753 Hz as the first two natural frequencies of the bridge.

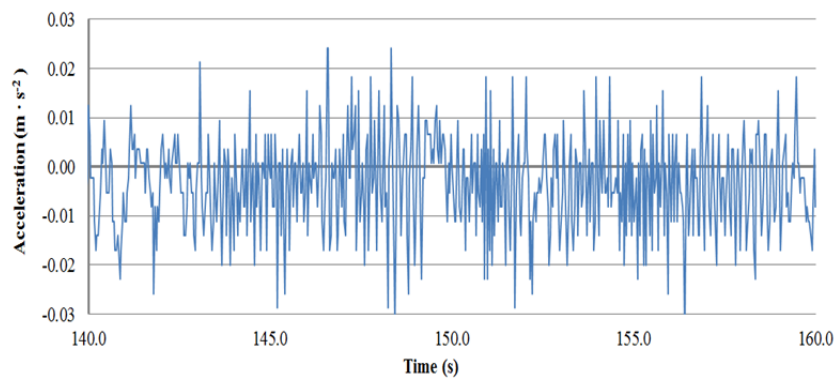


Fig. 4.63 – Detail of the time-history recorded during the quasi-static test

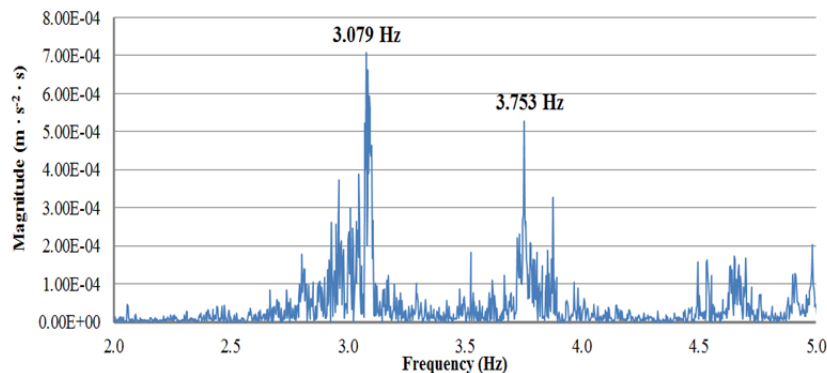


Fig. 4.64 – Detail of the frequency domain analysis recorded during the quasi-static test

In the second test, a group of eight people was left jumping, in correspondence of one quarter of the bridge's southeast approach ramp total length, with a frequency of approximately 3 Hz. The people kept jumping for nearly 30 s and then suddenly stopped. When the people stop moving, the input simulates a damped free vibration system, which, according to equation [1.28] has to oscillate

at its natural frequency ω_n before motion will die out. This test can be used for evaluating the damping factor of the system through equation [1.37]. The following Figures 4.65 and 4.66 plot the time and frequency domains responses recorded with the ALE for the above-described test. In Figure 4.65, the first part of the signal is clearly intelligible (0 through 30 s) when people jump on the bridge, and a second part (34 s on) when the motion starts to decrease until it dies out. On the other hand, from the frequency domain response, two frequency values are observed. 2.999 Hz is the frequency of the input solicitations (jump), while 3.069 Hz is the natural frequency of the bridge.

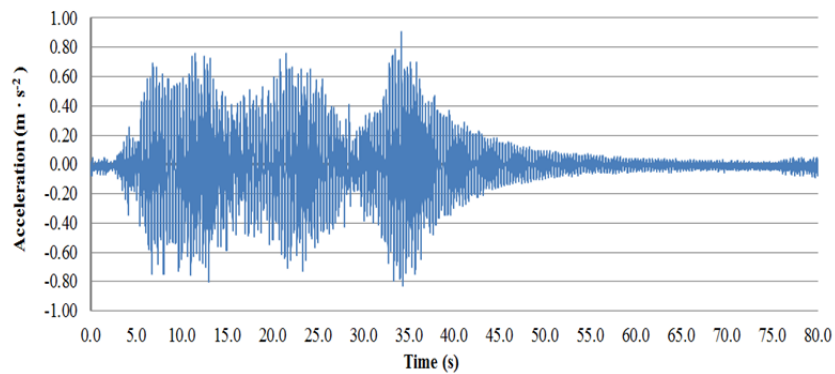


Fig. 4.65 – Detail of the time-history recorded during the 3 Hz-input solicitation test

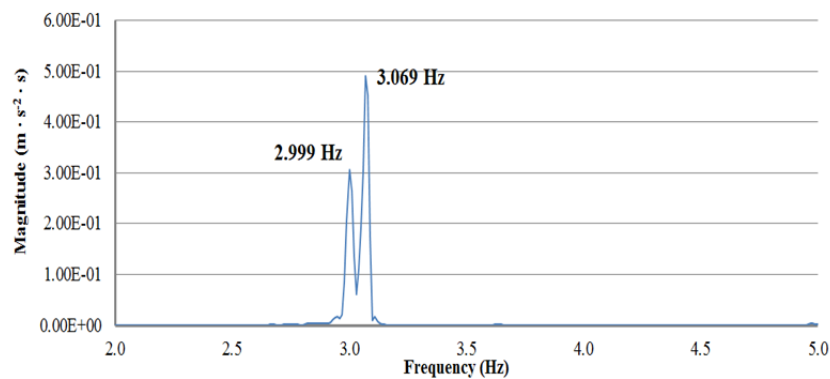


Fig. 4.66 – Detail of the frequency domain analysis recorded during the 3Hz-input solicitation test

To make sure that the measured frequencies are indeed the natural frequencies of the bridge and not the imposed frequencies, random running was also performed. During this experiment, the same group of eight people of the previous test was left running between the main span-ramp connection point and

half of the leg total length for nearly 3 minute. The results presented in Figures 4.67 and 4.68 show that the first two modes are the ones detected by the first two tests.

Since the tests were carried out only once, and the experiment conditions are unique and hardly repeatable, no statistical analyses can be carried out at this time. Data obtained are compared with results obtained from a literature review of previous studies carried out on the Streicker bridge [152 – 153].

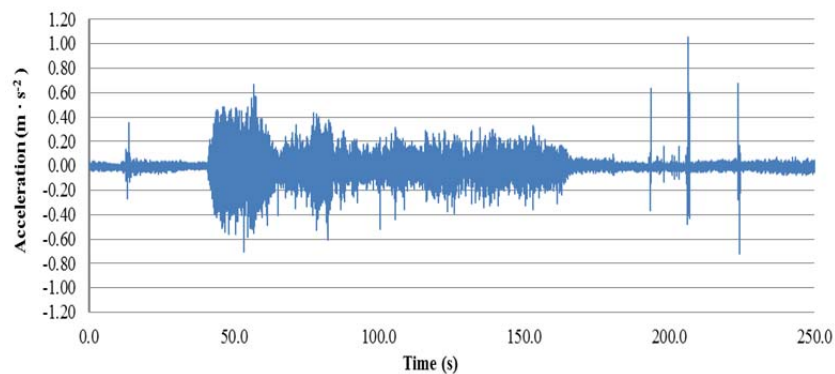


Fig. 4.67 – Detail of the time-history recorded during the random run-input solicitation test

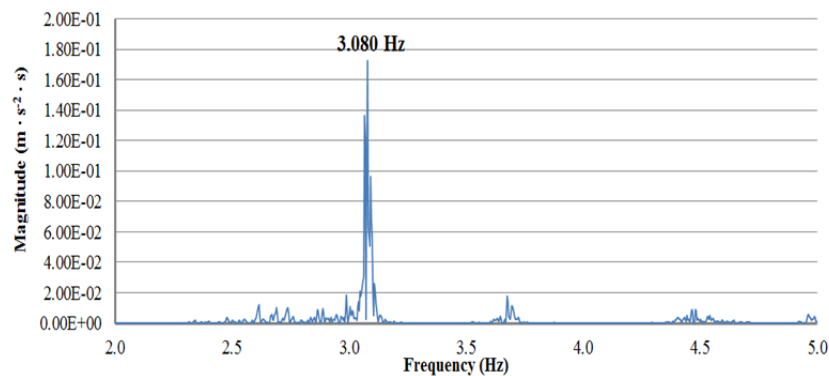


Fig. 4.68 – Detail of the frequency domain analysis recorded during the random run-input solicitation test

Frequencies measured with the ALE (3.080 and 3.753 Hz) are close to those evaluated in previous studies of the bridge, both experimentally (3.11 and 3.72 Hz) and analytically through a Finite Element Model (3.22 and 3.92 Hz). Table 4.9 lists a summary of the results obtained during the carried out tests together with results coming from a literature review of the Streicker Bridge.

Table 4.9 – Summary results of the pedestrian bridge test

Test	f ₁	f ₂
(-)	(Hz)	(Hz)
Literature [153]	3.11	3.72
FEM [153]	3.22	3.92
Quasi-static	3.08	3.75
3 Hz-Input	3.07	-
Random-Input	3.08	3.75

It can be observed that the frequencies evaluated from the record made using the ALE are close to those evaluated in previous studies of the bridge, both experimentally (3.11 ± 0.06 and 3.72 ± 0.06 Hz) and analytically through a Finite Element Model (3.22 and 3.92 Hz). The relative errors committed, equal to -0.97% and 0.80% respectively, are negligible in traditional engineering practices and similar to the other relative errors evaluated in this study for the prototype. Indeed, they could be due to the fact tests were carried out in different periods (i.e.: seasons, years); therefore, change in dynamic response may be due to different boundary conditions (e.g.: temperature, concrete assessment, concrete aging, etc.). Nevertheless, if the standard deviation ($\sigma = \pm 0.06$ Hz) associated to results obtained from the literature review was considered [153], the measurement interval of tolerance for the two frequencies would become [3.05 - 3.17 Hz] and [3.69 - 3.81 Hz] respectively. The results found with the ALE are within those intervals; therefore, a perfect match can be observed. Since data obtained with the ALE are the same of those obtained in other studies when different typologies of sensor were used, it demonstrates that the ALE can be used as wireless alternative to traditionally used sensors for carrying out vibration monitoring of large-sized structures without accuracy loss.

SUMMARY AND DISCUSSION

Wireless MEMS sensors suffer from low measurement accuracy when applied to monitor low-amplitude ambient vibration of large-sized civil engineering structures that often have low natural frequencies. To overcome this problem, this study presents the Acceleration Evaluator (ALE), a prototype of a new high-sensitivity, low-noise, wireless, MEMS-based accelerometer sensor board using low-cost, frequency-modulated analog RF transmission. The main goal of this prototype is to enable the measurement of accelerations with a precision comparable to that supplied by wired IEPE accelerometers even at very low-frequencies and low-amplitude, where other MEMS-based systems have shown their limitations. Analysis of vibration is one of the thorniest issues in the field of SHM. Indeed, natural frequencies in large civil structures are generally in the order of 10^{-1} to 10^1 Hz, amplitude is in the order of 10^1 to 10^{-2} $\text{m}\cdot\text{s}^{-2}$, and currently used MEMS-based systems cannot accurately detect vibrations having characteristics below a certain threshold. This is because of technical limitation embedded in the system (e.g.: low-resolution ADCs, high-noise sensors, etc.). It is demonstrated that the built MEMS accelerometer system can detect vibration having very low-frequency (below 1 Hz) and low-amplitude (in the order of 10^{-2} $\text{m}\cdot\text{s}^{-2}$).

The study begins with the description of the prototype. The ALE consists of a transmitter board and a receiver board. The transmitter board is equipped with a MEMS accelerometer, a V/F converter and a wireless RF transmitter, whereas the receiver board contains an RF receiver and a F/V converter for demodulating the signal. It should be observed that the Acceleration Evaluator system embeds one sensor only. A SiFlex 1600SN.A accelerometer has been selected as transducer for the transmitter board. It is a single-axis MEMS-based accelerometer, with low

noise-density, a wide linear output range and frequency response suitable for inertial, tilt, vibration, as well as seismic analyses.

One of the main characteristics of MEMS-based accelerometers is that they can be used for measuring static accelerations and tilt angles. For this reason, a unit for removing DC coupled to gravity is designed and embedded on-board. It permits correction of the sensor's output tension value to remove the DC signals associated with the sensor orientation. By means of this feature, it is possible to deploy the sensor horizontally, vertically or equivalently in any other position and correct the tension value in order to be sure that the given one corresponds to a null acceleration by simply turning a screw.

Furthermore, another difference between the ALE and other systems is that no computational operations are carried out on-board. In the proposed system, raw data are downloaded to an external laptop or computer to be post-processed. Even though one of the basic ideas of SHM is to transmit essential information only, the ALE moves in the opposite direction. Many other engineering sectors need copious data to determine the occurrence of possible critical scenarios; therefore, limiting the quantity of data transmitted may reduce their utility. Transmitting a large amount of data is definitely more power-expensive, but may result in more accurate analyses since these tasks could be carried out using more powerful microprocessors.

Nevertheless, the main difference introduced on the built Acceleration Evaluator compared with the previous systems, is the used signal conversion. The ALE does not embed any ADC. Considering the accelerometer resolution, installing an ADC with a resolution lower than 24-bit would nullify the decision to use such a sensitive accelerometer. Yet such an accurate ADS is extremely power-demanding and it is not well suited for low-power applications. To overcome this difficulty, the ALE converts the sensor output voltage to a FM signal using an AD650 V/F converter instead of conventional ADCs. Since the selected converter does not consider the amplitude of the signal (which degrades with transmission distance) but rather its frequency only, the decision to use this

device allows for signal which is more immune to noise. In addition, to provide a stable power supply to compensate for the gradual decrease in the battery power output over time, a DC/DC is embedded onboard. Furthermore, to conclude, a low-cost, four-channel, 2.4 GHz ISM, audio-video, omnidirectional antenna is connected to the sensor board. The insertion of an RF transmitter allows wireless data transmission, a feature that frees technicians from cable limitation and allows for an easier deployment of the system.

Once the prototype had been built, intensive laboratory tests and experiments on real-world engineering structures were carried out to demonstrate whether or not it is useful to achieve resolution necessary for vibrational analysis purposes. Laboratory tests consisted of static calibration testing, study regarding the effects of battery residual charge on ALE behavior, evaluation of the maximum RF transmission distance, and comparative dynamic tests with wired, high-sensitivity, IEPE accelerometers.

The first of these carried out using an angle meter machine, used the property of the MEMS-based accelerometers to be used as tilt angle detector. This test allowed evaluation of the transmitter board's calibration equation, which correlates the sensor's output tension values to well-known acceleration values. Data analyses confirm the linear relation between the acceleration and the sensor output voltage with a high correlation; furthermore, the ALE calibration equation is similar to that provided by the manufacturing company, a demonstration that no modifications occur due to the electronic elements placed on the transmitter board.

Tests to evaluate the transmitter board behavior when the battery runs out of power are required in order to check the utility of the embedded DC/DC converter. Many other systems, designed without a battery voltage up converter, have shown that an unstable battery power supply voltage would affect their performances. Instead, the Acceleration Evaluator's output values are constant and remain stable despite the battery level. Decreasing battery voltage does not influence the sensor output as with previous sensor boards. This means that the

DC/DC converter neutralizes the effect of battery residual charge. This feature is quite expensive in terms of board energy-consumption (125 mA), but it allows more stable data and then more accurate measurements. Furthermore, it is observed that the SF1600 output stays constant and then suddenly drops (below 7 V). This means that the system is able to operate up to a specific voltage and then it suddenly turns off. Tests have proved that the maximum fluctuation due to battery charge decrease is in the order of $10^{-3} \text{ m}\cdot\text{s}^{-2}$, a value comparable to SF1600 resolution.

One of the main strengths of the MEMS accelerometer system is that signal can be transmitted wirelessly. In order to evaluate the wireless signal transmission capability of the prototype sensor system, the above calibration tests were repeated by placing the receiver board at different distances (5, 10, 15, 20, 25, and 30 m) away from the transmitter board. It is observed that the quality of the wirelessly transmitted signal decreases, as the distance between the transmitter and the receiver increases. When the distance is equal to 5 m, an excellent agreement is observed between the data directly measured at the accelerometer output and those obtained at the receiver board. On the other hand, when the two boards are distanced 30 m apart, the wirelessly transmitted signals become less accurate. This problem can be observed when a dynamic test, exciting the accelerometer with a 100 Hz sinusoidal wave, is carried out. The test, carried out in two different operational conditions (indoor and outdoor), showed that the signal remains stable for distances between the two boards of less than 25 m, whereas the signal is distorted when the distance is 30 m, as confirmed by the relative error soaring from 0.42% to 7.26%. The performance further deteriorates in the outdoor environment, where relative errors soar from 1.08% at the 5-meter distance to 9.17% and 18.67%, respectively, at the 15-meter and 30-meter distances from the receiver board. These tests have demonstrated that, to date, the ALE maximum transmission distance depends on the surrounding environment. Interference with the surrounding RF noise causes significant concerns about the quality of signals. The massive presence of several Wi-Fi networks and RFs is a

clear problem for the selected antenna. The receiver cannot recognize the signal sent by the sensor board and thus it collects signals coming from different sources.

To conclude the protocol of laboratory tests, a comparison with a reference wired accelerometer was carried out. This consists of measuring low-frequency, well-known acceleration inputs (sinusoidal and periodic waves), with both the MEMS accelerometer system and the wired IEPE sensor. This test aims to demonstrate that the ALE behaves as a wired accelerometer even at very low frequencies (far below 1 Hz), overcoming the limitations highlighted by other commercial and academia-built systems. Tests showed a good agreement, both in time and frequency domains, between the data measured by the reference sensor and those by the MEMS sensor and obtained from the receiver board. To be accurate, it is observed that the measurement error increases as the vibration frequency decreases. Overall the relative error is less than 1% (sinusoidal wave input) and 2% (periodic wave input), and, thus, the MEMS sensor achieved performance comparable to that of the reference sensor, demonstrating its capability in measuring low-frequency vibration, with frequency as low as 0.2 Hz with a suitable accuracy for normal engineering practices. Furthermore, it is of interest to notice that the equivalent accelerations supplied with the reference sensor are slightly higher than those supplied with the MEMS one. However, this difference is always smaller than 0.40% (0.20 Hz case). On the contrary, signal magnitudes evaluated from data recorded with the MEMS accelerometer system result slightly higher than those computed from data sampled with the reference sensor. However, these differences can be considered as negligible for normal engineering practices.

After these tests, a number of experiments were carried out to demonstrate ALE efficacy in monitoring vibration of real engineering structures and practical cases of study. In the first experiment the MEMS accelerometer system was used to measure oil flow-induced vibration of a flow-loop pipeline. The second consisted of a study on the earthquake-induced vibration on a special lab-scale

model of one of the stone pinnacles of the Cathedral Church of St. Peter and St. Paul in Washington, DC. To conclude, the third experiment was carried out deploying the sensor on the Streicker Bridge, a pedestrian bridge which spans at the Southern edge of Princeton University campus, Princeton, NJ. These tests aimed to demonstrate that the prototype is extremely versatile. It can be used for detecting vibration arising from moving parts in industrial fields, for carrying out seismic analyses and eventually as alert devices, and for executing typical SHM analyses such as ambient vibration detection and modal identification on large civil structures.

The flow-loop pipeline test – independently of the flow rate passing in the oil tubing, showed a good agreement, in both time and frequency domains, between the measurements by the MEMS accelerometer system and the reference sensor. The small errors committed were comparable with those computed in the previous tests. In addition, consistent with the observations made in the shaking table tests, the measurement error increases as the first mode frequency decreases. Furthermore, this test proved the capability of the wireless MEMS accelerometer in measuring the closely coupled modes of vibration.

During the second test, seismic analyses were carried out from data sampled by the MEMS-based accelerometer and the sensors used as reference. The information regarding the PGA and the Arias Intensity computed with the different measuring systems showed errors smaller than 2%, demonstrating, once more, the reliability of the built prototype in achieving high standards for the seismic monitoring of structures. In particular, the ALE demonstrated the possibility of detecting vibrations with frequency below 1 Hz (i.e.: 0.746 Hz) with the same accuracy as sensors built for seismic monitoring purposes only.

To conclude, the test carried out on the Streicker Bridge confirmed the quality of the Acceleration Evaluator to be used as a device for ambient vibration detection and modal identification of large civil structures. Despite the different load and input conditions applied to the bridge (quasi-static load, sinusoidal input, and random input), the MEMS accelerometer system detected the amplitude of

very small vibration (in the order of $10^{-2} \text{ m}\cdot\text{s}^{-2}$), which led to modal identification of the natural frequencies of the bridge equivalent to those evaluated in previous studies and using FEM models.

The Acceleration Evaluator demonstrated its accuracy in measuring vibration relevant to civil and mechanical engineering structures, including those of low frequency (up to 0.2 Hz) and low amplitude (in the order of $10^{-2} \text{ m}\cdot\text{s}^{-2}$). The system showed reliability under draining battery power supply too. The only weakness highlighted in the study consists of the wireless RF antenna performance. Tests conducted revealed the necessity of reducing RF interferences over long-distance wireless transmission, which may reduce the accuracy of the measurement. One of the future ALE developments will be the identification of a more cost-effective transmission system, more immune to noise and interference especially in open and large areas. Several solutions have already been researched (e.g.: Zigbee, Arduino, AdeniusRF, etc.) to improve transmission range and accuracy. In addition, a different wireless RF antenna would allow powering of the transmitter board with a power supply different from $\pm 12 \text{ V}$. This may permit use of a different battery package, smaller than the one already used, which means a more compact and easy to deploy transmitter board. Another development would be the possibility of using more than one transmitter board with the same receiver board. Codifying the transmitted signal would make it possible to transmit data coming from different sensor boards to one central receiver and acquisition board.

Once all these problems are optimized and solved, it will be possible to miniaturize the transmitter board from its present dimensions to a few square centimeters and made it more suitable for deployment on civil structures and parts of machinery. Results provided by this analysis are extremely encouraging and lead one to presume a bright future for this device, if it can be developed further.

APPENDIX

Table A.1 – Calibration test data

α	α	a	Output	σ
(rad)	($^\circ$)	($\text{m}\cdot\text{s}^{-2}$)	(V)	(10^{-3} mV)
0	0	9.806	-0.362	8.262
$1/36\pi$	5	9.769	-0.368	8.266
$1/18\pi$	10	9.657	-0.374	8.271
$1/12\pi$	15	9.472	-0.399	8.193
$1/9\pi$	20	9.215	-0.424	8.225
$5/36\pi$	25	8.887	-0.468	8.175
$1/6\pi$	30	8.492	-0.512	8.125
$7/36\pi$	35	8.033	-0.569	8.225
$2/9\pi$	40	7.512	-0.626	8.175
$1/4\pi$	45	6.934	-0.698	8.366
$5/18\pi$	50	6.303	-0.771	8.556
$11/36\pi$	55	5.624	-0.855	8.284
$1/3\pi$	60	4.903	-0.938	8.012
$13/36\pi$	65	4.144	-1.034	7.554
$7/18\pi$	70	3.354	-1.129	7.964
$15/36\pi$	75	2.538	-1.232	7.860
$2/9\pi$	80	1.703	-1.335	7.756
$17/36\pi$	85	0.855	-1.437	7.797
$1/2\pi$	90	0.000	-1.540	7.838
$19/36\pi$	95	-0.855	-1.647	7.913
$5/9\pi$	100	-1.703	-1.755	7.987
$7/12\pi$	105	-2.538	-1.860	8.225
$11/18\pi$	110	-3.354	-1.966	8.714
$23/36\pi$	115	-4.144	-2.058	8.174
$2/3\pi$	120	-4.903	-2.151	7.633
$25/36\pi$	125	-5.624	-2.239	7.594
$13/18\pi$	130	-6.303	-2.327	7.554
$3/4\pi$	135	-6.934	-2.405	8.225
$14/18\pi$	140	-7.512	-2.483	7.379
$29/36\pi$	145	-8.033	-2.546	7.374
$5/6\pi$	150	-8.492	-2.610	7.370
$31/36\pi$	155	-8.887	-2.661	8.225
$8/9\pi$	160	-9.215	-2.712	7.471
$11/12\pi$	165	-9.472	-2.741	7.364
$17/18\pi$	170	-9.657	-2.770	7.257
$35/36\pi$	175	-9.769	-2.783	7.319
π	180	-9.806	-2.796	7.380

Table A.2 – Effect of battery residual charge test data

Battery voltage	Sensor output	σ	Battery voltage	Sensor output	σ
(V)	(V)	(10^{-3} mV)	(V)	(V)	(10^{-3} mV)
12.5	-0.343568	0.84	9.4	-0.343487	1.40
12.4	-0.343535	0.76	9.3	-0.343545	1.53
12.3	-0.343586	0.78	9.2	-0.343568	1.40
12.2	-0.343589	1.37	9.1	-0.343596	1.41
12.1	-0.343509	1.41	9.0	-0.343567	1.37
12.0	-0.343486	1.38	8.9	-0.343576	1.37
11.9	-0.343539	1.43	8.8	-0.343535	1.34
11.8	-0.343568	1.36	8.7	-0.343562	1.43
11.7	-0.343545	1.44	8.6	-0.343511	1.40
11.6	-0.343524	1.43	8.5	-0.343596	1.39
11.5	-0.343422	1.40	8.4	-0.343586	1.36
11.4	-0.343526	1.41	8.3	-0.343499	1.35
11.3	-0.343568	1.42	8.2	-0.343585	1.36
11.2	-0.343498	1.42	8.1	-0.343569	1.36
11.1	-0.343528	1.37	8.0	-0.343566	1.40
11.0	-0.343565	1.38	7.9	-0.343524	1.37
10.9	-0.343593	1.39	7.8	-0.343472	1.39
10.8	-0.343510	1.40	7.7	-0.343503	1.38
10.7	-0.343505	1.39	7.6	-0.343530	1.36
10.6	-0.343556	1.34	7.5	-0.343566	1.43
10.5	-0.343428	1.47	7.4	-0.343510	1.41
10.4	-0.343399	1.50	7.3	-0.343504	1.40
10.3	-0.343517	1.37	7.2	-0.343463	1.38
10.2	-0.343499	1.37	7.1	-0.343530	1.35
10.1	-0.343542	1.38	7.0	-0.327867	12.17
10.0	-0.343527	1.35	6.9	-0.328080	4.92
9.9	-0.343555	1.37	6.8	-0.321922	5.71
9.8	-0.343545	1.38	6.7	-0.319165	2.37
9.7	-0.343510	1.38	6.6	-0.324346	20.90
9.6	-0.343570	1.34	6.5	-0.315391	17.49
9.5	-0.343520	1.50			

Table A.3 – Calibration chart versus distance test data (5, 10 meters)

α	Sensor _{OUT}	a_{TR}	$a_{RE,5}$	σ	$a_{RE,10}$	σ
(rad)	(V)	(m·s ⁻²)	(m·s ⁻²)	(10 ⁻³ mV)	(m·s ⁻²)	(10 ⁻³ mV)
0	1.245074	9.8060	9.8124	8.272	9.8144	8.274
1/36 π	1.240459	9.7687	9.7730	8.276	9.7740	8.278
1/18 π	1.226650	9.6570	9.6521	8.281	9.6511	8.283
1/12 π	1.203751	9.4719	9.4766	8.203	9.4776	8.205
1/9 π	1.171936	9.2146	9.2095	8.235	9.2085	8.237
5/36 π	1.131449	8.8873	8.8822	8.185	8.8812	8.187
1/6 π	1.082596	8.4922	8.4966	8.135	8.4966	8.137
7/36 π	1.025750	8.0326	8.0390	8.235	8.0400	8.237
2/9 π	0.961344	7.5118	7.5182	8.185	7.5195	8.187
1/4 π	0.889867	6.9339	6.9382	8.376	6.9402	8.379
5/18 π	0.811864	6.3032	6.2983	8.567	6.3116	8.569
11/36 π	0.727928	5.6245	5.6309	8.294	5.6298	8.297
1/3 π	0.638698	4.9030	4.9073	8.022	4.8971	8.024
13/36 π	0.544853	4.1442	4.1393	7.563	4.1526	7.565
7/18 π	0.447107	3.3538	3.3585	7.974	3.3591	7.976
15/36 π	0.346205	2.5380	2.5329	7.870	2.5321	7.872
2/9 π	0.242914	1.7028	1.6977	7.766	1.7085	7.768
17/36 π	0.138020	0.8546	0.8590	7.807	0.8485	7.809
1/2 π	0.032322	0.0000	0.0064	7.848	0.0000	7.850
19/36 π	-0.073377	-0.8546	-0.8482	7.923	-0.8502	7.925
5/9 π	-0.178271	-1.7028	-1.6985	7.997	-1.6954	7.999
7/12 π	-0.281562	-2.5380	-2.5429	8.235	-2.5303	8.237
11/18 π	-0.382464	-3.3538	-3.3474	8.725	-3.3475	8.727
23/36 π	-0.480210	-4.1442	-4.1399	8.184	-4.1358	8.186
2/3 π	-0.574054	-4.9030	-4.9079	7.643	-4.8977	7.645
25/36 π	-0.663284	-5.6245	-5.6198	7.604	-5.6304	7.605
13/18 π	-0.747220	-6.3032	-6.3083	7.563	-6.2948	7.565
3/4 π	-0.825224	-6.9339	-6.9390	8.235	-6.9286	8.237
14/18 π	-0.896700	-7.5118	-7.5074	7.388	-7.5177	7.390
29/36 π	-0.961107	-8.0326	-8.0262	7.383	-8.0269	7.385
5/6 π	-1.017953	-8.4922	-8.4858	7.379	-8.4983	7.381
31/36 π	-1.066805	-8.8873	-8.8830	8.235	-8.8934	8.237
8/9 π	-1.107293	-9.2146	-9.2195	7.480	-9.2102	7.482
11/12 π	-1.139107	-9.4719	-9.4655	7.373	-9.4645	7.375
17/18 π	-1.162006	-9.6570	-9.6527	7.266	-9.6493	7.268
35/36 π	-1.175816	-9.7687	-9.7736	7.328	-9.7624	7.330
π	-1.180431	-9.8060	-9.8013	7.389	-9.7976	7.391

Table A.4 – Calibration chart versus distance test data (15, 20 meters)

α	Sensor _{OUT}	a _{TR}	a _{RE,15}	σ	a _{RE,20}	σ
(rad)	(V)	(m·s ⁻²)	(m·s ⁻²)	(10 ⁻³ mV)	(m·s ⁻²)	(10 ⁻³ mV)
0	1.245074	9.8060	9.8149	8.275	9.8149	8.276
1/36 π	1.240459	9.7687	9.7745	8.279	9.7746	8.280
1/18 π	1.226650	9.6570	9.6510	8.284	9.6510	8.285
1/12 π	1.203751	9.4719	9.4779	8.206	9.4779	8.207
1/9 π	1.171936	9.2146	9.2083	8.238	9.2085	8.239
5/36 π	1.131449	8.8873	8.8809	8.188	8.8810	8.189
1/6 π	1.082596	8.4922	8.4969	8.138	8.4970	8.139
7/36 π	1.025750	8.0326	8.0402	8.238	8.0402	8.239
2/9 π	0.961344	7.5118	7.5197	8.188	7.5196	8.189
1/4 π	0.889867	6.9339	6.9405	8.379	6.9405	8.380
5/18 π	0.811864	6.3032	6.3117	8.569	6.3122	8.570
11/36 π	0.727928	5.6245	5.6300	8.297	5.6305	8.298
1/3 π	0.638698	4.9030	4.8973	8.025	4.8961	8.025
13/36 π	0.544853	4.1442	4.1531	7.566	4.1538	7.567
7/18 π	0.447107	3.3538	3.3596	7.976	3.3633	7.977
15/36 π	0.346205	2.5380	2.5320	7.872	2.5447	7.873
2/9 π	0.242914	1.7028	1.7088	7.768	1.7117	7.769
17/36 π	0.138020	0.8546	0.8483	7.809	0.8605	7.810
1/2 π	0.032322	0.0000	0.0000	7.850	0.0000	7.851
19/36 π	-0.073377	-0.8546	-0.8499	7.925	-0.8486	7.926
5/9 π	-0.178271	-1.7028	-1.6952	8.000	-1.7089	8.000
7/12 π	-0.281562	-2.5380	-2.5301	8.238	-2.5443	8.239
11/18 π	-0.382464	-3.3538	-3.3472	8.728	-3.3490	8.729
23/36 π	-0.480210	-4.1442	-4.1357	8.187	-4.1366	8.188
2/3 π	-0.574054	-4.9030	-4.8975	7.645	-4.8952	7.646
25/36 π	-0.663284	-5.6245	-5.6302	7.606	-5.6179	7.607
13/18 π	-0.747220	-6.3032	-6.2943	7.566	-6.2942	7.567
3/4 π	-0.825224	-6.9339	-6.9281	8.238	-6.9279	8.239
14/18 π	-0.896700	-7.5118	-7.5178	7.391	-7.5187	7.391
29/36 π	-0.961107	-8.0326	-8.0266	7.386	-8.0230	7.386
5/6 π	-1.017953	-8.4922	-8.4985	7.382	-8.4827	7.382
31/36 π	-1.066805	-8.8873	-8.8937	8.238	-8.8806	8.239
8/9 π	-1.107293	-9.2146	-9.2099	7.483	-9.2057	7.484
11/12 π	-1.139107	-9.4719	-9.4643	7.376	-9.4660	7.376
17/18 π	-1.162006	-9.6570	-9.6491	7.268	-9.6630	7.269
35/36 π	-1.175816	-9.7687	-9.7621	7.330	-9.7627	7.331
π	-1.180431	-9.8060	-9.7975	7.392	-9.8121	7.392

Table A.5 – Calibration chart versus distance test data (25, 30 meters)

α	Sensor _{OUT}	a _{TR}	a _{RE,25}	σ	a _{RE,30}	σ
(rad)	(V)	(m·s ⁻²)	(m·s ⁻²)	(10 ⁻³ mV)	(m·s ⁻²)	(10 ⁻³ mV)
0	1.245074	9.8060	9.7965	8.276	8.9160	18.200
1/36 π	1.240459	9.7687	9.7632	8.280	9.1287	18.209
1/18 π	1.226650	9.6570	9.6645	8.285	10.6070	18.220
1/12 π	1.203751	9.4719	9.4662	8.207	7.9119	18.048
1/9 π	1.171936	9.2146	9.2219	8.239	8.1746	18.119
5/36 π	1.131449	8.8873	8.8960	8.189	8.0173	18.009
1/6 π	1.082596	8.4922	8.4857	8.139	8.9622	17.899
7/36 π	1.025750	8.0326	8.0281	8.239	7.2726	18.119
2/9 π	0.961344	7.5118	7.5216	8.189	8.1818	18.009
1/4 π	0.889867	6.9339	6.9244	8.381	6.0439	18.429
5/18 π	0.811864	6.3032	6.2977	8.571	5.6632	18.848
11/36 π	0.727928	5.6245	5.6320	8.298	6.5745	18.249
1/3 π	0.638698	4.9030	4.8973	8.026	3.3430	17.650
13/36 π	0.544853	4.1442	4.1515	7.567	3.1042	16.641
7/18 π	0.447107	3.3538	3.3625	7.978	2.4838	17.544
15/36 π	0.346205	2.5380	2.5315	7.874	3.0080	17.315
2/9 π	0.242914	1.7028	1.6983	7.770	0.9428	17.086
17/36 π	0.138020	0.8546	0.8644	7.811	1.5246	17.176
1/2 π	0.032322	0.0000	-0.0095	7.852	-0.8900	17.266
19/36 π	-0.073377	-0.8546	-0.8601	7.927	-1.4946	17.432
5/9 π	-0.178271	-1.7028	-1.6953	8.001	-0.7528	17.595
7/12 π	-0.281562	-2.5380	-2.5437	8.239	-4.0980	18.119
11/18 π	-0.382464	-3.3538	-3.3465	8.729	-4.3938	19.196
23/36 π	-0.480210	-4.1442	-4.1355	8.188	-5.0142	18.007
2/3 π	-0.574054	-4.9030	-4.9095	7.646	-4.4330	16.815
25/36 π	-0.663284	-5.6245	-5.6290	7.607	-6.3845	16.729
13/18 π	-0.747220	-6.3032	-6.2934	7.567	-5.6332	16.641
3/4 π	-0.825224	-6.9339	-6.9434	8.239	-7.8239	18.119
14/18 π	-0.896700	-7.5118	-7.5173	7.392	-8.1518	16.255
29/36 π	-0.961107	-8.0326	-8.0251	7.387	-7.0826	16.244
5/6 π	-1.017953	-8.4922	-8.4979	7.383	-10.0522	16.235
31/36 π	-1.066805	-8.8873	-8.8800	8.239	-9.9273	18.119
8/9 π	-1.107293	-9.2146	-9.2059	7.484	-10.0846	16.458
11/12 π	-1.139107	-9.4719	-9.4784	7.377	-9.0019	16.222
17/18 π	-1.162006	-9.6570	-9.6615	7.270	-10.4170	15.986
35/36 π	-1.175816	-9.7687	-9.7589	7.332	-9.0987	16.123
π	-1.180431	-9.8060	-9.8155	7.393	-10.6960	16.257

Table A.6 – Mean values and standard deviations for the 5 Hz sinusoidal wave excitation

Time	\bar{x}_{Ref}	σ_{Ref}	\bar{x}_{MEMS}	σ_{MEMS}
(s)	(m·s ⁻²)	(m·s ⁻²)	(m·s ⁻²)	(m·s ⁻²)
0.00	-0.0138	0.0002	0.0002	0.0002
0.01	-0.0194	0.0002	0.0002	0.0003
0.02	-0.0224	0.0004	0.0004	0.0003
0.03	-0.0234	0.0004	0.0004	0.0003
0.04	-0.0228	0.0004	0.0004	0.0003
0.05	-0.0203	0.0006	0.0006	0.0004
0.06	-0.0157	0.0006	0.0006	0.0005
0.07	-0.0094	0.0005	0.0005	0.0003
0.08	-0.0025	0.0004	0.0004	0.0004
0.09	0.0044	0.0003	0.0003	0.0003
0.10	0.0111	0.0004	0.0004	0.0005
0.11	0.0169	0.0006	0.0006	0.0006
0.12	0.0210	0.0006	0.0006	0.0006
0.13	0.0225	0.0004	0.0004	0.0004
0.14	0.0213	0.0005	0.0005	0.0004
0.15	0.0182	0.0006	0.0006	0.0004
0.16	0.0141	0.0004	0.0004	0.0005
0.17	0.0089	0.0005	0.0005	0.0006
0.18	0.0020	0.0004	0.0004	0.0004
0.19	-0.0061	0.0001	0.0001	0.0002
0.20	-0.0138	0.0002	0.0002	0.0003

Table A.7 – Mean values and standard deviations for the 2 Hz sinusoidal wave excitation

Time	\bar{x}_{Ref}	σ_{Ref}	\bar{x}_{MEMS}	σ_{MEMS}	Time	\bar{x}_{Ref}	σ_{Ref}	\bar{x}_{MEMS}	σ_{MEMS}
(s)	(m·s ⁻²)	(m·s ⁻²)	(m·s ⁻²)	(m·s ⁻²)	(s)	(m·s ⁻²)	(m·s ⁻²)	(m·s ⁻²)	(m·s ⁻²)
0.00	0.0214	0.0004	0.0213	0.0004	0.37	-0.0113	0.0002	-0.0113	0.0002
0.01	0.0228	0.0003	0.0227	0.0005	0.38	-0.0088	0.0001	-0.0087	0.0002
0.02	0.0238	0.0005	0.0239	0.0005	0.39	-0.0060	0.0004	-0.0060	0.0002
0.03	0.0242	0.0001	0.0244	0.0005	0.40	-0.0030	0.0005	-0.0030	0.0001
0.04	0.0242	0.0002	0.0242	0.0005	0.41	0.0002	0.0004	0.0002	0.0001
0.05	0.0235	0.0002	0.0234	0.0005	0.42	0.0036	0.0001	0.0036	0.0001
0.06	0.0224	0.0001	0.0225	0.0005	0.43	0.0069	0.0001	0.0069	0.0002
0.07	0.0209	0.0000	0.0210	0.0004	0.44	0.0099	0.0003	0.0100	0.0002
0.08	0.0192	0.0000	0.0191	0.0004	0.45	0.0125	0.0003	0.0125	0.0002
0.09	0.0171	0.0001	0.0172	0.0003	0.46	0.0146	0.0002	0.0147	0.0003
0.10	0.0149	0.0002	0.0148	0.0003	0.47	0.0164	0.0000	0.0164	0.0003
0.11	0.0125	0.0004	0.0126	0.0003	0.48	0.0180	0.0003	0.0181	0.0004
0.12	0.0099	0.0006	0.0099	0.0002	0.49	0.0196	0.0004	0.0197	0.0004
0.13	0.0073	0.0007	0.0073	0.0002	0.50	0.0214	0.0000	0.0215	0.0004
0.14	0.0045	0.0006	0.0046	0.0002					
0.15	0.0016	0.0006	0.0016	0.0001					
0.16	-0.0015	0.0005	-0.0015	0.0001					
0.17	-0.0047	0.0003	-0.0048	0.0001					
0.18	-0.0080	0.0001	-0.0080	0.0002					
0.19	-0.0110	0.0000	-0.0111	0.0002					
0.20	-0.0137	0.0002	-0.0136	0.0003					
0.21	-0.0160	0.0002	-0.0160	0.0003					
0.22	-0.0181	0.0001	-0.0182	0.0004					
0.23	-0.0199	0.0000	-0.0200	0.0004					
0.24	-0.0215	0.0001	-0.0215	0.0004					
0.25	-0.0229	0.0002	-0.0230	0.0005					
0.26	-0.0240	0.0000	-0.0239	0.0005					
0.27	-0.0248	0.0002	-0.0249	0.0005					
0.28	-0.0251	0.0003	-0.0252	0.0005					
0.29	-0.0250	0.0004	-0.0250	0.0005					
0.30	-0.0244	0.0003	-0.0244	0.0005					
0.31	-0.0234	0.0002	-0.0232	0.0005					
0.32	-0.0219	0.0001	-0.0219	0.0004					
0.33	-0.0202	0.0003	-0.0203	0.0004					
0.34	-0.0182	0.0005	-0.0183	0.0004					
0.35	-0.0160	0.0006	-0.0161	0.0003					
0.36	-0.0137	0.0004	-0.0139	0.0003					

Table A.8 – Mean values and standard deviations for the 1 Hz sinusoidal wave excitation

Time	\bar{x}_{Ref}	σ_{Ref}	\bar{x}_{MEMS}	σ_{MEMS}	Time	\bar{x}_{Ref}	σ_{Ref}	\bar{x}_{MEMS}	σ_{MEMS}
(s)	(m·s ⁻²)	(m·s ⁻²)	(m·s ⁻²)	(m·s ⁻²)	(s)	(m·s ⁻²)	(m·s ⁻²)	(m·s ⁻²)	(m·s ⁻²)
0.00	0.0108	0.0001	0.0107	0.0002	0.37	-0.0185	0.0002	-0.0185	0.0005
0.01	0.0101	0.0001	0.0103	0.0002	0.38	-0.0186	0.0001	-0.0186	0.0005
0.02	0.0094	0.0001	0.0093	0.0002	0.39	-0.0187	0.0001	-0.0188	0.0005
0.03	0.0086	0.0002	0.0087	0.0003	0.40	-0.0188	0.0001	-0.0188	0.0005
0.04	0.0078	0.0002	0.0077	0.0003	0.41	-0.0189	0.0004	-0.0189	0.0005
0.05	0.0070	0.0003	0.0071	0.0004	0.42	-0.0189	0.0004	-0.0189	0.0005
0.06	0.0061	0.0003	0.0061	0.0004	0.43	-0.0188	0.0004	-0.0189	0.0004
0.07	0.0052	0.0004	0.0053	0.0004	0.44	-0.0186	0.0006	-0.0186	0.0004
0.08	0.0043	0.0004	0.0043	0.0003	0.45	-0.0184	0.0006	-0.0185	0.0003
0.09	0.0034	0.0004	0.0035	0.0003	0.46	-0.0181	0.0005	-0.0180	0.0003
0.10	0.0025	0.0005	0.0025	0.0002	0.47	-0.0176	0.0004	-0.0176	0.0003
0.11	0.0016	0.0005	0.0016	0.0002	0.48	-0.0171	0.0003	-0.0173	0.0002
0.12	0.0007	0.0005	0.0007	0.0005	0.49	-0.0165	0.0002	-0.0167	0.0002
0.13	-0.0002	0.0005	-0.0002	0.0004	0.50	-0.0158	0.0002	-0.0156	0.0002
0.14	-0.0012	0.0005	-0.0012	0.0004	0.51	-0.0150	0.0001	-0.0152	0.0001
0.15	-0.0022	0.0002	-0.0022	0.0005	0.52	-0.0142	0.0003	-0.0140	0.0001
0.16	-0.0033	0.0004	-0.0032	0.0006	0.53	-0.0133	0.0005	-0.0134	0.0001
0.17	-0.0043	0.0004	-0.0044	0.0004	0.54	-0.0124	0.0006	-0.0125	0.0002
0.18	-0.0055	0.0004	-0.0054	0.0002	0.55	-0.0115	0.0006	-0.0115	0.0002
0.19	-0.0066	0.0006	-0.0067	0.0001	0.56	-0.0105	0.0004	-0.0106	0.0003
0.20	-0.0078	0.0006	-0.0077	0.0004	0.57	-0.0096	0.0004	-0.0095	0.0003
0.21	-0.0090	0.0005	-0.0088	0.0005	0.58	-0.0086	0.0004	-0.0086	0.0004
0.22	-0.0101	0.0004	-0.0102	0.0004	0.59	-0.0076	0.0005	-0.0076	0.0004
0.23	-0.0112	0.0003	-0.0111	0.0001	0.60	-0.0067	0.0006	-0.0067	0.0004
0.24	-0.0123	0.0004	-0.0124	0.0001	0.61	-0.0057	0.0004	-0.0057	0.0005
0.25	-0.0133	0.0006	-0.0132	0.0003	0.62	-0.0047	0.0006	-0.0047	0.0003
0.26	-0.0142	0.0006	-0.0144	0.0003	0.63	-0.0036	0.0006	-0.0037	0.0003
0.27	-0.0149	0.0001	-0.0149	0.0002	0.64	-0.0026	0.0001	-0.0025	0.0004
0.28	-0.0156	0.0003	-0.0156	0.0000	0.65	-0.0015	0.0003	-0.0015	0.0004
0.29	-0.0162	0.0002	-0.0163	0.0003	0.66	-0.0004	0.0003	-0.0004	0.0004
0.30	-0.0167	0.0001	-0.0168	0.0002	0.67	0.0007	0.0002	0.0007	0.0005
0.31	-0.0172	0.0002	-0.0172	0.0002	0.68	0.0018	0.0002	0.0018	0.0006
0.32	-0.0175	0.0004	-0.0176	0.0002	0.69	0.0029	0.0002	0.0029	0.0004
0.33	-0.0178	0.0003	-0.0177	0.0001	0.70	0.0039	0.0001	0.0039	0.0002
0.34	-0.0180	0.0003	-0.0183	0.0003	0.71	0.0050	0.0001	0.0049	0.0003
0.35	-0.0182	0.0002	-0.0180	0.0003	0.72	0.0060	0.0001	0.0059	0.0005
0.36	-0.0184	0.0002	-0.0183	0.0004	0.73	0.0069	0.0004	0.0069	0.0004

Time	\bar{x}_{Ref}	σ_{Ref}	\bar{x}_{MEMS}	σ_{MEMS}
(s)	(m·s ⁻²)	(m·s ⁻²)	(m·s ⁻²)	(m·s ⁻²)
0.74	0.0079	0.0005	0.0078	0.0004
0.75	0.0088	0.0004	0.0088	0.0003
0.76	0.0097	0.0001	0.0096	0.0002
0.77	0.0105	0.0001	0.0105	0.0002
0.78	0.0113	0.0003	0.0113	0.0004
0.79	0.0121	0.0003	0.0121	0.0004
0.80	0.0128	0.0002	0.0129	0.0004
0.81	0.0134	0.0000	0.0134	0.0006
0.82	0.0140	0.0003	0.0139	0.0006
0.83	0.0144	0.0004	0.0143	0.0005
0.84	0.0148	0.0000	0.0148	0.0004
0.85	0.0151	0.0006	0.0149	0.0003
0.86	0.0153	0.0005	0.0154	0.0004
0.87	0.0154	0.0003	0.0155	0.0006
0.88	0.0155	0.0001	0.0154	0.0006
0.89	0.0155	0.0000	0.0154	0.0004
0.90	0.0154	0.0002	0.0154	0.0005
0.91	0.0152	0.0002	0.0153	0.0006
0.92	0.0149	0.0001	0.0149	0.0004
0.93	0.0146	0.0000	0.0146	0.0005
0.94	0.0142	0.0001	0.0142	0.0004
0.95	0.0137	0.0002	0.0137	0.0001
0.96	0.0132	0.0000	0.0132	0.0002
0.97	0.0127	0.0002	0.0126	0.0003
0.98	0.0121	0.0003	0.0120	0.0003
0.99	0.0115	0.0004	0.0114	0.0002
1.00	0.0108	0.0003	0.0107	0.0002

Table A.9 – Mean values and standard deviations for the 0.5 Hz sinusoidal wave excitation

Time	\bar{x}_{Ref}	σ_{Ref}	\bar{x}_{MEMS}	σ_{MEMS}	Time	\bar{x}_{Ref}	σ_{Ref}	\bar{x}_{MEMS}	σ_{MEMS}
(s)	(m·s ⁻²)	(m·s ⁻²)	(m·s ⁻²)	(m·s ⁻²)	(s)	(m·s ⁻²)	(m·s ⁻²)	(m·s ⁻²)	(m·s ⁻²)
0.00	-0.0180	0.0002	-0.0176	0.0001	0.37	0.0072	0.0006	0.0071	0.0005
0.01	-0.0171	0.0002	-0.0167	0.0002	0.38	0.0086	0.0001	0.0088	0.0004
0.02	-0.0163	0.0004	-0.0166	0.0002	0.39	0.0100	0.0003	0.0104	0.0001
0.03	-0.0154	0.0004	-0.0151	0.0003	0.40	0.0116	0.0004	0.0117	0.0001
0.04	-0.0147	0.0004	-0.0150	0.0003	0.41	0.0131	0.0003	0.0132	0.0001
0.05	-0.0139	0.0006	-0.0143	0.0004	0.42	0.0145	0.0002	0.0142	0.0002
0.06	-0.0132	0.0006	-0.0133	0.0004	0.43	0.0158	0.0001	0.0161	0.0002
0.07	-0.0125	0.0005	-0.0126	0.0004	0.44	0.0169	0.0003	0.0164	0.0003
0.08	-0.0118	0.0004	-0.0115	0.0005	0.45	0.0177	0.0005	0.0175	0.0003
0.09	-0.0110	0.0003	-0.0113	0.0003	0.46	0.0183	0.0006	0.0184	0.0004
0.10	-0.0102	0.0004	-0.0098	0.0003	0.47	0.0185	0.0004	0.0191	0.0004
0.11	-0.0095	0.0006	-0.0094	0.0004	0.48	0.0186	0.0002	0.0190	0.0004
0.12	-0.0087	0.0006	-0.0088	0.0004	0.49	0.0185	0.0001	0.0179	0.0005
0.13	-0.0080	0.0004	-0.0082	0.0004	0.50	0.0183	0.0004	0.0183	0.0005
0.14	-0.0072	0.0005	-0.0074	0.0005	0.51	0.0181	0.0005	0.0177	0.0005
0.15	-0.0065	0.0004	-0.0063	0.0006	0.52	0.0179	0.0004	0.0174	0.0005
0.16	-0.0058	0.0004	-0.0058	0.0004	0.53	0.0179	0.0001	0.0183	0.0005
0.17	-0.0051	0.0004	-0.0050	0.0002	0.54	0.0179	0.0001	0.0175	0.0002
0.18	-0.0043	0.0006	-0.0041	0.0003	0.55	0.0181	0.0003	0.0184	0.0004
0.19	-0.0036	0.0006	-0.0037	0.0005	0.56	0.0184	0.0003	0.0189	0.0004
0.20	-0.0028	0.0005	-0.0027	0.0004	0.57	0.0188	0.0002	0.0190	0.0004
0.21	-0.0020	0.0004	-0.0021	0.0004	0.58	0.0194	0.0000	0.0196	0.0006
0.22	-0.0014	0.0003	-0.0014	0.0003	0.59	0.0199	0.0003	0.0195	0.0006
0.23	-0.0008	0.0002	-0.0008	0.0002	0.60	0.0205	0.0004	0.0210	0.0005
0.24	-0.0003	0.0002	-0.0003	0.0002	0.61	0.0211	0.0006	0.0208	0.0004
0.25	0.0000	0.0001	0.0000	0.0004	0.62	0.0216	0.0006	0.0214	0.0003
0.26	0.0003	0.0003	0.0003	0.0006	0.63	0.0220	0.0004	0.0222	0.0004
0.27	0.0005	0.0005	0.0005	0.0005	0.64	0.0223	0.0004	0.0227	0.0006
0.28	0.0007	0.0006	0.0007	0.0004	0.65	0.0224	0.0004	0.0229	0.0006
0.29	0.0009	0.0006	0.0009	0.0003	0.66	0.0225	0.0005	0.0220	0.0001
0.30	0.0012	0.0004	0.0012	0.0004	0.67	0.0224	0.0006	0.0224	0.0003
0.31	0.0017	0.0004	0.0017	0.0006	0.68	0.0223	0.0004	0.0219	0.0002
0.32	0.0022	0.0004	0.0022	0.0006	0.69	0.0222	0.0002	0.0219	0.0001
0.33	0.0030	0.0005	0.0030	0.0004	0.70	0.0222	0.0002	0.0227	0.0002
0.34	0.0038	0.0006	0.0038	0.0005	0.71	0.0224	0.0002	0.0219	0.0004
0.35	0.0048	0.0004	0.0045	0.0006	0.72	0.0227	0.0002	0.0231	0.0003
0.36	0.0060	0.0006	0.0062	0.0004	0.73	0.0231	0.0003	0.0236	0.0003

Time	\bar{x}_{Ref}	σ_{Ref}	\bar{x}_{MEMS}	σ_{MEMS}	Time	\bar{x}_{Ref}	σ_{Ref}	\bar{x}_{MEMS}	σ_{MEMS}
(s)	(m·s ⁻²)	(m·s ⁻²)	(m·s ⁻²)	(m·s ⁻²)	(s)	(m·s ⁻²)	(m·s ⁻²)	(m·s ⁻²)	(m·s ⁻²)
0.74	0.0237	0.0003	0.0239	0.0002	1.11	0.0055	0.0004	0.0056	0.0004
0.75	0.0242	0.0004	0.0245	0.0004	1.12	0.0049	0.0004	0.0047	0.0002
0.76	0.0247	0.0004	0.0242	0.0003	1.13	0.0044	0.0005	0.0044	0.0001
0.77	0.0251	0.0004	0.0255	0.0005	1.14	0.0040	0.0005	0.0040	0.0004
0.78	0.0252	0.0003	0.0247	0.0001	1.15	0.0035	0.0005	0.0036	0.0005
0.79	0.0251	0.0003	0.0249	0.0002	1.16	0.0030	0.0005	0.0031	0.0004
0.80	0.0248	0.0002	0.0251	0.0002	1.17	0.0024	0.0005	0.0024	0.0001
0.81	0.0243	0.0002	0.0250	0.0001	1.18	0.0018	0.0005	0.0018	0.0001
0.82	0.0236	0.0005	0.0241	0.0000	1.19	0.0011	0.0005	0.0010	0.0003
0.83	0.0228	0.0004	0.0225	0.0000	1.20	0.0002	0.0004	0.0002	0.0003
0.84	0.0219	0.0004	0.0219	0.0001	1.21	-0.0008	0.0004	-0.0008	0.0002
0.85	0.0210	0.0005	0.0206	0.0002	1.22	-0.0018	0.0004	-0.0018	0.0000
0.86	0.0202	0.0006	0.0200	0.0004	1.23	-0.0029	0.0003	-0.0030	0.0003
0.87	0.0194	0.0004	0.0200	0.0006	1.24	-0.0040	0.0003	-0.0042	0.0004
0.88	0.0187	0.0002	0.0183	0.0007	1.25	-0.0051	0.0002	-0.0052	0.0000
0.89	0.0181	0.0001	0.0185	0.0006	1.26	-0.0061	0.0002	-0.0062	0.0002
0.90	0.0177	0.0004	0.0182	0.0006	1.27	-0.0071	0.0002	-0.0069	0.0002
0.91	0.0174	0.0005	0.0176	0.0005	1.28	-0.0079	0.0001	-0.0081	0.0002
0.92	0.0172	0.0004	0.0174	0.0003	1.29	-0.0087	0.0005	-0.0084	0.0003
0.93	0.0171	0.0001	0.0168	0.0001	1.30	-0.0095	0.0004	-0.0094	0.0003
0.94	0.0171	0.0001	0.0176	0.0000	1.31	-0.0102	0.0003	-0.0103	0.0004
0.95	0.0170	0.0003	0.0164	0.0002	1.32	-0.0108	0.0004	-0.0112	0.0004
0.96	0.0168	0.0003	0.0167	0.0002	1.33	-0.0115	0.0006	-0.0117	0.0004
0.97	0.0166	0.0002	0.0168	0.0001	1.34	-0.0121	0.0006	-0.0117	0.0003
0.98	0.0162	0.0000	0.0167	0.0000	1.35	-0.0126	0.0004	-0.0126	0.0003
0.99	0.0157	0.0003	0.0160	0.0001	1.36	-0.0132	0.0005	-0.0129	0.0002
1.00	0.0150	0.0002	0.0146	0.0002	1.37	-0.0137	0.0006	-0.0139	0.0002
1.01	0.0142	0.0002	0.0142	0.0000	1.38	-0.0143	0.0004	-0.0149	0.0005
1.02	0.0133	0.0002	0.0130	0.0002	1.39	-0.0150	0.0005	-0.0147	0.0004
1.03	0.0123	0.0001	0.0115	0.0003	1.40	-0.0157	0.0004	-0.0160	0.0004
1.04	0.0112	0.0003	0.0117	0.0004	1.41	-0.0164	0.0002	-0.0169	0.0005
1.05	0.0102	0.0003	0.0100	0.0003	1.42	-0.0172	0.0002	-0.0174	0.0006
1.06	0.0092	0.0004	0.0094	0.0002	1.43	-0.0179	0.0002	-0.0181	0.0004
1.07	0.0083	0.0005	0.0086	0.0001	1.44	-0.0186	0.0003	-0.0182	0.0002
1.08	0.0075	0.0005	0.0076	0.0003	1.45	-0.0192	0.0003	-0.0198	0.0001
1.09	0.0068	0.0005	0.0068	0.0005	1.46	-0.0197	0.0004	-0.0192	0.0004
1.10	0.0061	0.0004	0.0060	0.0006	1.47	-0.0200	0.0001	-0.0198	0.0005

Time	\bar{x}_{Ref}	σ_{Ref}	\bar{x}_{MEMS}	σ_{MEMS}	Time	\bar{x}_{Ref}	σ_{Ref}	\bar{x}_{MEMS}	σ_{MEMS}
(s)	(m·s ⁻²)	(m·s ⁻²)	(m·s ⁻²)	(m·s ⁻²)	(s)	(m·s ⁻²)	(m·s ⁻²)	(m·s ⁻²)	(m·s ⁻²)
1.48	-0.0203	0.0001	-0.0205	0.0004	1.85	-0.0266	0.0002	-0.0260	0.0003
1.49	-0.0205	0.0001	-0.0210	0.0001	1.86	-0.0263	0.0005	-0.0263	0.0004
1.50	-0.0207	0.0002	-0.0211	0.0001	1.87	-0.0259	0.0004	-0.0254	0.0003
1.51	-0.0210	0.0002	-0.0205	0.0003	1.88	-0.0255	0.0004	-0.0250	0.0005
1.52	-0.0214	0.0003	-0.0214	0.0003	1.89	-0.0251	0.0005	-0.0256	0.0006
1.53	-0.0220	0.0003	-0.0215	0.0002	1.90	-0.0248	0.0006	-0.0243	0.0006
1.54	-0.0228	0.0004	-0.0224	0.0000	1.91	-0.0244	0.0004	-0.0249	0.0004
1.55	-0.0237	0.0004	-0.0242	0.0003	1.92	-0.0242	0.0002	-0.0246	0.0004
1.56	-0.0249	0.0004	-0.0244	0.0002	1.93	-0.0239	0.0001	-0.0242	0.0004
1.57	-0.0261	0.0005	-0.0266	0.0002	1.94	-0.0237	0.0002	-0.0240	0.0005
1.58	-0.0272	0.0005	-0.0277	0.0002	1.95	-0.0235	0.0003	-0.0230	0.0006
1.59	-0.0283	0.0005	-0.0285	0.0001	1.96	-0.0232	0.0003	-0.0237	0.0004
1.60	-0.0291	0.0005	-0.0294	0.0003	1.97	-0.0228	0.0002	-0.0228	0.0002
1.61	-0.0297	0.0005	-0.0291	0.0003	1.98	-0.0222	0.0002	-0.0220	0.0003
1.62	-0.0300	0.0002	-0.0305	0.0004	1.99	-0.0215	0.0002	-0.0217	0.0005
1.63	-0.0300	0.0004	-0.0298	0.0005	2.00	-0.0207	0.0006	-0.0203	0.0001
1.64	-0.0298	0.0004	-0.0295	0.0005					
1.65	-0.0294	0.0004	-0.0297	0.0005					
1.66	-0.0290	0.0006	-0.0293	0.0005					
1.67	-0.0285	0.0006	-0.0290	0.0005					
1.68	-0.0279	0.0005	-0.0274	0.0005					
1.69	-0.0274	0.0004	-0.0274	0.0004					
1.70	-0.0269	0.0003	-0.0264	0.0004					
1.71	-0.0265	0.0004	-0.0259	0.0003					
1.72	-0.0261	0.0006	-0.0267	0.0003					
1.73	-0.0259	0.0006	-0.0254	0.0003					
1.74	-0.0258	0.0001	-0.0263	0.0002					
1.75	-0.0258	0.0003	-0.0262	0.0002					
1.76	-0.0259	0.0002	-0.0261	0.0002					
1.77	-0.0261	0.0001	-0.0263	0.0001					
1.78	-0.0263	0.0002	-0.0258	0.0002					
1.79	-0.0266	0.0004	-0.0264	0.0003					
1.80	-0.0263	0.0003	-0.0258	0.0003					
1.81	-0.0270	0.0003	-0.0267	0.0003					
1.82	-0.0271	0.0002	-0.0274	0.0003					
1.83	-0.0270	0.0002	-0.0276	0.0004					
1.84	-0.0269	0.0002	-0.0274	0.0005					

Table A.10 – Mean values and standard deviations for the 0.2 Hz sinusoidal wave excitation

Time	\bar{x}_{Ref}	σ_{Ref}	\bar{x}_{MEMS}	σ_{MEMS}	Time	\bar{x}_{Ref}	σ_{Ref}	\bar{x}_{MEMS}	σ_{MEMS}
(s)	(m·s ⁻²)	(m·s ⁻²)	(m·s ⁻²)	(m·s ⁻²)	(s)	(m·s ⁻²)	(m·s ⁻²)	(m·s ⁻²)	(m·s ⁻²)
0.00	-0.0064	0.0002	-0.0067	0.0001	0.37	-0.0052	0.0006	-0.0050	0.0005
0.01	-0.0069	0.0002	-0.0073	0.0002	0.38	-0.0055	0.0001	-0.0057	0.0004
0.02	-0.0074	0.0004	-0.0070	0.0002	0.39	-0.0059	0.0003	-0.0062	0.0001
0.03	-0.0077	0.0004	-0.0081	0.0003	0.40	-0.0063	0.0004	-0.0064	0.0001
0.04	-0.0081	0.0004	-0.0078	0.0003	0.41	-0.0067	0.0003	-0.0068	0.0001
0.05	-0.0083	0.0006	-0.0079	0.0004	0.42	-0.0071	0.0002	-0.0068	0.0002
0.06	-0.0084	0.0006	-0.0083	0.0004	0.43	-0.0075	0.0001	-0.0078	0.0002
0.07	-0.0085	0.0005	-0.0084	0.0004	0.44	-0.0080	0.0003	-0.0075	0.0003
0.08	-0.0085	0.0004	-0.0088	0.0005	0.45	-0.0084	0.0005	-0.0082	0.0003
0.09	-0.0085	0.0003	-0.0081	0.0003	0.46	-0.0089	0.0006	-0.0090	0.0004
0.10	-0.0084	0.0004	-0.0088	0.0003	0.47	-0.0093	0.0004	-0.0098	0.0004
0.11	-0.0082	0.0006	-0.0083	0.0004	0.48	-0.0097	0.0002	-0.0101	0.0004
0.12	-0.0080	0.0006	-0.0079	0.0004	0.49	-0.0101	0.0001	-0.0095	0.0005
0.13	-0.0078	0.0004	-0.0075	0.0004	0.50	-0.0104	0.0004	-0.0104	0.0005
0.14	-0.0075	0.0005	-0.0074	0.0005	0.51	-0.0107	0.0005	-0.0104	0.0005
0.15	-0.0072	0.0004	-0.0074	0.0006	0.52	-0.0110	0.0004	-0.0105	0.0005
0.16	-0.0069	0.0004	-0.0069	0.0004	0.53	-0.0112	0.0001	-0.0116	0.0005
0.17	-0.0066	0.0004	-0.0067	0.0002	0.54	-0.0114	0.0001	-0.0110	0.0002
0.18	-0.0062	0.0006	-0.0065	0.0003	0.55	-0.0115	0.0003	-0.0119	0.0004
0.19	-0.0059	0.0006	-0.0058	0.0005	0.56	-0.0116	0.0003	-0.0121	0.0004
0.20	-0.0056	0.0005	-0.0057	0.0004	0.57	-0.0116	0.0002	-0.0118	0.0004
0.21	-0.0053	0.0004	-0.0053	0.0004	0.58	-0.0115	0.0000	-0.0117	0.0006
0.22	-0.0050	0.0003	-0.0050	0.0003	0.59	-0.0114	0.0003	-0.0110	0.0006
0.23	-0.0048	0.0002	-0.0048	0.0002	0.60	-0.0112	0.0004	-0.0117	0.0005
0.24	-0.0045	0.0002	-0.0045	0.0002	0.61	-0.0110	0.0006	-0.0107	0.0004
0.25	-0.0043	0.0001	-0.0043	0.0004	0.62	-0.0108	0.0006	-0.0106	0.0003
0.26	-0.0042	0.0003	-0.0042	0.0006	0.63	-0.0105	0.0004	-0.0107	0.0004
0.27	-0.0040	0.0005	-0.0040	0.0005	0.64	-0.0102	0.0004	-0.0107	0.0006
0.28	-0.0040	0.0006	-0.0040	0.0004	0.65	-0.0099	0.0004	-0.0103	0.0006
0.29	-0.0039	0.0006	-0.0039	0.0003	0.66	-0.0095	0.0005	-0.0090	0.0001
0.30	-0.0039	0.0004	-0.0040	0.0004	0.67	-0.0091	0.0006	-0.0091	0.0003
0.31	-0.0040	0.0004	-0.0040	0.0006	0.68	-0.0088	0.0004	-0.0083	0.0002
0.32	-0.0041	0.0004	-0.0040	0.0006	0.69	-0.0084	0.0002	-0.0081	0.0001
0.33	-0.0042	0.0005	-0.0042	0.0004	0.70	-0.0081	0.0002	-0.0086	0.0002
0.34	-0.0044	0.0006	-0.0043	0.0005	0.71	-0.0078	0.0002	-0.0073	0.0004
0.35	-0.0046	0.0004	-0.0043	0.0006	0.72	-0.0075	0.0002	-0.0080	0.0003
0.36	-0.0049	0.0006	-0.0051	0.0004	0.73	-0.0073	0.0003	-0.0078	0.0003

Time	\bar{x}_{Ref}	σ_{Ref}	\bar{x}_{MEMS}	σ_{MEMS}	Time	\bar{x}_{Ref}	σ_{Ref}	\bar{x}_{MEMS}	σ_{MEMS}
(s)	(m·s ⁻²)	(m·s ⁻²)	(m·s ⁻²)	(m·s ⁻²)	(s)	(m·s ⁻²)	(m·s ⁻²)	(m·s ⁻²)	(m·s ⁻²)
0.74	-0.0071	0.0003	-0.0073	0.0002	1.11	-0.0141	0.0004	-0.0143	0.0004
0.75	-0.0070	0.0004	-0.0072	0.0004	1.12	-0.0143	0.0004	-0.0141	0.0002
0.76	-0.0069	0.0004	-0.0064	0.0003	1.13	-0.0145	0.0005	-0.0145	0.0001
0.77	-0.0068	0.0004	-0.0073	0.0005	1.14	-0.0147	0.0005	-0.0148	0.0004
0.78	-0.0069	0.0003	-0.0064	0.0001	1.15	-0.0150	0.0005	-0.0151	0.0005
0.79	-0.0070	0.0003	-0.0067	0.0002	1.16	-0.0153	0.0005	-0.0154	0.0004
0.80	-0.0071	0.0002	-0.0073	0.0002	1.17	-0.0157	0.0005	-0.0156	0.0001
0.81	-0.0073	0.0002	-0.0080	0.0001	1.18	-0.0161	0.0005	-0.0161	0.0001
0.82	-0.0075	0.0005	-0.0080	0.0000	1.19	-0.0165	0.0005	-0.0165	0.0003
0.83	-0.0078	0.0004	-0.0075	0.0000	1.20	-0.0170	0.0004	-0.0170	0.0003
0.84	-0.0081	0.0004	-0.0081	0.0001	1.21	-0.0175	0.0004	-0.0175	0.0002
0.85	-0.0084	0.0005	-0.0080	0.0002	1.22	-0.0181	0.0004	-0.0181	0.0000
0.86	-0.0088	0.0006	-0.0086	0.0004	1.23	-0.0186	0.0003	-0.0186	0.0003
0.87	-0.0092	0.0004	-0.0098	0.0006	1.24	-0.0192	0.0003	-0.0191	0.0004
0.88	-0.0096	0.0002	-0.0092	0.0007	1.25	-0.0198	0.0002	-0.0198	0.0000
0.89	-0.0100	0.0001	-0.0103	0.0006	1.26	-0.0204	0.0002	-0.0204	0.0002
0.90	-0.0103	0.0004	-0.0109	0.0006	1.27	-0.0210	0.0002	-0.0212	0.0002
0.91	-0.0107	0.0005	-0.0109	0.0005	1.28	-0.0216	0.0001	-0.0214	0.0002
0.92	-0.0111	0.0004	-0.0112	0.0003	1.29	-0.0222	0.0005	-0.0225	0.0003
0.93	-0.0114	0.0001	-0.0111	0.0001	1.30	-0.0228	0.0004	-0.0229	0.0003
0.94	-0.0117	0.0001	-0.0122	0.0000	1.31	-0.0233	0.0003	-0.0232	0.0004
0.95	-0.0120	0.0003	-0.0114	0.0002	1.32	-0.0238	0.0004	-0.0234	0.0004
0.96	-0.0123	0.0003	-0.0121	0.0002	1.33	-0.0242	0.0006	-0.0240	0.0004
0.97	-0.0125	0.0002	-0.0127	0.0001	1.34	-0.0246	0.0006	-0.0250	0.0003
0.98	-0.0127	0.0000	-0.0132	0.0000	1.35	-0.0250	0.0004	-0.0250	0.0003
0.99	-0.0129	0.0003	-0.0132	0.0001	1.36	-0.0253	0.0005	-0.0256	0.0002
1.00	-0.0131	0.0002	-0.0126	0.0002	1.37	-0.0256	0.0006	-0.0254	0.0002
1.01	-0.0132	0.0002	-0.0132	0.0000	1.38	-0.0258	0.0004	-0.0252	0.0005
1.02	-0.0133	0.0002	-0.0131	0.0002	1.39	-0.0259	0.0005	-0.0262	0.0004
1.03	-0.0134	0.0001	-0.0127	0.0003	1.40	-0.0261	0.0004	-0.0258	0.0004
1.04	-0.0135	0.0003	-0.0139	0.0004	1.41	-0.0262	0.0002	-0.0257	0.0005
1.05	-0.0136	0.0003	-0.0134	0.0003	1.42	-0.0262	0.0002	-0.0260	0.0006
1.06	-0.0136	0.0004	-0.0138	0.0002	1.43	-0.0262	0.0002	-0.0260	0.0004
1.07	-0.0137	0.0005	-0.0140	0.0001	1.44	-0.0262	0.0003	-0.0266	0.0002
1.08	-0.0138	0.0005	-0.0139	0.0003	1.45	-0.0261	0.0003	-0.0256	0.0001
1.09	-0.0139	0.0005	-0.0140	0.0005	1.46	-0.0261	0.0004	-0.0266	0.0004
1.10	-0.0140	0.0004	-0.0139	0.0006	1.47	-0.0260	0.0001	-0.0262	0.0005

Time	\bar{x}_{Ref}	σ_{Ref}	\bar{x}_{MEMS}	σ_{MEMS}	Time	\bar{x}_{Ref}	σ_{Ref}	\bar{x}_{MEMS}	σ_{MEMS}
(s)	(m·s ⁻²)	(m·s ⁻²)	(m·s ⁻²)	(m·s ⁻²)	(s)	(m·s ⁻²)	(m·s ⁻²)	(m·s ⁻²)	(m·s ⁻²)
1.48	-0.0259	0.0001	-0.0257	0.0004	1.85	-0.0228	0.0002	-0.0234	0.0003
1.49	-0.0258	0.0001	-0.0252	0.0001	1.86	-0.0224	0.0005	-0.0224	0.0004
1.50	-0.0256	0.0002	-0.0252	0.0001	1.87	-0.0220	0.0004	-0.0225	0.0003
1.51	-0.0255	0.0002	-0.0261	0.0003	1.88	-0.0216	0.0004	-0.0221	0.0005
1.52	-0.0254	0.0003	-0.0254	0.0003	1.89	-0.0212	0.0005	-0.0207	0.0006
1.53	-0.0253	0.0003	-0.0257	0.0002	1.90	-0.0208	0.0006	-0.0213	0.0006
1.54	-0.0252	0.0004	-0.0256	0.0000	1.91	-0.0203	0.0004	-0.0198	0.0004
1.55	-0.0251	0.0004	-0.0246	0.0003	1.92	-0.0199	0.0002	-0.0194	0.0004
1.56	-0.0250	0.0004	-0.0255	0.0002	1.93	-0.0194	0.0001	-0.0192	0.0004
1.57	-0.0249	0.0005	-0.0244	0.0002	1.94	-0.0190	0.0002	-0.0188	0.0005
1.58	-0.0249	0.0005	-0.0244	0.0002	1.95	-0.0186	0.0003	-0.0190	0.0006
1.59	-0.0248	0.0005	-0.0246	0.0001	1.96	-0.0181	0.0003	-0.0176	0.0004
1.60	-0.0248	0.0005	-0.0245	0.0003	1.97	-0.0177	0.0002	-0.0176	0.0002
1.61	-0.0248	0.0005	-0.0254	0.0003	1.98	-0.0173	0.0002	-0.0176	0.0003
1.62	-0.0248	0.0002	-0.0243	0.0004	1.99	-0.0170	0.0002	-0.0168	0.0005
1.63	-0.0248	0.0004	-0.0250	0.0005	2.00	-0.0166	0.0006	-0.0170	0.0001
1.64	-0.0249	0.0004	-0.0252	0.0005	2.01	-0.0163	0.0004	-0.0166	0.0006
1.65	-0.0249	0.0004	-0.0246	0.0005	2.02	-0.0160	0.0006	-0.0159	0.0006
1.66	-0.0250	0.0006	-0.0246	0.0005	2.03	-0.0158	0.0006	-0.0159	0.0004
1.67	-0.0250	0.0006	-0.0244	0.0005	2.04	-0.0155	0.0004	-0.0158	0.0004
1.68	-0.0251	0.0005	-0.0256	0.0005	2.05	-0.0153	0.0005	-0.0155	0.0004
1.69	-0.0251	0.0004	-0.0251	0.0004	2.06	-0.0152	0.0004	-0.0153	0.0005
1.70	-0.0251	0.0003	-0.0257	0.0004	2.07	-0.0151	0.0004	-0.0148	0.0006
1.71	-0.0252	0.0004	-0.0258	0.0003	2.08	-0.0150	0.0004	-0.0153	0.0004
1.72	-0.0252	0.0006	-0.0246	0.0003	2.09	-0.0150	0.0006	-0.0145	0.0002
1.73	-0.0252	0.0006	-0.0257	0.0003	2.10	-0.0150	0.0006	-0.0147	0.0002
1.74	-0.0251	0.0001	-0.0246	0.0002	2.11	-0.0150	0.0005	-0.0152	0.0002
1.75	-0.0251	0.0003	-0.0246	0.0002	2.12	-0.0150	0.0004	-0.0156	0.0002
1.76	-0.0250	0.0002	-0.0247	0.0002	2.13	-0.0151	0.0003	-0.0155	0.0003
1.77	-0.0249	0.0001	-0.0246	0.0001	2.14	-0.0153	0.0002	-0.0147	0.0003
1.78	-0.0247	0.0002	-0.0252	0.0002	2.15	-0.0154	0.0002	-0.0154	0.0004
1.79	-0.0245	0.0004	-0.0247	0.0003	2.16	-0.0156	0.0001	-0.0152	0.0004
1.80	-0.0243	0.0003	-0.0249	0.0003	2.17	-0.0158	0.0003	-0.0153	0.0004
1.81	-0.0241	0.0003	-0.0243	0.0003	2.18	-0.0160	0.0005	-0.0164	0.0003
1.82	-0.0238	0.0002	-0.0235	0.0003	2.19	-0.0162	0.0006	-0.0159	0.0003
1.83	-0.0235	0.0002	-0.0230	0.0004	2.20	-0.0164	0.0006	-0.0168	0.0002
1.84	-0.0232	0.0002	-0.0226	0.0005	2.21	-0.0167	0.0004	-0.0172	0.0002

Time	\bar{x}_{Ref}	σ_{Ref}	\bar{x}_{MEMS}	σ_{MEMS}	Time	\bar{x}_{Ref}	σ_{Ref}	\bar{x}_{MEMS}	σ_{MEMS}
(s)	(m·s ⁻²)	(m·s ⁻²)	(m·s ⁻²)	(m·s ⁻²)	(s)	(m·s ⁻²)	(m·s ⁻²)	(m·s ⁻²)	(m·s ⁻²)
2.22	-0.0169	0.0004	-0.0171	0.0005	2.59	-0.0011	0.0004	-0.0007	0.0003
2.23	-0.0171	0.0006	-0.0173	0.0004	2.60	-0.0006	0.0003	-0.0003	0.0003
2.24	-0.0173	0.0006	-0.0169	0.0004	2.61	0.0000	0.0002	0.0002	0.0004
2.25	-0.0175	0.0001	-0.0179	0.0002	2.62	0.0005	0.0002	0.0000	0.0004
2.26	-0.0176	0.0003	-0.0173	0.0003	2.63	0.0010	0.0001	0.0015	0.0004
2.27	-0.0177	0.0002	-0.0174	0.0003	2.64	0.0015	0.0003	0.0016	0.0005
2.28	-0.0178	0.0001	-0.0184	0.0002	2.65	0.0020	0.0005	0.0018	0.0003
2.29	-0.0178	0.0002	-0.0173	0.0002	2.66	0.0025	0.0006	0.0027	0.0003
2.30	-0.0178	0.0004	-0.0180	0.0002	2.67	0.0030	0.0006	0.0028	0.0004
2.31	-0.0177	0.0003	-0.0180	0.0006	2.68	0.0035	0.0004	0.0032	0.0004
2.32	-0.0176	0.0003	-0.0173	0.0004	2.69	0.0040	0.0004	0.0045	0.0004
2.33	-0.0174	0.0002	-0.0170	0.0006	2.70	0.0044	0.0004	0.0040	0.0005
2.34	-0.0172	0.0002	-0.0166	0.0006	2.71	0.0049	0.0005	0.0054	0.0006
2.35	-0.0169	0.0002	-0.0174	0.0004	2.72	0.0054	0.0006	0.0057	0.0004
2.36	-0.0165	0.0002	-0.0165	0.0005	2.73	0.0059	0.0004	0.0057	0.0002
2.37	-0.0161	0.0005	-0.0166	0.0004	2.74	0.0064	0.0006	0.0057	0.0003
2.38	-0.0156	0.0004	-0.0162	0.0004	2.75	0.0070	0.0006	0.0065	0.0005
2.39	-0.0151	0.0004	-0.0145	0.0004	2.76	0.0075	0.0001	0.0078	0.0004
2.40	-0.0145	0.0005	-0.0150	0.0006	2.77	0.0080	0.0003	0.0080	0.0004
2.41	-0.0139	0.0006	-0.0134	0.0006	2.78	0.0085	0.0004	0.0089	0.0003
2.42	-0.0132	0.0004	-0.0127	0.0005	2.79	0.0090	0.0003	0.0092	0.0002
2.43	-0.0125	0.0002	-0.0122	0.0004	2.80	0.0095	0.0002	0.0090	0.0002
2.44	-0.0118	0.0001	-0.0115	0.0003	2.81	0.0100	0.0001	0.0104	0.0004
2.45	-0.0110	0.0002	-0.0115	0.0002	2.82	0.0105	0.0002	0.0101	0.0006
2.46	-0.0103	0.0003	-0.0105	0.0002	2.83	0.0110	0.0002	0.0104	0.0005
2.47	-0.0095	0.0003	-0.0101	0.0001	2.84	0.0114	0.0004	0.0112	0.0004
2.48	-0.0087	0.0002	-0.0090	0.0003	2.85	0.0118	0.0004	0.0116	0.0003
2.49	-0.0079	0.0002	-0.0077	0.0005	2.86	0.0121	0.0004	0.0125	0.0004
2.50	-0.0072	0.0006	-0.0067	0.0006	2.87	0.0125	0.0006	0.0120	0.0006
2.51	-0.0064	0.0004	-0.0059	0.0006	2.88	0.0128	0.0006	0.0133	0.0006
2.52	-0.0057	0.0005	-0.0063	0.0004	2.89	0.0130	0.0005	0.0132	0.0004
2.53	-0.0050	0.0004	-0.0050	0.0004	2.90	0.0132	0.0004	0.0130	0.0005
2.54	-0.0043	0.0004	-0.0048	0.0006	2.91	0.0133	0.0003	0.0128	0.0006
2.55	-0.0036	0.0004	-0.0041	0.0006	2.92	0.0134	0.0004	0.0131	0.0004
2.56	-0.0029	0.0006	-0.0024	0.0001	2.93	0.0135	0.0006	0.0139	0.0005
2.57	-0.0023	0.0006	-0.0028	0.0002	2.94	0.0134	0.0006	0.0134	0.0004
2.58	-0.0017	0.0005	-0.0012	0.0002	2.95	0.0134	0.0004	0.0136	0.0001

Time	\bar{x}_{Ref}	σ_{Ref}	\bar{x}_{MEMS}	σ_{MEMS}	Time	\bar{x}_{Ref}	σ_{Ref}	\bar{x}_{MEMS}	σ_{MEMS}
(s)	(m·s ⁻²)	(m·s ⁻²)	(m·s ⁻²)	(m·s ⁻²)	(s)	(m·s ⁻²)	(m·s ⁻²)	(m·s ⁻²)	(m·s ⁻²)
2.96	0.0133	0.0005	0.0140	0.0001	3.33	0.0155	0.0002	0.0160	0.0005
2.97	0.0131	0.0004	0.0126	0.0001	3.34	0.0161	0.0003	0.0156	0.0001
2.98	0.0129	0.0004	0.0131	0.0002	3.35	0.0167	0.0003	0.0172	0.0002
2.99	0.0126	0.0004	0.0125	0.0002	3.36	0.0173	0.0004	0.0177	0.0002
3.00	0.0124	0.0006	0.0121	0.0003	3.37	0.0179	0.0004	0.0181	0.0001
3.01	0.0120	0.0006	0.0120	0.0003	3.38	0.0184	0.0004	0.0186	0.0000
3.02	0.0117	0.0005	0.0116	0.0004	3.39	0.0189	0.0005	0.0184	0.0000
3.03	0.0114	0.0004	0.0115	0.0004	3.40	0.0193	0.0005	0.0198	0.0001
3.04	0.0110	0.0003	0.0108	0.0004	3.41	0.0196	0.0005	0.0197	0.0002
3.05	0.0106	0.0002	0.0108	0.0005	3.42	0.0199	0.0005	0.0197	0.0004
3.06	0.0103	0.0002	0.0103	0.0005	3.43	0.0201	0.0005	0.0204	0.0006
3.07	0.0100	0.0001	0.0099	0.0005	3.44	0.0203	0.0002	0.0201	0.0007
3.08	0.0096	0.0003	0.0095	0.0005	3.45	0.0204	0.0004	0.0201	0.0006
3.09	0.0094	0.0005	0.0093	0.0005	3.46	0.0204	0.0004	0.0209	0.0006
3.10	0.0091	0.0006	0.0092	0.0002	3.47	0.0204	0.0004	0.0199	0.0005
3.11	0.0089	0.0006	0.0089	0.0004	3.48	0.0202	0.0006	0.0208	0.0003
3.12	0.0087	0.0004	0.0087	0.0004	3.49	0.0201	0.0005	0.0203	0.0001
3.13	0.0086	0.0004	0.0086	0.0004	3.50	0.0199	0.0004	0.0196	0.0000
3.14	0.0085	0.0004	0.0079	0.0006	3.51	0.0196	0.0003	0.0189	0.0002
3.15	0.0084	0.0005	0.0078	0.0006	3.52	0.0193	0.0004	0.0188	0.0002
3.16	0.0084	0.0006	0.0090	0.0005	3.53	0.0190	0.0006	0.0192	0.0001
3.17	0.0085	0.0004	0.0080	0.0004	3.54	0.0186	0.0006	0.0186	0.0000
3.18	0.0086	0.0005	0.0091	0.0003	3.55	0.0182	0.0004	0.0187	0.0001
3.19	0.0087	0.0006	0.0092	0.0004	3.56	0.0179	0.0005	0.0181	0.0002
3.20	0.0089	0.0004	0.0092	0.0006	3.57	0.0175	0.0004	0.0169	0.0000
3.21	0.0092	0.0005	0.0095	0.0006	3.58	0.0171	0.0004	0.0175	0.0002
3.22	0.0095	0.0004	0.0090	0.0001	3.59	0.0168	0.0004	0.0164	0.0003
3.23	0.0099	0.0002	0.0097	0.0003	3.60	0.0164	0.0006	0.0159	0.0004
3.24	0.0103	0.0002	0.0097	0.0002	3.61	0.0161	0.0006	0.0160	0.0003
3.25	0.0107	0.0002	0.0105	0.0001	3.62	0.0159	0.0005	0.0157	0.0002
3.26	0.0112	0.0003	0.0115	0.0002	3.63	0.0156	0.0004	0.0160	0.0001
3.27	0.0118	0.0003	0.0123	0.0004	3.64	0.0154	0.0003	0.0149	0.0003
3.28	0.0123	0.0004	0.0129	0.0003	3.65	0.0153	0.0002	0.0159	0.0005
3.29	0.0129	0.0001	0.0123	0.0003	3.66	0.0152	0.0002	0.0154	0.0006
3.30	0.0136	0.0001	0.0136	0.0002	3.67	0.0152	0.0001	0.0150	0.0004
3.31	0.0142	0.0001	0.0137	0.0004	3.68	0.0152	0.0003	0.0147	0.0002
3.32	0.0148	0.0002	0.0143	0.0003	3.69	0.0152	0.0005	0.0149	0.0001

Time	\bar{x}_{Ref}	σ_{Ref}	\bar{x}_{MEMS}	σ_{MEMS}	Time	\bar{x}_{Ref}	σ_{Ref}	\bar{x}_{MEMS}	σ_{MEMS}
(s)	(m·s ⁻²)	(m·s ⁻²)	(m·s ⁻²)	(m·s ⁻²)	(s)	(m·s ⁻²)	(m·s ⁻²)	(m·s ⁻²)	(m·s ⁻²)
3.70	0.0153	0.0006	0.0158	0.0004	4.07	0.0189	0.0003	0.0189	0.0003
3.71	0.0155	0.0006	0.0155	0.0005	4.08	0.0187	0.0002	0.0187	0.0003
3.72	0.0157	0.0004	0.0160	0.0004	4.09	0.0186	0.0002	0.0186	0.0002
3.73	0.0159	0.0004	0.0167	0.0001	4.10	0.0184	0.0002	0.0184	0.0000
3.74	0.0162	0.0004	0.0158	0.0001	4.11	0.0183	0.0006	0.0183	0.0003
3.75	0.0165	0.0005	0.0167	0.0003	4.12	0.0182	0.0004	0.0182	0.0002
3.76	0.0169	0.0006	0.0167	0.0003	4.13	0.0181	0.0006	0.0182	0.0002
3.77	0.0172	0.0006	0.0170	0.0002	4.14	0.0181	0.0006	0.0181	0.0002
3.78	0.0176	0.0006	0.0175	0.0000	4.15	0.0181	0.0002	0.0180	0.0001
3.79	0.0180	0.0005	0.0179	0.0003	4.16	0.0181	0.0001	0.0180	0.0003
3.80	0.0184	0.0004	0.0185	0.0004	4.17	0.0181	0.0003	0.0181	0.0003
3.81	0.0187	0.0003	0.0186	0.0000	4.18	0.0181	0.0005	0.0181	0.0004
3.82	0.0191	0.0004	0.0193	0.0002	4.19	0.0181	0.0006	0.0182	0.0005
3.83	0.0195	0.0006	0.0195	0.0002	4.20	0.0182	0.0006	0.0185	0.0005
3.84	0.0198	0.0006	0.0198	0.0002	4.21	0.0182	0.0004	0.0180	0.0005
3.85	0.0201	0.0001	0.0200	0.0003	4.22	0.0183	0.0004	0.0185	0.0005
3.86	0.0204	0.0003	0.0199	0.0003	4.23	0.0184	0.0004	0.0182	0.0005
3.87	0.0206	0.0002	0.0209	0.0004	4.24	0.0185	0.0005	0.0182	0.0005
3.88	0.0208	0.0001	0.0205	0.0004	4.25	0.0186	0.0006	0.0185	0.0004
3.89	0.0209	0.0002	0.0212	0.0004	4.26	0.0187	0.0006	0.0185	0.0004
3.90	0.0210	0.0004	0.0215	0.0003	4.27	0.0189	0.0006	0.0184	0.0003
3.91	0.0211	0.0003	0.0212	0.0003	4.28	0.0190	0.0005	0.0185	0.0003
3.92	0.0211	0.0003	0.0213	0.0002	4.29	0.0191	0.0004	0.0195	0.0006
3.93	0.0211	0.0002	0.0209	0.0002	4.30	0.0192	0.0003	0.0192	0.0006
3.94	0.0211	0.0002	0.0214	0.0005	4.31	0.0193	0.0004	0.0197	0.0005
3.95	0.0210	0.0002	0.0206	0.0004	4.32	0.0194	0.0006	0.0197	0.0004
3.96	0.0209	0.0002	0.0208	0.0004	4.33	0.0194	0.0006	0.0190	0.0003
3.97	0.0208	0.0005	0.0208	0.0005	4.34	0.0195	0.0001	0.0200	0.0004
3.98	0.0206	0.0004	0.0208	0.0006	4.35	0.0195	0.0003	0.0191	0.0002
3.99	0.0204	0.0004	0.0206	0.0004	4.36	0.0196	0.0002	0.0191	0.0002
4.00	0.0202	0.0005	0.0200	0.0002	4.37	0.0196	0.0001	0.0193	0.0002
4.01	0.0200	0.0006	0.0200	0.0001	4.38	0.0196	0.0002	0.0193	0.0003
4.02	0.0198	0.0004	0.0197	0.0004	4.39	0.0195	0.0004	0.0200	0.0003
4.03	0.0196	0.0002	0.0194	0.0005	4.40	0.0195	0.0003	0.0190	0.0004
4.04	0.0194	0.0001	0.0196	0.0004	4.41	0.0194	0.0003	0.0199	0.0004
4.05	0.0192	0.0002	0.0192	0.0001	4.42	0.0193	0.0002	0.0196	0.0004
4.06	0.0190	0.0003	0.0191	0.0001	4.43	0.0192	0.0002	0.0190	0.0003

Time	\bar{x}_{Ref}	σ_{Ref}	\bar{x}_{MEMS}	σ_{MEMS}	Time	\bar{x}_{Ref}	σ_{Ref}	\bar{x}_{MEMS}	σ_{MEMS}
(s)	(m·s ⁻²)	(m·s ⁻²)	(m·s ⁻²)	(m·s ⁻²)	(s)	(m·s ⁻²)	(m·s ⁻²)	(m·s ⁻²)	(m·s ⁻²)
4.44	0.0191	0.0002	0.0184	0.0003	4.81	0.0197	0.0005	0.0197	0.0002
4.45	0.0190	0.0002	0.0185	0.0002	4.82	0.0194	0.0006	0.0195	0.0002
4.46	0.0189	0.0005	0.0191	0.0002	4.83	0.0191	0.0005	0.0192	0.0004
4.47	0.0187	0.0004	0.0187	0.0005	4.84	0.0188	0.0004	0.0188	0.0006
4.48	0.0186	0.0004	0.0190	0.0004	4.85	0.0184	0.0003	0.0184	0.0005
4.49	0.0184	0.0005	0.0186	0.0004	4.86	0.0180	0.0002	0.0180	0.0004
4.50	0.0183	0.0006	0.0177	0.0005	4.87	0.0175	0.0002	0.0178	0.0003
4.51	0.0182	0.0004	0.0185	0.0006	4.88	0.0170	0.0005	0.0177	0.0004
4.52	0.0181	0.0002	0.0177	0.0004	4.89	0.0164	0.0004	0.0160	0.0006
4.53	0.0180	0.0001	0.0174	0.0002	4.90	0.0158	0.0003	0.0160	0.0006
4.54	0.0179	0.0002	0.0177	0.0001	4.91	0.0152	0.0004	0.0150	0.0004
4.55	0.0178	0.0003	0.0177	0.0004	4.92	0.0146	0.0006	0.0143	0.0004
4.56	0.0178	0.0003	0.0181	0.0005	4.93	0.0139	0.0006	0.0138	0.0005
4.57	0.0178	0.0002	0.0173	0.0004	4.94	0.0132	0.0004	0.0131	0.0006
4.58	0.0178	0.0002	0.0184	0.0001	4.95	0.0125	0.0005	0.0126	0.0004
4.59	0.0178	0.0002	0.0180	0.0002	4.96	0.0118	0.0004	0.0117	0.0002
4.60	0.0179	0.0006	0.0177	0.0002	4.97	0.0111	0.0004	0.0113	0.0003
4.61	0.0180	0.0004	0.0175	0.0003	4.98	0.0104	0.0004	0.0105	0.0005
4.62	0.0181	0.0006	0.0178	0.0003	4.99	0.0097	0.0006	0.0097	0.0003
4.63	0.0183	0.0006	0.0187	0.0004	5.00	0.0091	0.0006	0.0090	0.0003
4.64	0.0184	0.0004	0.0184	0.0004					
4.65	0.0186	0.0004	0.0188	0.0004					
4.66	0.0188	0.0006	0.0195	0.0005					
4.67	0.0189	0.0006	0.0185	0.0003					
4.68	0.0191	0.0005	0.0193	0.0003					
4.69	0.0193	0.0004	0.0191	0.0004					
4.70	0.0195	0.0003	0.0192	0.0004					
4.71	0.0197	0.0002	0.0196	0.0004					
4.72	0.0198	0.0002	0.0197	0.0005					
4.73	0.0199	0.0001	0.0200	0.0006					
4.74	0.0200	0.0003	0.0199	0.0004					
4.75	0.0201	0.0005	0.0203	0.0002					
4.76	0.0201	0.0006	0.0202	0.0003					
4.77	0.0201	0.0006	0.0201	0.0005					
4.78	0.0201	0.0004	0.0200	0.0004					
4.79	0.0200	0.0004	0.0199	0.0004					
4.80	0.0199	0.0004	0.0199	0.0003					

Table A.11 – Mean values and standard deviations for the 5 Hz periodic wave excitation

Time	\bar{x}_{Ref}	σ_{Ref}	\bar{x}_{MEMS}	σ_{MEMS}
(s)	(m·s ⁻²)	(m·s ⁻²)	(m·s ⁻²)	(m·s ⁻²)
0.00	0.0063	0.0012	0.0065	0.0012
0.01	0.0147	0.0014	0.0152	0.0014
0.02	0.0190	0.0016	0.0195	0.0016
0.03	0.0170	0.0019	0.0175	0.0020
0.04	0.0152	0.0020	0.0156	0.0020
0.05	0.0175	0.0018	0.0180	0.0019
0.06	0.0211	0.0018	0.0217	0.0019
0.07	0.0205	0.0018	0.0211	0.0018
0.08	0.0101	0.0017	0.0104	0.0018
0.09	-0.0134	0.0017	-0.0138	0.0018
0.10	-0.0422	0.0015	-0.0435	0.0015
0.11	-0.0556	0.0013	-0.0574	0.0013
0.12	-0.0408	0.0014	-0.0420	0.0015
0.13	-0.0120	0.0015	-0.0124	0.0015
0.14	0.0090	0.0016	0.0093	0.0017
0.15	0.0212	0.0019	0.0219	0.0020
0.16	0.0310	0.0018	0.0320	0.0019
0.17	0.0311	0.0013	0.0321	0.0014
0.18	0.0178	0.0012	0.0184	0.0012
0.19	0.0054	0.0011	0.0056	0.0012
0.20	0.0064	0.0012	0.0065	0.0012

Table A.12 – Mean values and standard deviations for the 2 Hz periodic wave excitation

Time	\bar{x}_{Ref}	σ_{Ref}	\bar{x}_{MEMS}	σ_{MEMS}	Time	\bar{x}_{Ref}	σ_{Ref}	\bar{x}_{MEMS}	σ_{MEMS}
(s)	(m·s ⁻²)	(m·s ⁻²)	(m·s ⁻²)	(m·s ⁻²)	(s)	(m·s ⁻²)	(m·s ⁻²)	(m·s ⁻²)	(m·s ⁻²)
0.00	-0.0098	0.0018	-0.010	0.002	0.37	0.01428	0.00214	-0.010	0.002
0.01	-0.0075	0.0016	-0.008	0.002	0.38	-0.00652	0.00189	-0.008	0.002
0.02	-0.0054	0.0015	-0.006	0.002	0.39	-0.03759	0.00153	-0.006	0.002
0.03	-0.0085	0.0015	-0.009	0.002	0.40	-0.04787	0.00152	-0.009	0.002
0.04	-0.0174	0.0013	-0.018	0.001	0.41	-0.02104	0.00165	-0.018	0.001
0.05	-0.0292	0.0015	-0.030	0.002	0.42	0.01289	0.00145	-0.030	0.002
0.06	-0.0365	0.0018	-0.038	0.002	0.43	0.01655	0.00133	-0.038	0.002
0.07	-0.0273	0.0018	-0.028	0.002	0.44	-0.00386	0.00134	-0.028	0.002
0.08	0.0055	0.0018	0.006	0.002	0.45	-0.01621	0.00162	0.006	0.002
0.09	0.0425	0.0016	0.044	0.002	0.46	-0.00956	0.00195	0.044	0.002
0.10	0.0471	0.0016	0.049	0.002	0.47	0.00051	0.00210	0.049	0.002
0.11	0.0146	0.0016	0.015	0.002	0.48	0.00028	0.00194	0.015	0.002
0.12	-0.0163	0.0015	-0.017	0.001	0.49	-0.00645	0.00180	-0.017	0.001
0.13	-0.0157	0.0016	-0.016	0.002	0.50	-0.00961	0.00179	-0.016	0.002
0.14	0.0034	0.0014	0.003	0.001					
0.15	0.0131	0.0013	0.013	0.001					
0.16	0.0062	0.0014	0.006	0.001					
0.17	-0.0043	0.0015	-0.004	0.002					
0.18	-0.0066	0.0015	-0.007	0.002					
0.19	-0.0024	0.0015	-0.002	0.002					
0.20	0.0001	0.0016	0.000	0.002					
0.21	-0.0016	0.0015	-0.002	0.002					
0.22	-0.0025	0.0017	-0.003	0.002					
0.23	0.0003	0.0018	0.000	0.002					
0.24	0.0038	0.0015	0.004	0.002					
0.25	0.0043	0.0016	0.004	0.002					
0.26	0.0024	0.0017	0.002	0.002					
0.27	0.0010	0.0015	0.001	0.002					
0.28	0.0021	0.0016	0.002	0.002					
0.29	0.0057	0.0019	0.006	0.002					
0.30	0.0098	0.0021	0.010	0.002					
0.31	0.0117	0.0021	0.012	0.002					
0.32	0.0107	0.0019	0.011	0.002					
0.33	0.0087	0.0018	0.009	0.002					
0.34	0.0090	0.0018	0.009	0.002					
0.35	0.0129	0.0019	0.013	0.002					
0.36	0.0174	0.0021	0.018	0.002					

Table A.13 – Mean values and standard deviations for the 1 Hz periodic wave excitation

Time	\bar{x}_{Ref}	σ_{Ref}	\bar{x}_{MEMS}	σ_{MEMS}	Time	\bar{x}_{Ref}	σ_{Ref}	\bar{x}_{MEMS}	σ_{MEMS}
(s)	(m·s ⁻²)	(m·s ⁻²)	(m·s ⁻²)	(m·s ⁻²)	(s)	(m·s ⁻²)	(m·s ⁻²)	(m·s ⁻²)	(m·s ⁻²)
0.00	-0.0012	0.0082	0.001	0.005	0.37	0.0015	0.0009	0.007	0.002
0.01	-0.0029	0.0080	0.001	0.005	0.38	0.0010	0.0024	0.006	0.003
0.02	-0.0007	0.0082	0.003	0.006	0.39	0.0026	0.0043	0.005	0.004
0.03	0.0022	0.0082	0.004	0.006	0.40	0.0036	0.0053	0.004	0.004
0.04	0.0019	0.0081	0.003	0.006	0.41	0.0014	0.0053	0.002	0.004
0.05	-0.0015	0.0083	0.001	0.006	0.42	-0.0026	0.0060	0.001	0.005
0.06	-0.0037	0.0083	0.000	0.006	0.43	-0.0043	0.0066	0.001	0.004
0.07	-0.0029	0.0101	0.000	0.007	0.44	-0.0019	0.0069	0.003	0.004
0.08	-0.0015	0.0108	-0.001	0.008	0.45	0.0018	0.0075	0.004	0.005
0.09	-0.0014	0.0080	-0.002	0.005	0.46	0.0024	0.0076	0.004	0.004
0.10	-0.0020	0.0054	-0.001	0.003	0.47	-0.0008	0.0080	0.002	0.005
0.11	-0.0021	0.0052	0.000	0.004	0.48	-0.0037	0.0081	0.001	0.005
0.12	-0.0017	0.0038	0.000	0.003	0.49	-0.0027	0.0082	0.002	0.005
0.13	-0.0019	0.0030	-0.004	0.002	0.50	0.0010	0.0086	0.004	0.005
0.14	-0.0047	0.0027	-0.008	0.002	0.51	0.0025	0.0084	0.004	0.005
0.15	-0.0108	0.0018	-0.012	0.002	0.52	-0.0002	0.0087	0.002	0.006
0.16	-0.0161	0.0017	-0.014	0.002	0.53	-0.0035	0.0087	0.001	0.006
0.17	-0.0121	0.0014	-0.009	0.002	0.54	-0.0030	0.0087	0.002	0.006
0.18	0.0059	0.0014	0.007	0.002	0.55	0.0007	0.0089	0.004	0.005
0.19	0.0282	0.0012	0.025	0.002	0.56	0.0026	0.0087	0.004	0.005
0.20	0.0335	0.0007	0.025	0.002	0.57	0.0004	0.0096	0.002	0.006
0.21	0.0141	0.0008	0.003	0.002	0.58	-0.0025	0.0113	0.002	0.008
0.22	-0.0092	0.0007	-0.019	0.002	0.59	-0.0020	0.0110	0.003	0.007
0.23	-0.0123	0.0006	-0.016	0.001	0.60	0.0011	0.0080	0.006	0.004
0.24	0.0015	0.0004	0.004	0.001	0.61	0.0022	0.0059	0.006	0.003
0.25	0.0101	0.0002	0.013	0.001	0.62	-0.0002	0.0055	0.005	0.003
0.26	0.0041	0.0003	0.003	0.001	0.63	-0.0030	0.0038	0.003	0.002
0.27	-0.0060	0.0003	-0.010	0.001	0.64	-0.0027	0.0032	0.003	0.003
0.28	-0.0076	0.0005	-0.008	0.001	0.65	0.0006	0.0028	0.003	0.002
0.29	-0.0007	0.0005	0.003	0.001	0.66	0.0033	0.0020	0.003	0.002
0.30	0.0058	0.0003	0.010	0.001	0.67	0.0031	0.0019	0.002	0.002
0.31	0.0058	0.0002	0.005	0.001	0.68	0.0012	0.0015	0.003	0.001
0.32	0.0017	0.0003	-0.003	0.001	0.69	0.0002	0.0013	0.007	0.001
0.33	-0.0008	0.0002	-0.006	0.001	0.70	0.0011	0.0010	0.011	0.002
0.34	0.0005	0.0004	-0.003	0.001	0.71	0.0030	0.0007	0.014	0.002
0.35	0.0030	0.0008	0.003	0.002	0.72	0.0047	0.0008	0.014	0.001
0.36	0.0032	0.0008	0.007	0.002	0.73	0.0056	0.0007	0.012	0.001

Time	\bar{x}_{Ref}	σ_{Ref}	\bar{x}_{MEMS}	σ_{MEMS}
(s)	(m·s ⁻²)	(m·s ⁻²)	(m·s ⁻²)	(m·s ⁻²)
0.74	0.0057	0.0007	0.011	0.001
0.75	0.0020	0.0006	0.008	0.002
0.76	-0.0083	0.0003	-0.001	0.002
0.77	-0.0201	0.0007	-0.014	0.002
0.78	-0.0206	0.0009	-0.019	0.001
0.79	-0.0066	0.0006	-0.007	0.001
0.80	0.0066	0.0003	0.009	0.001
0.81	0.0045	0.0002	0.009	0.001
0.82	-0.0065	0.0004	-0.002	0.001
0.83	-0.0108	0.0003	-0.007	0.002
0.84	-0.0060	0.0005	-0.003	0.002
0.85	-0.0021	0.0021	0.002	0.003
0.86	-0.0037	0.0045	-0.001	0.005
0.87	-0.0052	0.0060	-0.004	0.006
0.88	-0.0018	0.0053	-0.001	0.004
0.89	0.0026	0.0053	0.004	0.004
0.90	0.0021	0.0067	0.005	0.005
0.91	-0.0015	0.0063	0.002	0.004
0.92	-0.0024	0.0069	0.001	0.005
0.93	0.0005	0.0074	0.002	0.006
0.94	0.0023	0.0071	0.004	0.005
0.95	0.0002	0.0078	0.003	0.006
0.96	-0.0025	0.0076	0.002	0.005
0.97	-0.0017	0.0079	0.002	0.005
0.98	0.0014	0.0081	0.003	0.006
0.99	0.0023	0.0078	0.004	0.006
1.00	-0.0004	0.0083	0.002	0.005

Table A.14 – Mean values and standard deviations for the 0.5 Hz periodic wave excitation

Time	\bar{x}_{Ref}	σ_{Ref}	\bar{x}_{MEMS}	σ_{MEMS}	Time	\bar{x}_{Ref}	σ_{Ref}	\bar{x}_{MEMS}	σ_{MEMS}
(s)	(m·s ⁻²)	(m·s ⁻²)	(m·s ⁻²)	(m·s ⁻²)	(s)	(m·s ⁻²)	(m·s ⁻²)	(m·s ⁻²)	(m·s ⁻²)
0.00	-0.0091	0.0150	-0.0382	0.1023	0.37	-0.0091	0.0150	0.1978	0.1630
0.01	0.0917	0.0117	0.0426	0.0947	0.38	0.0917	0.0117	0.0963	0.2227
0.02	0.0705	0.0124	0.1122	0.0896	0.39	0.0705	0.0124	0.0028	0.2814
0.03	-0.0618	0.0115	0.0629	0.0928	0.40	-0.0618	0.0115	0.0562	0.2956
0.04	-0.1578	0.0071	-0.0704	0.1032	0.41	-0.1578	0.0071	0.0821	0.2857
0.05	-0.1234	0.0113	-0.1389	0.1163	0.42	-0.1234	0.0113	-0.0298	0.2604
0.06	-0.0308	0.0095	-0.0747	0.1238	0.43	-0.0308	0.0095	-0.1011	0.2640
0.07	0.0018	0.0065	0.0243	0.1221	0.44	0.0018	0.0065	0.0188	0.3070
0.08	-0.0418	0.0065	0.0395	0.1190	0.45	-0.0418	0.0065	0.1828	0.3369
0.09	-0.0924	0.0048	-0.0264	0.1216	0.46	-0.0924	0.0048	0.1511	0.3263
0.10	-0.0967	0.0067	-0.0882	0.1277	0.47	-0.0967	0.0067	-0.0841	0.2933
0.11	-0.0651	0.0055	-0.0923	0.1322	0.48	-0.0651	0.0055	-0.3046	0.2783
0.12	-0.0408	0.0051	-0.0579	0.1314	0.49	-0.0408	0.0051	-0.3325	0.2891
0.13	-0.0445	0.0060	-0.0334	0.1286	0.50	-0.0445	0.0060	-0.2035	0.2949
0.14	-0.0580	0.0036	-0.0388	0.1284	0.51	-0.0580	0.0036	-0.0880	0.2758
0.15	-0.0552	0.0071	-0.0537	0.1307	0.52	-0.0552	0.0071	-0.0764	0.2248
0.16	-0.0221	0.0058	-0.0516	0.1324	0.53	-0.0221	0.0058	-0.0838	0.1634
0.17	0.0745	0.0080	-0.0201	0.1308	0.54	0.0745	0.0080	-0.0115	0.1208
0.18	0.2842	0.0156	0.0582	0.1258	0.55	0.2842	0.0156	0.0577	0.1219
0.19	0.5438	0.0130	0.1976	0.1195	0.56	0.5438	0.0130	-0.0350	0.1532
0.20	0.5982	0.0183	0.3296	0.1171	0.57	0.5982	0.0183	-0.2457	0.1512
0.21	0.2482	0.0255	0.2915	0.1254	0.58	0.2482	0.0255	-0.3359	0.1369
0.22	-0.2933	0.0127	0.0183	0.1314	0.59	-0.2933	0.0127	-0.1881	0.1339
0.23	-0.5133	0.0187	-0.2808	0.1172	0.60	-0.5133	0.0187	0.0422	0.1144
0.24	-0.1768	0.0275	-0.3041	0.1036	0.61	-0.1768	0.0275	0.1326	0.1121
0.25	0.3380	0.0184	-0.0519	0.1070	0.62	0.3380	0.0184	0.0390	0.1200
0.26	0.4096	0.0317	0.1084	0.1187	0.63	0.4096	0.0317	-0.0989	0.1172
0.27	-0.1317	0.0444	-0.1359	0.1528	0.64	-0.1317	0.0444	-0.1269	0.1158
0.28	-0.7830	0.0347	-0.6467	0.1778	0.65	-0.7830	0.0347	-0.0180	0.1153
0.29	-0.9075	0.0172	-0.9630	0.1563	0.66	-0.9075	0.0172	0.1290	0.1372
0.30	-0.4248	0.0188	-0.7737	0.1313	0.67	-0.4248	0.0188	0.2034	0.1595
0.31	0.1389	0.0240	-0.2089	0.1574	0.68	0.1389	0.0240	0.1849	0.1762
0.32	0.2746	0.0244	0.2725	0.2278	0.69	0.2746	0.0244	0.1277	0.1860
0.33	0.0320	0.0194	0.3145	0.2986	0.70	0.0320	0.0194	0.0679	0.1622
0.34	-0.1473	0.0208	0.0557	0.2986	0.71	-0.1473	0.0208	0.0030	0.1244
0.35	-0.0288	0.0288	-0.0598	0.2549	0.72	-0.0288	0.0288	-0.0377	0.1118
0.36	0.1901	0.0408	0.0908	0.2052	0.73	0.1901	0.0408	0.0110	0.1189

Time	\bar{x}_{Ref}	σ_{Ref}	\bar{x}_{MEMS}	σ_{MEMS}	Time	\bar{x}_{Ref}	σ_{Ref}	\bar{x}_{MEMS}	σ_{MEMS}
(s)	(m·s ⁻²)	(m·s ⁻²)	(m·s ⁻²)	(m·s ⁻²)	(s)	(m·s ⁻²)	(m·s ⁻²)	(m·s ⁻²)	(m·s ⁻²)
0.74	0.0670	0.0152	0.1278	0.1437	1.11	-0.6389	0.0372	-0.6605	0.2009
0.75	-0.0269	0.0109	0.1715	0.1710	1.12	0.1720	0.0114	-0.5950	0.1924
0.76	-0.1261	0.0262	0.0734	0.1922	1.13	0.4881	0.0186	0.1865	0.1826
0.77	-0.1443	0.0468	-0.0328	0.2144	1.14	0.1296	0.0143	0.5292	0.1942
0.78	-0.0889	0.0390	-0.0053	0.2468	1.15	-0.2620	0.0077	0.2055	0.2029
0.79	-0.0656	0.0148	0.0677	0.2759	1.16	-0.2402	0.0140	-0.1799	0.2007
0.80	-0.1464	0.0306	-0.0241	0.2713	1.17	0.0283	0.0067	-0.1715	0.1935
0.81	-0.2756	0.0382	-0.3074	0.2388	1.18	0.1646	0.0054	0.0862	0.1870
0.82	-0.3215	0.0208	-0.5401	0.2135	1.19	0.0663	0.0069	0.2167	0.1863
0.83	-0.2190	0.0154	-0.4522	0.2067	1.20	-0.1237	0.0075	0.1111	0.1841
0.84	-0.0472	0.0270	-0.0487	0.2054	1.21	-0.3050	0.0109	-0.0709	0.1705
0.85	0.0609	0.0172	0.3541	0.2011	1.22	-0.3868	0.0156	-0.2002	0.1516
0.86	0.0678	0.0158	0.4273	0.1801	1.23	-0.2015	0.0230	-0.2147	0.1503
0.87	0.0261	0.0241	0.1611	0.1512	1.24	0.1741	0.0284	-0.0180	0.1602
0.88	-0.0413	0.0109	-0.1346	0.1504	1.25	0.3275	0.0308	0.3356	0.1721
0.89	-0.1384	0.0314	-0.1773	0.1940	1.26	0.1028	0.0312	0.5477	0.1838
0.90	-0.1939	0.0501	-0.0152	0.2281	1.27	-0.1263	0.0286	0.4612	0.1867
0.91	-0.0987	0.0378	0.0847	0.2279	1.28	-0.0421	0.0229	0.2931	0.1890
0.92	0.1230	0.0136	0.0169	0.2606	1.29	0.1892	0.0200	0.2846	0.1749
0.93	0.2785	0.0117	-0.0601	0.2991	1.30	0.2475	0.0152	0.3650	0.1547
0.94	0.2056	0.0206	-0.0311	0.3110	1.31	0.0824	0.0084	0.3096	0.1635
0.95	-0.0290	0.0207	-0.0029	0.3512	1.32	-0.1135	0.0126	0.0794	0.1821
0.96	-0.2207	0.0169	-0.0710	0.3615	1.33	-0.1767	0.0168	-0.1426	0.1959
0.97	-0.3840	0.0411	-0.1640	0.3015	1.34	-0.1232	0.0177	-0.2239	0.1922
0.98	-0.8587	0.0789	-0.3452	0.2519	1.35	-0.0787	0.0167	-0.2219	0.1534
0.99	-1.6379	0.1371	-0.9663	0.3147	1.36	-0.1221	0.0236	-0.2034	0.1171
1.00	-1.6808	0.1726	-1.9309	0.4765	1.37	-0.2231	0.0349	-0.1359	0.0939
1.01	0.0496	0.1315	-2.0194	0.5798	1.38	-0.3032	0.0293	-0.0431	0.0794
1.02	2.4848	0.0921	-0.1400	0.5684	1.39	-0.3017	0.0158	-0.0413	0.1072
1.03	2.9040	0.1318	2.4973	0.5008	1.40	-0.2042	0.0360	-0.1215	0.1242
1.04	0.5340	0.0795	3.0385	0.3935	1.41	-0.0610	0.0502	-0.1246	0.1276
1.05	-1.8672	0.0673	0.6968	0.2624	1.42	0.0479	0.0481	-0.0185	0.1335
1.06	-1.5494	0.0937	-1.7540	0.2214	1.43	0.0875	0.0348	0.0215	0.1423
1.07	0.5419	0.0298	-1.5324	0.2284	1.44	0.0748	0.0225	-0.1029	0.1333
1.08	1.4512	0.0553	0.5092	0.2011	1.45	0.0375	0.0198	-0.2354	0.1118
1.09	0.4008	0.0401	1.4731	0.2090	1.46	0.0006	0.0210	-0.1663	0.1062
1.10	-0.7638	0.0234	0.5029	0.2070	1.47	-0.0230	0.0205	0.0955	0.1130

Time	\bar{x}_{Ref}	σ_{Ref}	\bar{x}_{MEMS}	σ_{MEMS}	Time	\bar{x}_{Ref}	σ_{Ref}	\bar{x}_{MEMS}	σ_{MEMS}
(s)	(m·s ⁻²)	(m·s ⁻²)	(m·s ⁻²)	(m·s ⁻²)	(s)	(m·s ⁻²)	(m·s ⁻²)	(m·s ⁻²)	(m·s ⁻²)
1.48	-0.0461	0.0187	0.3298	0.1364	1.85	-0.1345	0.0189	-0.4841	0.1134
1.49	-0.0762	0.0230	0.3430	0.1461	1.86	-0.1700	0.0194	-0.5031	0.1368
1.50	-0.0847	0.0258	0.1613	0.1284	1.87	-0.1231	0.0169	-0.1607	0.1736
1.51	-0.0445	0.0200	-0.0123	0.1210	1.88	-0.0305	0.0083	0.1596	0.1824
1.52	0.0129	0.0088	-0.0353	0.1460	1.89	0.0686	0.0204	0.1755	0.1637
1.53	0.0227	0.0247	0.0180	0.1806	1.90	0.0915	0.0290	0.0040	0.1490
1.54	-0.0234	0.0311	-0.0017	0.1854	1.91	-0.0183	0.0208	-0.0537	0.1556
1.55	-0.0611	0.0174	-0.0716	0.1555	1.92	-0.1923	0.0118	0.0552	0.1836
1.56	-0.0479	0.0101	-0.0280	0.1302	1.93	-0.2813	0.0125	0.1123	0.1762
1.57	-0.0258	0.0190	0.1571	0.1350	1.94	-0.2057	0.0138	0.0176	0.1260
1.58	-0.0462	0.0102	0.2849	0.1477	1.95	-0.0417	0.0129	-0.0620	0.1103
1.59	-0.0593	0.0408	0.1888	0.1529	1.96	0.0551	0.0207	-0.0013	0.1106
1.60	0.0313	0.0816	-0.0275	0.1562	1.97	0.0126	0.0317	0.0849	0.1058
1.61	0.1642	0.0599	-0.1212	0.1586	1.98	-0.0857	0.0276	0.0599	0.1178
1.62	0.1095	0.0578	-0.0341	0.1449	1.99	-0.1046	0.0170	-0.0249	0.1146
1.63	-0.1879	0.1385	0.0456	0.1309	2.00	-0.1345	0.0189	-0.0377	0.1019
1.64	-0.3979	0.0693	-0.0208	0.1379					
1.65	-0.1919	0.1355	-0.1109	0.1767					
1.66	0.2459	0.2043	-0.0514	0.2037					
1.67	0.3917	0.0648	0.0834	0.1320					
1.68	0.0619	0.1671	0.0719	0.0944					
1.69	-0.3516	0.1739	-0.1097	0.1719					
1.70	-0.4007	0.0455	-0.2392	0.1492					
1.71	-0.1233	0.1659	-0.1592	0.1636					
1.72	0.0828	0.1279	0.0061	0.1991					
1.73	0.0063	0.0239	0.0217	0.1482					
1.74	-0.1568	0.0869	-0.1318	0.0973					
1.75	-0.1375	0.0402	-0.2274	0.1087					
1.76	0.0402	0.0437	-0.1234	0.1389					
1.77	0.1442	0.0636	0.0292	0.1559					
1.78	0.0793	0.0227	0.0322	0.1234					
1.79	-0.0118	0.0328	-0.0400	0.0968					
1.80	0.0308	0.0493	0.0553	0.1112					
1.81	0.1822	0.0362	0.3563	0.1141					
1.82	0.2756	0.0177	0.5815	0.1455					
1.83	0.1982	0.0140	0.4298	0.1763					
1.84	0.0118	0.0175	-0.0556	0.1499					

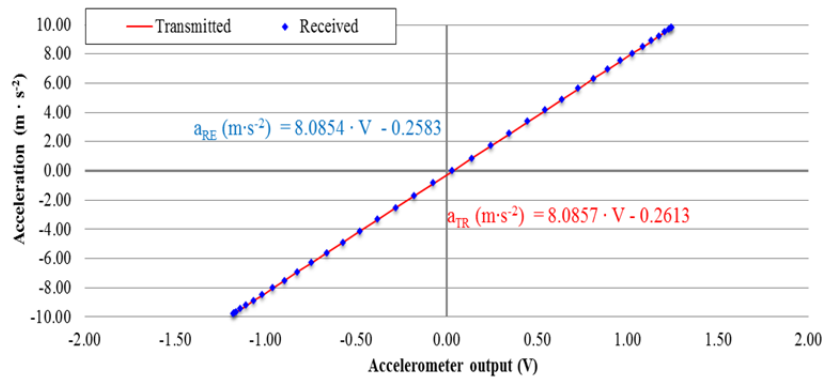


Fig. A.1 - Calibration chart when receiver is 10 m away from transmitter

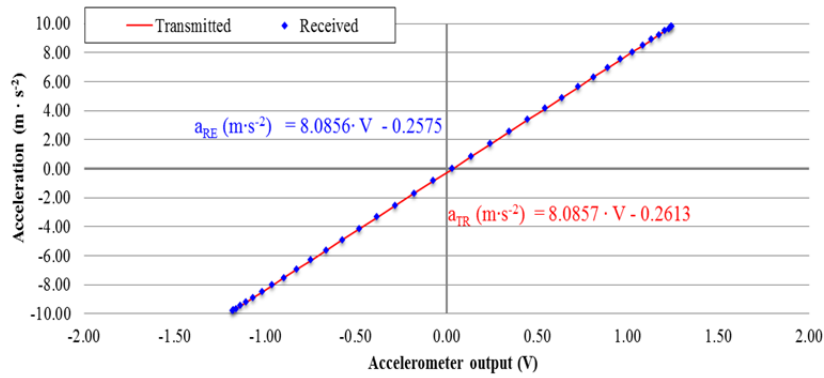


Fig. A.2 - Calibration chart when receiver is 20 m away from transmitter

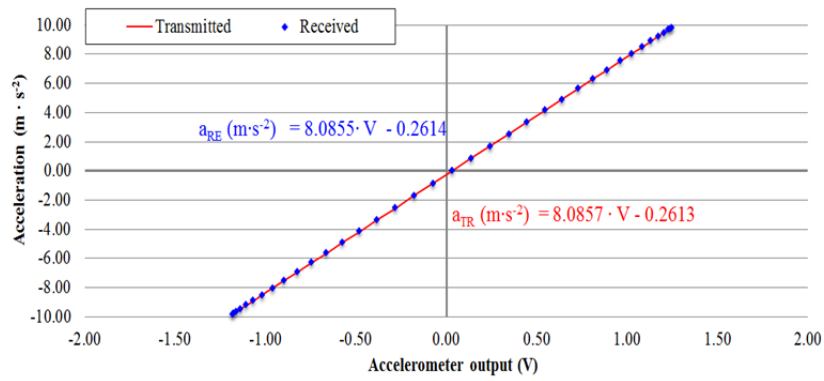


Fig. A.3 - Calibration chart when receiver is 25 m away from transmitter

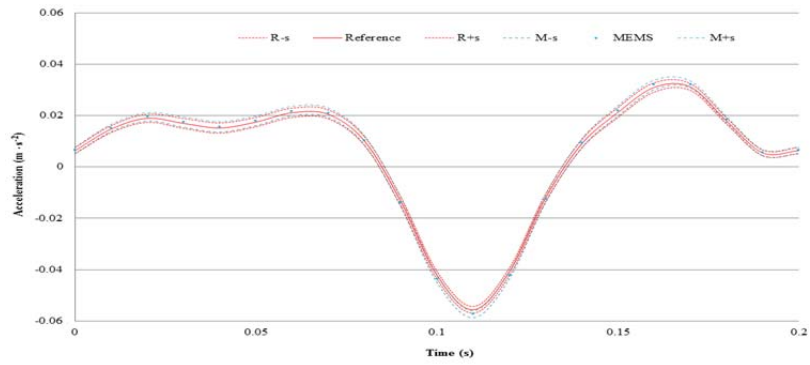


Fig. A.4 - Comparison of measurement uncertainties (5 Hz)

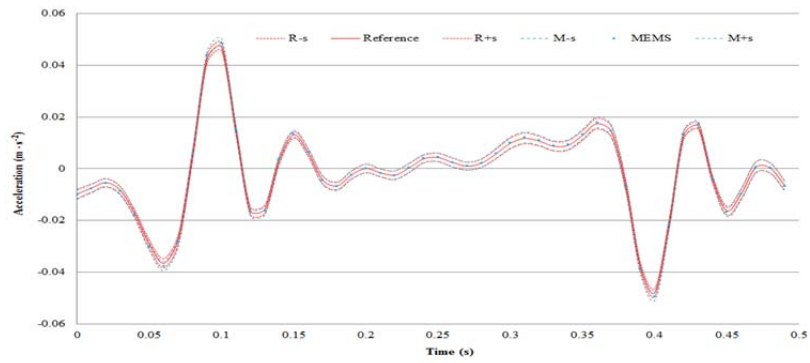


Fig. A.5 - Comparison of measurement uncertainties (2 Hz)

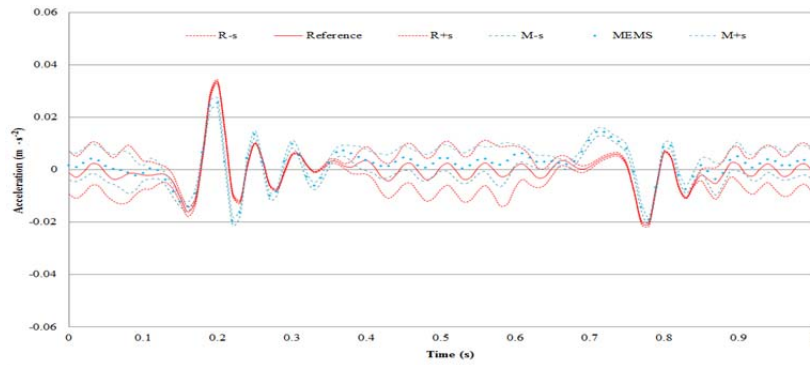


Fig. A.6 - Comparison of measurement uncertainties (1 Hz)

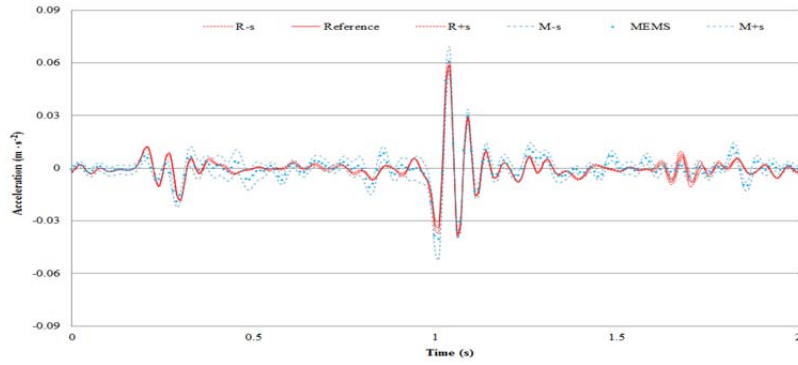


Fig. A.7 - Comparison of measurement uncertainties (0.5 Hz)

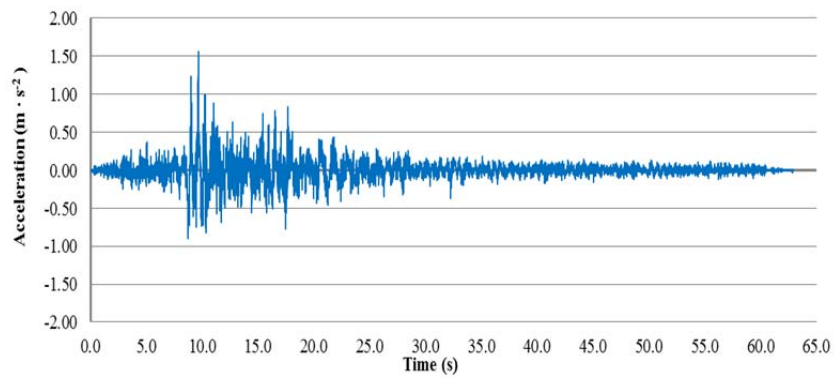


Fig. A.8 – Corbin's simulated earthquake acceleration time-history

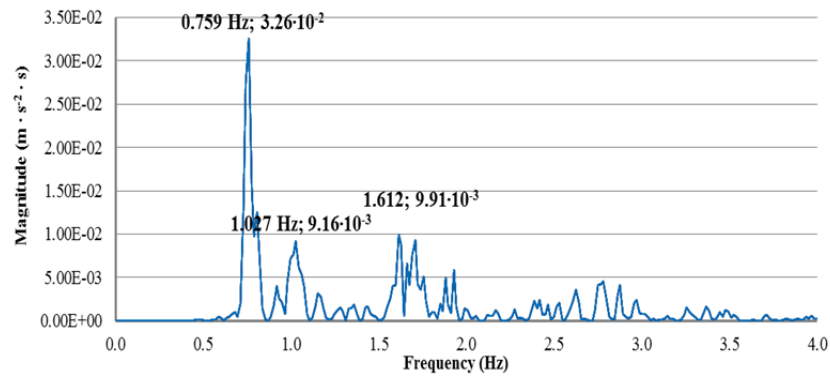


Fig. A.9 – Corbin's simulated earthquake frequency response

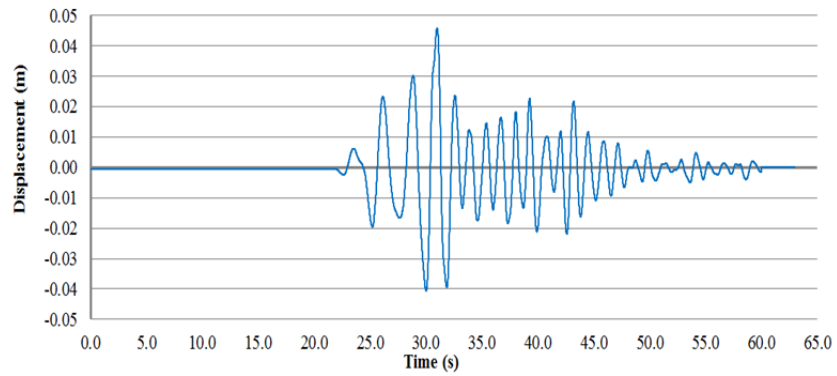


Fig. A.10 – Pinnacle displacement measured with the LVDT

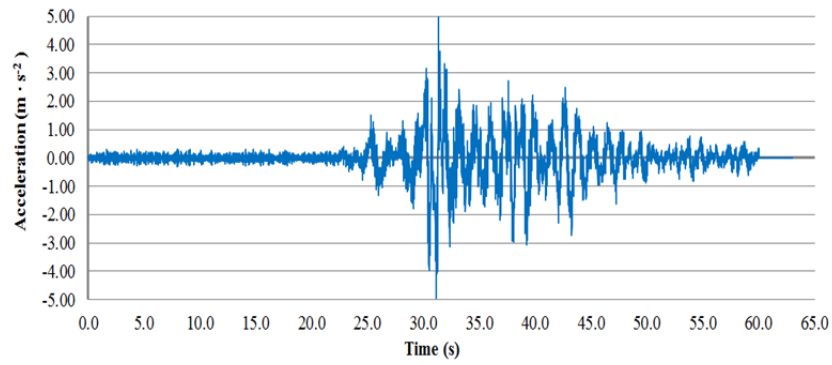


Fig. A.11 – Acceleration time-history derived from the LVDT readings

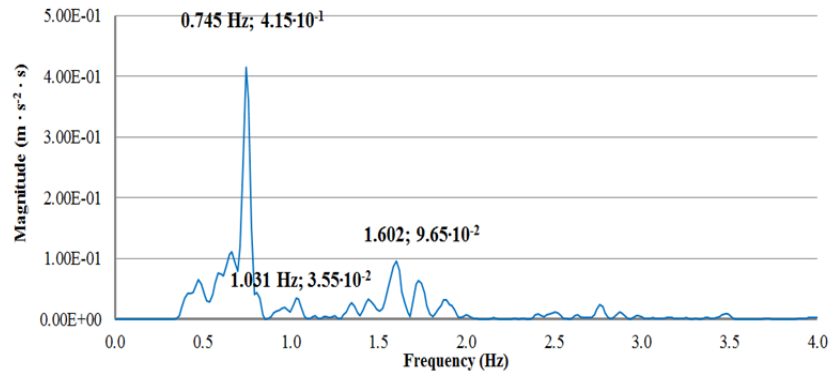


Fig. A.12 – Acceleration frequency response derived from the LVDT readings

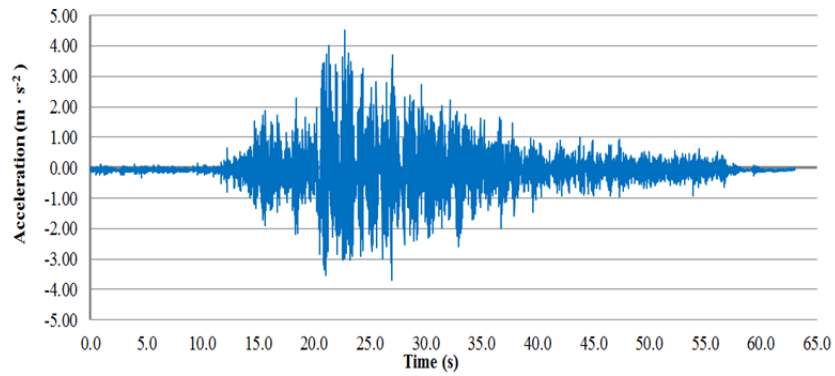


Fig. A.13 – Time-history recorded with the MEMS sensor

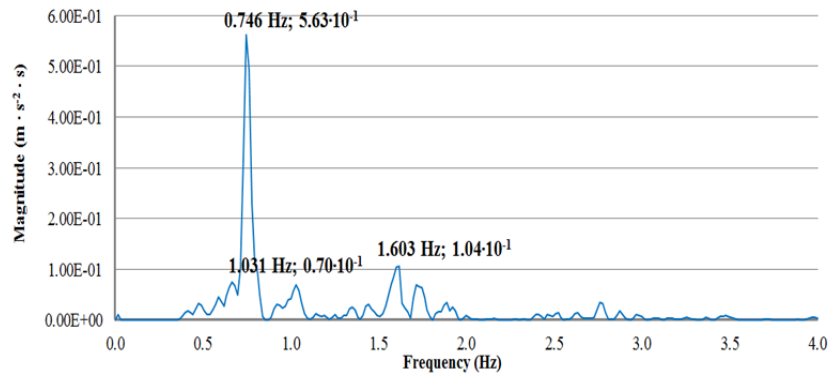


Fig. A.14 – Frequency response recorded with the MEMS sensor

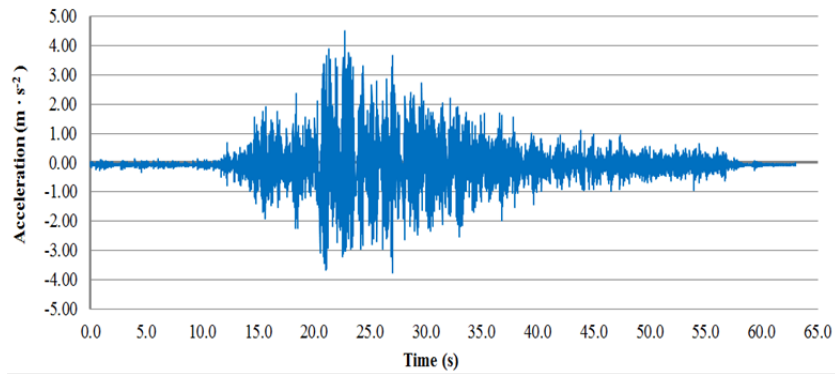


Fig. A.15 – Time-history recorded with the reference sensor

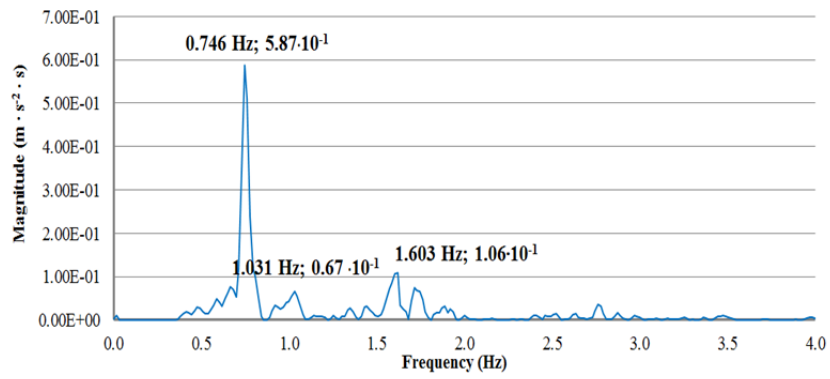


Fig. A.16 – Frequency response recorded with the reference sensor

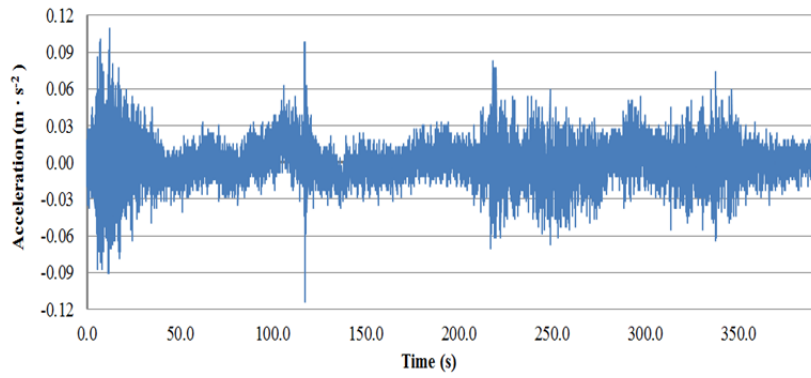


Fig. A.17 – Time-history recorded during the quasi-static test

REFERENCES

- [1] Lalanne, C. *Mechanical Vibration and Shock Analysis*. Vol. 2. Hoboken, NJ: Wiley, 2009.
- [2] McConnell, K. G., and P. S. Varoto. *Vibration Testing: Theory and Practice*. 2nd ed. Hoboken, NJ: John Wiley & Sons, 2008.
- [3] Thompson, D. J. *Railway Noise and Vibration: Mechanisms, Modeling and Means*. 1st ed. Amsterdam: Elsevier, 2009.
- [4] Crocker, M. J. *Handbook of Noise and Vibration Control*. Hoboken, NJ: Wiley, 2007.
- [5] Piersol, A. G., T. L. Paez, and C. M. Harris. *Harris' Shock and Vibration Handbook*. 6th ed. New York: McGraw-Hill, 2010.
- [6] Bishop, R. E. D., and C. D. Johnson. *Mechanics of Vibration*. 3rd ed. Cambridge: Cambridge Univ, 2011.
- [7] Vierck, R. K. *Vibration Analysis. 2d Ed.* New York: Crowell, 1979.
- [8] Ingard, K. U. *Notes on Acoustics*. Hingham, MA: Infinity Science, 2008.
- [9] Ginsberg, J. H. *Mechanical and Structural Vibrations: Theory and Applications*. 1st ed. New York: John Wiley & Sons, 2001.
- [10] Doderò, N., P. Baroncini, and R. Manfredi. *Nuovi Elementi Di Matematica: Per Il Triennio Dei Licei*. Vol. 3. Milano: Ghisetti e Corvi, 1997.
- [11] Abramowitz, M., and I. A. Stegun. *Handbook of Mathematical Functions: With Formulas, Graphs, and Mathematical Tables*. 9th ed. New York: Dover Publications, 1970.
- [12] Adhikari, S. *Structural Dynamic Analysis with Generalized Damping Models: Identification*. Hoboken, NJ: Wiley, 2013.
- [13] Santacroce, J. P. "Baseline Experiments on Columbus Damping Due to Rotational Slip." Thesis. Air Force Institute of Technology, 1992.

- [14] Córdova, C. C. J. *Elastodynamics with Hysteretic Damping*. Delft, Netherlands: DUP Science, 2002.
- [15] Rudin, W. *Real and Complex Analysis*. New York: McGraw-Hill, 1974.
- [16] Dodero, N., P. Baroncini, and R. Manfredi. *Nuovi Elementi Di Matematica: Per Il Triennio Dei Licei*. Vol. 2. Milano: Ghisetti e Corvi, 1997.
- [17] *ASCE'S 2013 Report Card for America's Infrastructure*. Rep. American Society of Civil Engineering, 19 Mar. 2013. Available online: <http://www.infrastructurereportcard.org> (accessed on 24 April 2014).
- [18] Buzdugan, Gh, E. Mihăilescu, and M. Radeş. *Vibration Measurement*. Dordrecht: M. Nijhoff, 1986.
- [19] Serridge, M., and T. R. Licht. *Piezoelectric Accelerometer and Vibration Preamplifier Handbook*. Nærum, Denmark: Brüel & Kjær, 1986.
- [20] Marín, P. J., and N. Garatachea. "Accelerometers Types and Applications." *Accelerometers: Principles, Structure and Applications*. Hauppauge, NY: Nova Science, 2013. 10 – 36.
- [21] *Data Acquisition Handbook*. Santa Clara, CA: Measurement Computing, 2013. Print. Available online: <http://www.mccdaq.com/support/data-acquisition-handbook.aspx> (accessed on: 26 April 2014).
- [22] Sill, R. D., and E. J. Seller. *Accelerometer Transverse Sensitivity Measurement Using Planar Orbital Motion*. 77th Shock and Vibration Symposium, Monterey, CA, USA, 2006, 126 – 135.
- [23] Bono, R. W., and E. J. Seller. "The Effect of High Transverse Inputs on Accelerometer Calibration." *Cal Lab-International Journal of Metrology* 18.1 (2011): 31 - 40.
- [24] Norton, H. N. *Handbook of Transducers for Electronic Measuring Systems*. Englewood Cliffs, NJ: Prentice-Hall, 1969.
- [25] Pedro, J. C., and N. B. Carvalho. *Intermodulation distortion in microwave and wireless circuits*. New York: Artech House, 2002.
- [26] Liu, C. *Foundations of MEMS*. 2nd ed. Upper Saddle River, NJ: Prentice Hall, 2006.

- [27] Smith, C. S. "Piezoresistance effect in germanium and silicon." *Physical review* 94.1 (1954): 42 – 59.
- [28] Kanda, Y. "Piezoresistance effect of silicon." *Sensors and Actuators A: Physical* 28.2 (1991): 83-91.
- [29] Doll, J. C., and B. Pruitt. *Piezoresistor Design and Applications*. New York: Springer, 2013.
- [30] Ekelof, S. "The genesis of the Wheatstone bridge." *Engineering Science and Education Journal* 10.1 (2001): 37-40.
- [31] Vlassis, S., S. Siskos, and Th. Laopoulos. "A piezoresistive pressure sensor interfacing circuit." *Instrumentation and Measurement Technology Conference, 1999. IMTC/99. Proceedings of the 16th IEEE*. Vol. 1. IEEE, 1999, 303 - 308.
- [32] Angell, J. B., P. W. Barth, and S. C. Terry. "Silicon micromechanical devices." *Scientific American* 248 (1983): 44-55.
- [33] Bao, M. *Micro Mechanical Transducers: Pressure Sensors, Accelerometers, and Gyroscopes*. Amsterdam: Elsevier, 2000.
- [34] Baxter, L. K. *Capacitive Sensors: Design and Applications*. New York: IEEE, 1997.
- [35] Gardner, J. W., V. K. Varadan, and O. O. Awadelkarim. *Microsensors, MEMS, and Smart Devices*. Chichester, NY: Wiley, 2001.
- [36] Kaajakari, V. *Practical MEMS*. Las Vegas, NV: Small Gear Publications, 2009.
- [37] Boyes, W. *Instrumentation Reference Book*. Boston: Butterworth-Heinemann, 2003.
- [38] Harun, S. W., H. Ahmad, H. Z. Yang, and M. Yasin. *Fiber Optic Displacement Sensors and Their Applications*. N.p.: INTECH Open Access, (2012): 359 - 393.
- [39] Udd, E., and W. B. Spillman. *Fiber Optic Sensors: An Introduction for Engineers and Scientists*. 2nd ed. Hoboken, NJ: John Wiley & Sons, 2011.

- [40] Antunes, P., C. Leitão, H. Rodrigues, R. Travanca, J. L. Pinto, A. Costa, H. Varum, and P. André. "Optical Fiber Bragg Grating Based Accelerometers and Applications." *Accelerometers: Principles, Structure and Applications*. Hauppauge, NY: Nova Science, 2013: 37 – 60.
- [41] Corelli, D., and M. Bakewell. "Vibration Accelerometers - Shear vs Compression Designs." *ME Maintenance & Engineering*. Vol. 8, Issue 5: 19 – 20. September/October 2008. Available online: <http://www.maintenanceonline.co.uk/maintenanceonline/magazine-pdfs/Sept-08.pdf> (accessed on: 28 April 2014).
- [42] Gautschi, G. *Piezoelectric Sensorics: Force, Strain, Pressure, Acceleration and Acoustic Emission Sensors, Materials and Amplifiers*. Berlin: Springer, 2002.
- [43] Levinzon, F. *Piezoelectric Accelerometers with Integral Electronics*. New York: Springer, 2014.
- [44] Chu, A. "Choosing the Right Type of Accelerometers." *Measurement Specialties*: 1 – 5. Available online: http://www.yeint.fi/pr/pr/files/Choosing_the_Right_Type_of_Accelerometers.pdf (accessed on: 28 April 2014).
- [45] Alonso, M., and E. J. Finn. *Physics*. Wokingham, England: Addison-Wesley Pub. 1992.
- [46] Allen, J. J. *Micro Electro Mechanical System Design*. Boca Raton, FL: Taylor & Francis, 2005.
- [47] Kovacs, G. T.A. *Micromachined Transducers Sourcebook*. Boston, MA: McGraw-Hill, 1998.
- [48] Gad-el-Hak, M. *The MEMS Handbook*. Boca Raton, FL: Taylor & Francis, 2002.
- [49] Schein, L. B. and G. S. P. Castle. "Triboelectricity." *Wiley Encyclopedia of Electrical and Electronics Engineering*. 1999. 1 - 14. Available online: <http://onlinelibrary.wiley.com/doi/10.1002/047134608X.W3233/abstract> (accessed on: 30 April 2014).
- [50] Sohn, H., C. R. Farrar, M. H. Francois, J. C. Jerry, D. S. Devin, W. S. Daniel, and R. N. Brett. *A review of structural health monitoring literature: 1996-2001*. Los Alamos, NM: Los Alamos National Laboratory, 2004. Available online: http://institute.lanl.gov/ei/shm/pubs/LA_13976_MSa.pdf (accessed on 18 July 2014).

- [51] Park, G., H. Sohn, C. R. Farrar, and D. J. Inman. "Overview of piezoelectric impedance-based health monitoring and path forward." *Shock and Vibration Digest* 35.6 (2003): 451-464.
- [52] Bhalla, S., and C. K. Soh. "Structural health monitoring by piezo-impedance transducers. II: applications." *Journal of Aerospace Engineering* 17.4 (2004): 166-175.
- [53] Park, S., J. J. Lee, C. B. Yun, and D. J. Inman. "Electro-mechanical impedance-based wireless structural health monitoring using PCA-data compression and k-means clustering algorithms." *Journal of Intelligent Material Systems and Structures* (2008): 509 - 520.
- [54] Annamdas, V. G.M, and M. A. Radhika. "Electromechanical impedance of piezoelectric transducers for monitoring metallic and non-metallic structures: A review of wired, wireless and energy-harvesting methods." *Journal of Intelligent Material Systems and Structures* (2013): 1021–1042.
- [55] Kim, J.W., C. Lee, S. Park, and K. T. Koh. "Real-time strength development monitoring for concrete structures using wired and wireless electro-mechanical impedance techniques" *KSCE Journal of Civil Engineering* (2013): 1432–1436.
- [56] Lynch, J. P., and K. J. Loh. "A summary review of wireless sensors and sensor networks for structural health monitoring." *Shock and Vibration Digest* 38.2 (2006): 91-130.
- [57] Lynch, J. P. "An overview of wireless structural health monitoring for civil structures." *Philosophical Transactions of the Royal Society A: Mathematical, Physical and Engineering Sciences* 365.1851 (2007): 345-372.
- [58] Cho, S., C. B. Yun, J. P. Lynch, A. T. Zimmerman, and B. F. Spencer Jr. "Smart wireless sensor technology for structural health monitoring of civil structures." *Steel Structures* 8.4 (2008): 267-275.
- [59] Chopra, A. K. *Dynamics of Structures: Theory and Applications to Earthquake Engineering*. 4th ed. Boston: Prentice Hall, 2012.
- [60] Pister, K. S. J. *Smart dust BAA97-43 Proposal Abstract*. Berkeley, CA: UC Berkeley, 1997. Available online: <http://robotics.eecs.berkeley.edu/~pister/SmartDust/SmartDustBAA97-43-Abstract.pdf> (accessed on 2 September 2014).
- [61] Straser, E. G., and A. S. Kiremidjian. *A modular, wireless damage monitoring system for structures*. Stanford, CA, USA: John A. Blume Earthquake Engineering Center, 1998.

- [62] Bennett, R., B. Hayes-Gill, J. A. Crowe, R. Armitage, D. Rodgers, and A. Hendroff. "Wireless monitoring of highways." *1999 Symposium on Smart Structures and Materials*. International Society for Optics and Photonics, 1999: 173 – 182.
- [63] Lynch, J. P., K. H. Law, A. S. Kiremidjian, J. E. Carryer, T. W. Kenny, A. Partridge, and A. Sundararajan. "Validation of a wireless modular monitoring system for structures". *9th Annual International Symposium on Smart Structures and Materials*. International Society for Optics and Photonics, 2002: 124 – 135.
- [64] Lynch, J. P., K. H. Law, A. S. Kiremidjian, T. W. Kenny, J. E. Carryer, and A. Partridge. "The design of a wireless sensing unit for structural health monitoring." *Proceedings of the 3rd International Workshop on Structural Health Monitoring*. 2001: 12 – 14.
- [65] Lynch, J. P., A. Partridge, K. H. Law, T. W. Kenny, A. S. Kiremidjian, and J. E. Carryer. "Design of piezoresistive MEMS-based accelerometer for integration with wireless sensing unit for structural monitoring." *Journal of Aerospace Engineering* 16.3 (2003): 108-114.
- [66] Liu, C. R., L. Zhou, X. Chen, and S. T. Mau. "Wireless sensors for structural monitoring." *Strong Motion Instrumentation for Civil Engineering Structures*. Springer Netherlands, 2001: 253-266.
- [67] Wang, D. H., and W. H. Liao. "Instrumentation of a wireless transmission system for health monitoring of large infrastructures." *Instrumentation and Measurement Technology Conference, 2001. IMTC 2001. Proceedings of the 18th IEEE*. Vol. 1. IEEE, 2001: 634 – 639.
- [68] Mitchell, K., N. Dang, P. Liu, V. S. Rao, and H. J. Pottinger. "Web-controlled wireless network sensors for structural health monitoring." *SPIE's 8th Annual International Symposium on Smart Structures and Materials*. International Society for Optics and Photonics, 2001: 234 - 243.
- [69] Kottapalli, V. A., A. S. Kiremidjian, J. P. Lynch, E.D. Carryer, T. W. Kenny, K. H. Law, and Y. Lei. "Two-tiered wireless sensor network architecture for structural health monitoring." *SPIE's 10th Annual International Symposium on Smart Structures and Materials*. International Society for Optics and Photonics, 2003: 8 - 13.
- [70] Lynch, J.P, K.H. Law, A. S. Kiremidjian, E. D. Carryer, C. R. Farrar, H. Sohn, and J. R. Wait. "Design and performance validation of a wireless sensing unit for structural monitoring applications." *Structural Engineering and Mechanics* 17.3-4 (2004): 393-408.

- [71] Lynch, J. P., G. Parra-Montesinos, B. A. Canbolat, and T. C. Hou. "Real-time damage prognosis of high-performance fiber reinforced cementitious composite structures." *Proc. Advances in Structural Engineering and Mechanics (ASEM'04)*, Seoul, Korea (2004).
- [72] Ou, J., H. Li, and Y. Yu. "Development and performance of wireless sensor network for structural health monitoring." *Smart Structures and Materials*. International Society for Optics and Photonics, 2004: 765 - 773.
- [73] Institute of Electrical and Electronic Engineers (IEEE), 802.15.4-2003 - IEEE Standard for Information Technology - Telecommunications and Information Exchange Between Systems - Local and Metropolitan Area Networks Specific Requirements Part 15.4: Wireless Medium Access Control (MAC) and Physical Layer (PHY) Specifications for Low-Rate Wireless Personal Area Networks (LR-WPANs). Available online: <http://ieeexplore.ieee.org> (accessed on 3 September 2014).
- [74] Sazonov, E., K. Janoyan, and R. Jha. "Wireless intelligent sensor network for autonomous structural health monitoring." *Smart Structures and Materials*. International Society for Optics and Photonics, 2004: 305 - 314.
- [75] Lynch, J.P. "An overview of wireless structural health monitoring for civil structures." *Philosophical Transactions of the Royal Society A: Mathematical, Physical and Engineering Sciences* 365.1851 (2007): 345-372.
- [76] Spencer, B. F., M. E. Ruiz Sandoval, and N. Kurata. "Smart sensing technology: opportunities and challenges." *Structural Control and Health Monitoring* 11.4 (2004): 349-368.
- [77] Sabato, A. *Configurazione E Messa a Punto Di Apparecchiature Sperimentali per L'analisi Dei Moti Vibrazioni E Comparazione Con Strumentazione Di Tipo Tradizionale*. M.S. Diss. Università Della Calabria, 2010.
- [78] Zhao, F., and L. J. Guibas. *Wireless Sensor Networks: An Information Processing Approach*. Amsterdam: Morgan Kaufmann, 2004.
- [79] Madan, V., and S. N. R. Reddy. "Review of Wireless Sensor Mote Platforms". *VSDR International Journal of Electrical, Electronics, and Communication Engineering*. 2.2 (2012): 50 – 55.
- [80] Leopold, M. "Sensor Network Motes: Portability and Performance." Ph. D. Diss. Københavns Universitet, 2008. Available online: <http://www.diku.dk/~leopold> (accessed on 6 September 2014).

- [81] Hill, J. L., and D. E. Culler. "Mica: A wireless platform for deeply embedded networks." *Micro, IEEE* 22.6 (2002): 12-24.
- [82] Levis, P., S. Madden, D. Gay, J. Polastre, R. Szewczyk, A. Woo, and D. E. Culler. "The Emergence of Networking Abstractions and Techniques in TinyOS." Proc. of 1st conference on Symposium on Networked Systems Design and Implementation (NSDI '04) . Vol. 4. 2004.
- [83] Sabato, Ad., and Al. Sabato. "Construction and Validation of Small Electro-mechanical Vibration Sensors." *International Journal of Computational Methods and Experimental Measurements* 1.1 (2012): 72-79.
- [84] Kling, R. M." Intel Mote: an Enhanced Sensor Network Node" .*Proc. of the International Workshop on Advanced Sensors, Structural Health Monitoring and Smart Structures*. Keio University, Japan, 2003.
- [85] Agre, J. R., L. P. Clare, G. J. Pottie, and N. P. Romanov. "Development platform for self-organizing wireless sensor networks." *AeroSense'99*. International Society for Optics and Photonics, 1999: 257 - 268.
- [86] Shimmer – Wireless Sensor Networks. Available online: www.shimmersensing.com/, Datasheet (accessed on 10 September 2014).
- [87] TelosB – Telos Mote platform. Available online: http://www.memsic.com/userfiles/files/Datasheets/WSN/telosb_datasheet.pdf, Datasheet (accessed on 10 September 2014).
- [88] SunSpot – Main Board Technical Datasheet. Available online: <http://www.sunspotworld.com/docs/Yellow/eSPOT8ds.pdf>, Datasheet (accessed on 10 September 2014).
- [89] Kurata, N., B. F. Spencer, and M. Ruiz Sandoval. "Risk monitoring of buildings with wireless sensor networks." *Structural Control and Health Monitoring* 12.3-4 (2005): 315-327.
- [90] ADXL202 – Low-cost, Low-power, complete Dual-axis iMEMS Accelerometer. Available online: <http://www.analog.com/en/memsensors/mems-inertialsensors/adxl202/products/product.html>, Datasheet (accessed on 10 September 2014).
- [91] Ruiz Sandoval M. E., B. F. Spencer, and N. Kurata. "Development of a high sensitivity accelerometer for the Mica platform." *Proceedings of the 4th International Workshop on Structural Health Monitoring*. 2003.

- [92] 393B04: ICP Seismic Accelerometer. Available online: <http://www.pcb.com/products.aspx?m=393C> (accessed on 15 April 2014).
- [93] SD-1221: Low-noise Analog Accelerometer. Available online: <http://www.silicondesigns.com/pdfs/1221.pdf> (accessed on 12 September 2014).
- [94] Ruiz-Sandoval, M. E. ""Smart" Sensors for Civil Infrastructure Systems." P. hD Diss. U of Notre Dame, 2004. Available online: <http://etd.nd.edu/ETD-db/theses/available/etd05212004175346/unrestricted/RuizSandovalME052004.pdf>.
- [95] Glaser, S. D. "Some real-world applications of wireless sensor nodes." *Smart Structures and Materials*. International Society for Optics and Photonics, 2004: 344 – 355.
- [96] Mitrani, J., J. Goethals, and S. D. Glaser, Field Testing of Wireless Interactive Sensor Nodes, report submitted to Port and Airport Research Institute, February 13, 2002.
- [97] Pakzad, S.N.; S. Kim, G. L. Fenves, S. D. Glaser, D. E. Culler, and J. W. Demmel, Multi-purpose wireless accelerometer for civil infrastructure monitoring. *Proc. of 5th International Workshop on Structural Health Monitoring (IWSHM)*, 2005: 125–132.
- [98] Kim, S., S. N. Pakzad, D. E. Culler, J. W. Demmel, G. L. Fenves, S. D. Glaser, and M. TUron. "Health monitoring of civil infrastructures using wireless sensor networks." *Information Processing in Sensor Networks, 2007. IPSN 2007. 6th International Symposium on*. IEEE, 2007: 254 – 263.
- [99] Pakzad, S. N. "Development and deployment of large scale wireless sensor network on a long-span bridge." *Smart Structures and Systems* 6.5-6 (2010): 525-543.
- [100] Pakzad, S. N., G. L. Fenves, S. Kim, and D. E. Culler. "Design and implementation of scalable wireless sensor network for structural monitoring." *Journal of Infrastructure Systems* 14.1 (2008): 89-101.
- [101] Cho, S., C. B. Yun, J. P. Lynch, A.T. Zimmerman, B. F. Spencer Jr., T. Nagayama. "Smart wireless sensor technology for structural health monitoring of civil structures." *Steel Structures* 8.4 (2008): 267-275.

- [102] Wang, Y., J. P. Lynch, and K. H. Law. "A wireless structural health monitoring system with multithreaded sensing devices: design and validation." *Structure and Infrastructure Engineering* 3.2 (2007): 103-120.
- [103] W352C67: ICP Miniature Accelerometer. Available online: <https://www.pcb.com/Products.aspx?m=352C67> (accessed on 15 April 2014).
- [104] Whelan, M., and K. Janoyan. "Design of a robust, high-rate wireless sensor network for static and dynamic structural monitoring." *Journal of Intelligent Material Systems and Structures* (2008): 849–863.
- [105] TMote Sky – Ultra low power IEEE 802.15.4 compliant wireless sensor module. Available online: <http://www.eecs.harvard.edu/~konrad/projects/shimmer/references/tmote-sky-datasheet.pdf>, Datasheet (accessed on 15 September 2014).
- [106] LIS2I02AL – MEMS Inertial Sensor. Available online: <http://www.st.com/web/en/resource/technical/document/datasheet/CD00002102.pdf>, Datasheet (accessed on 15 September 2014).
- [107] Jo, H., B. F. Spencer Jr., and T. Nagayama. "Development of high-sensitivity accelerometer board for structural health monitoring." *SPIE Smart Structures and Materials+ Nondestructive Evaluation and Health Monitoring*. International Society for Optics and Photonics, 2010: 764 - 776.
- [108] Jo, H., T. Nagayama, and B. F. Spencer Jr. "Development and application of high-sensitivity wireless smart sensors for decentralized stochastic modal identification." *Journal of Engineering Mechanics* 138.6 (2011): 683-694.
- [109] ITS400 – Intel Sensor Board. Available online: <http://wsn.cse.wustl.edu/images/0/07/Intel.ITS400.DataSheet.pdf>, Datasheet (accessed on 15 September 2014).
- [110] LIS3L02DQ – MEMS Inertial Sensor. Available online: <http://www.st.com/web/en/resource/technical/document/datasheet/CD00005106.pdf>, Datasheet (accessed on 15 September 2014).
- [111] Rice, J. A., K. Mechitov, S. H. Sim, T. Nagayama, S. Jang, R. Kim, B. F. Spencer, Jr., and Y. Fujino. "Flexible smart sensor framework for autonomous structural health monitoring." *Smart Structures and Systems* 6.5-6 (2010): 423-438.

- [112] LIS344ALH - MEMS Inertial Sensor. Available online: <http://www.st.com/web/en/resource/technical/document/datasheet/CD00182781.pdf>, Datasheet (accessed on 15 September 2014).
- [113] QF4A512 – 4 Channel Programmable Signal Converter. Available online: <http://www.quickfiltertech.com/files/QF4A512revD8.pdf>, Datasheet (accessed on 15 September 2014).
- [114] Jang, S., H. Jo, S. Cho, K. Mechitov, J. A. Rice, S. H. Sim, G. Agha. "Structural health monitoring of a cable-stayed bridge using smart sensor technology: deployment and evaluation." *Smart Structures and Systems* 6.5-6 (2010): 439-459.
- [115] Celebi, M. "Seismic instrumentation of buildings (with emphasis on federal buildings)." *Special GSA/USGS Project, an administrative report* (2002).
- [116] Farrar, C. R., and K. Worden. "An introduction to structural health monitoring." *Philosophical Transactions of the Royal Society A: Mathematical, Physical and Engineering Sciences* 365.1851 (2007): 303-315.
- [117] Mainwaring, A, E. D. Culler, J. Polastre, R. Szewczyk, and J. Anderson. "Wireless sensor networks for habitat monitoring." *Proceedings of the 1st ACM international workshop on Wireless sensor networks and applications*. ACM, 2002: 88.97.
- [118] Juang, P., H. Oki, Y. Wang, M. Martonosi, L. S. Phe, and D. Rubenstein. "Energy-efficient computing for wildlife tracking: Design tradeoffs and early experiences with ZebraNet." *ACM Sigplan Notices*. Vol. 37. No. 10. ACM, 2002: 96 - 107.
- [119] Yarvis, M. D., W. S. Conner, L. Krishnamurthy, J. Chabra, B. Elliot, and A. Mainwaring. "Real-world experiences with an interactive ad hoc sensor network." *Parallel Processing Workshops, 2002. Proceedings. International Conference on*. IEEE, 2002: 143 - 151.
- [120] Camilli, A., C. E. Cugnasca, A. M. Saraiva, A. R. Hirakawa, and P. L. Corrêa. "From wireless sensors to field mapping: Anatomy of an application for precision agriculture." *Computers and Electronics in Agriculture* 58.1 (2007): 25-36.
- [121] Burrell, J., T. Brooke, and R. Beckwith. "Vineyard computing: Sensor networks in agricultural production." *Pervasive Computing, IEEE* 3.1 (2004): 38-45.

- [122] Varshney, U. "Pervasive healthcare and wireless health monitoring." *Mobile Networks and Applications* 12.2-3 (2007): 113-127.
- [123] Malinowski, M., M. Moskwa, M. Feldmeier, M. Laibowitz, and J. A. Paradiso. "CargoNet: a low-cost micropower sensor node exploiting quasi-passive wakeup for adaptive asynchronous monitoring of exceptional events." *Proc. of the 5th international conference on Embedded networked sensor systems*. ACM, 2007: 145 - 159.
- [124] Farrar, C. R., and N. A. J. Lieven. "Damage prognosis: the future of structural health monitoring." *Philosophical Transactions of the Royal Society A: Mathematical, Physical and Engineering Sciences* 365.1851 (2007): 623-632.
- [125] Dargie, W. "Dynamic power management in wireless sensor networks: State-of-the-art." *Sensors Journal, IEEE* 12.5 (2012): 1518-1528.
- [126] Mascareñas, D., D. Flynn, C. R. Farrar, G. Park, and M. Todd. "A mobile host approach for wireless powering and interrogation of structural health monitoring sensor networks." *Sensors Journal, IEEE* 9.12 (2009): 1719-1726.
- [127] SF1600S.A—SF1600SN.A: Single Axis Best in Class Seismic Accelerometer. Available online: [http://www.colibrys.ch/files/pdf/products/30S%20SF1600S%20A%2011%](http://www.colibrys.ch/files/pdf/products/30S%20SF1600S%20A%2011%20) (accessed on 15 April 2014).
- [128] Cuniberti, E., L. De Lucchi, *Elettronica Analogica*. Torino: Petrini, 2000.
- [129] Levine, W. S. *Control System Applications*. Boca Raton, FL: CRC, 2011.
- [130] AD650: Voltage-to-Frequency and Frequency-to-Voltage Converter. Available online: http://www.analog.com/static/imported-files/data_sheets/AD650, Datasheet (accessed on 15 April 2014).
- [131] Hellerstein, J. *Feedback Control of Computing Systems*. New York, NY: IEEE, 2004.
- [132] Thornhill, N.F, R. Zunino, and S. Rovetta. *Elettronica Analogica*. Milano: McGraw-Hill, 1999.
- [133] Wang, D.H, and W.H. Liao. "Wireless transmission for health monitoring of large structures." *Instrumentation and Measurement, IEEE Transactions on* 55.3 (2006): 972-981.
- [134] Sinha, A., and A. Chandrakasan. "Dynamic power management in wireless sensor networks." *Design & Test of Computers, IEEE* 18.2 (2001): 62-74.

- [135] De Gloria, A. *Fondamenti di Progettazione Elettronica Analogica e Digitale*. Milano: Franco Angeli: Milano, 2002.
- [136] TL082 - Wide Bandwidth Dual JFET Input Operational Amplifier. Available Online: <http://www.ti.com/lit/ds/symlink/tl082-n.pdf>, Datasheet (accessed on 20 September 2014).
- [137] TMR3 1222E: Traco-Power DC/DC Converters TMR 3 Series, 3 Watt. Available online: <http://www.tracopower.com/products/tmr3.pdf> (accessed on 21 January 2014).
- [138] RD-0512D: Recom DC/DC Converters, 2 Watt. Available online: <http://www.recom-power.com/pdf/Econoline/RD.pdf> (accessed on 15 April 2014).
- [139] NI-USB6009 – Portable Data Acquisition. Available online: <http://sine.ni.com/nips/cds/view/p/lang/en/nid/201987>, Datasheet (accessed on 21 May 2014).
- [140] PWS4602 – Programmable DC Power Supply. Available online: <https://www.tektronix.com>, Datasheet (accessed on 15 April 2014).
- [141] Mechanical vibration and shock - Mechanical mounting of accelerometers. ISO Standards. ISO 5348:2007. International Organization for Standardization: Geneva, Switzerland, 2014.
- [142] Sujatha, C. *Vibration and Acoustics: Measurement and Signal Analysis*. New Delhi: Tata McGraw Hill Education Private, 2010.
- [143] Acoustics—Preferred Reference Values for Acoustical and Vibratory Levels. ISO Standards. ISO 1683-2:2008. International Organization for Standardization: Geneva, Switzerland, 2014.
- [144] Pressure fluids - Hydraulic oils - Part 2: HLP hydraulic oils; Minimum requirements. DIN 51524-2 (2006-04) Deutsches Institut für Normung: Berlin, Germany, 2014.
- [145] W352C67: ICP Miniature Accelerometer. Available online: <https://www.pcb.com/Products.aspx?m=352C67> (accessed on 15 April 2014).
- [146] Mechanical vibration and shock -- Vibration of fixed structures -- Guidelines for the measurement of vibrations and evaluation of their effects on structures. ISO Standards. ISO 4866: 2010. International Organization for Standardization: Geneva, Switzerland, 2014.

[147] Mechanical vibration and shock -- Parameters to be specified for the acquisition of vibration data. ISO Standards. ISO 21289: 2008. International Organization for Standardization: Geneva, Switzerland, 2014.

[148] Mechanical vibration and shock -- Signal processing -- Part 1: General introduction. ISO Standards. ISO 18431-1:2005. International Organization for Standardization: Geneva, Switzerland, 2014.

[149] Mechanical vibration -- Evaluation of machine vibration by measurements on non-rotating parts - Part 6: Reciprocating machines with power ratings above 100 kW. ISO 10816-6:1995. International Organization for Standardization: Geneva, Switzerland, 2014.

[150] <http://earthquake.usgs.gov/earthquakes/eqinthenews/2011/se082311a/>

[151] Sigurdardottir, D. H., and B. Glisic, "Measures of structural art: A case study using Streicker Bridge," in Khaled Mahmoud (Ed.) "Durability of Bridge Structures" – Proc. NYCBC, New York City, NY, 2013, pp. 275-284.

[152] Sigurdardottir, D. H., D. Hubbell, J. P.S. Afonso, and B. Glisic. Streicker Bridge: Assessment of Structural Health Condition Through Static and Dynamic Monitoring. Proc. *International Conference on Structural Health Monitoring of Intelligent Infrastructure, (SHMII)*, Cancun, Mexico (2011).

[153] Sigurdardottir, D. H., B. Glisic, and J. P. S. Afonso. "Streicker Bridge in Its Early Years: Structural Identification and Damage Characterization." *Transportation Research Board 92nd Annual Meeting*. No. 13-2714. 2013.

ACKNOWLEDGMENTS

First, I would like to thank my advisor, Professor Giuseppe Oliveti, that gave me the chance I needed to continue working on this project started a long time ago with my Master's dissertation. I will be always grateful to him for trusting my visionary idea and supporting me. Even if the topic of my research did not properly belong to his scientific field.

I would also like to thank Professor Giancarlo Fortino for opening my eyes to the beautiful world of Wireless Sensor Network systems. Nowadays, Engineering has become such a complex science that miscellaneous knowledge is indispensable. Mechanical and Civil Engineering topics are always more connected to Computer Sciences and Electronics.

Having an opportunity, while at Columbia University, to work for 18 months with some of the best researchers and professionals in the world has been a real honor to me. Many thanks are owed to Professor Maria Q. Feng for sharing her knowledge of sensors for Structural Health Monitoring and to her endless contribution of ideas which helped me in bettering the efforts to exploit my research. Furthermore, she gave me the opportunity to interact with the real-world engineering, proving that a Ph. D program is not only a mere intellectual display, but also an enriching journey through knowledge and experience. That period allowed me growing as a professional, as a researcher, and as a person especially.

I will be forever indebted to Doctor Vito Fabio, for helping me design and assemble the prototype, which laid the foundation for my research. His wide Electronics knowledge, together with his patience and availability, have been a milestone during this three years.

I am grateful to Engineer Francesco La Monaca for sharing with me, as a friend, his experience in signal processing. The design choices made for building the prototype comes from our endless chats.

I would also like to thank Adrian Brugger, Manager of the Carleton Laboratory at the Columbia University, and its staff for helping me in the flow-loop pipeline and stone pinnacle experiments. Also, special thanks are owed to Professor Branko Glisic, Doctor Dorotea Sigurdardottir, and Doctor Hiba Abdel-Jabber from the Civil and Environmental Engineering Department of the Princeton University, and the SHMlab at Princeton University. They have shared their research results and allowed me to use the Streicker Bridge in Princeton, NJ as real-world test-bed.

An endeavor of this nature and magnitude cannot be attempted without the support of a wide cast of family and friends. First I would like to thank my parents, Adolfo and Maria Pia, for their encouragements over the years and supporting during all of the challenges I have ever faced. My strength to see this task through the end serves as a tribute to them. My sister Tiziana, my brothers Massimiliano and Valerio, my grandmother Anna, and my aunt Antonella, they all have been incredibly supportive during this journey. They were always by my side, the living demonstration you are always home even when you live thousands of kilometers away.

Alessia and my “bro” Buk, for proving me special people exist, even when they are “an ocean” apart. Buk for tearing me a smile when I needed it, despite he was busy pretending to be a kind of Indiana Jones somewhere East of the civilized world’s end. Alessia for being the first one to believe I could achieve this result and never stop spurring me (even if her ways are still a mystery to me).

I want to express my deepest and sincere gratitude to all of my colleagues and friends, in the School of Engineering and Applied Sciences and in the Carleton Laboratory (Andrea, Dongming, Ekin, Janelle, Lindsay, Noureen, Sebastian, and Undrakh). The entire Columbia University experience would not have been the same without you.

This amazing journey, starting from the desperate study at the beginning - passing through the tears at Penn Station (when I felt alone and lost), the endless nights spent in underground laboratories, in shining libraries, or sitting in a living

room pretending to study - until now when I am smiling while writing this, is the proof that dreams may become true. I was so blessed for having crossed my existence with that of extraordinary people who, even with just a smile in an elevator, a joke during a break, a walk in the park at the sunset, or a simple special-moment, have always gave me the strength to continue. When amazing and special people surround you, limits you did not think you had can be pushed and overcome.

This dissertation is thanks to you all.

A. S.

This research is part of a PhD program funded at Università della Calabria, Italy by European Union social funds (FSE - Fondo Sociale Europeo) within the POR Calabria FSE 2007 - 2013 project. The experiments were carried out at the SMaRT Laboratory and the Carlton Laboratory, Department of Civil Engineering and Engineering Mechanics, Columbia University.